Mechanical Properties and High Temperature Deformation Behavior of Al–Cu–Mg Alloys Microalloyed with Sn

A Thesis Submitted in

Partial Fulfillment of the Requirements

for the Degree of

DOCTOR OF PHILOSOPHY

by

Sanjib Banerjee

(Roll No. 05610303)

DEPARTMENT OF MECHANICAL ENGINEERING

INDIAN INSTITUTE OF TECHNOLOGY GUWAHATI

GUWAHATI-781039, INDIA

August 2010

DEPARTMENT OF MECHANICAL ENGINEERING
INDIAN INSTITUTE OF TECHNOLOGY GUWAHATI
GUWAHATI-781039, INDIA

CERTIFICATE

It is certified that the work contained in the thesis entitled **"Mechanical Properties and High Temperature Deformation Behavior of Al–Cu–Mg Alloys Microalloyed with Sn"** submitted by **Mr. Sanjib Banerjee** to the Indian Institute of Technology Guwahati for the award of the degree of Doctor of Philosophy has been carried out under our supervision in the Department of Mechanical engineering, Indian Institute of Technology Guwahati. This work has not been submitted elsewhere for the award of any other degree or diploma.

31st August, 2010

Prof. P.S. Robi
Department of Mechanical Engineering
Indian Institute of Technology Guwahati
Guwahati – 781039, India

Prof. A. Srinivasan
Department of Physics
Indian Institute of Technology Guwahati
Guwahati – 781039, India

ACKNOWLEDGEMENTS

The joy and satisfaction that accompany the successful completion of any task would be incomplete without mentioning those who made it possible.

I would like to express my sincere appreciation to ***Prof. P.S. Robi*** *and* ***Prof. A. Srinivasan****, my advisors, mentors and friends, who have been a role model to me for the last five years. Their perpetual optimism is contagious, and they gave me the confidence to undertake and conquer the Ph.D process. Their persistent patience and friendliness in the moments of difficulties have always been remembered.*

I am also grateful to members of my doctoral committee, ***Prof. U.S. Dixit, Prof. A.K. Das*** *and* ***Prof. R. Ganesh Narayanan****, all of whom have shown interest in this work and provided countless advice, insightful comments and discussion. I am equally thankful to* ***Prof. Ujjal K. Saha****, who once acted as my administrative guide, for his help during my research work at IIT Guwahati.*

I thank ***Prof. Debabrata Chakraborty****, Head, Department of Mechanical Engineering for extending all the help during the research work. I am also grateful to all the faculty members of Mechanical Engineering Department for giving me a comfortable and active environment for pursuing my research.*

I would like to express my sense of gratitude to ***Dr. D. K. Sharma****, Assistant Workshop Superintendent and all the staffs of the workshop for extending their help in fabrication of the different experimental set-ups for this work. The undersigned is very much thankful for the cooperation and assistance received from the M.Tech student* ***Mr. Praveen Kumar Lakavath****. I sincerely acknowledge the assistance received from* ***Mr. Rituraj Saikia, Mr.Sanjib Sarma*** *and* ***Dr. Sidananda Sarma*** *in various experimental proceedings.*

The financial support of this research, which was provided by the Department of Mechanical Engineering, Indian Institute of Technology Guwahati, is gratefully acknowledged.

The most important support for this work came from my parents, ***Sri Sujit Kumar Banerjee*** *and* ***Smt. Indrani Banerjee****, for encouraging me to go still further at every points of life. I would like to thank my parents for all of their love and support through the years, especially at peak of the economy encouraged me to pursue Ph.D on a modest stipend.*

Last but certainly not least, I would like to express my wholehearted gratitude to my family members, classmates, friends and every individual who are associated with this Ph.D course for their help and support during my work.

I consider myself privileged and fortunate to work in the Indian Institute of Technology Guwahati.

Above all, I am thankful to the Almighty.

Dedicated to

My Mother,

Smt. Indrani Banerjee

Whose unending and unconditional love, blessings, encouragement and sacrifices were the chief ingredients of my success, whatever I have achieved, at each and every point of my career, since childhood…

And

My Father,

Sri Sujit Kumar Banerjee

For, without his love, blessings, encouragement, unconditional sacrifices and continuous support through the years, it would have never been possible for me to achieve my goal…

ABSTRACT

One of the prime research objectives in the area of structural materials for aircraft and space applications is to develop light weight alloys exhibiting high strength, reasonable ductility, high fracture toughness and good corrosion resistance properties. In this respect, Al alloys, especially the precipitation strengthened wrought 2xxx, 6xxx and 7xxx series of alloys have been investigated extensively. Though the mechanisms of strengthening and toughening of these age hardenable alloys are now fairly well understood, there exists a great demand for the development of alloys exhibiting still higher strength to weight ratio. Microalloying alloys with elements such as Sn, In, Cd, Ag, Si, *etc*. is one of the strategies being explored to achieve this goal.

While the influence of alloying elements on the structure and properties of commercial aluminum alloys is well documented, detailed investigations on the effect of trace additions of elements like Sn, In, Cd, Ag, in heat treatable 2xxx series of aluminum alloys are still very few. The effect of systematic variation of trace amounts of Sn on the microstructure, mechanical properties and high temperature deformation behavior of these wrought Al alloys has not yet been explored. Processing of these microalloyed wrought alloys by a sequence of casting, intermediate heat-treatments, hot deformation and final heat treatment would lead to the development of alloys with required microstructure and mechanical properties suitable for structural applications. The general lack of information in the literature in the above area gives rise to several issues worth investigating. The present thesis work was undertaken with the following objectives:

- To process Al–5.9%Cu–0.5%Mg (by weight) alloys microalloyed with Sn of varying wt.% (from 0 to 0.1) by a casting route.
- To study the microstructures and mechanical properties of the alloys in the cast, annealed and rolled conditions.
- To optimize the age hardening conditions required to achieve peak hardness value.

- To study the precipitation kinetics, evaluate the kinetic parameters and thereby generate the kinetic rate equation for the investigated alloys.
- To study the effect of Sn addition on the high temperature deformation behavior of the investigated alloy system.
- To generate constitutive equation for modeling the high temperature flow characteristics and predicting peak flow stress of the alloys with varying Sn contents and at different deformation conditions.
- To generate a model and thereby predict the flow stress as a function of strain, strain rate and temperature of all the investigated alloys at different deformation conditions by Artificial Neural Network and Multiple Linear Regressions analysis techniques.
- To generate processing maps for the investigated alloy system.

Six different alloys with varying Sn contents were prepared by casting route. Optical and scanning electron microscope studies revealed dendritic structures for the alloys in the as-cast condition. Two types of second phases were observed at the grain boundary regions of the alloy matrix, both in as-cast as well as in cast and homogenized conditions. One of the second phases (Al–Cu–Si–Fe–Mn phase) existed with script morphology. The other phase was identified as $CuAl_2$ (θ-phase). The grain size of the as-cast alloys was not influenced by Sn content. But the hardness of the alloys was dependent on the Sn content in the alloy. The maximum hardness of both as-cast and solutionized alloys could be observed in the alloy with 0.06 wt.% of Sn. For the cast and homogenized alloys, the yield strength and ultimate tensile strength increased and the ductility reduced with increase in Sn content up to 0.06 wt.%. Age hardening studies revealed that Sn addition had no influence on the peak ageing time of the alloy system. Peak hardness in all the alloys was attained on ageing at 170 °C for 24 h. In both homogenized and peak aged conditions, the optimal mechanical properties of the rolled alloys were obtained for the addition of 0.06 wt.% of Sn.

Peak flow stress of the alloys increased with increase in strain rate and decrease in deformation temperature. The constants in the constitutive equation for hot deformation were determined and successfully used to predict the peak flow stress during deformation

with a reasonably good accuracy. The activation energy values for hot deformation obtained for the alloys with Sn wt.% > 0.04 were higher than that of the base alloy. .

Prediction of flow stress during hot deformation was carried out by Multiple Linear Regression (MLR) analysis as well as by Artificial Neural Network (ANN) modeling. ANN modeling yielded excellent prediction of flow stress. Deformation mechanism maps were generated for all the alloys and the regions of instability were identified from them. The power dissipation efficiency maps revealed that the maximum efficiency of the Al–Cu–Mg alloy without Sn was 60 % for a true strain of 0.6. This efficiency value dropped to a value of 40 % with trace addition of 0.06 wt.% Sn. However, further addition of Sn up to 0.1 wt.%, resulted in an increase in power dissipation efficiency up to 70 %. The maximum power dissipation efficiency zone for the alloy without Sn content was observed in the strain rate range of 0.001-0.003 s^{-1} and temperature range of 300 - 400 °C. This zone shifted towards the domain of lower strain rate and higher deformation temperatures for all the alloys containing Sn.

Dynamic recrystallization was observed to be the predominant phenomenon in the domains of maximum power dissipation efficiency values of the investigated alloys. Adiabatic shear band formation and matrix cracking were identified as the main factors leading to instability in the alloys at the different deforming conditions. High amount of shear band formation could be observed in the alloy with 0.06 wt.% Sn deformed at strain rate of 0.1 s^{-1} and temperature of 350 °C. This shear band formation continued but reduced with increase in deformation temperature for the same alloy. Matrix cracking was observed to be predominant in this alloy deformed at high strain rate (1.0 s^{-1}) and high temperature (500 °C). For the alloy with 0.1 wt.% of Sn, the instability zones were predominantly due to matrix cracking phenomenon. Matrix cracking continued to be observed even at the lower temperatures (deformed at strain rate of 0.01 s^{-1} and temperature of 300 °C) for this alloy.

In summary, this thesis presents the procedure for processing Al–5.9%Cu–0.5%Mg alloys containing trace additions of Sn up to 0.1 wt.% under different conditions and the influence of processing conditions and compositional variation on the microstructure and mechanical properties of these alloys. Hot deformation studies coupled with flow stress

modeling have resulted in the generation of processing maps which are useful for identifying safe processing zones for these wrought alloys. These studies and the others suggested at the end of this thesis are expected to help in developing high strength light weight Al alloys.

CONTENTS

List of Figures

List of Tables

Nomenclature

a	Atomic size
d	Particle diameter
d_c	Critical particle diameter
E	Young's modulus
e_f	Fracture strain
G	Shear modulus
K	Strength coefficient
k_0	The frequency factor
m	Strain rate sensitivity
N	Strain hardening exponent
P	Pressure
Q	Activation energy for high temperature deformation
R	Universal gas constant (8.314 J/mol.K)
S	Interparticle spacing
S_o	Yield strength
S_u	Ultimate tensile strength
T	Absolute temperature
t	Time
T_e	Peak end temperature
T_m	Melting temperature
T_o	Peak onset temperature
T_p	Peak temperature
U_T	Tensile toughness
V	Volume
Y	Mole fraction transformed
Z	Zener-Hollomon parameter

Greek

$\dot{\varepsilon}$	True strain rate
$\xi\left(\dot{\varepsilon}\right)$	Instability parameter
σ	Flow stress
θ	$CuAl_2$
ε	True strain
σ_p	Peak flow stress
ε_p	Peak strain
α	Stress multiplier
ΔE	Activation energy for precipitation reaction
η	Efficiency of power dissipation
σ_s	Steady state flow stress
ϕ	Heating rate

Abbreviations

AAS	Atomic absorption spectroscopy
ANN	Artificial neural network
ASTM	American society for testing and materials
BCT	Body centered tetragonal
DMM	Dynamic materials model
DRX	Dynamic recrystallization
DSC	Differential scanning calorimetry
DTA	Differential thermal analysis
EDS	Energy dispersive X-ray spectrometer
FDM	Finite difference method
FEM	Finite element method
GP Zones	Guinier-Preston zones
GPB zones	Guinier-Preston-Bagaryatsky zones
HV	Vickers hardness
MSE	Mean squared error
RMS	Root mean square
S.R.	Strain rate
SEM	Scanning electron microscope
SFE	Stacking fault energy
SWG	Standard wire gauge
TTT	Time-Temperature-Transformation diagram
UTM	Universal testing machine
UTS	Ultimate tensile strength
VHN	Vickers hardness number
XRD	X-Ray diffraction
YS	Yield strength

Chapter 1

Introduction

The search for new materials with enhanced properties for industrial and structural applications has led to the development of many metallic alloys. A metallic alloy is a solid solution made of two or more metal elements or metal and non-metal elements in a metallic matrix [WILL1997]. Alloys can be a homogeneous solid solution, a heterogeneous mixture of tiny crystals, a true chemical compound, or a mixture of these. Alloys tend to have properties which often happen to be superior to that of their constituent elements. For example, iron which in the pure form exhibits poor mechanical strength, shows very high strength when trace amounts of carbon is added to it [WILL1997]. Ferrous alloys are the most widely used materials for engineering applications due to their favorable mechanical properties that can be tailored by heat treatments and/or mechanical working [ASMHVOL2]. However, the high density of the ferrous alloys compared to non-ferrous alloys such as titanium, aluminium, and magnesium, impede their use especially in aircraft and space applications. The high demand in aircraft and space industry for structural materials has resulted in a thrust in development of light weight alloys exhibiting better mechanical properties. Several decades of intense research was aimed at development of non-ferrous alloys having high specific strength, reasonable ductility, high fracture toughness, and good corrosion resistance properties [HEIN2000, ASMHVOL2]. Most of these research activities were centered mainly on alloys of aluminum, titanium, magnesium *etc*. Out of these light weight alloy systems, the wrought and precipitation strengthened aluminum alloys such as Al-Cu, Al-Mg-Si, and Al-Cu-Zn-Mg alloys have been the most promising alloys.

Almost all high strength aluminum alloys are used in the wrought form because of their superior high strength to weight ratio achievable by plastic deformation and/or heat treatment. These wrought alloys for structural application need to undergo a thermo-mechanical treatment to reduce the defects (*viz.* segregations, dendrite structures, gas defects, inclusions *etc*.) induced during casting. The mechanical properties of these alloys are affected by the composition, strain history and the microstructure resulting from the thermo-mechanical treatment imparted before the final use. The strengthening of these alloys after deformation is achieved by age hardening (or precipitation hardening). It is now well established that precipitation of extremely small and uniformly dispersed hard second phase particle in the alloy matrix enhances the strength and hardness of these alloys [ASMHVOL2]. A clear understanding of the process parameters during the sequence of casting, secondary processing, hardening heat treatments and high temperature deformation behavior is necessary for obtaining the required shapes and sizes with desired mechanical properties.

The present research trend in alloy development is to microalloy [addition of trace (< 0.1 wt.%) amounts] these alloys with elements like Sn, In, Cd, Ag, *etc.,* in order to achieve materials exhibiting higher strength combined with reasonable toughness and low density [HEIN2000, HIRO2000, OCEN2001, SCHA2001, SERC1999, SILC2002, VESN2003]. Literature is available regarding the influence of several alloying elements on the structure and properties of some commercial aluminum alloys. However, investigations on the effect of microalloying on the heat treatable 2xxx series of aluminum alloys are still limited in number. In particular, the influence of trace content of Sn on the different aspects of Al–Cu–Mg alloys has not been extensively explored. The benefits of microalloying and the general lack of information on such studies on Al-Cu-Mg alloys motivated the investigations presented in this thesis work.

In the present study, Al–Cu–Mg alloys microalloyed with 0 to 0.1 wt.% Sn were processed by casting technique. The microstructure and mechanical properties of these cast alloys after thermo-mechanical treatments were investigated. These investigations also include the effect of trace additions of Sn on the age hardening behavior, precipitation kinetics, and high temperature deformation behavior of these alloys. The flow stress during

hot deformation was predicted using Multiple Linear Regression analysis and Artificial Neural Network modeling. Subsequently, processing maps were generated for identifying the safe process zones for these alloys.

This thesis is arranged in five chapters**.** This chapter (chapter-1) serves as a brief introduction to the contents of this thesis. This is followed by chapter-2, which summarizes the available literature on topics relevant to the contents of this thesis and presents the aims of this thesis work. Chapter-3 describes in detail the methodology adopted in the investigations carried out. This includes details of the experimental set-ups used and procedures followed for processing and characterizing the alloys. The modeling work performed for predicting the flow stress and procedure for generation of processing maps are also described in this chapter. The results obtained are presented and discussed in chapter-4. The major conclusions drawn from the study and future scope of investigation in this area are enumerated in chapter-5.

Chapter 2

Literature Survey

2.1 Introduction

Last two centuries saw a tremendous increased interest in the development of metallic alloys for industrial applications. An alloy is a solid solution made of two or more metal elements or metal and non-metal elements in a metallic matrix. Alloys can be a homogeneous solid solution, a heterogeneous mixture of tiny crystals, a true chemical compound, or a mixture of these. Alloys tend to have properties which often happen to be superior to that of their constituent elements. For example, iron which in the pure form exhibits poor mechanical strength. When 0.1 wt.% carbon is added to it, the resultant alloy (steel) exhibits very high strength and is used extensively for structural applications. Ferrous alloys are the most widely used materials for engineering structural applications due to their favourable mechanical properties that can be tailored by either heat treatments or mechanical working or a combination of these. However, the high density and comparatively poor electrical and thermal conductivity compared to many non-ferrous alloys such as titanium, aluminium, and magnesium, restrict their use especially in aircraft and space applications. The high demand and interest in aircraft and space related applications in the recent years has resulted in a thrust in development of light weight alloys exhibiting better mechanical properties. Several decades of intense research work has focused in the development of such alloys having high specific strength, reasonable ductility, high fracture toughness, and good corrosion resistance properties [HEIN2000, ASMHVOL2].

The focus was specifically on the alloys of aluminum, titanium, magnesium *etc*. Out of these entire alloy systems, aluminum alloys, especially the wrought and precipitation

strengthened Al-Cu (2xxx), Al-Mg-Si (6xxx) and Al-Cu-Zn-Mg (7xxx) series of alloys, were developed because of their high strength to weight ratio. The mechanisms of strengthening and toughening of these materials are now fairly established (ASMHVOL2). The mechanical properties of these alloys are affected by the composition, strain history and the microstructure resulting from the thermo-mechanical treatment imparted before the final use. These may be influenced even by small variations in the composition and microstructure of the alloys. The present research trend is to microalloy (alloying elements < 0.1 wt. percentage) these alloys with elements like Sn, In, Cd, Ag, *etc.* in order to achieve materials exhibiting higher strength combined with reasonable toughness and low density [HEIN2000, HIRO2000, OCEN2001, SCHA2001, SERC1999, SILC2002, VESN2003].

Since this thesis work is based on microalloying of Al-Cu alloy, the relevant reports in the literature related to this topic are reviewed below. These include the earlier research and investigations on structure, various heat treatments, mechanical properties, strengthening theories, and high temperature deformation behavior of wrought aluminum alloys. Generation of processing maps is important since they demonstrate the hot workability of these alloys which is important for the commercial viability. Since this process involves computational modeling, the recent reports on various models are also covered in this survey.

2.2 Aluminum alloys

Aluminum alloys are generally classified as cast and wrought alloys. The cast alloys like Al-Si, Al-Mg, Al-Mn, are extensively used in automobile applications due to their good fluidity in the molten state thereby enabling good castings. Almost all high strength aluminum alloys are used in the wrought form because of their high strength to weight ratio achievable by plastic deformation and/or heat treatment. The strengthening of these alloys after deformation is achieved by age hardening (or precipitation hardening). The pioneering work on improving the strength of aluminum alloys by precipitation hardening can be traced back to a patent on an Al-3.5 to 5.5 wt.% Cu alloy containing < 1 wt.% Mg and Mn by Alfred Wilm in 1906 [WILM1906]. In spite of the huge success of this alloy which is

commercially known as Duralumin, the mechanism of strengthening was not understood for a long time though precipitation hardening was suggested as a possibility in 1919. It took another 16 years to arrive at a conceptual answer to this phenomenon, *viz.*, precipitation from solid solution, though the precipitated phases could not be observed directly by that time. In 1935 the idea of precipitation of intermediate metastable Cu-rich zones, coherent with the matrix during age hardening was recognized by X-ray diffraction. Though the hardening effect during ageing in Al-Cu alloys was theoretically established in 1948 [OROW1948], the first direct observation of the nanometer sized Guiner-Priston zones (GP-zones) was possible only in 1959 with the invention of Transmission Electron Microscope (TEM). These GP-zones are formed by clustering of Cu atoms on the {100} cubic planes of the Al matrix. These zones are said to be coherent with the matrix lattice when Cu atoms replace Al atoms and the matrix lattice strains tetragonally. Subsequently, the 2xxx, 6xxx and 7xxx series of aluminum alloys were developed, which have their specific applications and limitations [ASMHVOL2].

The 6xxx series alloys, with Mg and Si as main alloying elements are heat-treatable and are generally rolled or extruded in to bars or sheets [ASMHVOL2, ESABNAUS]. The 7xxx series alloys, with Zn as main alloying element, (along with other elements, primarily Mg and/or Cu) are heat-treatable aluminum alloys exhibiting highest strength. However, some of these alloys are susceptible to stress corrosion cracking. These alloys find extensive use in aerospace applications [ASMHVOL2, ESABNAUS, KEYMETAL].

The 2xxx series has Cu as main alloying element with smaller amounts of other elements. Cu provides substantial increase in strength by precipitation hardening mechanism with or without the presence of Mg. Hardening is attained by precipitation heat treatment. Conventional 2024 and 2014 type alloys with low Cu content have sufficient formability, spot weldability and good corrosion resistance, and hence are extensively used in automotive industry [ASMHVOL2, ALUMMATT]. These alloys posses good fatigue characteristics, good high-temperature behavior and good machinability. The 2xxx series of alloys are used for high strength structural applications such as aircraft fittings and wheels, rocket fins, military vehicles and bridges, forgings for trucks, *etc* [ALUMMATT]. Al–Cu–

Mg alloys of this series, such as 2124, 2219 and 2618 are extensively used in aerospace application up to 150 °C [NAGA2007, SUKU2008, WANG2008, YULI2004].

2.3 Effect of alloying elements in Aluminum alloys

Considerable amount of studies have been carried to understand the effect of traditional alloying elements such as Cu, Mg, Zn, Si, Ag, *etc*. on the mechanical properties of some commercial aluminum alloys. The strengthening process in wrought but non-precipitation hardening aluminum alloys is attributed to grain refinement and/or solid solution strengthening. In the case of the former mechanism, the Hall-Petch equation is used to estimate the yield strength and other mechanical properties based on the grain size [HALL1951, PETC1953, HANS1982, WILL1997]. In the case of the latter, the alloying element(s) present as solute atoms in the solvent lattice sites are responsible for strengthening [GEOR1988, WILL1997].

For solid solution strengthening, the criteria laid down by Hume-Rothery have to be satisfied [HUME1942, BHAD2007]. These are (i) size factor *i.e*, radius of the solute and solvent atoms should not differ by more than 15%. (ii) The relative valence of the solute and solvent *i.e* the solubility of a metal with higher valence in a solvent of lower valence is more extensive than for the reverse situation. (iii) The solvent and solute should lie close to each other in the electrochemical series. (iv) The solute and solvent atoms should have the same crystal structure. Once the above criteria for the formation of solid solution are satisfied, the strengthening that can be achieved is influenced by the electron-atom (*e/a*) ratio of the alloy. For certain solvent metals, the limit of solubility occurs at approximately the same *e/a* ratio. Generally, the yield strength of a metallic alloy of constant lattice parameter increases with an increase in *e/a* ratio. Moreover, the alloys having equal grain size, lattice parameter and *e/a* ratio have the same initial yield stress, but then flow curves differ from each other.

The significant effects of several alloying elements on the 2xxx series Al alloys have been well studied and established. The influences of some of the common alloying elements on the structure and properties of the Al alloys are mentioned below:

The addition of Cu to Al facilitates strengthening by solid state strengthening and/or precipitation hardening mechanisms. Hardening is achieved through the precipitation of $CuAl_2$ or $CuAl_2Mg$ intermetallic phases during ageing. Cu also improves the fatigue properties, elevated temperature properties and the machinability of the alloy. Presence of Cu in excess of 6 % is however not desirable for applications requiring corrosion resistance. Excess Cu in the alloy precipitates at the grain boundaries, making the metal very susceptible to pitting, intergranular corrosion and stress corrosion. The susceptibility to solidification cracking in Al-Cu alloys increases with Cu addition. Cu addition to Al–Mg–Si alloys has been found to influence the strengthening and grain refinement [CHAK1998, CHAT1973, LIVA1982, MIAO2000, SAKU1992, SUZU1980, TAMI1992].

Mg in Al alloys increases the strength by solid solution strengthening and improves their strain hardening ability. In wrought material of certain alloys of this type, an increase in strength accompanied by high ductility occurs on ageing at room temperature. On artificial ageing, a further increase in strength, especially in yield strength can be obtained, but at a substantial sacrifice in tensile elongation. No significant effect on tensile ductility, strain-rate sensitivity or flow stress could be observed in Al-Mg alloys when Mg was in the range of 2.8 % to 5.5 % [TALE1998]. However, these mechanical properties improved when the amount of Mg was increased beyond 5.5 %.

Si as an alloying element in Al yields cast alloys. Increase in Si wt.% increases the fluidity of the melt thereby facilitating casting into any desired form. 6xxx series Al alloys containing small amounts of Si and Mg are precipitation hardenable high strength alloys. Magnesium silicide (Mg_2Si) precipitation during heat treatment strengthens these alloys.

Addition of Mn increases the strength of Al-Cu-Mg alloys through solution strengthening or formation of finely precipitated intermetallic phase and improves strain hardening without reducing ductility or corrosion resistance. Tensile strength and yield strength increase with increase in Mn and Mg levels. However, Mn causes a loss in ductility. Hence, its content is limited to $\leq$ 1 %. Ryen *et al.* [RYEN2006] investigated a number of commercial and high-purity non heat-treatable aluminum alloys. It was observed that addition of both Mg and Mn in the solid solution resulted in nearly linear concentration

dependence of the strength at a given strain value. Moreover, Mn was found to cause higher strengthening effect per atom than Mg.

Fe in Al–4%Cu–0.5%Mg, even at very low levels of 0.5 %, reduces the tensile properties in the heat-treated condition [ALUMMATT, KEYMETAL]. Excess Fe forms Cu_2FeAl_7. Fe in Al-Cu-Ni alloys improves the elevated temperature strength. Addition of Zn to Al (along with Mg and Cu) produces heat-treatable aluminum alloys, with the highest strength among all Al alloys. Ag in trace levels substantially increases the strength of age hardenable Al-Cu-Mg alloys [ALUMMATT]. Up to 0.3 % Cd in Al-Cu alloys accelerates the rate of age hardening apart from increasing the strength and corrosion resistance. Up to 0.2 % of In in Al-Cu alloys, reduces room temperature ageing. V, Zr and Ti raise the recrystallization temperature of Cu containing Al alloys, thereby permitting to retain their properties at elevated temperatures [ALUMMATT, SUBSTECH]. Ti is added to aluminum primarily as a grain refiner [KEYMETAL, ESABNAUS]. Ni up to 2 % increases the strength of high-purity aluminum but reduces its ductility. Pb is primarily added to improve machinability of Al alloys [ALUMMATT].

Researchers are engaged in developing Al alloys with increased strength, reasonable toughness and low density. One strategy being adopted to achieve the above combination of properties is by microalloying, *i.e*., by trace addition of elements like Sn, In, Cd, Ag, Si, *etc.* in the alloy matrix [HEIN2000, HIRO2000, OCEN2001, SCHA2001, SERC1999, SILC2002, VESN2003].

Microalloying

Several investigations have been carried out on the influence of adding trace amounts (< 0.1 wt.%) of different alloying elements on the microstructure and mechanical properties of some commercial aluminum alloys. Even small variations in compositions and microstructure have been found to result in major changes in strength, toughness, ductility and other properties of the alloy. Therefore, microalloying with different elements like Sn, Cd, In, Ag, Si *etc*. is being exploited to develop materials with improved properties.

Investigation of trace additions of Sn revealed the precipitation of β-Sn particles within the $CuAl_2$ network and fine Mg_2Sn precipitates in the eutectic Si phase present in Al–Si–Cu–Mg and Al–Si–Mg alloys respectively [MOHA2008]. Addition of 0.15 wt.% Sn increased ductility and toughness but reduced the strength and hardness of the cast alloys. Addition of 0.05 wt.% Sn resulted in achieving the best mechanical properties for Al–7wt.%Si–0.35wt.%Mg alloy.

Xiao Yan Liu *et al*. reported accelerated age hardening and increase in the peak hardness with better thermal stability for Al–Cu–Mg–Mn–Zr alloy containing 0.48 wt.% of Ag [XIAO2009]. However, no effect on grain refinement or recrystallization was observed in this case. The yield strength was found to increase with increase in Ag content at both room and elevated temperatures with concomitant reduction in ductility. Moreover, the strength observed by the addition of Ag is higher than that due to θ' precipitation. This is attributed to the formation of fine plate-like Ω precipitates in Al {111} planes. The effect of Ag on age hardening and mechanical properties was further substantiated by studies on 2519 Al alloys [VIET1966, ZHON2006]. Brittle modes of fracture reduced the ductility in these alloys upon Ag addition. Addition of 0.3 wt.% Ag in 2519 Al alloy accelerated age hardening and increased peak hardness at a precipitation temperature of 180 °C. Strength of Al–Cu–Li alloy increased due to the precipitation of T-Al_2LiCu upon addition of 0.1 wt.% Ag [HONG1999, MURA2001, ZHEN1996, ZHEN1998].

Sc addition up to 0.4 wt.% increased the strength of Al–Mg alloys [ZAKH2003]. The strengthening was due to the direct hardening by formation of dispersed Al_3Sc particles in the matrix and the sub-structural hardening for preservation of non-recrystallized structure. Addition of Zr intensified the effect of Sc addition and stabilized the structure of these alloys. Trace addition of Sc was found to improve the yield strength more than the tensile strength of Al–6wt.%Mg alloys [KAIS2008]. This is due to the fine coherent Al_3Sc precipitates being more responsive to the yield behavior. The beneficial strengthening effect of these alloys was however found to be limited to 0.4 wt.% of Sc addition.

The elevated temperature strength of Al–Mg–Mn–Zr alloy was increased by addition of trace amount of Er due to the precipitation of secondary Al_3Er particles in the alloy matrix [WENS2009]. Though addition of Er up to 0.4 wt.% resulted in grain

refinement, no increase in strength was observed due to the formation of primary Al_3Er at the grain boundaries. Microalloying of 357 cast aluminum alloy with 0.1 wt.% In increased the peak hardness value, delayed the precipitation of GP-zones and increased the volume fraction of β'' precipitates during artificial ageing [WANG2007]. Effect of 0.14-0.1 wt.% of Y and Cr addition on the recrystallization behavior of Al–Sc alloys was studied and the recrystallization temperature was found to depend on the Sc content [ROKH2007]. The phase composition and the influence of processing on the mechanical properties of Al-Mg alloys containing trace elements of Ce and Y have been investigated and the phase diagrams have been generated [BOCH2007].

Trace addition (around 0.07 wt.%) of elements like Pb, Sn or In promoted liquid phase sintering in Al–Zn–Mg–Cu alloys [SCHA2001]. Extensive spreading of the liquid phase by the addition of 0.1 % Pb, Sn or In was inferred from this study. This enhancement in liquid phase sintering was attributed to the segregation of trace elements at the liquid-vapor interface. Since the above microalloying elements have low surface tension, they can lower the effective surface tension of the liquid, thereby reducing the wetting angle and promoting spreading of the liquid throughout the matrix.

Spray-deposited Al–5Cu–0.4Mg–0.4Ag–0.4Ti alloys containing trace elements of Zr and Mn exhibiting high strength and fracture toughness have been developed for use at ambient and moderately high temperatures [BEFF1995]. Better mechanical properties were observed in age hardened alloys. Addition of 0.15 wt.% Zr and 0.2 wt.% Mn exhibited a combination of high fracture toughness and yield strength during ageing at temperatures up to 180 °C. The mechanical properties of the alloys were better than those of conventional 2xxx series aluminum alloys. Addition of 0.5 wt.% Zr and 0.4 wt.% Mn in Al–4Cu–0.8Mg–0.4Ag alloy resulted in the best combination of yield strength and fracture toughness ever achieved for an aluminum alloy. For example, at 23 °C, the 0.2 % offset yield strength ($R_{P0.2}$) and fracture toughness (K_{IC}) values were 378 MPa and 100 MPa $m^{1/2}$, respectively in the 'T4' temper condition. However, in the 'T6' temper condition the corresponding values were 452 MPa and 77 MPa $m^{1/2}$, respectively. The superior mechanical properties obtained were influenced by the microstructural characteristics, *viz.* size, density and distribution of the precipitates as revealed by TEM studies.

The microstructure and high temperature stability of age hardenable 2219 aluminum alloy (Al–6.3wt.%Cu alloy) modified by 0.2 to 0.8 wt.% of Sc, Mg and Zr additions, were investigated by Naga Raju *et al*. [NAGA2007]. Addition of Sc, Mg and Zr to the base metal resulted in improved high temperature stability due to formation of fine equiaxed grains, refined eutectics and large number of high temperature stable and finer precipitates. Out of all the compositions studied by them, the alloy with 0.8 % Sc + 0.45 % Mg + 0.2 % Zr was found to be the best in terms of high temperature stability.

The reported results on the effect of trace additions of Cd, In, or Sn on the nucleation and growth of θ' phase in Al–Cu alloys have been compared [SILC2002]. Trace additions of Cd, In and Sn resulted in accelerated ageing and higher peak hardness in Al–Cu alloys. This phenomenon was reported to be due to the formation of very small diameter platelets of θ' in alloys containing Sn. The growth rate of θ' platelets in these alloys was found to be very slow. Two mechanisms have been proposed for the θ' formation during precipitation heat treatment of Al–Cu alloys microalloyed with *X* (where *X* = Cd, In or Sn), *viz*., (i) heterogeneous nucleation on small particles containing trace elements *X* at temperatures of 200 °C and above and (ii) incorporation of atoms of *X* into the θ' nuclei resulting in reduced misfit between θ' and the aluminum matrix at lower temperatures.

The effect of 0.2-0.51 wt.% Si and 0.69 wt.% Ge additions on the microstructure and hardness of 2219 aluminum alloy during ageing was investigated by Vesna Maksimovic *et al*. [VESN2003]. It was found that for the same level of microalloying, the alloy 2219SG (containing Si and Ge) achieved a maximum hardness three times faster than in alloy 2219S (without Ge). The precipitation kinetics was accelerated due to the presence of fine Si-Ge particles which act as heterogeneous precipitation sites for the metastable θ'' phase. Addition of small amount of Ge also increased the hardness as compared to the alloy 2219S (without Ge).

Very few reports are available on the effect of Sn addition on heat treatable aluminum alloys. Emadi *et al*. [EMAD2002] studied the effect of Sn on the mechanical properties of 319 Al alloys. Although Sn addition did not affect the ultimate tensile strength (UTS), it reduced the yield strength and hardness at concentration levels above 0.035 % during heat treatment. The elongation was found to increase from 0.7 % to more than 1.1

%. Investigations on the effect of trace additions of Sn and different heat treatments on the microstructure and mechanical properties of sintered 2xxx series Al–4.4Cu–0.8Si–0.5Mg alloys have been carried out [SERC1999]. Sn concentration was limited to ≤ 0.1 wt.% to avoid incipient melting during solution treatment. The study revealed a tensile strength of 375 MPa, which was almost 20 % higher than that of the alloy without Sn.

Effect of Sc and Zr on the properties of 5754 Al alloy was investigated by Ocenasek and Margarita [OCEN2001]. Aluminum alloys containing 0.0005-0.25 wt.% Sc and 0.002-0.081 wt.% Zr exhibited very high resistance to recrystallization, revealing the possibility of high temperature strength retention. The strengthening effect was due to presence of $Al_3(Sc_xZr_{1-x})$ precipitates which could only be dissolved at very high temperatures. The AA5754 base alloy was fully recrystallized after 5 minutes of annealing at 360 °C, whereas the alloys containing 0.25 wt.% Sc and 0.08 wt.% Zr resisted recrystallization even when annealed for 8 h at 520 °C. Moreover, these alloys exhibited only partial recrystallization even when annealed at 600 °C.

Monte Carlo computer simulation was carried out to understand the role of the microalloying elements in several Al alloys such as Al–Cu, Al–Li–Cu and Al–Cu–Mg [HIRO2000]. Pair-interactions between same atomic species, between different atomic species and between an atom and a vacancy were obtained from these studies. Small addition of Mg to Al–Cu alloys exhibited strong tendency to form Mg/Cu/vacancy complexes. Combined addition of Ag or Si with Mg significantly increased the number of Mg/Cu/vacancy complexes in Al–Cu–Mg alloys. From the comparison with experimental results, these complexes are regarded as effective heterogeneous nucleation sites for GP-zones, GPB zones (Guinier-Preston-Bagaryatsky zones, which are rod-shaped precipitating particles in Al–Cu–Mg alloys) and/or the Ω phase. Through this work, it was possible to analyze the role of some of the microalloying elements in terms of their characteristic features and applicability.

Although information is available regarding the influence of alloying elements like Ag, Sn, In, Sc, *etc*. on the structure and properties of some commercial aluminum alloys, only few reports are available regarding the effect of trace additions on the heat treatable 2xxx series of aluminum alloys. It is to be noted that the influence of trace content of Sn on

the Al–Cu–Mg alloys has not been extensively explored. Microalloying is generally attempted in precipitation hardenable Al alloys mainly because of the fact that high strength Al alloys are invariably precipitation hardenable alloys. The precipitation strengthening mechanisms in precipitation hardenable alloys are discussed in the following sections.

2.4 Precipitation strengthening

The strength and hardness of metallic alloys can be enhanced by the precipitation of extremely small and uniformly dispersed second phase particles in the alloy matrix. Such precipitation is induced by a heat treatment process called precipitation strengthening or age hardening. Examples of a few precipitation hardenable alloy systems are Al-Cu, Cu-Be, Cu-Sn, Mg-Al, *etc.* Such alloys need to exhibit an appreciable solubility of one component in the other and a rapid decrease in solubility limit of the solute atom with a decrease in temperature. Hornbogen has extensively reviewed [HORN2001] the activities related to precipitation hardening in Al alloys.

Precipitation strengthening mechanisms

The relation between dislocation motion and mechanical behavior is central to the understanding of the strengthening mechanism in metals and alloys. Since macroscopic plastic deformation corresponds to the motion of a large number of dislocations, the ability of a metal to plastically deform depends on the ability of the dislocations to move. Hardness and strength signify the ability of the material to resist plastic deformation. Hence, the mechanical strength can be enhanced by impeding the mobility of dislocations through the matrix.

In the case of precipitation strengthening, the motion of dislocations is impeded by the presence of finely dispersed brittle second phase particles in the alloy matrix, there by making the alloy stronger and harder. The extent of strengthening resulting from second phase particles depends on its volume fraction, distribution, size, shape and interparticle space in the ductile matrix.

Orowan, through a model [OROW1948], could quantitatively explain the hardening effect during ageing in Al–Cu alloys. The three conditions to be fulfilled in Orowan's theory of strengthening mechanism are given below:

i) The material should have a two-phase microstructure, *viz.* one being the ductile continuous phase (matrix) and the other being very fine precipitates uniformly distributed in the matrix. These fine precipitates impede the motion of dislocations in the matrix.

ii) The particle diameter (d) and interparticle spacing (S) should generally be less than $100a$, where a is the atomic size.

iii) Particles need to be strong enough to promote looping of dislocations without being sheared, for which $d_c < d$, where d_c is the critical particle diameter.

Consider a material containing a uniform distribution of hard second phase precipitates. During the application of an external load, plastic deformation commences by movement of the dislocations through the matrix. When the moving dislocations encounter the second phase precipitates, their motion is impeded. This will eventually lead to the piling up of dislocations near the precipitates and impose a force on the particles. The force F, which a particle is able to sustain, depends on its intrinsic strength and on the particle diameter. Two mechanisms are possible for the movement of the dislocations, *viz.* (i) dislocations cut through (shear) the particle when the particle strength is weak and (ii) dislocations by-pass the particle resulting in a dislocation loop around the particle, when the particle is strong. Both these mechanisms are illustrated in Figure 2.1 [OROW1948].

In the latter case, the force

$$F > G\boldsymbol{B}^2 \tag{2.1}$$

where, G is the shear modulus of the particle and $\boldsymbol{B}$ is the Burger's vector of the dislocation.

For ordered particles which are coherent with the matrix,

$$F = C\,\gamma_{APB}\,d \tag{2.2}$$

where, γ_{APB} is energy of the antiphase domain boundaries.

The critical particle diameter, d_c is obtained as

$$d_c = C\frac{GB^2}{\gamma_{APB}} \tag{2.3}$$

where, C is a geometrical factor given by the shape of the particle. For a particle non-coherent with the matrix and having a high shear modulus G_β, dislocation will have to be generated in order to shear the particle. In such a case, the critical diameter is very small and is given by

$$d_c = \frac{4\pi b G_\alpha}{G_\beta} \tag{2.4}$$

where G_α is the high shear modulus of the matrix. In the case of the Al–Cu alloy system, θ' is typically coherent with the matrix, whereas, the hard θ ($CuAl_2$) phase is the non-coherent particle. The increase in yield stress due to dispersoid particles, $\Delta\sigma_P$, is given by [OROW1948]

$$\Delta\sigma_P = \frac{GB}{S_{eff}} = \frac{GB}{S-d} = \frac{GB}{d} f_P^{1/3}, \tag{2.5}$$

where S is the spacing of the particle centers and f_p is the volume fraction of particles in the matrix. Generally in Al alloys, $S_{eff} \approx S$ for small volume fractions $f_p \leq 1$ %. The condition $d < d_c$ limits the applicability of Eq. (2.5). However, this relation provides a good estimate of the strengthening which can be achieved in precipitation hardenable alloys.

Precipitation strengthening process

The precipitation hardening behavior in alloys is now fairly well established, especially with regard to Al-Cu alloys. Since the precipitation hardening mechanism is similar for all precipitation hardenable alloys, the following discussions will be limited to those concerning Al-Cu alloys only. The precipitation strengthening is possible only when the matrix is a solid solution and when the solubility limit of the solute in the solid solution increases with increase in temperature as depicted by the solvus line in Figure 2.2. In such cases, the precipitation hardening process involves the following steps:

(i) ***Solution heat treatment or solutionizing***, where the alloy is heated to an elevated temperature and is held until a uniform solid solution is formed. In this step all the second phase particles completely dissolve in the α-phase.

(ii) ***Quenching***, *i.e.* the sample is rapidly cooled to a lower temperature (generally room temperature). Under this condition, the alloy exists as a supersaturated solid solution.

(iii) ***Precipitation heat treatment***, where the alloy is heated to some intermediate temperature and is held there for sufficient period of time. In this stage, the excess solute in supersaturated solid solution precipitates as fine and uniformly distributed brittle particles.

Ageing the alloy at room temperature is called natural ageing, whereas ageing at elevated temperatures is called artificial ageing. Most of the alloys require artificial ageing, and ageing temperature is usually intermediate to the room temperature and solutionizing treatment temperature. Strengthening achieved is determined by the size, crystal structure, and distribution of the second phase particles, which in turn depend on the precipitation sequence or stages involved.

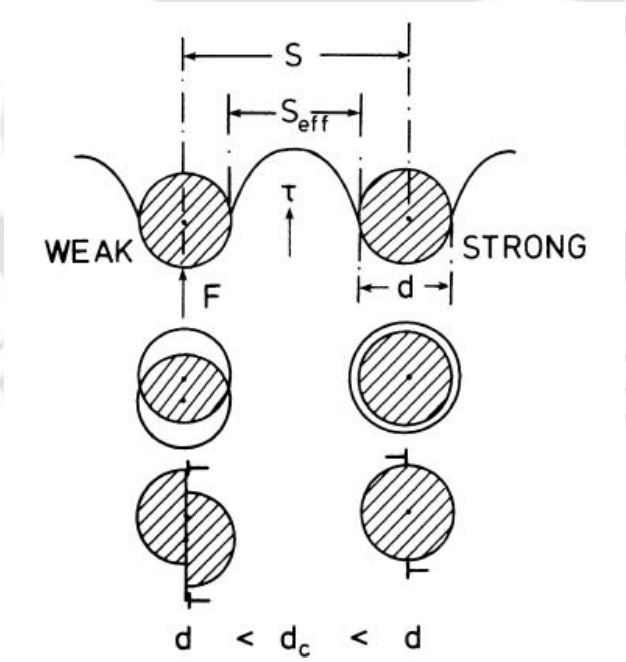

Fig.2.1. Schematic representation of the force, *F* exerted on the particle by looping of dislocations

Precipitation stages

Typical precipitation strengthening behavior and the evolution of precipitates during ageing heat treatment of Al–4%Cu (Duralumin) alloy can be explained using the part of the phase diagram shown in Figure 2.2. The alloy with up to 4 wt.% Cu exists as a single-phase (α) solid solution at around 550 °C. At room temperature, the same alloy exists as a stable mixture of α (with less than 0.5 % Cu) and an intermetallic compound, $CuAl_2$ (θ). The complete equilibrium phase diagram for the binary Al-Cu system is shown in Figure 2.3. When this alloy is quenched to room temperature from 550 °C, it exists as a solid solution supersaturated with the solute Cu atoms. Just below 500 °C (solvus temperature), though the diffusivity of Cu is high enough to facilitate Cu precipitation, the low chemical potential hinders precipitation of Cu from the supersaturated solution due to the low concentration of Cu atoms in it. On the other hand, at room temperature, the chemical potential might favour Cu precipitation from the supersaturated solution. However, the low diffusivity of Cu at these temperatures will result in impractically high precipitation time to achieve satisfactory strengthening effect. Hence, ageing is carried at an intermediate temperature where a trade-off can be made between the chemical potential and diffusivity factors in order to achieve reasonable strengthening at a reasonable ageing time. It has been found that for a typical 2014 Al alloy, ageing for 5 h around 200 °C results in a reasonable strength of 500 MPa [METHVOL2].

Diffusion of excess Cu atoms (assisted by vacancies) results in the precipitation of spherical $CuAl_2$ in a sequential manner. The first stage of precipitation is the formation of clusters (Guinier Preston zones or GP-zones) which are generally mono-atomic layers of Cu on (001) planes of the Al lattice. With increase in the ageing time, Cu atoms diffuse in to the GP-zones and form additional layers on the GP-zones. This increases the size and changes the shape of the precipitates until they attain the stable, equilibrium and spherical $CuAl_2$ form. During this process, the GP-zones undergo the intermediate meta-stable transition zones (θ'' and θ'). Moreover, the initial GP-zones that were fully coherent with the matrix gradually loose coherency and finally become precipitates that are fully

incoherent with the matrix. The actual sequence of precipitation is shown in Figure 2.4, and the same can be written as:

GP1-zones → GP2-zone θ'' (thin discs, fully coherent with the matrix) → θ' (disc shaped and semi-coherent with the matrix → θ ($CuAl_2$, which is spherical and incoherent at the precipitate-matrix interface).

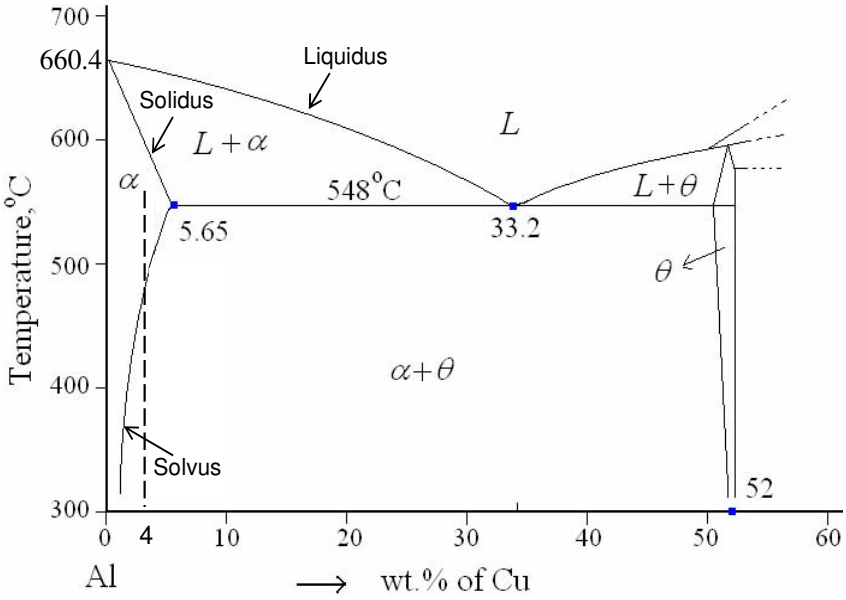

Fig.2.2. Al rich region of the binary Al-Cu phase diagram [WILL1997]

In Al–Cu alloy system, the stable precipitate is generally $CuAl_2$ (θ) exhibiting body centered tetragonal (BCT) crystal structure with lattice parameters of $a = b = 0.607$ nm and $c = 0.487$ nm and having a microhardness (HV) of 400 to 600 kgf/mm^2 [ELAG2007, MIAO2000, XIAO2009]. The peak hardness is usually attained at the start of incoherency or towards the later stages of semi-coherency. A brief account of the precipitates at various stages of the process is given below [RAJA1997, WILL1997]:

(i) GP1-zones: These are formed by clustering of Cu atoms in matrix, which are about 10 nm long and about three atoms thick. They form on the {100} cubic planes of the Al matrix. These zones are said to be coherent with the matrix lattice when Cu atoms replace Al atoms and the matrix lattice strains tetragonally.

(ii) GP2-zones / θ'' phase: With increase of ageing time, ordering of Cu atoms on {100} planes of the matrix occurs. These zones have tetragonal structure, which introduces coherency with {100} planes of the matrix lattice. As ageing proceeds, their sizes range from 15 nm thick to 150 nm in diameter. Formation of this precipitation phase is accompanied by further hardening of the alloy.

(iii) θ' phase: This phase has tetragonal structure and is partially coherent with the matrix. It also nucleates heterogeneously in the matrix, especially on dislocations. This phase takes the form of platelets with thickness of 10-150 nm.

(iv) θ phase: With still further ageing, the equilibrium θ-phase ($CuAl_2$) is formed. It has a BCT structure. These particles are no longer coherent with the matrix lattice. Hence, at this stage, the hardness of the material gets lowered than the previous stages with coherency. Over-ageing results in further growth of these particles which is controlled by diffusion.

The strength and ductility achieved by the alloy depend on the composition, ageing time, ageing temperature and activation energy (ΔE) of precipitation. For a particular composition, ΔE is assumed to be constant for a precipitation reaction, and the kinetics of the reaction is governed by the precipitation temperature and time. Differential scanning calorimetry (DSC) is generally used for determining the kinetic parameters of the precipitation hardening process.

The DSC technique was developed by Watson and O'Neill in 1960 [USPATENT], and introduced commercially in 1963. The term DSC was coined to describe this instrument which measures energy directly and allows precise measurements of heat capacity [WUND1990].

DSC is a thermo-analytical technique in which the difference in the amount of heat required to increase the temperature of a sample and reference is measured as a function of temperature. Both the sample and reference are maintained at nearly the same temperature throughout the experiment. Generally, the temperature program for a DSC analysis is designed such that the sample holder temperature increases linearly as a function of time. The reference sample should have a well-defined heat capacity over the range of temperatures to be scanned.

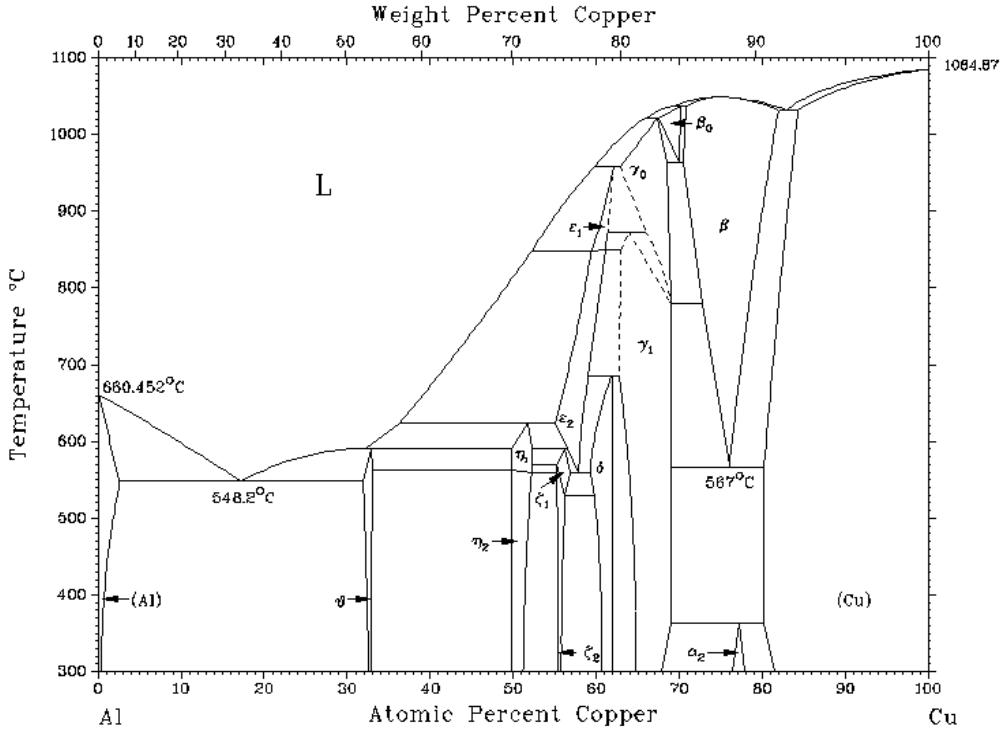

Fig.2.3. The complete equilibrium phase diagram of the binary Al-Cu alloy system

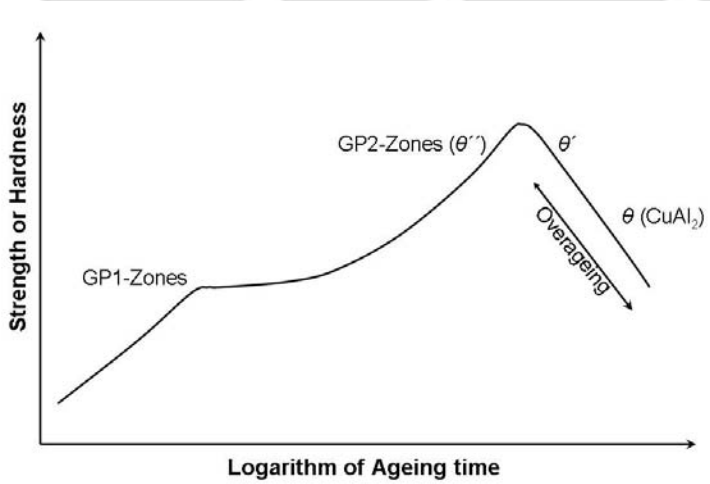

Fig.2.4. Typical curve showing the variation of hardness with ageing time for Al–4%Cu alloy

The basic principle underlying this technique is that, when the sample undergoes a phase transformation, heat needs to flow into the sample (endothermic) or out of the sample (exothermic) with respect to a reference material so as to maintain both at the same temperature. By observing the difference in heat flow between the sample and reference, the amount of heat absorbed or released during such transitions is measured. Typical DSC thermograms showing the exothermic precipitation reactions of an Al–Cu–Mg alloy system at four different heating rates are shown in Figure 2.5.

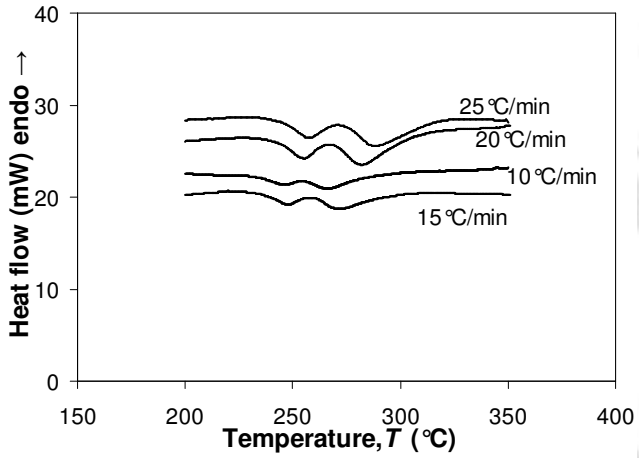

Fig.2.5. Typical DSC thermograms showing the exothermic precipitation reactions of an Al–Cu–Mg alloy at four different heating rates

In any kinetically controlled reaction such as a precipitation reaction, the peak temperature of the reaction shifts with heating rate. The activation energy of the precipitation reaction can be evaluated by means of the *Kissinger's method* using the equation [AUGI1978, KISS1957],

$$\ln\left(\frac{T_p^{\,2}}{\varphi}\right) = \frac{\Delta E}{RT_p} + C \qquad (2.6)$$

where, T_p = peak temperature of the reaction (K), ϕ = heating rate (K/s), ΔE = activation energy (Joule/mole), R = Universal gas constant (8.314 Joule/ mole.K), and C = constant. Plots of $\ln(T_p^2/\phi)$ versus $(1/T_p)$ are made for each heating rate and the activation energy of the precipitation reaction can be estimated from their slopes. A typical Arrhenius plot of this type is shown in Figure 2.6.

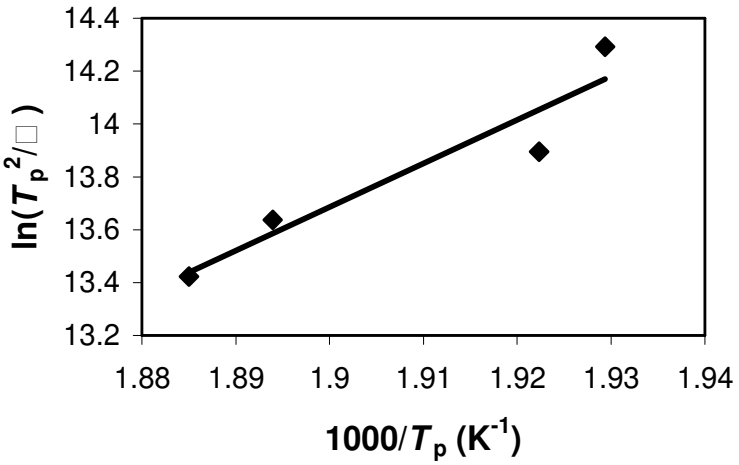

Fig.2.6. A typical Kissinger plot generated from the DSC thermogram of an Al–Cu–Mg alloy

The precipitation process in as-quenched Al-l.53 wt.% Cu-0.79 wt.% Mg alloy was analyzed from DSC thermograms [JENA1989]. The following kinetic equation was used to evaluate the activation energy involved in the precipitation process:

$$\frac{\partial Y}{\partial t} = f\left(Y\right) k_0 \, e^{-\frac{\Delta E}{RT}} \qquad (2.7)$$

where, $f(Y)$ is a function of mole fraction transformed Y, k_0 is the frequency factor, ΔE is the activation energy for the reaction and R is the universal gas constant. ΔE for the reaction is determined from the mean slope of plots of $\ln[(dY/dT)\phi]$ *vs.* $(1000/T)$ for given Y values, where the function $f(Y)$ is not required to be known. The function value of $f(Y)$ and the other kinetic parameters of the rate equation have been evaluated for a few Al alloys. Literature indicates that there is no single solution for $f(Y)$, which in turn depends on the alloy composition and the corresponding precipitate morphology. The dissolution kinetics of GP-zones in Al–Zn–Mg alloys was studied by a three dimensional diffusion equation using two different expressions for $f(Y)$: one for planar particles and the other for spherical particles [DONO1985]. These kinetic equations were based on physical models that consider decrease in precipitate half-thickness for planar particles or radius for spherical particles [DONO1983], and are of the forms,

$$f(Y) = [1-(1-Y)^{1/3}]^2 \quad \text{(for planar precipitates)} \qquad (2.8)$$

$$f(Y) = 1-(1-Y)^{2/3} \qquad \text{(for spherical precipitates)} \qquad (2.9)$$

It is worthy to point out that the Johnson-Mehl-Avarami equation [AVRA1939, AVRA1940, AVRA1941], originally developed for studying the precipitation process in an Al–Cu–Mg alloy used the functional form $f(Y) = (1-Y)$. Precipitation kinetics of Al–1.53wt.%Cu–0.79wt.%Mg was studied by Jena *et al*. where the function $f(Y)$ was selected from Johnson-Mehl-Avrami equation and by satisfactory fitting the same with the experimental data. ΔE value was evaluated by substituting the function in the rate equation [GUPT1988, JENA1989].

Kissinger was able to evaluate ΔE and k_0 values from differential thermal analysis (DTA) experiments by studying homogenous reactions obeying first order rate equation [KISS1957]. Augis *et al*. [AUGI1978] developed an extension of Kissinger's method and applied it to heterogeneous solid state reactions described by Avrami expression. A method was specifically developed for studying the precipitation and dissolution kinetics in aluminum alloy 2219 [PAPA1981] from first order reaction kinetics. Subsequently, another method was developed for 2219 and 7075 alloys [PAPA1982] which involved a comparative fitting of the experimental and theoretical plots of mole fraction transformed (Y) *vs*. temperature (T) during the reaction.

Johnson-Mehl-Avrami equation relating the degree of reaction (α), rate constant (K) and growth exponent (n), empirically describes most reactions occurring in solid metallic phases [AVRA1939, AVRA1940, AVRA1941, JOHN1939]. This equation was modified by Sarkar *et al*. [SARK1990] to get a true kinetic equation and was used to evaluate a true rate constant. Muraleedharan proposed a modified true kinetic equation from the Johnson-Mehl equation itself [MURA1991].

The kinetics of precipitation in Al–Mg_2Si–Cu and Al–Mg_2Si–Si alloys has been studied and the peak hardening of the former alloy was found to be higher due to coexistence of β' and Q' precipitates [GABA2007]. Precipitation kinetics of solutionized Al alloy 2124 [SMIT1998] and Al–0.8%Mg–0.9%–Si alloy [GUPT1999] has been investigated. The sequence of precipitation and dissolution of Al–Li–Cu–Mg alloy under constant heating rates was analyzed using combined results of electrical resistivity, DSC and hardness measurements [LUOA1993]. Precipitation kinetics of several Al–Cu–Mg

alloys has also been studied. Other investigations include studies on precipitates and intermetallic phases of Al–Cu–Mg–(Li) [WANG2005], Al–Mg and Al–Mg–Cu alloys [VONC2007]. Precipitation sequence studies carried out on Al–Cu–Mg alloys microalloyed with Si revealed that the precipitation process depends on the total solute content of the alloy apart from the Cu/Mg ratio [HUTC2000]. Thermal analysis of Al–Cu–Mg–Si alloy with Ag/Zr additions has also been carried out [BASS2008].

Garg *et al.* [GARG1993] investigated the interfacial defect structure and transformation mechanism of the Ω phase precipitation in A1–3.9Cu–0.5Mg–0.5Ag alloy. The defects were found to be ledges, which exhibited $\frac{a}{6}\langle 112\rangle_\alpha$ and $\frac{a}{2}\langle 110\rangle_\alpha$ dislocation contrast. The Ω precipitates were found to be completely coherent with the matrix at early stages of growth. A possible mechanism for the atomic correspondence between the α - matrix and Ω - phase during the precipitation process was subsequently proposed.

The effect of solutionizing and precipitation heat treatment on the microstructural evolution in age hardenable cast Al alloys has been investigated [MUKH1999]. The phases present in the as-cast microstructure dissolved during the solution treatment and re-precipitated in the alloy during ageing. The re-precipitated phases consisted of those present in the as-cast microstructure, or their metastable versions. The effect of temperature and ageing time on the morphology of the precipitates, strength and ductility in Al–Cu, Al–Zn–Mg–(Cu), Al–Mg–Si–(Cu) alloys has been studied [BERL2000]. The maximum strength of the Al–Cu alloy increased with increase in volume fractions of θ'' and θ' precipitates. Deforming the alloy by 2 % after quenching resulted in (i) shifting of the existing θ'-phase region towards the lower temperature region on the Time-Temperature-Transformation (TTT) diagram, (ii) reduction in size of the θ'-phase particles and (iii) increase in the strength of the alloys. Large volume fractions of fine η and η' precipitates resulted in high strength for Al–Zn–Mg–Cu alloys. Maximum strength was achieved for the Al–Mg–Si alloys at ageing temperatures in the range of 165 °C to 180 °C for exposures more than 8 h. For the Al–Mg–Si–Cu alloys, maximum strength was achieved at the temperature range from 165 °C to 200 °C.

Room temperature hardening behavior of Al–Cu–Mg alloys has been studied [STAR2004]. The most commonly cited mechanisms for the rapid age hardening of Al–Cu–Mg alloys at about 100 - 200 °C were hardening by GPB-zone formation, formation of Cu–Mg co-clusters and a dislocation-solute interaction mechanism. New experiments on ageing-deformation-ageing cycles at room temperature indicated no substantial additional age hardening with the addition of deformation to the cycle.

The study on precipitate-dislocation interaction of deformed Al–Mg–Si alloys revealed that the dislocation motion in the matrix occurs either by shearing of the precipitates by dislocations or by bypassing of precipitates (Orowan's mechanism) [OROW1948, PATR2002]. The effect of process variables on the microstructure and tensile properties of cast as well as squeeze-cast and heat treated Al–6Si–0.3Mg alloys has been explored [ABOU2005]. The results revealed that precipitation occurred within about 30 min for both cast and squeeze cast alloys. The hardness increased with ageing time and the maximum value was observed after 10 h for the as-cast alloy. Increasing the squeeze pressure to 160 MPa resulted in achieving the peak hardness in 4 h of ageing while it took 8 h to achieve the same under 70 MPa.

Jones and Humphreys [JONE2003] investigated the kinetics and mechanisms of recrystallization in high purity binary Al–Sc alloys. The strengthening Ω phase, which precipitated in the form of thin plates on Al {111} planes, is a chemically modified coherent form similar to the θ ($CuAl_2$) phase. In deformed supersaturated Al–0.12Sc solid solutions, recrystallization was impeded below ~370 °C due to precipitation starting before recrystallization. Above this temperature, recrystallization and precipitation occurred simultaneously, resulting in irregular microstructure. At temperatures above ~400 °C, recrystallization precedes precipitation, resulting in a microstructure typical of a single-phase Al alloy.

Crystallization behavior and microstructure of ternary Al–Sn–Si alloys were reported by Yuan *et al*. [YUAN2000]. The Sn/Si ratio was observed to influence the volume fraction and distribution of the second phase. The best microstructure was formed with a Sn/Si ratio in range of 3~4. Nie and Muddle [NIEJ2001] modeled the increase in

critical resolved shear stress (CRSS) accompanying ageing of selected high strength Al alloys.

The above survey of the literature shows the extent of studies performed on Al-Cu-Mg alloys. It is observed that the precipitation mechanism in Al–Cu–Mg alloys microalloyed with Sn has not been explored so far. It is also found that the effect of systematic variation of the microalloying elements in Al-Cu-Mg alloys has not been reported in the literature. Considering the importance of these alloys, such a study would be worthy of pursuit.

2.5 High temperature deformation behavior

The wrought alloys for structural application need to undergo a thermo-mechanical treatment prior to their final use. The mechanical properties of the wrought Al alloys are affected by the composition, strain history and the microstructure resulting from these thermo-mechanical treatments imparted. These alloys are required to be plastically deformed to reduce the defects (*viz.* segregations, dendrite structures, gas defects, inclusions *etc.*) induced during casting. The deformation process is generally carried out at high homologous temperatures *i.e.* $T/T_m > 0.5$, where T and T_m are the absolute working temperature and melting temperature of the material, respectively. In high temperature deformation, the two main research areas are (i) creep deformation, and (ii) metal forming by hot working. The major objectives in hot working are to reduce the flow stress and raise the fracture strain at high strain rates (10^{-2} s^{-1} < $\dot{\varepsilon}$ < 10^{2} s^{-1}), whereas the emphasis in creep research is for low strain rates and curtailment of total strain, even though both these studies are carried out at almost the same temperature range [MCQU2002, MCQU2005].

A clear understanding of the process variables and material parameters is required for successfully deforming these materials within a range of strain rates and temperatures. The deformation behavior of these materials, *i.e.* the relationship between flow stress (σ), strain (ε), strain rate ($\dot{\varepsilon}$) and process temperature (T) is dependent on the activation energy (Q) for deformation, which is a measure of the degree of difficulty for deformation. Composition and microstructure strongly influence the Q value of the materials.

Considering hot deformation similar to the creep phenomenon occurring at high strain rates and stresses [LIAN2008], various constitutive relationships have been developed to model the high temperature deformation behavior of materials.

A thermo-viscoplastic finite element method (FEM) model was developed using hot compression test data to predict the microstructural evolution in Al–5wt.% Mg alloys during hot deformation [CHOJ2001]. Based on experimental results, a unified creep-plasticity constitutive model for the stress-strain behavior of cast Al–Cu–Si alloys under complex loading conditions has been proposed [SMIT1999]. Kaibyshev *et al*. [KAIB2002] investigated the deformation behavior of a 2219 Al alloy (Al–6.4%Cu–0.3%Mn–0.18%Cr–0.19%Zr–0.06%Fe) in the temperature range from 250 °C to 500 °C, which is the widely used hot working temperature range for this alloy. The results indicated an increase in stress exponent and apparent activation energy with decrease in *T*. A power law equation of the form, $\dot{\varepsilon} = A\left(\frac{\sigma}{G}\right)^n \exp\left(\frac{-Q}{RT}\right)$, where $\dot{\varepsilon}$ is strain rate, *A* is a constant, *n* is the stress exponent, σ is the flow stress, *G* is the shear modulus, *Q* is the activation energy for plastic deformation, *R* is universal gas constant and *T* is the absolute temperature, was used for modeling the variation of flow stress with $\dot{\varepsilon}$. The value of the energy term, *Q*, was evaluated as 35 kJ/mol in the *T* range of 250 ^{o}C to 450 ^{o}C, which decreased at higher *T*. Deformation behavior of this 2219 Al alloy indicated the presence of a threshold stress which was found to be temperature dependent. Microstructural studies of this alloy also revealed localization of dislocation glide with decrease in *T* and increase in $\dot{\varepsilon}$. On the other hand an increase in *T* resulted in possible cross-slip and a transition from multiple slip to single slip. Superplastic deformation behavior of the same alloy has also been studied [KAIB2001]. Thermo-mechanical processing was necessary for obtaining the appropriate microstructure (*viz*., large secondary particles of size ~1μm), favourable for superplastic deformation of the alloy. The alloy exhibited a maximum strain of 675 % at 500 °C with an initial grain size of 12 μm and a constant $\dot{\varepsilon}$ of 2.2×10^{-4} s^{-1}.

Hot and warm formability studies on as-solutionized 2618 Al alloy (Al–2.3%Cu–1.6%Mg–1.1%Fe–1.0%Ni–0.07%Ti–0.18%Si) at various strain rates and temperatures by torsion testing revealed precipitation of second phase particles during deformation

[CAVA2002]. The flow curves showed a temperature dependent behavior with (i) a continuous increase of flow stress up to 250 °C due to precipitation, and (ii) a peak in the flow curves above 250 °C due to precipitation and coarsening of precipitates followed by softening. The high temperature tensile deformation behavior of Al–Cu–Mg–Zr alloy, 2014, and 6082 Al alloys in a wide range of T and $\dot{\varepsilon}$ were described by a modified hyperbolic sine equation, where the peak flow stress (σ_p) was substituted by an effective stress, *i.e.* the difference between peak stress and a threshold stress representing the strengthening effect of the second phase precipitates in the matrix [BARD2003, SPIG2003]. Flow stress behaviors of Al–Cu–Li–Zr, Al–Mg, Al–Cu–Mg–Ag, and Al–Mg–Si–Cu alloys have been studied extensively [GHOL2009, LIAN2008, QING2009, ZHAN2007] by hot compression tests. These studies indicated that the plastic deformation of these alloys at elevated temperatures ($T > 0.5\ T_m$) is a thermally activated process with an activation energy Q. The flow stress has either an exponential or hyperbolic sine relationship with the $\dot{\varepsilon}$ and T.

The Zener-Hollomon parameter, Z, is used for representing the hot deformation behavior of metallic alloys. The constitutive relationships and the modeling procedures developed for predicting the flow stress behavior related are discussed below in the following section.

2.5.1 Constitutive models

Models for the high temperature deformation behavior of metallic materials were developed based on the principles of creep deformation. Similar to the creep deformation, high temperature deformation of metallic alloys is also a thermally activated process controlled by $\dot{\varepsilon}$ and T. During hot deformation, the $\dot{\varepsilon}$ is higher by several orders of magnitude as compared to creep deformation. Hence, the theories of hot deformation can be regarded as an extension of the creep deformation under high strain rate and at high stresses. Both the processes have very similar deformation and softening mechanisms.

The initial development of the constitutive relationships was based on the assumption that the flow stress (σ) is a function of only the instantaneous values of ε, $\dot{\varepsilon}$ and T [GEOR1988], *i.e.*

$$f(\sigma, \varepsilon, \dot{\varepsilon}, T) = 0 \tag{2.10}$$

This is analogous to the expression for a thermodynamic system in equilibrium, which can be expressed by the state variables *viz.*, pressure (P), volume (V) and temperature (T), *i.e.*

$$f(P, V, T) = 0 \tag{2.11}$$

It was soon realized that plastic deformation is an irreversible process, so that ε and $\dot{\varepsilon}$ are not state functions like P, V and T. Instead, σ depends on the dislocation structure which in turn is related to the metallurgical factors, ε, $\dot{\varepsilon}$ and T.

A sine hyperbolic relationship which is particularly useful for correlating stress, T and $\dot{\varepsilon}$ under hot working conditions was first proposed by Sellars and Tegart [SELL1966, TEGA1968]. Subsequently, a set of constitutive relations were developed [GHOS1980], to analyze constant true-strain-rate, strain-rate change, stress-relaxation and creep test data. A computer representation of the constitutive relations (MATMOD) was developed [SCHM1981] for analyzing high temperature deformation.

Strain rate ($\dot{\varepsilon}$) is related to the T and activation energy for deformation by an Arrhenius type equation which can be expressed as [LIAN2008]:

$$\dot{\varepsilon} = A f(\sigma) \exp\left(-\frac{Q}{RT}\right) \tag{2.12}$$

where, Q is the activation energy for deformation (J/mole), A is a constant and $f(\sigma)$ is the stress function which can be expressed by any of the following relationships [CHEN2008, EVAN1990, LIAN2008, MEDI1996, QING2009, SHAO2008, TAKU1998, YANG2006, ZHAN2007]:

$$f(\sigma) = \sigma^{n_1} \tag{2.13}$$

$$f(\sigma) = \exp(\beta\sigma) \tag{2.14}$$

$$f(\sigma) = [\sinh(\alpha\sigma)]^n \tag{2.15}$$

Combining Eq. (2.12) with Eq. (2.13), (2.14) and (2.15), the following constitutive equations can be obtained:

$$\dot{\varepsilon} = A_1 \sigma^{n_1} \exp\left(-\frac{Q}{RT}\right) \tag{2.16}$$

$$\dot{\varepsilon} = A_2 \exp(\beta\sigma) \exp\left(-\frac{Q}{RT}\right) \tag{2.17}$$

$$\dot{\varepsilon} = A_3 [\sinh(\alpha\sigma)]^n \exp\left(-\frac{Q}{RT}\right) \tag{2.18}$$

In the above equations, though σ is generally taken as the peak flow stress (σ_p) [MCQU2002, MEDI1996], the steady state flow stress (σ_s) has also been used in a few instances. The term α is the stress multiplier used in the mathematical fitting procedure. The terms of n_1, β, n, A_1, A_2 and, A_3 are material constants. The power law equation (Eq. 2.16) breaks down at high stress values where as the exponential equation (Eq. 2.17) breaks down at low stress values [CHEN2008, LIAN2008, MCQU2002, MEDI1996, SHAO2008, ZHAN2007]. Over a wide range of stresses, the hyperbolic sine law (Eq. 2.18) is found to be most suitable form for describing high temperature deformation behavior of materials.

It has been observed in many instances that σ_p and σ_s have a linear relationship. It has also been found that the Zener-Hollomon parameter is a useful tool in describing the high temperature deformation behavior of metallic materials.

Zener-Hollomon parameter (*Z*) and activation energy (*Q*)

In high temperature deformation processes, the σ can be expressed as [ZENE1944, SELL1966, TEGA1968, YANG2006]:

$$\sigma = \sigma(\varepsilon, \dot{\varepsilon}, T) \tag{2.19}$$

The peak stresses obtained from the hot compression tests for various $\dot{\varepsilon}$ and T values constitute a group of parallel straight lines. Generalized prediction of σ_p from these plots is possible using the Z parameter. The Z, which correlates the $\dot{\varepsilon}$, deformation T, and Q, can be expressed as [GEOR1988]:

$$Z = \dot{\varepsilon} \exp\left(\frac{Q}{RT}\right) \tag{2.20}$$

The physical meaning of Z is the so called temperature-modified strain rate.

Combining Eq. (2.18) and Eq. (2.20), the expression for Z can be obtained as:

$$Z = \dot{\varepsilon} \exp\left(\frac{Q}{RT}\right) = A_3 \left[\sinh(\alpha\sigma)\right]^n \tag{2.21}$$

The activation energy, Q, indicates the energy barrier required to be overcome for plastic deformation and is determined from the following relationship [CAVA2002, CERR2007, CHEN2008, BARD2003, BJØR2001, GHOL2009, LIAN2008, SPIG2003]:

$$Q = R \left[\frac{\partial \ln \dot{\varepsilon}}{\partial \ln[\sinh(\alpha\sigma)]}\right]_T \left[\frac{\partial \ln[\sinh(\alpha\sigma)]}{\partial\left(\frac{1}{T}\right)}\right]_{\dot{\varepsilon}} \tag{2.22}$$

$$= R\, n\, S$$

In the above relationship, n is the mean slope of $\ln(\dot{\varepsilon})$ *vs.* $\ln[\sinh(\alpha\sigma)]$ plots obtained at different T and S the mean slope of the $\ln[\sinh(\alpha\sigma)]$ *vs.* $(1000/T)$ plots at various $\dot{\varepsilon}$.

Survey of the literature indicates that the focus so far has been to determine Z, Q, α, n, *etc.* of commercially available Al alloys. These parameters are known to be influenced by even small variations in the composition and microstructure of the alloys. Investigations on the effect of microalloying on the high temperature deformation behavior of the wrought Al alloys are still rare.

2.5.2 Artificial neural network (ANN) modeling

A neural network is similar to the biological nervous system, which is basically a connectionist system, in which various nodes called neurons are interconnected. An artificial neural network (ANN) can be defined as a model of reasoning similar to the human brain, where a large amount of complex information can be stored and processed simultaneously by each neuron along the entire domain. A typical neuron receives one or more input signals and provides an output signal depending on the processing function of

the neuron. This output is transferred to connected neurons in varying intensities, the signal intensity being decided by the weights assigned. ANN has the advantages of (i) modelling the data where the input-output relation is either unknown or nonlinear, (ii) adaptive learning during training (iii) real time applications aided by a very fast computational speed. The conventional computational techniques follow an algorithmic approach, where a set of instructions in the specified order is followed to solve a problem. The relationship between each stage is required for solving the problem. On the other hand, neural network technique is data driven and the solution can be obtained even if the exact relationship is unknown. This can be obtained if a number of input-output data sets are available. Once the ANN architecture is fixed, the output for any combination of input variables can be predicted.

The most popular neural networks are feed forward networks. A feed forward network architecture consists of three distinct layers: the input layer, the hidden layer(s), and the output layer. Each layer consists of a number of neurons. The output from the neurons of one layer is transferred as input to neurons of the succeeding layer. The first layer, called an input layer, receives data from the outside world. The second layer, called the hidden layer, does not have any direct contact with the outside world and is used to help in extracting higher-level features and to facilitate generalization of outputs. The last layer is the output layer, which sends information out to users. For a given input vector, it generates the output vector by a forward pass. The data are fed to the network at the input layer and propagated with weights and activation functions to the output layer to provide the response. Once the data at the output neuron is reached, the mean squared error (MSE), which is the difference between the network output vector and the known target vector, is computed and back-propagated through ANN to modify the weights for the entire network. This process is referred to as training. Learning can be of three types: supervised, unsupervised or reinforced. The most popular method practiced for supervised training of neural networks is the back-propagation training algorithm. Here, the training process involves two passes. In the forward pass, the input signals propagate from the network input to the output. In the reverse pass, the calculated error signals propagate backwards through the network where they are used to adjust the weights. Any efficient optimization

method can be used for minimizing the error through weight adjustment. The calculation of the output is carried out, layer by layer, in the forward direction. The output of one layer is the input to the next layer. In the reverse pass, the weights of the output neurons are adjusted first, since the target value of each output neuron is available to guide the adjustment of the associated weights. Next, the weights of the middle layers are adjusted, since the middle layers have no target values. As the errors of succeeding layers, after proper transformations, are propagated back through the network, layer by layer, this algorithm is termed as the back propagation algorithm.

After presenting the sets of inputs and associated outputs, the network is able to learn the relationships between them by changing the weights of its connections, *i.e.* training. Once the network has been trained according to the assigned learning rule, it is capable of computing the output values associated with new input vectors. The trained neural network has to be tested by supplying testing data. If the testing error is much more compared to training error, the network is said to over-fit the data. A properly fitted network will give nearly equal training and testing errors.

During hot working process, flow stress (σ) of the material is a function of three independent parameters, and is expressed as: $\sigma = \sigma(\varepsilon, \dot{\varepsilon}, T)$ (as discussed in Eq. 2.19). This σ of a particular material can be modeled by ANN architecture, as shown in Figure 2.7. In such a network, the input layer can consist of three neurons representing the three parameters *viz.*, ε, $\dot{\varepsilon}$, and T. The output layer on the other hand consists of one neuron representing σ. Once the proper network architecture is determined, σ can be successfully predicted for any combination of the input variables within the process domain. The σ values thus obtained can be successfully applied to generate processing maps to determine the safe processing zones.

Traditional curve fitting techniques have been used for obtaining these processing maps [PRAS1997]. Strain rate values generally used for carrying out experiments cover a range of four to five orders of magnitude. Hence, the traditional curve fitting techniques may not be appropriate for modeling such highly complex phenomena. On the other hand, neural network techniques have been found capable of learning from a data set to describe the non-linear and interaction effects with great success [ZURA1997]. The advantages of

neural networks are that the functional relationship between various variables can be obtained even if the form of non-linear relationship is unknown and some of the experimental data are faulty. This makes the neural network technique a robust technique for obtaining the functional relationship in any engineering problem. The application of neural network modeling in generating the processing maps for hot workability is covered in the following section. Neural network has been successfully demonstrated as a more robust technique than any other conventional methods for generating the processing maps [ROBI2003].

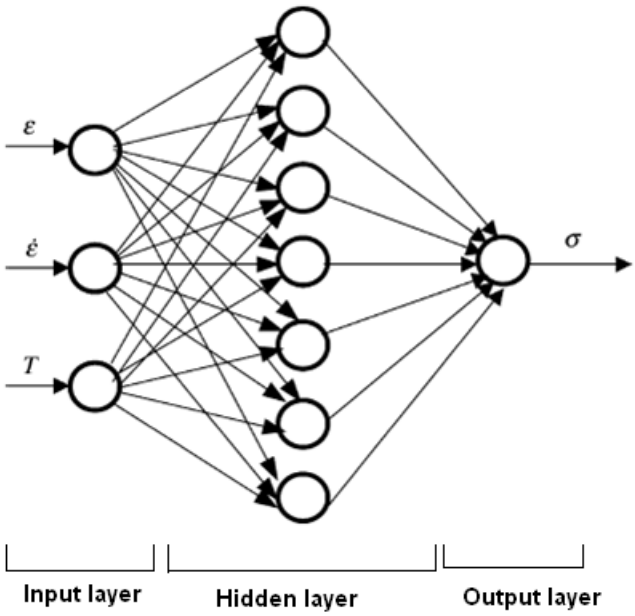

Fig.2.7. A typical neural network architecture [ROBI2003]

2.5.3 Processing map for hot workability

'Workability' is an important parameter in mechanical working of materials, which refers to the relative ease with which a metal can be shaped through plastic deformation without introducing any defect in it. One of the most important methods to express or demonstrate hot workability of a material is by means of processing maps. Various models

developed for understanding deformation behavior of metallic alloys are briefly discussed below:

***Kinetic models*:** The earlier developed models were of kinetic nature. The first one was based on kinetic analysis using the standard kinetic rate equation proposed by Dorn [DORN1961]. This model related the creep rate to the applied stress (power law creep) and temperature by the equation,

$$\dot{\varepsilon} = A\sigma^{n} \exp\left(-\frac{Q}{RT}\right) \tag{2.23}$$

where $\dot{\varepsilon}$ = strain rate, A = constant, σ = flow stress, n = stress exponent, Q = activation energy, R = gas constant and T = temperature. The application of kinetic analysis to hot deformation was reviewed in 1969 by Jonas *et al.* [JONA1969] and this methodology has been used extensively thereafter. On the basis of an activated process, the deformation mechanism could be evaluated and the microstructural features may be correlated with the Zener-Hollomon parameter (Z). The kinetic analysis is applicable for pure metals and dilute alloys but when applied to analyze the hot deformation behavior of complex alloys, the apparent activation energy values become too complex to interpret in terms of a single atomic mechanism. It is important to note that the kinetic rate equation is obeyed in the deterministic regimes of process parameters where a single rate controlling mechanism operates. Further, it is obvious that the kinetic analysis does not help in optimizing the hot workability.

***Atomistic mechanism maps*:** Ashby maps [FROS1982] were the first to represent the materials response in the form of deformation mechanism maps. These are plots of normalized stress *vs.* homologous temperature showing the area of dominance of each mechanism calculated using fundamental atomistic parameters. The emphasis in the Ashby maps has been on the creep mechanisms applicable to lower strain rates and so the maps are very useful in predicting the creep behaviors of the alloys. However, these were of not much use for predicting processes involving high strain rates such as those encountered in industrial deformation of alloys. Considering strain rate as one of the direct variables and temperature as the other, Raj [RAJR1981] extended the concept of Ashby maps to construct processing maps. Raj considered two different fracture nucleating mechanisms and

calculated the limiting conditions for avoiding the microstructural damage. These are: (i) cavity formation at hard particles in a soft matrix occurring at lower T and higher $\dot{\varepsilon}$, and (ii) wedge cracking at grain boundary triple junctions occurring at higher T and lower $\dot{\varepsilon}$. At very high $\dot{\varepsilon}$, a regime representing adiabatic shear band formation was considered. In principle, there is always a region which may be termed 'safe' for processing where neither of the two damage mechanisms nor adiabatic shear band formation occurs.

***Dynamic materials modeling*:** Dynamic materials model (DMM) has been developed [PRAS1984, PRAS1997] for studying the workability parameter. DMM was developed based on principles of continuum mechanics of large plastic flow using the concepts of physical systems modeling and extremum principles of irreversible thermodynamics. This model for hot deformation is expected to predict: (i) the response of the workpiece material in terms of microstructural evolution, (ii) optimum process parameters without trial and error, and (iii) process limits for controlling the manufacturing environment. The approaches available for modeling hot deformation behavior have been reviewed earlier by Prasad [PRAS1990] and Rao and Rajagopalachary [KUTU1996]. It was possible by DMM to bridge the principles of continuum mechanics of large plastic deformation and microstructural evolution in materials. In this model, the workpiece is considered to have the following characteristics [PRAS1997]:

1. The workpiece dissipates power during hot deformation and does not store energy significantly.
2. The constitutive response of the material at a given T during hot deformation depends essentially on the $\dot{\varepsilon}$ and to a small extent on the ε, *i.e.*, the workpiece is visco-plastic.
3. The flow stress response of the workpiece to the imposed variables like ε, $\dot{\varepsilon}$ and T is non-linear.
4. The large plastic flow at high T causes irreversible changes in the microstructure of the workpiece.

The major irreversible changes in the microstructure and their salient features are discussed below:

Dynamic recrystallization (DRX): The DRX domain generally occurs in the temperature range of 0.7 T_m - 0.8 T_m and at intermediate $\dot{\varepsilon}$ of 0.1 - 1 s^{-1} for materials with low stacking

fault energy (SFE) while it occurs at $\dot{\varepsilon}$ of 0.001 s^{-1} for high SFE materials. The maximum efficiency of power dissipation is about 30-35 % for low SFE materials, 40 % for medium SFE metals and 50-55 % for high SFE materials. Flow-softening with an initial peak stress generally suggests DRX. However similar behavior can also be due to certain flow instabilities which can be confirmed by the material modeling and microstructural observations. The grain boundaries of the DRX domain are more irregular and wavy in nature. The grain size variation with ln ($\dot{\varepsilon}$) at the DRX temperature exhibits a minimum at the peak efficiency. DRX process refers to the occurrence of simultaneous recrystallization during deformation by nucleation and growth processes [MCQU1990, PRAS1991, ROBE1984, SAKA1984, ZHAN2000]. The nucleation consists of the formation of grain boundary due to dislocation generation and simultaneous recovery. The growth of the nucleus is by grain boundary migration. When nucleation and growth occur simultaneously, the one with slower rate controls DRX. DRX differs from static recrystallization in the sense that DRX characteristics are decided by the rate of nucleation versus rate of growth under given conditions of $\dot{\varepsilon}$ and *T*. In static recrystallization on the other hand, a fixed amount of stored energy, depending on cold work, is released by thermally activated process.

DRX is a beneficial process [GAND1982] in hot deformation since it gives stable flow and good workability to the material by simultaneous softening and reconstituting the microstructure [STYL1994]. The as-cast (columnar, dendritic or microcrystalline) structure may be 'broken-down' to produce wrought microstructure. The acicular preform microstructure may be spheroidized as in Ti and Zr alloys, the prior particle boundary defects may be redistributed in powder metallurgy compacts or the discrete particle effects in P/M compacts may be eliminated by transferring mechanical energy across the hard particle interfaces to refine them by recrystallization. DRX is a chosen domain for optimizing hot workability and controlling the microstructure and is accepted as a safe domain for bulk metal working [PRAS1997].

Dynamic recovery: Thermal recovery of dislocations due to their climb causes dynamic recovery which occurs generally in the homologous temperature range of 0.4-0.6 and is thus relevant to warm working of materials. The dynamic recovered microstructure has

well defined subgrains with relatively dislocation free interiors. Dynamic recovery causes work hardening of the material, the rate of which is lower than that obtained in cold working

Adiabatic shear bands: During deformation at higher $\dot{\varepsilon}$, the lack of sufficient time to dissipate the heat generated results in local temperature rise in the workpiece. This results in non-homogeneous deformation in the form of localized shear bands. The flow localization results in a decrease in σ. The shear bands thus formed get intensified under adiabatic conditions [NARA2000, PRAS2000]. The adiabatic shear bands occur at an angle of 45^{o} with respect to the applied stress axis. Under intense conditions, these may result in internal cracks along these shear bands.

Void formation: Void formation at hard particles simultaneously becomes predominant at high $\dot{\varepsilon}$ and low T [PRAS1997, RAJR1981, RAVI1991]. If hard particles are present in a soft matrix, deformation causes voids to nucleate at the particle-matrix interface by debonding or by particle fracture. This ultimately leads to the microstructural damage in the workpiece.

Intercrystalline cracking: This feature is generally encountered at higher T and higher $\dot{\varepsilon}$. The fast propagation of cracks along the grain boundaries results in intercrystalline cracking. This may be due to the segregation of low melting phases / compounds at the grain boundaries. Adiabatic temperature rise at higher $\dot{\varepsilon}$ may aggravate cracking by incipient melting.

Wedge cracking and super plasticity: *S*uperplasticity and wedge cracking are two irreversible phenomena which can occur at temperatures in the range of 0.7 T_m - 0.8 T_m and at $\dot{\varepsilon} < 0.01\ s^{-1}$. Both processes are characterized by high efficiency of power dissipation (> 60 %) and a steep rise of efficiency with decrease in $\dot{\varepsilon}$. During wedge cracking, which is the zone identified at lower $\dot{\varepsilon}$ and higher T, grain boundary sliding occurs under shear stress. Wedge cracks are produced at triple junction points to relieve the stress concentration [PRAS1997]. If the $\dot{\varepsilon}$ is so high that the matrix deforms at a rate faster than the rate at which the boundaries can slide, then the sliding effect would be negligible, thereby preventing wedge cracking. However, at lower $\dot{\varepsilon}$, there is enough time to relax the high stress at the triple junctions. Wedge cracking may be identified by microscopic

observation of the grain boundary triple junctions particularly in the area of the specimen where a tensile component of the stress occurs (*e.g.* bulge region of a compression specimen).

Materials with stable fine-grained structure when deformed at low $\dot{\varepsilon}$ and high T exhibit abnormal elongations and the process is called superplasticity [LUTO1969]. If the stress concentration is relieved by diffusion-aided flow, superplasticity occurs [PRAS1997].

The above mentioned damage processes are sometimes very efficient in dissipating power for the generation of new surfaces. On the other hand, the safe processes become less efficient, because power dissipates through annihilation of dislocations. However, DRX holds a higher efficiency than dynamic recovery [RAVI1991].

σ-ε curves provide information related to the mechanisms of hot deformation. Different 'safe' and 'damage' mechanisms occur at various combinations of $\dot{\varepsilon}$ and deformation T. The safe mechanisms comprise of dynamic recovery occurring at lower T and $\dot{\varepsilon}$, and DRX occurring at higher T and intermediate $\dot{\varepsilon}$ [RAVI1991]. Among the above mentioned mechanisms, the superplastic deformation is also considered to be safe while the others are to be avoided during hot deformation. However, for optimizing hot workability and controlling the microstructure, dynamic recrystallization is a chosen domain.

Flow behavior and processing maps

The flow behavior of materials varies with $\dot{\varepsilon}$ and T.

The general expression of σ at constant ε and T is given by:

$$\sigma = K\dot{\varepsilon}^{m}\Big|_{\varepsilon,T} \tag{2.24}$$

where K and m are constants. A typical $\ln(\sigma)$ *vs.* $\ln(\dot{\varepsilon})$ plot at constant T is shown in Figure 2.8. The term m, the strain rate sensitivity, is given by the expression:

$$m = \frac{\partial \ln \sigma}{\partial \ln \dot{\varepsilon}}\Big|_{\varepsilon,T} \tag{2.25}$$

Values of m lie between 0 and 1, for a stable material flow. However, m varies with $\dot{\varepsilon}$ values. The power dissipated per unit volume is given by:

$$P = G + J = \sigma \dot{\varepsilon} \tag{2.26}$$

where G and J are the dissipater content and dissipater co-content, respectively, given by the following equations:

$$G = \int_0^{\dot{\varepsilon}} \sigma \, d\dot{\varepsilon} \tag{2.27}$$

$$J = \int_0^{\sigma} \dot{\varepsilon} \, d\sigma \tag{2.28}$$

The maximum value of dissipater co-content can be expressed as:

$$J_{\max} = \frac{1}{2} \sigma \dot{\varepsilon} \tag{2.29}$$

The schematic representation of G content, J co-content and J_{max}, is shown in Figure 2.9. The efficiency of power dissipation (η) can be defined as:

$$\eta = \frac{J}{J_{\max}} \tag{2.30}$$

If m is considered as constant corresponding to its value at limiting $\dot{\varepsilon}$, J can be obtained from the following expression

$$J = \frac{m \sigma \dot{\varepsilon}}{m+1} \tag{2.31}$$

The efficiency of power dissipation according to the DMM model [PRAS1984] is

$$\eta = \frac{2m}{m+1} \tag{2.32}$$

Efficiency was directly computed by calculating J by numerical integration [NARA2000], where the assumption of m as a constant term with respect to $\dot{\varepsilon}$ is not required. The efficiency of power dissipation can be obtained from the flow stress as:

$$\eta = \frac{J}{J_{\max}} = \frac{P - G}{J_{\max}} = 2\left(1 - \frac{1}{\sigma \dot{\varepsilon}} \int_0^{\dot{\varepsilon}} \sigma \, d\dot{\varepsilon}\right) \tag{2.33}$$

The above integral in Eq. (2.33) can be split and expressed as:

$$\int_0^{\dot{\varepsilon}} \sigma \, d\dot{\varepsilon} = \int_0^{10^{-3}} \sigma \, d\dot{\varepsilon} + \int_{10^{-3}}^{\dot{\varepsilon}} \sigma \, d\dot{\varepsilon}$$
$$= \left(\frac{\sigma \dot{\varepsilon}}{m+1} \right)_{\dot{\varepsilon}=10^{-3}} + \int_{10^{-3}}^{\dot{\varepsilon}} \sigma \, d\dot{\varepsilon} \qquad (2.34)$$

Ziegler [ZIEG1965] applied continuum mechanics principles for large plastic flow, which was used by Kumar [KUMA1987] to arrive at the following metallurgical instability criteria:

$$\xi\left(\dot{\varepsilon}\right) = \frac{\partial \ln\left(\frac{m}{m+1}\right)}{\partial \ln \dot{\varepsilon}} + m \leq 0 \qquad (2.35)$$

The parameter $\xi\left(\dot{\varepsilon}\right)$ is evaluated as a function of T and $\dot{\varepsilon}$ to obtain an instability map, indicating metallurgical instability during plastic flow occurring at regimes where its values are negative.

The procedure of generating processing maps and their interpretations have been discussed in detail in the literature [PRAS1997]. These maps can be generated from hot compression tests data acquired at constant $\dot{\varepsilon}$ under isothermal conditions. A processing map is an explicit representation of the response of the material in terms of microstructural mechanisms, to the imposed process parameters. It is obtained by the superimposition of a power dissipation map and instability map developed on the basis of DMM [PRAS1997]. Typical examples of power dissipation efficiency map, instability map and processing map generated from them, are illustrated in Figure 2.10.

In a power dissipation map, the efficiency of power dissipation is contour plotted as a function of T and $\dot{\varepsilon}$ at a particular true strain value. It exhibits various domains in which specific microstructural mechanisms occur. The efficiency map itself represents the power transactions within a continuum and the understanding of its origin and its interpretation in terms of atomistic mechanisms requires a correlation with the concepts of irreversible thermodynamics. It helps in interpreting the microstructures resulting from hot deformation as 'dissipative' and characterizes them in terms of atomistic mechanisms. Instability map separates out the regions of stable and unstable flow.

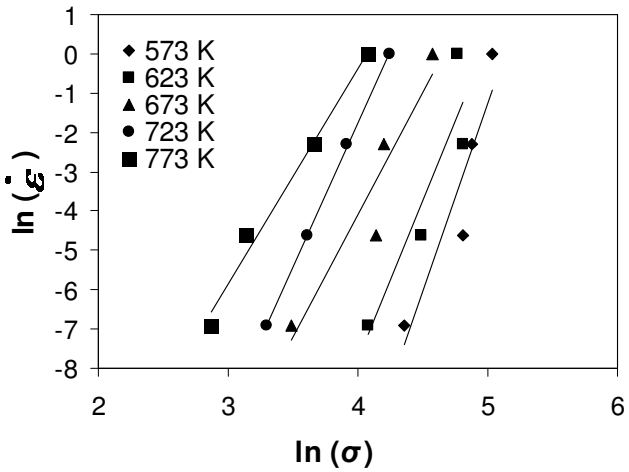

Fig.2.8. Plots of: ln $\dot{\varepsilon}$ *vs.* ln σ at constant T, for an Al-Cu-Mg alloy

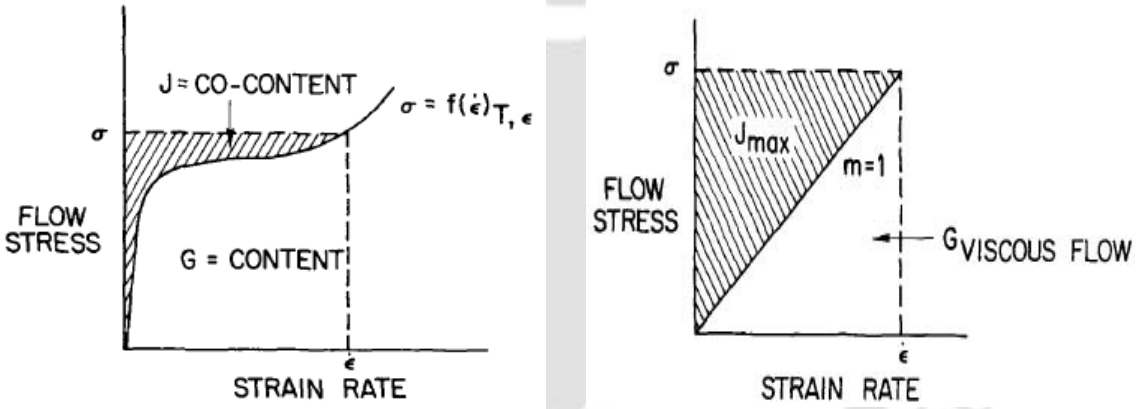

Fig.2.9. Schematic representation of (a) G content and J co-content for workpiece with a constitutive equation represented by the curve $\sigma = f(\dot{\varepsilon})_{T,\varepsilon}$, (b) J_{max}, when m=1 [PRAS1984]

Industrial metal working processes require the information provided by the processing maps. For newer materials, the process can be designed to suit the constitutive requirements of the material from the viewpoint of optimum workability and microstructural control. In addition, these maps can be used to optimize existing processes which can help improve the product quality and yield. Defects arising during hot deformation processing can be avoided with the knowledge of the limiting T and $\dot{\varepsilon}$ conditions, which lead to the flow instabilities.

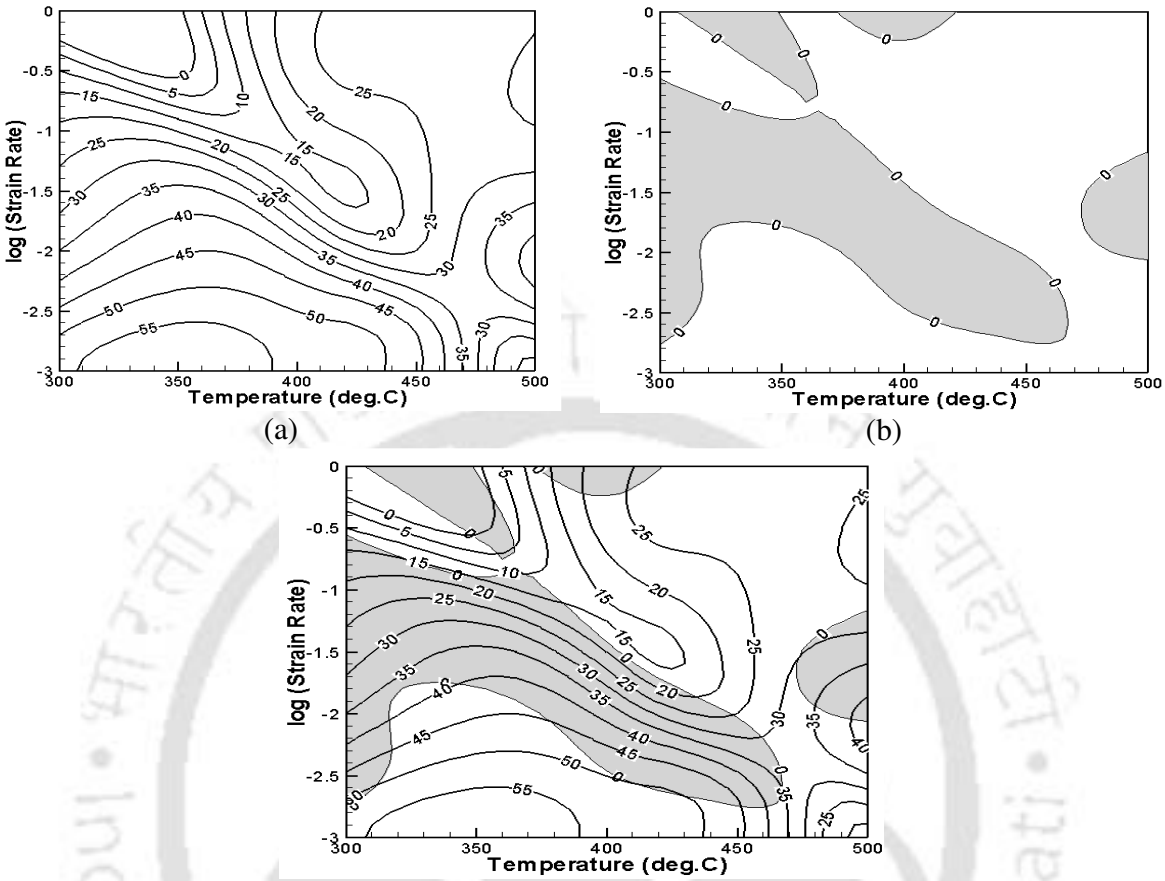

Fig.2.10. Typical examples of (a) power dissipation efficiency map (b) instability map (c) processing map obtained superimposing the previous two maps for an Al–Cu–Mg alloy

Processing maps for a large number of metals, alloys, intermetallics and metal matrix composites have been systematically compiled along with a summary of metallurgical interpretations [PRAS1997]. Maps have also been generated for TiAl/TiB_2 composites by Zhao *et al*. [ZHAO1994], microalloyed steel by Omar *et al*. [OMAR1996] and rolled aluminum [VENU1993].

Various structural defects arising in 2124 Al alloy produced by P/M technique at different deformation conditions have been studied. Flow instability in this alloy arising from adiabatic shear band formation and matrix cracking has been observed [RAMA2006]. In a study of Al with different purities in the temperature range of 250 °C to 600 °C, DRX was observed to occur at a particular $\dot{\varepsilon}$, while the DRX temperature increased with

decrease in the purity level of Al [RAVI1991]. Al–4Mg alloy exhibited wedge cracking when deformed at $\dot{\varepsilon} < 0.2$ s^{-1} and $T > 650$ K [RAOK1990]. 6061 Al alloy composite reinforced with 20% Al_2O_3 was investigated to evaluate the efficiency of forging process by generating processing maps [CERR2002]. The power dissipation efficiency, instability regimes, shear band formation and other structural defects have been investigated for various Ti alloys at various deforming conditions. These include the studies on forged Ti-6242 titanium alloy and commercially pure Ti [PRAS1984, SATI1993]. However, only a few reports are available on the effect of alloying elements and the corresponding microstructural changes occurring in Al alloys during hot deformation. Addition of Erbium was observed to restrain recrystallization in Al–5.7Mg alloy [GANG2009]. The apparent activation energies estimated for the two domains of dynamic recovery suggested cross-slip of dislocation and lattice self-diffusion as the deformation mechanisms. Yang Sheng *et al*. [YANG2008] while investigating the flow stress behavior and processing map of Al–Cu–Mg–Ag alloy observed two optimum domains for hot deformation at different ε, including the high $\dot{\varepsilon}$ domain between 623-773 K and the low $\dot{\varepsilon}$ domain in the 573-673 K range. Investigations on the hot deformation behavior of Al–Mg–Si–Cu alloys revealed dynamic flow softening resulting from dynamic recovery and DRX [ZHAN2007]. Microstructural characterization of hot deformed Al–Cu–Mg–Ag alloy revealed that with decreasing Z value, the subgrain size increased, dislocation density decreased and the major softening mechanism got transformed from dynamic recovery to DRX [QING2009].

Very few studies have been reported on the different mechanisms of high temperature deformation behavior correlated with kinetics of dislocation generation and annihilation, nucleation of new phases and zones, precipitation growth or recrystallization for some commercial 2xxx series Al alloys like 2219 and 2618 [CAVA2002, KAIB2002].

Literature reveals several studies on power dissipation maps and instability maps of some commonly used aluminum alloys. However, processing maps for Al–Cu–Mg alloys microalloyed with additive elements have not been generated so far. Since these alloys have considerable industrial applications, these maps are important.

2.5.4 Multiple Linear Regression (MLR) analysis

In statistics, regression analysis includes any techniques for modeling and analyzing several variables, when the focus is on the relationship between a dependent variable and one or more independent variables. More specifically, regression analysis helps us to understand how the typical value of the dependent variable changes when any one of the independent variables is varied, while the other independent variables are held fixed. In all cases, the estimation target is a function of the independent variables called the *regression function*. In regression analysis, it is also of interest to characterize the variation of the dependent variable around the regression function, which can be described by a probability distribution.

A large number of techniques have been developed for carrying out regression analysis. Familiar methods such as linear regression and ordinary least squares regression are parametric, in that the regression function is defined in terms of a finite number of unknown parameters that are estimated from the data. Nonparametric regression refers to techniques that allow the regression function to lie in a specified set of functions, which may be infinite-dimensional.

The performance of regression analysis methods in practice depends on the form of the data-generating process, and how it relates to the regression approach being used. Since the true form of the data-generating process is not known, regression analysis depends to some extent on making assumptions about this process. These assumptions are sometimes (but not always) testable if a large amount of data is available. Regression models for prediction are often useful even when the assumptions are moderately violated, although they may not perform optimally. [DAVI2005, DENN1982].

Applications of MLR to high temperature metal working process

During hot working process, flow stress of the material (σ) is a function of three independent parameters, *viz.* $\sigma = \sigma\ (\varepsilon,\ \dot{\varepsilon}\ , T)$ (as discussed in Eq. 2.19). The neural network modeling gives a methodology to predict the σ with reasonably good accuracy. However, this information may not be much useful for the research community, especially for modeling studies carried out by techniques like FEM, FDM, *etc*, since algebraic

relationships are required for carrying out these studies. Therefore attempts have been made to model algebraic relationship of the form $\sigma = f(\varepsilon, \dot{\varepsilon}, T)$, and subsequently predict the σ in high temperature deformation process.

The variation of σ with ε is given by the power law [GEOR1988]

$$\sigma = K\varepsilon^n \tag{2.36}$$

where, K is the strength coefficient and n is the strain hardening exponent of the material.

The general relationship between σ and $\dot{\varepsilon}$, at constant ε and T is expressed as [GEOR1988]:

$$\sigma = C(\dot{\varepsilon})^m \Big|_{\varepsilon,T} \tag{2.37}$$

where, C is a constant term and m is the strain-rate sensitivity of the material.

The temperature dependence of σ at constant ε and $\dot{\varepsilon}$ generally can also be represented by [GEOR1988]:

$$\sigma = C_2 e^{Q/RT} \Big|_{\varepsilon,\dot{\varepsilon}} \tag{2.38}$$

where, C_2 is a constant term, Q is the activation energy for plastic flow and R is the universal gas constant.

Considering the above relationships of σ with ε, $\dot{\varepsilon}$ and T, a power relation can be chosen for regression analysis and predicting σ during metal working. The σ during hot deformation can therefore be assumed to be of the form,

$$\sigma = A\ \varepsilon^m \dot{\varepsilon}^n T^l \tag{2.39}$$

where, σ is the flow stress, ε is the true strain, $\dot{\varepsilon}$ is the true strain rate and T is the deformation Temperature. The coefficient values of A, m, n, and l can be obtained by MLR. After successful evaluation of these coefficients, the σ of a material can be predicted using the Eq. (2.39).

The empirical relation is derived on the basis of obtained experimental results for predicting σ in terms of ε, $\dot{\varepsilon}$ and T. Assuming that the variables agree with the linear model, it may be expressed as:

$$Y = XB \tag{2.40}$$

Where, Y is the $i\times1$ matrix of output parameter, X is the $i\times p$ matrix of input parameter and B is the $p\times1$ matrix of coefficients. For the present model with three input variables, $P = 4$.

From Eq. (2.39), one can arrive at the following relationship, which can be used for the MLR fitting procedure:

$$\sigma_i = A \times (\varepsilon_i)^m \times (\dot{\varepsilon}_i)^n \times (T_i)^l \tag{2.41}$$

where, σ_i is the output for the i^{th} data set,

ε_i, $\dot{\varepsilon}_i$ and T_i are the input variables for the i^{th} data set, and A, m, n and l are the regression coefficients.

Taking logarithm of Eq. (2.41), it can be transformed into the linear form

$$\log(\sigma_i) = \log(A) + m \log(\varepsilon_i) + n \log(\dot{\varepsilon}_i) + l \log(T_i) \tag{2.42}$$

The above MLR model can thus be represented in the following matrix form

$$Y = XB \tag{2.40}$$

where,

$$Y = \begin{Bmatrix} \log(\sigma_1) \\ \log(\sigma_2) \\ : \\ \log(\sigma_i) \end{Bmatrix}, \quad X = \begin{bmatrix} 1 & \log(\varepsilon_1) & \log(\dot{\varepsilon}_1) & \log(T_1) \\ 1 & \log(\varepsilon_2) & \log(\dot{\varepsilon}_2) & \log(T_2) \\ : & : & : & : \\ 1 & \log(\varepsilon_i) & \log(\dot{\varepsilon}_i) & \log(T_i) \end{bmatrix}, \quad B = \begin{Bmatrix} A \\ m \\ n \\ l \end{Bmatrix}$$

Once the regression coefficients are determined, σ can be successfully predicted for any combination of the input variables within the process domain. The predicted σ values can be compared with the experimental results to check out with the accuracy of the adopted model.

2.6 Objectives of the present investigations

It has already been indicated from the literature that there is a keen interest in developing alloys exhibiting high strength and light weight for structural applications, especially in the areas of space and aircraft structures. Al alloys, especially the wrought and precipitation strengthened 2xxx series of alloys having high strength to weight ratio, were developed for the above purpose. These wrought alloys are generally used after deformation processing followed by a sequence of heat treatments. The mechanical

properties of these alloys are strongly influenced by factors like alloy composition, strain history and the microstructure resulting from the thermo-mechanical treatment imparted before the final use. A clear understanding of the process parameters related to casting, secondary processing, hardening heat treatments and high temperature deformation behavior is necessary for obtaining the required shapes and sizes with desired mechanical properties.

On the other hand, the mechanical properties of these alloys are affected even by small variations in the composition and microstructure of the alloys. The present trend to develop these materials with increased strength combined with reasonable toughness and low density is by the addition of trace elements (microalloying) like Sn, In, Cd, Ag, Si, *etc.* in the alloy matrix.

Literature is available on the investigations carried out to study structure and properties of some commercial Al alloys. However, detailed and systematic investigations on the effect of microalloying on the heat treatable 2xxx series of Al alloys are still very few. Especially, the influence of trace content of Sn on the mechanical properties of Al–Cu–Mg alloys has not been extensively explored. Hence, there is a need to investigate the microstructural evolution, precipitation behavior, evaluation of mechanical properties in the as-cast, rolled and heat treated conditions, and high temperature deformation characteristics of microalloyed Al-Cu-Mg alloys. The lack of sufficient literature in the above area gives rise to several issues worth investigating, some of which are listed below:

- Influence of trace additions of Sn on the microstructure and mechanical properties of the Al–Cu–Mg alloys in as-cast, annealed and rolled conditions.
- Effect of Sn addition on the age-hardening conditions required to achieve peak hardness of the alloy.
- Study of precipitation kinetics and evaluation of kinetic parameters in the rate equation for the Al–Cu–Mg alloys microalloyed with Sn.
- Effect of Sn addition on the high temperature deformation behavior of the Al–Cu–Mg alloys.
- Constitutive analysis and modeling of flow characteristics of Al–Cu–Mg alloys microalloyed with Sn.

- Computational modeling and prediction of flow stress by ANN technique or multiple linear regressions analysis of the relevant alloys.
- Generation of processing maps for Al–Cu–Mg alloys microalloyed with Sn.

The present study was therefore undertaken to process Al–Cu–Mg (Al–5.9%Cu–0.5%Mg) alloys microalloyed with varying contents (from 0 to 0.1 wt.%) of Sn, by a casting route. The primary objective was to study the microstructures and mechanical properties of the alloys in the cast, annealed and rolled conditions. Effect of trace additions of Sn on the age hardening behavior, precipitation kinetics and high temperature deformation behavior of the alloys were also taken up for study.

The objectives of the present study are,

1. To process the Al–5.9wt.%Cu–0.5wt.%Mg alloys microalloyed with Sn of varying weight percentages (from 0 to 0.1) by a casting route.
2. To study the microstructures and mechanical properties in the cast, annealed and rolled conditions.
3. To optimize the age hardening conditions required to achieve peak hardness value.
4. To study the precipitation kinetics, evaluate the kinetic parameters and thereby generate the kinetic rate equation of the investigated alloys.
5. To study the effect of Sn addition on the high temperature deformation behavior of the investigated alloy system.
6. To generate constitutive equation for modeling the high temperature deformation behavior and predicting peak flow stress of the alloy with varying Sn contents and at different deformation conditions.
7. To generate a model and therefore predict the flow stress (σ) as a function of strain (ε), strain rate ($\dot{\varepsilon}$) and temperature (T) of all the investigated alloys at different deformation conditions by ANN and multiple linear regressions analysis.
8. To generate processing maps for the investigated alloy system with different trace contents of Sn.

Chapter 3

Experimental Procedures and Methodology Adopted

This chapter describes the preparation and processing of Al-Cu-Mg alloys microalloyed with Sn. Details of the experimental set ups designed and fabricated in the course of the experimental investigations are given below. The characterization techniques used and the experimental procedures adopted in the investigations carried out in this thesis work are also detailed below.

3.1 Processing of Al–Cu–Mg alloys by casting technique

Al–Cu–Mg alloys microalloyed with varying percentages of Sn were prepared by casting route. The experimental set-ups, raw materials used and the detailed casting procedure adopted are described in the following sections.

3.1.1 Equipment used for the preparation of the alloys

The equipments fabricated / used in the preparation and processing of the investigated alloys are

a) An indigenously designed and fabricated resistance furnace for melting and casting Al–Cu–Mg alloys.
b) Graphite moulds for obtaining sample specimen of cylindrical shape.
c) Metallic moulds for obtaining alloy castings of rectangular cross section.
d) Muffle furnace for heat treatment of the alloy samples.

Details of these experimental set-ups are given below.

Design and fabrication of resistance furnace

A resistance heated furnace was designed and fabricated. It consists of a mild steel casing with an insulating lid at the top. The furnace chamber was made of a ceramic muffle of dimension 120×120×180 mm^3. SWG 16 gauge Kanthal wire wound around the muffle served as the heating element. The heating element was embedded in alumina powder with sodium silicate as the binder. The space between the muffle and the casing was then tightly packed with ceramic wool to ensure that the skin temperature of the casing did not exceed 50 ºC after prolonged use of the furnace at 800 ºC. Electrical power of 1.3 kW was sufficient to attain 750 ^{o}C in the furnace chamber. The temperature of the furnace was controlled using an on-off controller equipped with a *K*-type thermocouple as sensor. The temperature was measured using the thermocouple inserted into the crucible through a port provided on the furnace lid. Melting of the alloy components was carried out in a clay-graphite crucible kept inside the furnace chamber. The resistance furnace, rectangular and cylindrical moulds are displayed in Figure 3.1(a). Figure 3.1(b) shows an empty crucible used for the melting purpose.

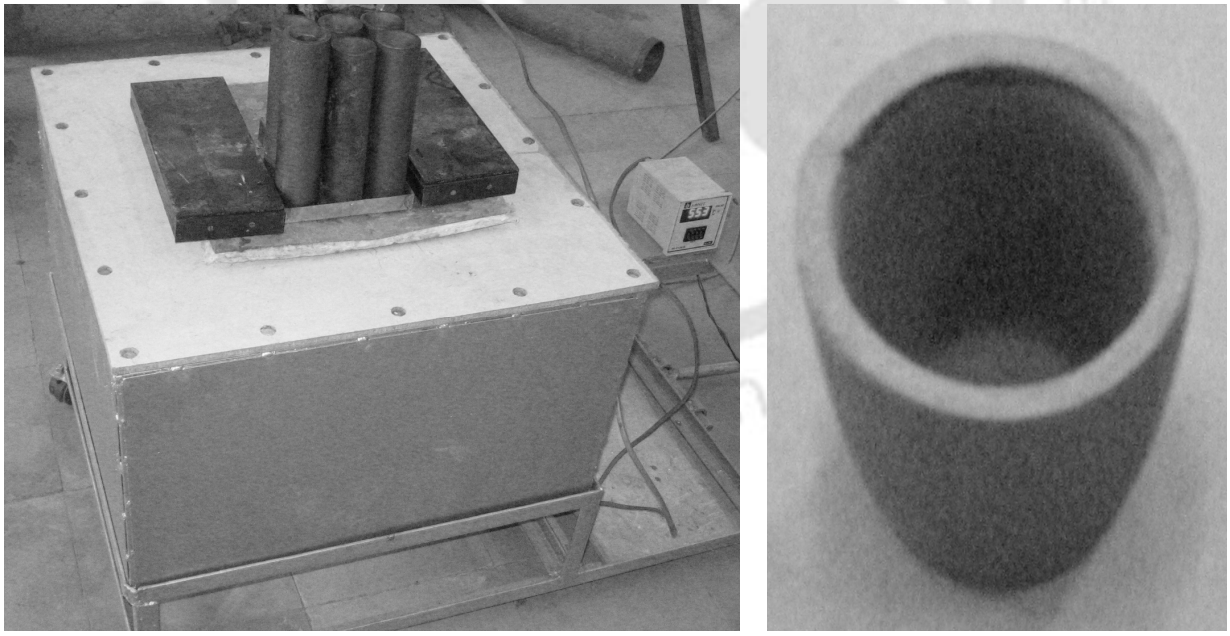

(a) (b)

Fig.3.1. (a) The furnace and the molds and (b) the clay-graphite crucible

Graphite moulds

In order to prepare samples suitable for tensile and compression tests, the alloys had to be cast in cylindrical shapes of required dimensions. For this, cylindrical moulds having a tapered cavity were fabricated out of high density graphite. Cylindrical alloy samples of dimensions ~ 12 mm diameter and 200 mm length could be obtained using these moulds. The drawing of the graphite mould is shown in Figure 3.2 (a).

Metallic moulds

To obtain rectangular castings, two split type metallic moulds were machined from mild steel. With these moulds, rectangular castings of dimension 300×100×12 mm^3 could be obtained. The drawing of the metallic mould is shown in Figure 3.2(b). The inside surfaces of the metallic moulds were surface grinded to obtain a smooth surface and a thin layer of a paste containing a mixture of sodium silicate and alumina powder was applied on the inner surface for easy removal of the cast samples. These rectangular alloy plates cast in the metallic moulds were used for microstructural investigation and mechanical property evaluation in cast and solutionized conditions. During the later stages of the investigations, warm rolling was carried out from these rectangular cast samples to determine the tensile properties of rolled alloys.

3.1.2 Raw materials used

The raw materials used for the preparation of the alloys are

a) commercially pure (99.9 % pure) aluminum ingot,
b) electrical grade copper (99 % pure),
c) high purity Sn powder (99 % pure),
d) commercially pure magnesium ingot (99.9 % pure), and
e) degasser tablets purchased (Degasser 190).

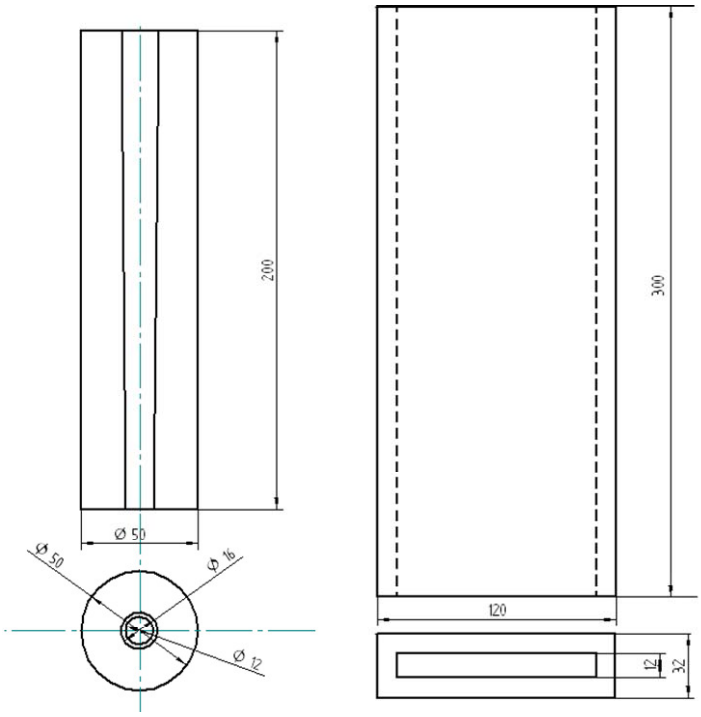

Fig.3.2. The design drawings of (a) graphite moulds and (b) metallic moulds.

3.1.3 Casting procedure

The clay-graphite crucibles pre-sintered for 3 h at 800 °C were used for melting the alloys. Following the common foundry practice, master alloys were first prepared with higher Cu and Sn contents. This was done to ensure proper control of composition during independent melting and to maintain low alloy melting point. Accordingly, Al–33wt.%Cu and Al–25wt.%Sn master alloys were first prepared independently by melting commercially pure Al, Cu/Sn of appropriate weight proportions. Care was taken to homogenize the molten alloy by frequent stirring during melting. The homogenized melt was then poured in to the metallic moulds and allowed to solidify.

The procedure followed for preparing alloys with nominal compositions of the desired Al-Cu-Mg with trace elements of Sn is as follows. Required quantity of Al–Cu master alloy was first melted with pure Al ingots to obtain a target composition of Al–

6.0%Cu. Once the melt temperature reached 670 °C, the dross accumulated at the top of the melt was removed. This was followed by degassing of the melt to remove dissolved gases by adding 0.5 wt.% of degasser tablets with simultaneous stirring. After ensuring complete degassing, the dross accumulated was skimmed and removed. Mg pieces of 0.6 wt.% of the total melt was then added in to the melt and stirred with a stainless steel rod to obtain a uniform target alloy composition. Appropriate amount of the Al–25wt.%Sn master alloy was then added to the melt. The melt was then stirred gently for a few minutes to ensure uniform mixing of Sn in the melt. The melt temperature was then raised and held at 700 ºC (corresponding to ~50 °C super heat) for 5 min before pouring the same in to the moulds for solidification.

Six different alloys with Sn content varying from 0 to 0.1 wt.% were prepared by this procedure. The alloys were designated as Alloy-*A* to Alloy-*F* based on their Sn contents as shown in Table 3.1.

Table 3.1. Labels of the alloys prepared.

Sl No.	Alloy designation	Sn content (wt.%)
1	Alloy-*A* (Base alloy)	0.00
2	Alloy-*B*	0.02
3	Alloy-*C*	0.04
4	Alloy-*D*	0.06
5	Alloy-*E*	0.08
6	Alloy-*F*	0.10

3.2 Composition analysis

In order to evaluate the exact percentage of the major elements (*i.e.* Al, Cu, Mg, Sn, Fe and Si) in the investigated cast alloys, composition analysis was carried out by atomic absorption spectrometry [AASMANUL]. The standard solutions were first prepared as specified in the user manual of flame atomic absorption spectrometer (AAS, VARIAN, SPECTRA DUO). 1 g of each sample taken in a polytetra fluoroethylene (PTFE) beaker kept in a water bath was digested by sequentially adding 20 ml of HCl and 4 ml of HNO_3

drop-wise. 100 ml stock solution was then prepared from this solution by addition of distilled water. 5 ml of the stock solution was added to 2 ml of 100 g/L of potassium solution. The resulting solution was made up to 100 ml with the addition of distilled water. The diluted solution thus prepared was analyzed using AAS in order to obtain the concentration of the elements in the investigated alloys.

3.3 Post casting heat treatments

Presence of metastable phases as well as coring and segregation is expected in the as-cast alloy microstructure of the alloys studied. These result in non-homogenous distribution of elements thereby resulting in variation of mechanical properties across the casting section. To ensure a homogeneous composition, removal of any metastable phases, coring and segregation formed in the as-cast alloys, they were subjected to a homogenizing heat treatment at 510 ^{o}C for 10 h. The microstructures of the alloys were studied and tensile properties were investigated. The samples for studying the hot deformation behavior were also subjected to the same heat treatment. The highest strength for the base alloy is obtained by solution strengthening heat treatment followed by precipitation hardening heat treatment. During the solution strengthening heat treatment, copper solute will dissolve in the Al matrix which when suddenly cooled will form a supersaturated solid solution of copper in aluminum matrix resulting in strengthening. The strength obtained will also depend on the cooling rate. Hence, the properties of these alloys were studied after solutionizing at 525 ^{o}C for 10 h followed by (i) furnace cooling and (ii) water quenching, which enabled the study of the effect of quenching rate on the alloy hardness. The solutionizing temperature of the Al–Cu–Mg alloy was based on the data obtained from the ASM Handbook [ASMHVOL4].

Since no information about the peak ageing time of Al–Cu–Mg alloy containing trace percentages of Sn was available, it was necessary to optimize the age hardening conditions. However, literature showed that the age hardening of most of the 2xxx series Al alloys were carried out at temperatures between 160 °C and 190 °C [ASMHVOL4, ELAG2007, XIAO2009, ZHON2006]. Hence, the alloys prepared in this investigation were

given a solutionizing heat treatment at 525 ^{o}C for 10 h and subsequently water quenched to obtain a supersaturated solid solution. They were than age hardened at 170 °C for periods up to 52 h (*cf.* Table 3.2; heat treatment-*4*). Samples were taken out at regular intervals of time and the hardness (VHN) values were evaluated and plotted against ageing time.

The details of the processing conditions and heat treatments adopted in the study are presented in Table 3.2.

Table 3.2. Details of heat treatments carried out on the investigated alloys

Heat treatment designation	Heat treatment conditions
1	Cast alloys homogenized at 510 ^{o}C for 10 h and furnace cooled
2	Cast alloys solutionized at 525 ^{o}C for 10 h followed by water quenching
3	Cast alloys solutionized at 525 ^{o}C for 10 h followed by furnace cooling
4	Cast alloys solutionized at 525 ^{o}C for 10 h and water quenching followed by age hardening heat treatment at 170 ^{o}C for 52 h
5	Alloys were warm rolled at 200 ^{o}C and subjected to heat treatment-*1*
6	Alloys were warm rolled at 200 ^{o}C, subjected to heat treatment-*2* and then peak aged at 170 ^{o}C for 24 h

3.4 Warm rolling of cast ingots

The Al-Cu-Mg alloys are wrought alloys. The best mechanical properties of these alloys are obtained when these alloys are plastically deformed at elevated temperature. This is achieved by elimination of inherent defects, refinement of the grains, and metal flow resulting in preferred orientation of the crystal grains, during the plastic deformation. Warm rolling was carried out on the cast rectangular plates having dimensions of 300×100×12 mm^3. These plates were machined to remove the thin cast surface features which may result

in surface defects during the rolling process. They were finally machined to obtain strips of size 300×25×10 mm^3 mm size for rolling operation.

The machined samples were subjected to a homogenizing heat treatment as mentioned in Table 3.2. Prior to rolling, they were preheated at 200 °C for 1 h and then warm rolled at the same temperature in a laboratory scale mill. Rolling was carried out in three passes to obtain strips of ~350 mm (length), ~30 mm (width) and 4 mm (thickness).

The rolled samples were homogenized (Heat treatment-5) before conducting the tensile tests. To study the effect of age hardening, the rolled samples were solutionized at 525 ^{o}C for 10 h followed by precipitation heat treatment at 170 ^{o}C for 24 h. These conditions were chosen based on the data obtained for achieving peak hardness for the cast alloys while studying the age hardening behavior of the cast alloys.

3.5 Microstructural characterization

Microstructural characterization of the alloys was carried out both in the as-cast as well as in heat-treated conditions. Samples were prepared by standard metallographic procedure and observed under both optical and scanning electron microscopes, to determine the microstructural features, grain sizes, different phases observed and their compositions. The detailed procedures followed are given below.

3.5.1 Metallographic sample preparation

Samples of dimension 10 mm × 10 mm were sectioned using low-speed precision saw (Buehler, ISOMET 2000). The sliced samples were mounted in thermosetting resin using a hot mounting press (Buehler, Simplimet-2). The mounted samples were then polished using a variable speed grinder-polisher (Buehler, Ecomet-6). Dry grinding was carried out using SiC coated papers of various grit sizes (240, 320, 400 and 600) in a progressive sequence. Subsequently, wet cloth polishing was carried out using 0.5 μm sized alumina suspension dispersed in distilled water as the abrasive medium. The samples were then ultrasonically cleaned in acetone, dried and preserved in a vacuum desiccator.

3.5.2 Optical microscopic (OM) investigation

The metallographically polished samples were etched by immersing the sample in Keller's reagent for 8-15 s, to reveal the grain boundaries and different phases present in the alloy matrix. The chemical composition of the Keller's reagent used for etching purpose is given in Table 3.3. The samples were then washed in running water and dried.

Table 3.3. The chemical composition of the Kellar's reagent [ASMHVOL9]

Chemical reagent	Percentage composition in every 200 ml reagent (in ml)
Hydrofluoric acid – 48% conc.	2
Hydrochloric acid – 35% conc.	3
Nitric acid – 70% conc.	5
Distilled water	190

The polished and etched specimens were observed under an upright optical microscope (Carl Ziess, Axiotech) equipped with Kontron KS-400 image analysis system. The grain size for each sample was determined by the standard line intercept method.

3.5.3 Scanning electron microscopic (SEM) investigation

The (unetched) polished samples were gold coated using a sputter coater and observed under a scanning electron microscope (SEM, LEO, 1430 VP) under an accelerating voltage range of 10-20 kV. Images were observed under both secondary electron (SE) mode as well as back scattered detector (BSD) image mode. The composition of different phases present were analyzed using an energy dispersive X-ray spectrometer (EDS, Oxford) attached to the SEM. The EDS analysis was carried out using high purity cobalt as the reference standard and maintaining a working distance of 15 mm.

3.6 Differential Scanning Calorimeter (DSC) studies

The kinetics of the precipitation and dissolution reactions observed during heat treatment of the Al–Cu–Mg alloys microalloyed with varying percentage of Sn were

studied using a differential scanning calorimeter (DSC, Perkin Elmer, DSC 7). Four sets of samples were prepared from each alloy so as to carry out the experiments at four different heating rates. Samples were prepared in the form of discs of 3 mm diameter with weights in the range of 18 mg to 20 mg. The discs were vacuum encapsulated (at ~10^{-3} Pa) in fused silica tubes and solutionized at 500 °C for 10 h followed by water quench to room temperature. The quenched samples were stored in a refrigerator at ~ 5 °C prior to the DSC run. The baseline data for each heating rate was recorded using high purity Al pan as the reference.

DSC curves were recorded from 50 °C to 550 °C under a constant heating rate and then subsequently cooled to 50 °C at the same rate. Heating rates of 10 °C/min, 15 °C/min, 20 °C/min and 25 °C/min were used to obtain information on the kinetics of the reactions. High purity dry nitrogen atmosphere was maintained during the DSC runs to prevent oxidation of the samples. The reaction peaks obtained during the heating cycle were analyzed. The characteristic temperatures (onset, peak and end) corresponding to the precipitation reactions were determined from the DSC curves.

Differential scanning calorimeter gives the differential heat flow (in mW) due to the corresponding reactions with respect to temperature (T) and hence with respect to time (t) for constant heating rates. The values of mole fractions of precipitate (Y) and the rates of precipitation (dY/dt) can be determined with respect to temperature from these calorimetric data and they are used to model the kinetics of the precipitation process.

The mole fraction $Y(T)$ transformed at any temperature T, can be determined by evaluating the partial area under the reaction curve by:

$$Y(T) = \frac{A(T)}{A(T_e)} \tag{3.1}$$

where, $A(T)$ is the area under the corresponding peak between onset temperature (T_o) and a given temperature T and $A(T_e)$ is the total area under the peak from T_o to peak end temperature (T_e). The shift in the peak temperatures with change in heating rate indicates that the reaction is kinetically controlled and the rate of reaction is generally expressed as [JENA1989]:

$$\frac{\partial Y}{\partial t} = f\left(Y\right) k_0 \, e^{-\frac{\Delta E}{RT}} \tag{2.7}$$

where, $f(Y)$ is a function of mole fraction transformed Y, k_0 is the frequency factor, ΔE is the activation energy for the reaction and R is the universal gas constant.

Expressing the rate of transformation with respect to time, Eq. (2.7) can be rewritten in terms of temperature, since ϕ is the constant heating rate $\left(\phi = \frac{\partial T}{\partial t}\right)$.

$$\frac{\partial Y}{\partial T}\varphi = f\left(Y\right) k_0 \, e^{-\frac{\Delta E}{RT}} \tag{3.2}$$

Taking logarithm on both sides, Eq. (3.2) can be expressed as:

$$\ln\left[\left(\frac{\partial Y}{\partial T}\right)\phi\right] = \ln\left[f\left(Y\right)k_0\right] - \frac{\Delta E}{R}\left(\frac{1}{T}\right) \tag{3.3}$$

The activation energy (ΔE) for the reaction is determined from the mean slope of plots of $\ln[(dY/dT)\phi]$ *vs.* $(1000/T)$ for given Y values, where the function $f(Y)$ is not required to be known. In the present study, the same plots are made for a wide range of Y values from 0.1 to 0.9, so as to obtain a good estimation of the ΔE values for the reaction peaks of the alloys. The activation energy values for the precipitation peaks were evaluated for all the investigated alloys.

The next step in modeling the kinetic equation is to evaluate the function $f(Y)$. As mentioned in the previous chapter, there is no single solution for $f(Y)$ and it depends on the material composition and the corresponding precipitate morphology.

Donoso [DONO1985] while studying the dissolution kinetics of GP zones for Al–Zn–Mg alloys by a three dimensional diffusion equation used two different expressions for $f(Y)$, one for planar particles and other for spherical particles. The kinetic equations were thus based on physical models that consider decrease in precipitate half thickness for planar particles or radius for spherical particles [DONO1983]. The corresponding expressions (*Cf.* Eq. 2.8 and 2.9) are

$f(Y) = [1-(1-Y)^{1/3}]^2$ (for planar precipitates) (2.8)

$f(Y) = 1-(1-Y)^{2/3}$ (for spherical precipitates) (2.9)

In an earlier study on Al–Cu–Mg alloy based on Johnson-Mehl-Avarami equation [AVRA1939], $f(Y)$ was taken as:

$$f(Y) = (1-Y) \tag{3.4}$$

In the present study, $f(Y)$ is not used from the data available in existing literature. Instead a new methodology was adopted for the determination of $f(Y)$ which would ensure a good fit of the kinetic equations to the experimental data corresponding to the precipitation peaks.

As stated earlier, the mean slope of plots of $\ln[(dY/dT)\phi]$ *vs.* $(1000/T)$ for given Y values, generated from Eq. (3.3) can determine the mean ΔE value of the reaction peak. On the contrary, the ΔE value is actually observed to vary with mole fraction transformed Y, and the slopes of the above plots give estimates of ΔE values for respective values of Y. These ΔE values are then plotted as a function of Y and a fourth order polynomial function $E(Y)$ is used to obtain a good fit.

Similarly, the values for the first term in the RHS of Eq. (3.3), *i.e.* $\ln[f(Y)k_0]$, are obtained from the intercepts of the straight lines from the plots of $\ln[(dY/dT)\phi]$ *vs.* $(1000/T)$ for different Y values. The intercept values are then plotted as a function of Y and fitted with a fourth order polynomial function. From this polynomial function, an exponential function is derived for $f(Y)$ and the frequency factor k_0 is also estimated.

To establish the confidence for $f(Y)$, the values of $f(Y)$, $E(Y)$ and k_0 obtained are substituted in Eq. (3.2) and the kinetic equation is modeled for each of the exothermic peaks. From this rate equation, $\frac{\partial Y}{\partial t}$ values are generated corresponding to different Y values, which gives the predicted variation of $\frac{\partial Y}{\partial t}$ with temperature T. The predicted curve fits well with the experimental plot of $\frac{\partial Y}{\partial t}$ *vs.* T for a wide range of Y values from 0.05 to 0.95. This establishes the reasonable accuracy of the kinetic equation modeled for the corresponding exothermic peak. The values of frequency factor k_0, and the functions $f(Y)$ and $E(Y)$ are determined by the above procedure to model the kinetic equations for all the exothermic peaks observed in the DSC thermograms of the investigated alloys.

3.7 X-Ray diffraction (XRD) analysis

An exothermic peak was observed in the temperature range of 200 ˚C to 300 ˚C in the DSC curves of the solutionized and quenched alloy samples. In order to understand the structural changes accompanying these exothermic reactions, XRD studies were carried out on the samples after appropriate heat treatment.

XRD studies were performed on three different alloy compositions with Sn wt.% of 0, 0.06 and 0.1. Samples of 10 mm × 10 mm size were sectioned and solutionized at 500 ˚C followed by water quenching. After the solutionizing heat treatment, one set of the samples was further annealed at 350 ˚C for 10 h. This annealing temperature was selected since the exothermic reaction was observed to be complete within this temperature, as revealed from the DSC thermograms.

A commercial powder X-ray diffractometer (Seifert XRD 3003 T/T) was used for the phase identification in the alloys at room temperature. Cu K_α radiation (1.541 Å) with nickel filter was used. The X-ray tube was operated with an acceleration voltage of 40 kV and tube current of 30 mA. A polymetamethylacrylate (PMMA) plate with a square depression of dimensions 25 mm × 25 mm × 0.5 mm coated with a thin layer of high vacuum grease was used as sample holder for XRD measurements. XRD data provides the variation of intensity/counts per second (cps), recorded by the scintillation detector as a function of 2θ, where θ is the glancing angle. XRD patterns were recorded over a 2θ range of 5° to 70° with a scan rate of 0.05°/s. The possible phase(s) present in the heat treated samples was (were) identified by comparing the peak position and intensity with data in the powder diffraction files available in ICPD database.

3.8 Mechanical property determination

Details of the mechanical property evaluation performed on various samples are described below.

3.8.1 Hardness test

The hardness of the samples was determined using Vickers hardness tester. The sample surfaces were given a mirror-like finish by dry polishing, prior to testing. Hardness testing was carried out using a diamond pyramid indenter (with 136° included angle) under a constant load of 10 kg applied for 10 s.

The diagonal lengths of the square-shaped impression formed in the indention process were measured and the Vickers hardness number (VHN) was determined using the following relation [GEOR1988]:

$$VHN = \frac{1.854\,F}{D^2} \tag{3.5}$$

where, F is the applied load in kg and D is the arithmetic mean of the two diagonal lengths of the indentation in mm. The hardness values presented in this thesis are the average of 15 independent indentations under identical loading conditions.

3.8.2 Tensile test

Cylindrical tensile specimens having 6 mm gauge diameter were machined from the cast and homogenized alloy rods. Tensile testing of the rolled alloys was carried out using flat specimens. Flat tensile specimens with 25 mm gauge length, 6 mm width and 4 mm thick as per ASTM standards [ASTM1997] were machined from the rolled and homogenized alloy strips. The geometries of the flat and cylindrical tensile specimens are shown in the Figure 3.3.

Uniaxial tensile tests were performed using a 100 kN capacity servo-hydraulic controlled dynamic universal testing machine (UTM, Instron, 8801). Tests were carried out with a constant actuator speed of 0.01 mm/s. An extensometer was used to measure the displacement across 25 mm gauge length during the test. The load *vs.* displacement data during the tensile testing was obtained and recorded and the tensile properties were evaluated. The yield strength reported was arrived at by 0.1 % offset strain method.

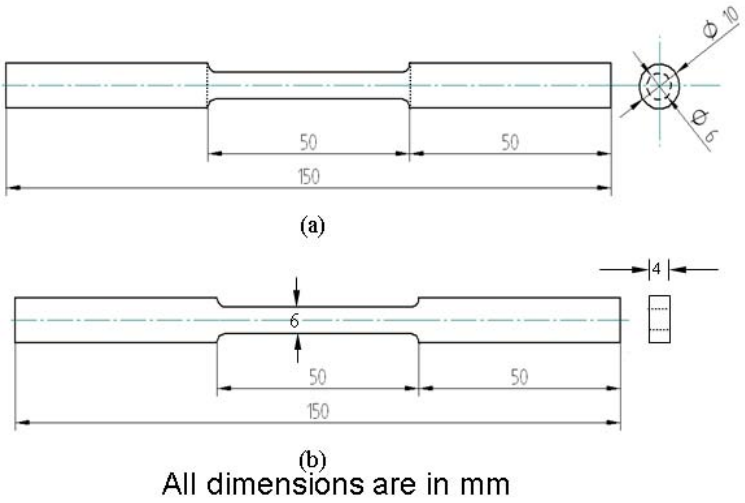

Fig.3.3. The geometry of (a) the cylindrical tensile sample (b) the flat tensile sample

3.8.3 High temperature compression test procedure

Hot compression tests were carried out using the dynamic 100 kN capacity UTM. A split-type resistance heated furnace was fabricated and attached to the UTM to maintain the test specimen at a constant test temperature. Machined and heat treated H-13 die steel compression platen was fabricated and used for the test. The platens were water jacketed to prevent transfer of heat to the UTM actuators and load cell. The compression testing set-up showing the split type furnace is shown in Figure 3.4.

The cast cylindrical samples were machined to 12 mm diameter and 200 mm length. The machined sample rods were then homogenized at 510 ^{o}C for 10 h and subsequently furnace cooled. Cylindrical compression specimen having dimensions of 10 mm diameter and 15 mm height as shown in Figure 3.5, were machined. Concentric grooves of 0.5 mm depth were machined on the top and bottom parallel surfaces of the specimens to retain the solid lubricant to minimize the friction at the sample-platen interface during the test. MoS_2 paste was used as lubricant. A hole of 1 mm diameter was drilled at the mid height region of the samples for introducing the thermocouple to measure the sample temperature during the compression test.

Hot compression tests were carried out using the same UTM as mentioned in earlier section (*cf.* section 3.8.2). The compression platens attached to the UTM was held inside

the furnace. The specimen was placed between the platens. The sample temperature was raised at a rate of 5 ^{o}C/s to the required test temperatures. After attaining the test temperature, the sample temperature was maintained with an accuracy of ±3 ^{o}C for 15 min to ensure homogeneous temperature throughout the entire sample volume prior to the compression test. Compression tests were carried out at constant true strain rates.

Fig.3.4. The high temperature compression testing set-up

The cross head velocity of the UTM actuator was varied such that a constant true strain rate was maintained during the entire duration of the test using the relation [GEOR1988]:

$$v = \dot{\varepsilon} L_o \exp(\dot{\varepsilon} t) \tag{3.6}$$

where v is the cross head velocity, $\dot{\varepsilon}$ is the strain rate, L_o is the initial specimen length, and t is the time elapsed. The actuator displacement at any instant of time was controlled by the closed loop servo-hydraulic control of the UTM. MAX^{TM} software was used for controlling the actuator movement. A computer code was used to carry out the test at constant true strain rates, ($\dot{\varepsilon}$). The deformation temperatures (T) and strain rates ($\dot{\varepsilon}$) were in the ranges of 300 ^{o}C - 500 ^{o}C and 0.001 s^{-1} - 1.0 s^{-1}, respectively. Table 3.4 shows the $\dot{\varepsilon}$ and T at which

experiments were performed. The compression tests were carried out up to a true strain (ε) of 0.6. The load *vs.* displacement plots for all the tests were recorded and true stress (σ) *vs.* true strain (ε) plots were obtained.

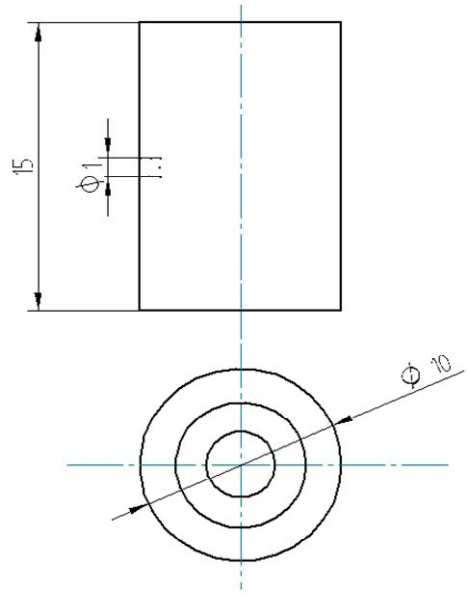

Fig.3.5. The geometry of a hot compression test sample

Table 3.4. Strain rates and temperatures of the compression tests

$\dot{\varepsilon}$ (s^{-1})	T (^{o}C)
0.001, 0.01, 0.1, and 1.0	300, 350, 400, 450 and 500

The following analyses were carried out on the compression test data obtained:

a) The peak flow stresses (σ_p) for each combination of $\dot{\varepsilon}$ and T were obtained from the flow curves of the alloys. The constitutive analysis (*cf.* section 2.5.1 and section 4.5.2) was carried out for all the alloys. The activation energy of deformation (Q), Zener-Hollomon parameter (Z) and other parameters of the constitutive model were determined and the effect of Sn addition on these parameters was investigated.

b) Multiple linear regression analysis was carried out to obtain an algebraic relationship for prediction of σ as a function of ε, $\dot{\varepsilon}$ and T (*cf.* section 2.5.4 and section 4.6).

c) The flow stress of all alloys was predicted by artificial neural network (ANN) modeling. The ANN modeling was carried out by the multiple layer perception (MLP) feed forward back propagation network. The input layer consisting of three neurons ($\dot{\varepsilon}$, ε, and T) and the flow stress, σ, in the output layer formed the data sets for training the network. The 'Neural Network' tool box available with the MATLAB (Release 7) software package was used for the present modeling. Training of the neural network was done using the ANN tool kit of MATLAB software, using 'TRAINLM' function. 'TRAINLM' is a network training function that updates weights and bias values in a back propagation algorithm according to Levenberg–Marquardt optimization. Levenberg–Marquardt algorithm is a highly efficient method for solving non-linear optimization problems [ROBI2003]. Single layer hidden neurons were used in the network architecture. The number of neurons in the hidden layer, the transfer functions at the input-to-hidden layer and hidden-to-output layer were optimized by trial and error method during the network training and testing stages. The mean square error (MSE) during the training and testing was determined for each trial. The network architecture was finally frozen based on the minimum MSE value obtained during both the training and testing stages. Out of the total 120 number of data sets, 48 and 36 data sets were used for respectively training and testing. 18 data sets from the remaining were used for evaluation using the trained network architecture. Once the proper network architecture was arrived at for an alloy, the flow stress (σ) could be successfully predicted for any combination of input parameters (ε, $\dot{\varepsilon}$, and T), within the specified domain range.

d) The flow stress values predicted by the ANN were used to generate the processing maps for all the alloys. The detailed procedure of generating the processing maps by DMM has been discussed in section 2.5.3. The relevant calculations were performed using MATLAB^{TM} software toolkit. The strain rate sensitivity factor m was evaluated using Eq. (2.25).

Flow stress (σ) value when determined at a particular $\dot{\varepsilon}$, the same can be generated at the neighboring regions of the $\dot{\varepsilon}$ values as explained in Figure 3.6. Let e be the value of $\dot{\varepsilon}$, corresponding to which the value of σ can be obtained by ANN.

The σ values are also determined at b (0.5 × e) and h (1.5 × e) values of $\dot{\varepsilon}$, considering both the directions. These three points of $\dot{\varepsilon}$, *i.e.* b, e and h are again used individually to generate two σ values at both sides of each of the three points. For example, from e, two more $\dot{\varepsilon}$ points are generated, d and f, which are respectively (e – 0.2e) and (e + 0.2e). Similarly, the points a, c, g and i are taken as (b – 0.2b), (b + 0.2b), (h – 0.2h) and (h + 0.2h), respectively. Therefore, nine different points of $\dot{\varepsilon}$ are presently obtained in total from the previous three points, as shown in Figure 3.6. σ values are determined at all these points, and the slopes of ln(σ) *vs.* ln($\dot{\varepsilon}$) give the incremental values of m parameter. The temperature (T) term is then included, and the same iteration is followed at the increment of 5 ºC within the temperature range studied. The power dissipation efficiency and the instability parameters are calculated by Eq. (2.33) and Eq. (2.35), respectively. The modeling gives the contour values of m, power dissipation efficiency and the instability parameters at different deforming conditions, *i.e.* at different values of $\dot{\varepsilon}$ and T.

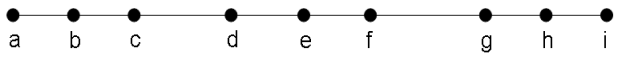

Fig.3.6. Points generated from a single $\dot{\varepsilon}$ value for calculation of σ values and m parameter

e) Microstructural observation of the samples was carried out after the compression tests in order to identify the irreversible changes induced in the microstructure as a result of deforming them to a true stain value of 0.6.

The results obtained using these experimental and computational procedure are presented in the following chapter and discussed in detail.

Chapter 4

Results and Discussion

The results and discussions of the experimental work carried out mentioned in the previous chapter are presented in this chapter.

4.1 Composition and alloy designation

Al-Cu-Mg and Al-Cu-Mg-Sn alloys were prepared from aluminum ingots of commercial purity by casting route. The cast alloys were further processed as explained in chapter 3. Since the subsequent processing of the alloys was performed in the solid state, it is expected that all the processed alloys should have the same overall composition as in the cast condition. The overall composition of the cast alloys determined by AAS technique (*cf.* section 3.2) is listed in Table 4.1. The base alloy (Alloy-*A*) which was chosen to have a composition close to the 2219Al alloy (In 2219Al, the wt.% of Cu, Mg, Si and Fe are expected to be in the range of 5.80-6.80, 0-0.02, 0-0.2, and 0-0.3, respectively). Alloy-*B* to Alloy-*F* correspond to the base alloy microalloyed with 0.02 to 0.1 wt.% Sn. The alloys will be referred by this designation henceforth in this thesis.

Table 4.1. Composition of the cast alloys estimated using AAS

Alloy designation	Composition in wt.%					
	Cu	Mg	Si	Fe	Sn	Al
Alloy-*A*	5.99	0.49	0.17	0.48	-	Balance
Alloy-*B*	5.85	0.51	0.18	0.46	0.02	Balance
Alloy-*C*	5.63	0.49	0.21	0.43	0.04	Balance
Alloy-*D*	6.07	0.44	0.19	0.47	0.06	Balance
Alloy-*E*	5.93	0.47	0.23	0.44	0.08	Balance
Alloy-*F*	6.01	0.51	0.20	0.45	0.10	Balance

4.2 Microstructure of the alloys

The microstructure and grain size of the as-cast and processed alloys were investigated using OM and SEM. The procedures followed for the microstructural observations have been discussed in chapter 3. The composition of the different phases present in the alloys was determined by EDS analysis.

4.2.1 Microstructure of as-cast alloys

Figure 4.1 and Figure 4.2 show the low magnification and high magnification optical micrographs of the cast Al–Cu–Mg alloys, respectively. Figure 4.3 shows the high magnification SEM micrographs of cast Al–Cu–Mg alloys containing 0, 0.06 and 0.1 wt.% Sn under back scattered electron imaging mode. Low magnification observation revealed dendrite structures in the cast condition. On the other hand, observation under high magnification (by SEM) revealed two different phases in the grain boundary regions of the alloy matrix: a white phase (Phase-*A*) segregated along the grain boundaries and a grey phase (Phase-*B*) having script morphology. A closer look at the micrographs shows that the volume of Phase-*A* is almost constant in all the alloys, whereas the volume of Phase-*B* increased with an increase in Sn content from 0.02 to 0.06 wt.%. Increase in Sn content beyond 0.06 wt.% did not reveal any further increase in the volume of Phase-*B*. Table 4.2 shows the compositions of the two phases observed in the matrix of the investigated alloys in the as-cast condition and Figure 4.4 shows the EDS spectrum of the different phases for the as-cast base alloy. The matrix composition was identified as Al with about 0.04 wt.% Cu. Phase-*A* and Phase-*B* were identified as $CuAl_2$ (θ-phase) and an Al-Cu-Si-Fe-Mn phase, respectively. Addition of trace amounts of Sn in the base alloy resulted in a drastic change in the components and compositions of Phase-*B*. Mn, which was not detected in the Phase-*B* of the base alloy was found in the microalloyed samples. Considerable reduction in Cu and Fe content was also observed in Phase-*B* of the microalloyed samples. 2219 Al alloy has a large freezing temperature range (543 °C – 643 °C). Similar freezing temperature range is also expected for all the six alloys processed in the present study due

to the close proximity of the base alloy (Alloy-*A*) composition with that of 2219 Al alloy. Due to the large freezing temperature range, dendrite structure is generally expected in the as-cast alloys.

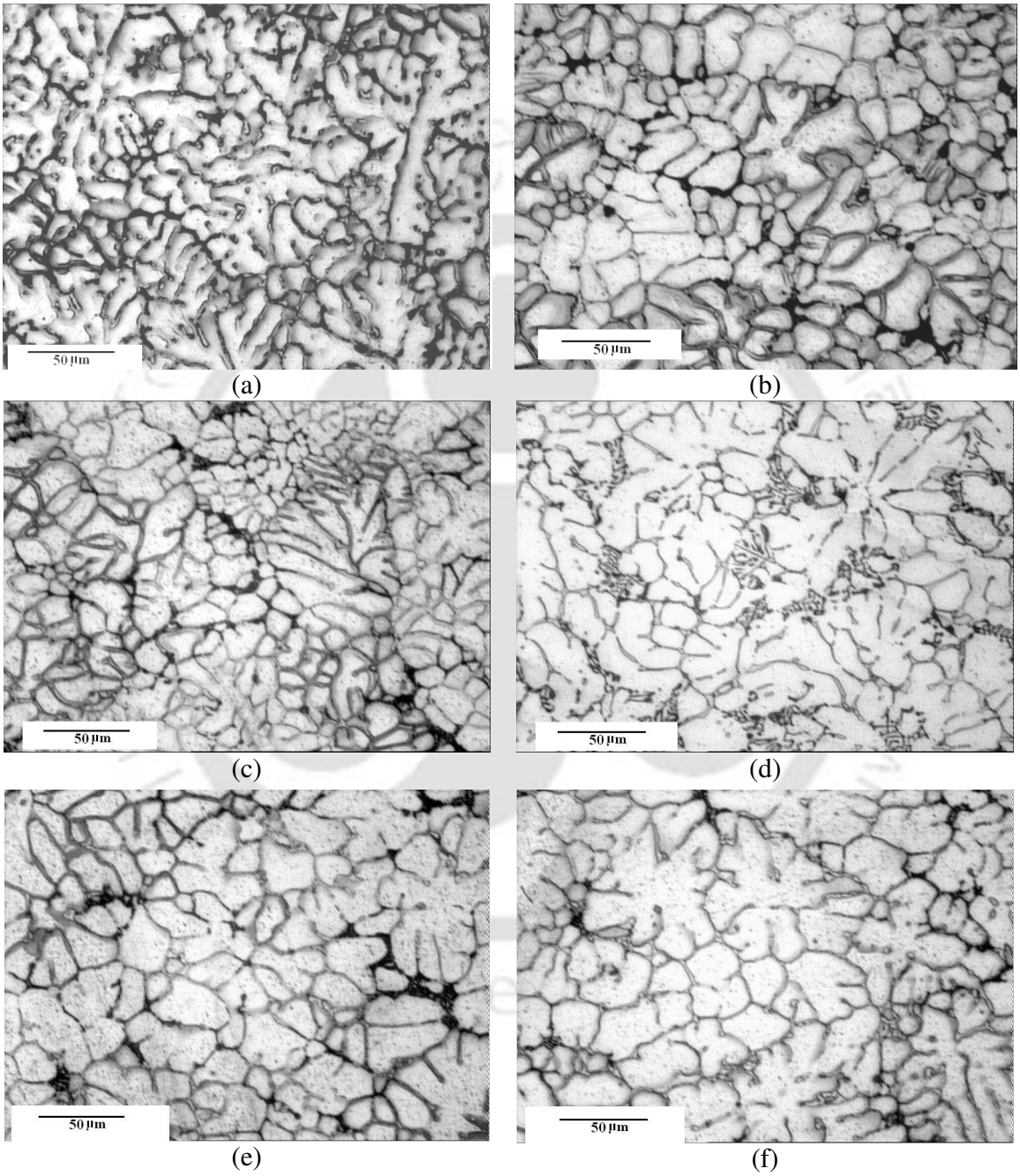

Fig.4.1. Low magnification optical micrographs of cast (a) Alloy-*A* (b) Alloy-*B* (c) Alloy-*C* (d) Alloy-*D* (e) Alloy-*E* and (f) Alloy-*F*

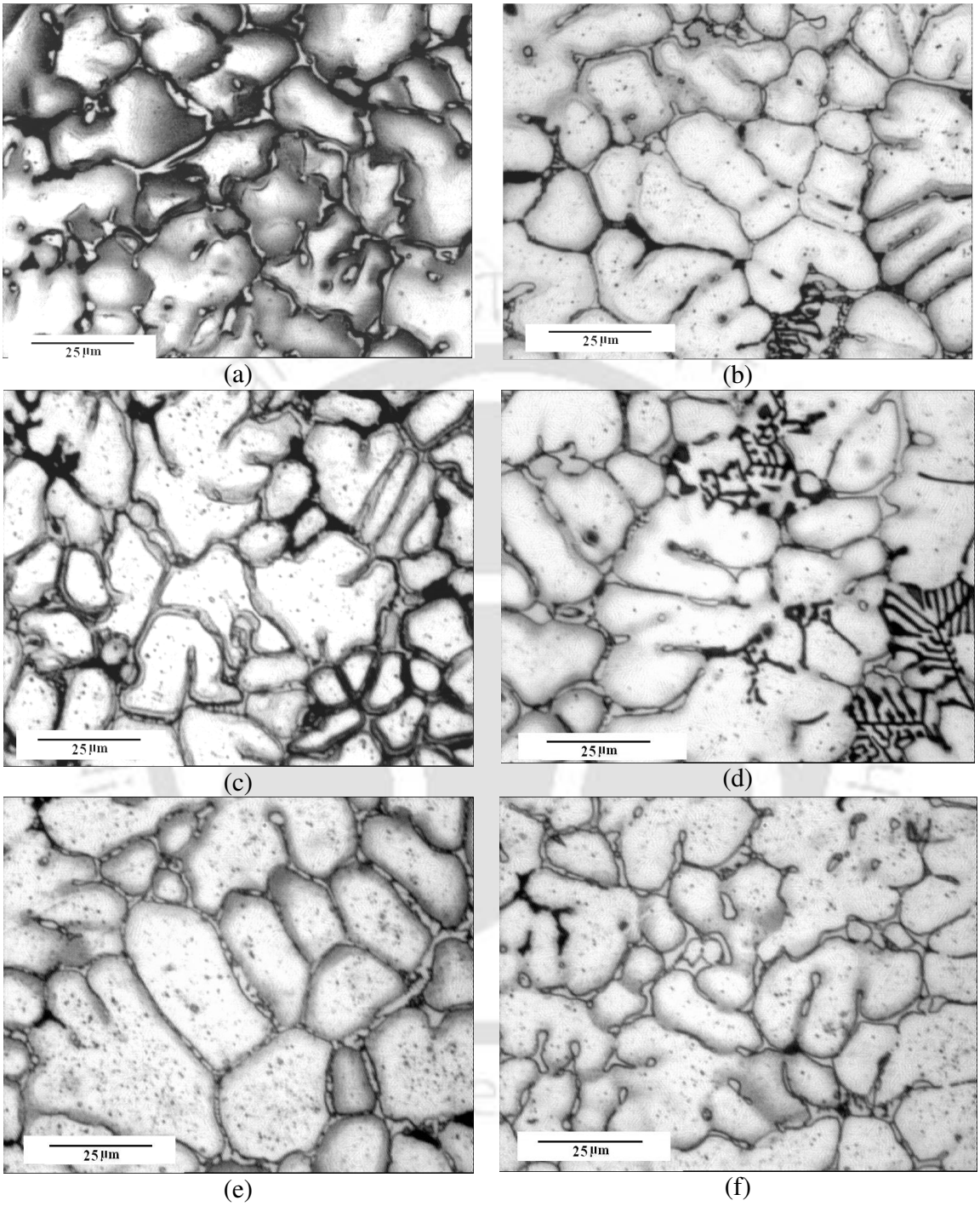

Fig.4.2. High magnification optical micrographs of cast (a) Alloy-*A* (b) Alloy-*B* (c) Alloy-*C* (d) Alloy-*D* (e) Alloy-*E* and (f) Alloy-*F*

The microstructure observed can be explained by referring to the Al-Cu binary equilibrium phase diagram shown in Figure 2.3. During cooling, as the temperature of the molten metal crosses the liquidus temperature (~643 °C), the primary solid phase (κ-phase) starts nucleating from the melt with simultaneous rejection of solute (Cu) atoms in to the liquid. As the temperature is further lowered, more amount of κ-phase is formed and the liquid gets further enriched with Cu. At the solidus temperature, the remaining liquid will have the eutectic composition. This liquid will solidify by a eutectic transformation resulting in a eutectic mixture of κ and θ-phases. Hence, the microstructure of the present alloys is expected to consist of pro-eutectic Al-phase (κ-phase) as the primary phase along with a eutectic mixture of κ and θ phases at the grain boundary regions. Fe-rich phases have been reported in the microstructure of 2219 Al alloys [MOND1976]. The Fe-rich phase (Phase-*B*) present in the as-cast alloys (with script morphology) can thus be attributed to non-equilibrium solidification.

The variation of average grain size of the alloy with Sn content in the as-cast as well as solutionized conditions is plotted in Figure 4.5. The figure shows a marginal increase in the average grain diameter from 16 μm to 19 μm as the Sn content is increased from 0 to 0.1 wt.%. This shows that microalloying the base alloy with Sn has no significant influence on the grain refinement during casting. Trace addition of Ag in Al–Cu–Mg–Mn–Zr alloys has also been reported to have no effect on grain refinement [XIAO2009]. These results can be reasoned out by the fact that trace amounts of these elements do not induce sufficient heterogeneous nucleation sites required for significant grain refinement.

Table 4.2. Compositions of different phases in the as-cast alloys

Alloy designation	Matrix	Phase-*A*	Phase-*B*
Alloy-*A*	Al–0.04 % Cu	$CuAl_2$	$Al_{75.3}Cu_{7.6}Si_{1.4}Fe_{15.7}$
Alloy-*B*	Al–0.04 % Cu	$CuAl_2$	$Al_{83.3}Cu_{2.2}Si_{0.8}Fe_{8.1}Mn_{5.6}$
Alloy-*C*	Al–0.04 % Cu	$CuAl_2$	$Al_{84.6}Cu_{1.9}Si_{0.5}Fe_{7.8}Mn_{5.2}$
Alloy-*D*	Al–0.04 % Cu	$CuAl_2$	$Al_{84.2}Cu_{1.8}Si_{0.4}Fe_{8.7}Mn_{5.1}$
Alloy-*E*	Al–0.04 % Cu	$CuAl_2$	$Al_{83.8}Cu_{1.7}Si_{0.7}Fe_{8.5}Mn_{5.3}$
Alloy-*F*	Al–0.04 % Cu	$CuAl_2$	$Al_{84.1}Cu_{1.5}Si_{0.3}Fe_{8.9}Mn_{5.7}$

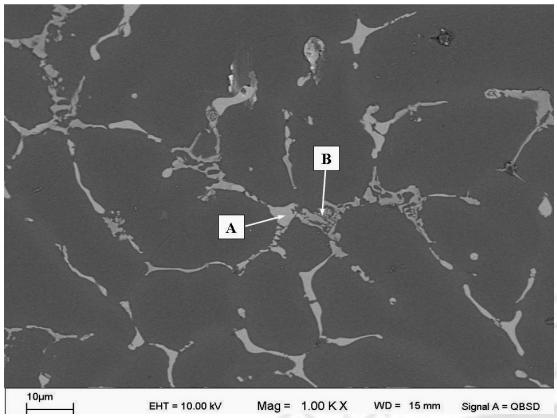

(a)

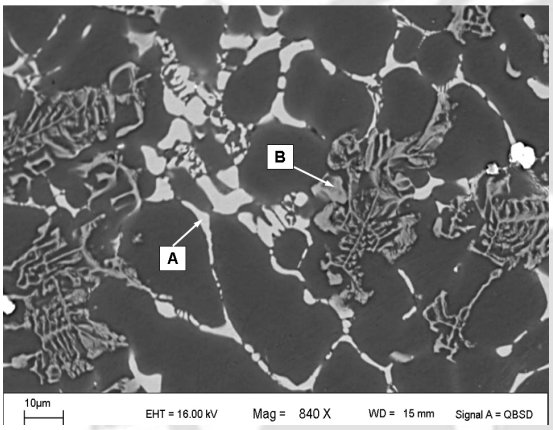

(b)

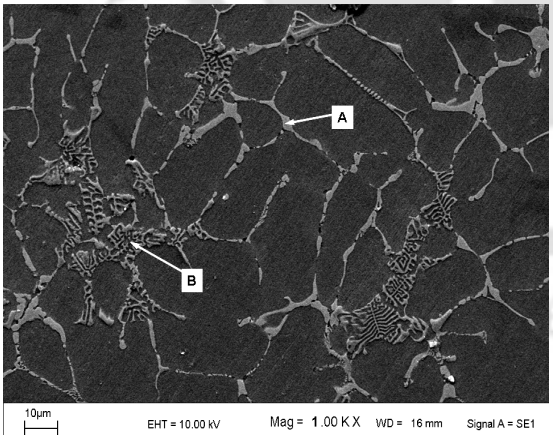

(c)

Fig.4.3. SEM micrographs of cast (a) Alloy-*A* (b) Alloy-*D* and (c) Alloy-*F* showing the grain boundary phases.

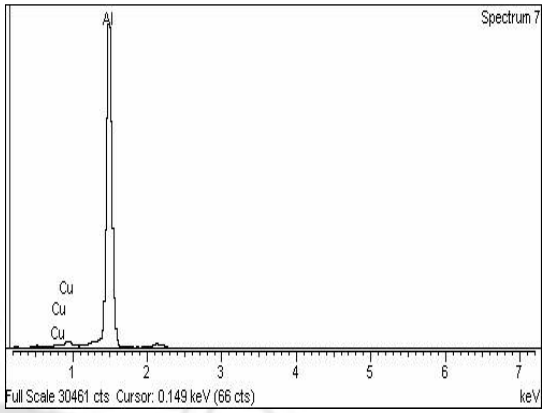

(a)

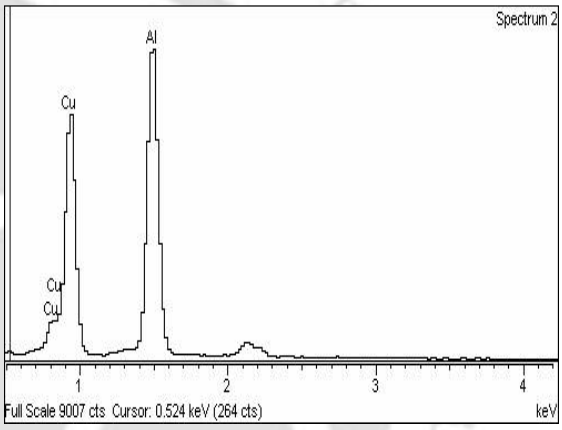

(b)

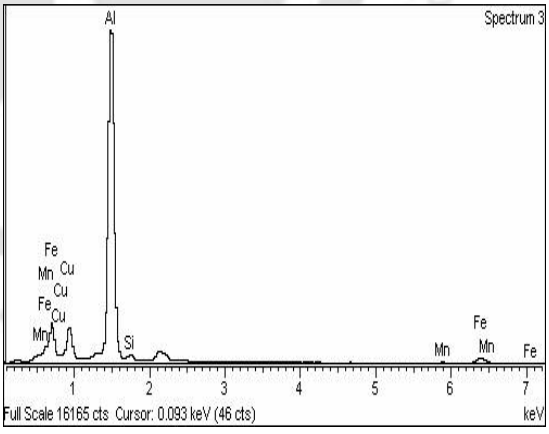

(c)

Fig.4.4. EDS spectrum of the (a) matrix (b) phase-*A* and (c) phase-*B* in as-cast Alloy-*A*

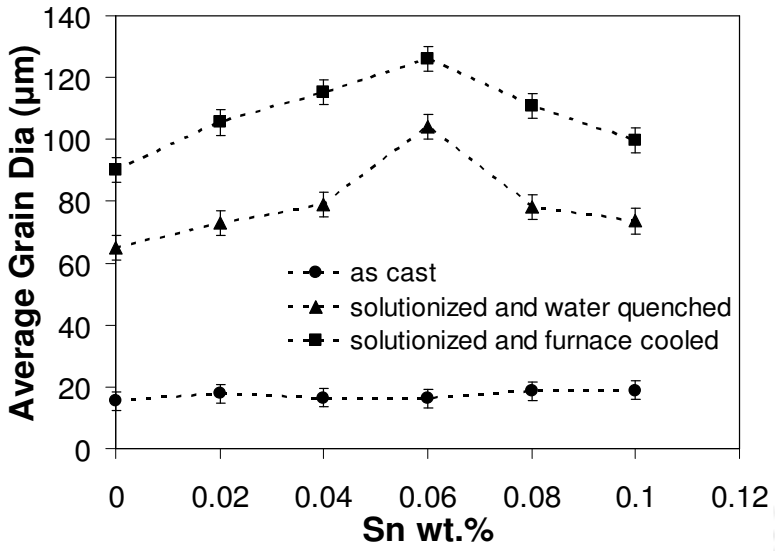

Fig.4.5. Variation of average grain size with Sn content of Al–Cu–Mg alloys processed under different conditions

4.2.2 Cast and homogenized alloys

As-cast Al–Cu–Mg alloys containing varying Sn wt.% were subjected to homogenizing heat treatment, as per procedures laid out in section 3.3 (*cf.* Table 3.2; heat treatment-*1*). The results of the studies on these alloys are presented to highlight the major features of the current investigations. The micrographs reveal the elimination of dendritic structures present in the as-cast condition, by the heat treatment. These observations are in line with the earlier reports on 2xxx series of Al alloys [XIAO2009]. Figure 4.6 (a), (b) and (c) show the SEM micrographs of the heat-treated Al–Cu–Mg alloys containing 0, 0.06 and 0.1 wt.% Sn, respectively. SEM micrographs of the homogenized samples revealed two different types of phases present at the grain boundary regions: a white platelet like phase (Phase-*C*) and a grey discontinuous platelet like phase (Phase-*D*). With increase in Sn content in the alloy, the volume of Phase-*D* increased and at the same time the morphology of this phase changed from a discontinuous platelet form to script form. On further increase in Sn wt.%, it was observed that the Phase-*D* did not show script like features. Maximum amount of Phase-*D* was observed for alloy having 0.06 wt.% Sn (Alloy-*D*). EDS analysis of the two phases present in the matrix of the investigated alloys in homogenized condition are given in Table 4.3. Phase-*C* was identified to be θ-phase ($CuAl_2$) and its morphology

remained unchanged after the heat treatment. However, the composition of Phase-*D* varied with Sn addition. The matrix composition in all cases was found to be $Al_{99.3}Cu_{0.5}Mn_{0.2}$. A comparison of the content of Phase-*B* in the as-cast base alloy and Phase-*D* in the homogenized base alloy (*cf*. Table 4.2 and 4.3) shows that the heat treatment resulted in the diffusion of Mn into this phase from the alloy matrix. On the other hand, the amount of Mn present in Phase-*D* decreased upon Sn addition in the homogenized alloys. The Phase-*B* and Phase-*D* observed in the as-cast and homogenized alloys are similar to the previously reported plate like Fe–Mn–Cu–Si–Al phase observed in some aluminum alloys [MOND1976, VESN2003].

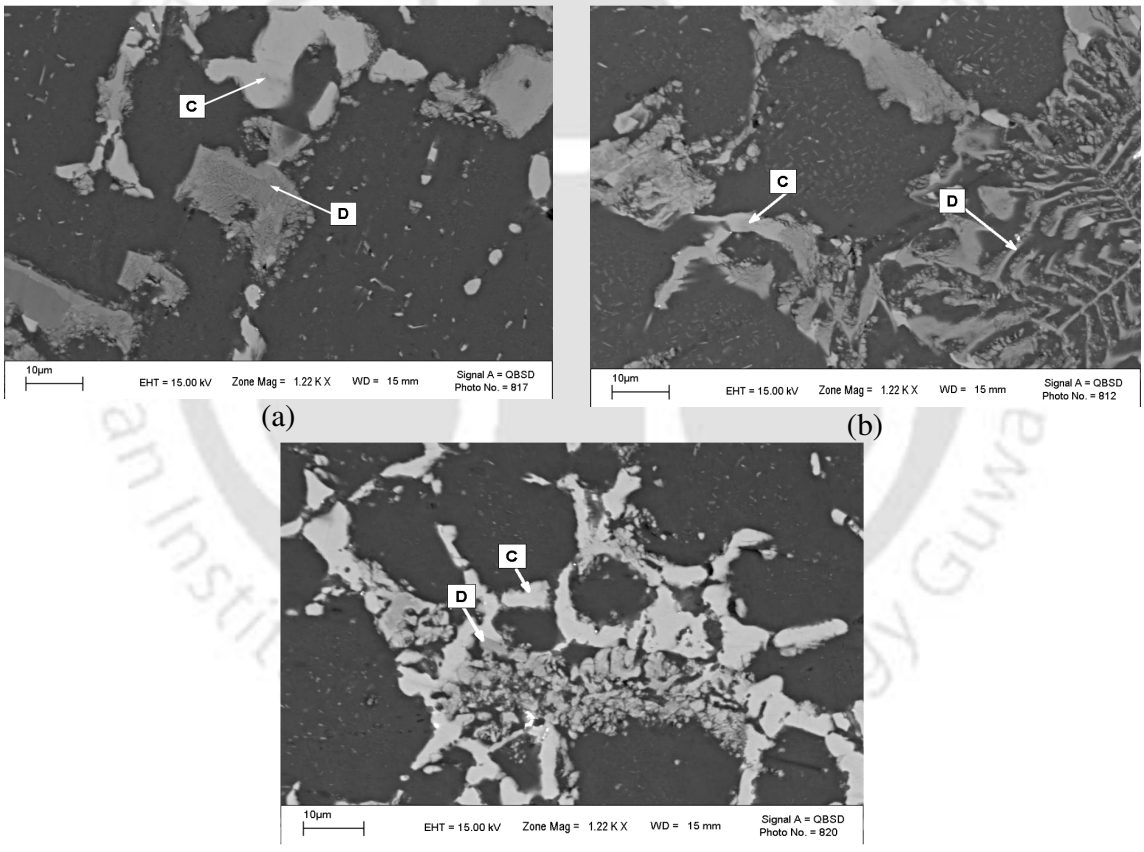

Fig.4.6. SEM micrographs of homogenized (a) Alloy-*A* (b) Alloy-*D* and (c) Alloy-*F* showing the grain boundary phases

Table 4.3. Compositions of different phases in the homogenized alloys

Alloy designation	Matrix	Phase-*C*	Phase-*D*
Alloy-*A*	$Al_{99.3}Cu_{0.5}Mn_{0.2}$	$CuAl_2$	$Al_{75.9}Cu_{1.3}Si_{5.9}Fe_{8.3}Mn_{8.6}$
Alloy-*B*	$Al_{99.3}Cu_{0.5}Mn_{0.2}$	$CuAl_2$	$Al_{78.5}Cu_{3.6}Si_{5.6}Fe_{7.9}Mn_{4.4}$
Alloy-*C*	$Al_{99.3}Cu_{0.5}Mn_{0.2}$	$CuAl_2$	$Al_{79.5}Cu_{4.1}Si_{5.4}Fe_{7.3}Mn_{3.7}$
Alloy-*D*	$Al_{99.3}Cu_{0.5}Mn_{0.2}$	$CuAl_2$	$Al_{78.9}Cu_{4.5}Si_{6.2}Fe_{7.0}Mn_{3.4}$
Alloy-*E*	$Al_{99.3}Cu_{0.5}Mn_{0.2}$	$CuAl_2$	$Al_{77.9}Cu_{5.3}Si_{6.4}Fe_{7.5}Mn_{2.9}$
Alloy-*F*	$Al_{99.3}Cu_{0.5}Mn_{0.2}$	$CuAl_2$	$Al_{70.9}Cu_{9.8}Si_{6.2}Fe_{11.0}Mn_{2.1}$

4.2.3 Cast and solutionized alloys

The as-cast alloys had undesirable microstructures as seen from the optical micrographs shown in Figure 4.1 and figure 4.2. In order to improve the microstructure, these alloys were given a solutionizing heat treatment. The heat treated alloys could either be slowly cooled or quenched to room temperature. In order to obtain a qualitative understanding of the changes in the microstructure upon the two modes of cooling, Alloy-*A* and Alloy-*D* were solutionized at 525 ºC and subsequently cooled naturally inside the furnace (*cf.* Table 3.2; heat treatment-*3*) or quenched in water (*cf.* Table 3.2; heat treatment-*2*).

Figure 4.7 and Figure 4.8 show the optical micrographs of the solutionized and furnace cooled alloys. The microstructure of both the alloys reveals the presence of two second phases along the grain boundaries, one with script-like morphology and the other with platelet morphology. In the case of Alloy-*D*, *i.e.* the alloy with 0.06 wt.% Sn, the second phase with script-like morphology is more prominent, whereas in the case of Alloy-*A*, the plate-like phase is more dominant. This comparison brings out the influence of small amounts of Sn addition on the microstructure of the furnace cooled base alloy. Presence of Sn seems to favour the formation of the second phase with script-like morphology when allowed to cool inside the furnace, indicating that it is a low melting point phase. It can also be inferred that the platelet like phase is the $CuAl_2$ phase (as confirmed by SEM-EDS studies).

Figure 4.9 and Figure 4.10 show the optical micrographs of the solutionized and water quenched alloys. It is evident that only the platelet like phase ($CuAl_2$) is observed in

these alloys, indicating that the script-like second phase has dissolved in the Al matrix during the high temperature treatment. The water quenching was sufficiently rapid to prevent the diffusion of the elements from the matrix to nucleate the script-like second phase. It is also observed that the relative vol.% of this second phase shows considerable variation with Sn content as depicted in Table 4.4. The table shows that the maximum vol.% of this second phase is observed in Alloy-*D* (with 0.06 wt.% Sn). This study shows that cooling the solutionized alloys by water quenching yields a matrix which is super saturated with the alloying elements, along with the eutectic $CuAl_2$ phase.

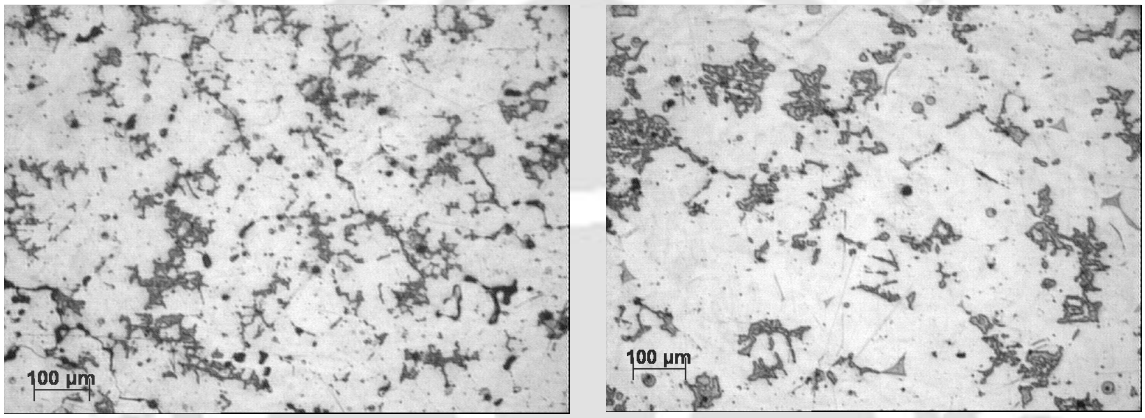

(a) (b)

Fig.4.7. Low magnification optical micrographs of solutionized and furnace cooled (a) Alloy-*A* and (b) Alloy-*D*

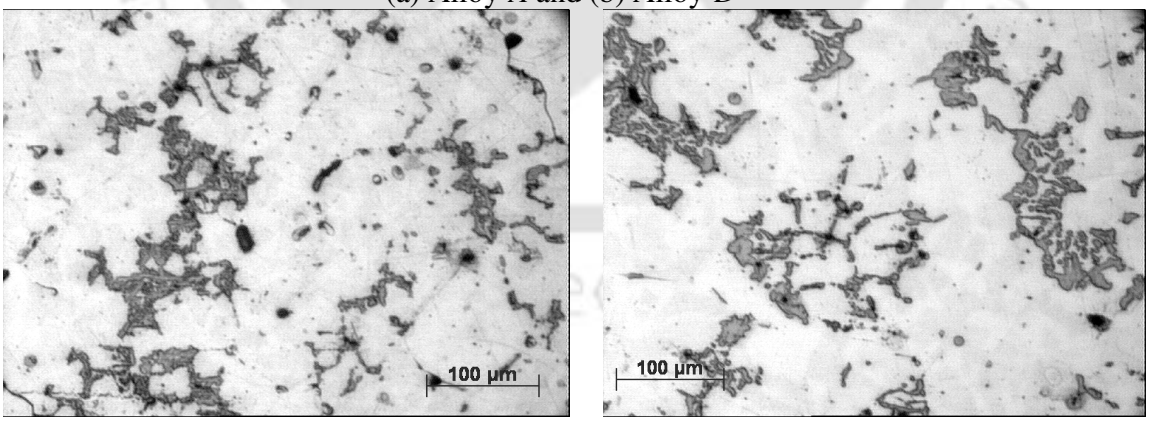

(a) (b)

Fig.4.8. High magnification optical micrographs of solutionized and furnace cooled (a) Alloy-*A* and (b) Alloy-*D*

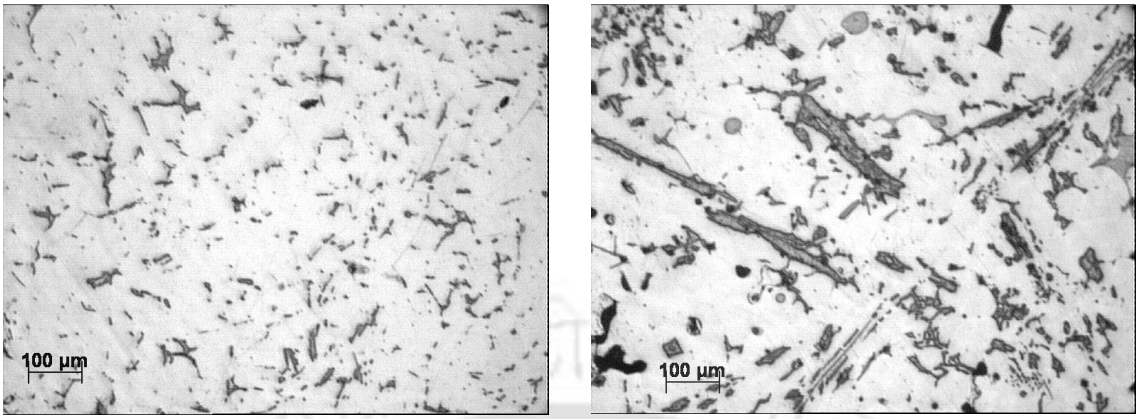

(a) (b)

Fig.4.9. Low magnification optical micrographs of solutionized and water quenched (a) Alloy-*A* and (b) Alloy-*D*

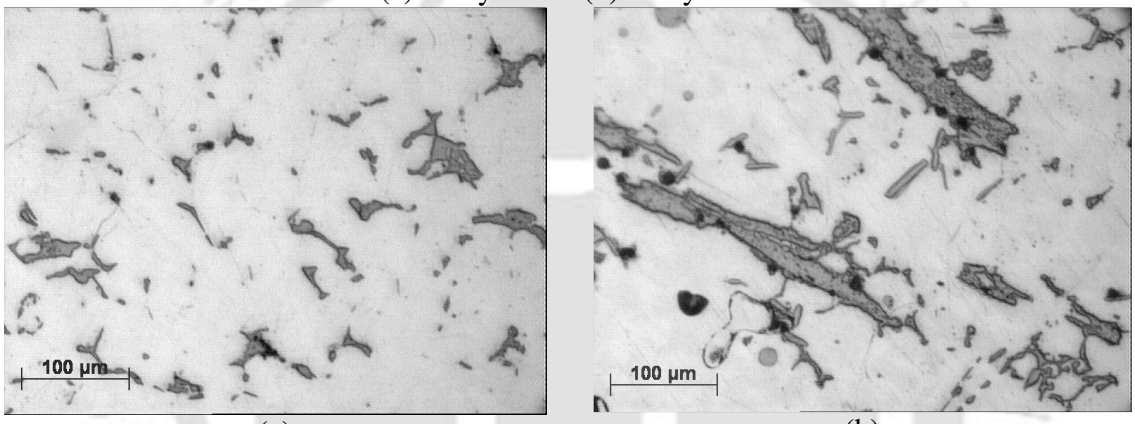

(a) (b)

Fig.4.10. High magnification optical micrographs of solutionized and water quenched (a) Alloy-*A* and (b) Alloy-*D*

The micrographs (*cf.* Figure 4.7, 4.8, 4.9, 4.10) indicate coarsening of the grains of base alloy with 0.06 wt.% Sn addition. This is further supported by Figure 4.5, which shows the variation of the average grain size with Sn content after solutionizing. For the solutionized and water quenched alloys, the average grain size of the base alloy increased from 65 µm to 104 µm when the Sn content is increased from 0 to 0.06 wt.%. Where as for solutionized and furnace cooled alloys, the average grain size increased from 90 µm to 126 µm upon addition of 0.06 wt.% Sn. For both the cooling rates, further increase in Sn content beyond 0.06 wt.%, resulted in a reduction of grain size in the case of both water quenched and furnace cooled alloys. Solutionizing resulted in higher grain size for all the

alloys as compared to the as-cast condition. However, higher cooling rate from the solutionizing temperature reduced the grain size, or resulted in grain refinement.

Table 4.4. Volume fraction of second phase in solutionized and water quenched alloys

Sample ID	Volume fraction (%)
Alloy-*A*	10.5
Alloy-*B*	14.3
Alloy-*C*	18.2
Alloy-*D*	20.2
Alloy-*E*	15.6
Alloy-*F*	11.7

4.3 Mechanical Properties

Mechanical properties of the alloys in the as-cast as well as in different heat treated conditions were determined. Details of Vickers hardness, uni-axial tensile properties and precipitation hardening behavior of the alloys are presented in the following sections.

4.3.1 Hardness

Figure 4.11 shows the variation of hardness values of the alloys processed under different conditions. As the Sn content in the alloy in the as-cast condition was increased from 0 to 0.06 wt.%, the VHN increased from 90 GPa to 105 GPa. Further increase in Sn content decreased the hardness value. Similar trend was observed for the solutionized alloys. Maximum hardness was obtained for the solutionized and water quenched alloys (*cf.* Table 3.2; heat treatment-*2*) whereas the lowest values were exhibited by alloys in the furnace cooled condition (*cf.* Table 3.2; heat treatment-*3*). For water quenched samples, the hardness was observed to be 113 GPa, 131 GPa and 114 GPa corresponding to alloys with 0, 0.06 and 0.1 wt.% Sn, respectively. Hardness of the cast alloys increased by about 25 % upon solutionizing at 525 ºC followed by water quenching whereas it decreased by about 33 % for the same alloys obtained by solutionizing followed by furnace cooling. The results indicate that solutionizing followed by water quenching results in the highest hardness in these alloys. The distinct microstructure of the solutionized and water quenched alloy with

0.06 wt.% Sn as revealed by the micrographs shown in Figures 4.9(b) and Figure 4.10(b) holds the key for the highest hardness exhibited by this alloy.

The microstructures (Figure 4.9 and 4.10) reveal the absence of the script-like second phase which could be observed in the cast alloys as well as in the solutionized and furnace cooled alloys. At the solutionizing temperature, the low melting point phases present in the cast alloys (Figure 4.1, 4.2 and 4.3), dissolve in the matrix forming a super-saturated solid solution as explained earlier. During the furnace cooling stage, these elements start diffusing out of the super saturated solid solution of the matrix and form thermodynamically stable second phases at the grain boundary regions due to the slow cooling rate (Figure 4.7 and 4.8). This results in a soft alloy matrix. During the water quenching process, the cooling rate is very fast and the alloying elements dissolved in the solid solution do not have sufficient time to diffuse out at the higher temperatures and remain in the solid solution. This results in a strained matrix. The high hardness values observed for the water quenched alloys can be attributed to the high residual stresses present in the alloy matrix. The increasing trend in hardness value up to 0.06 wt.% Sn may be due to the limited solubility of Sn (which appears to be 0.06 wt.%). Beyond this limit, it is possible for elemental Sn to segregate at the grain boundary region. Since Sn addition was in trace amounts, the presence of Sn in the κ-phase or θ-phase could not be confirmed experimentally.

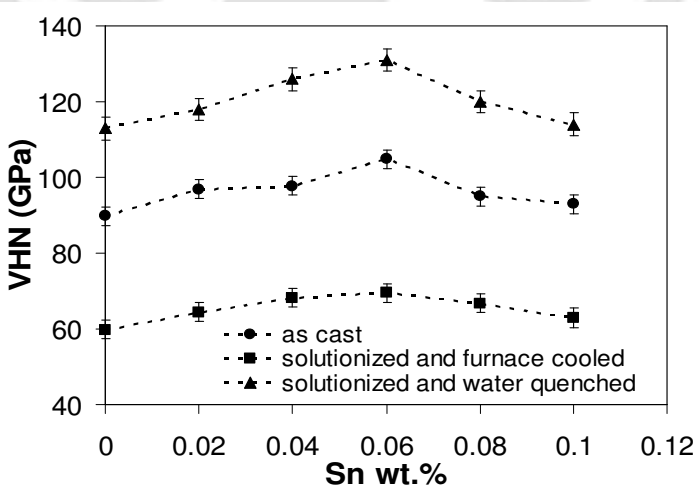

Fig.4.11. Variation of Vickers Hardness Number (VHN) with Sn content of Al–Cu–Mg alloys for various processing conditions

4.3.2 Tensile properties

4.3.2.1 Cast and homogenized alloys

Tensile test results obtained for the homogenized alloys (*cf.* Table 3.2; heat treatment-*1*) are shown in Table 4.5. Figure 4.12 plots the variation of yield strength (YS) and ultimate tensile strength (UTS) with Sn content of the alloy system. YS and UTS of the alloy increased with increase in Sn content up to 0.06 wt.%. YS and UTS gradually decreased upon further additions of Sn. The alloy with 0.06 wt.% Sn was observed to have the maximum YS of 99 MPa and maximum UTS of 187 MPa among all the investigated alloys. The YS and UTS of the base alloy increased by 21 % and 56 % respectively upon addition of 0.06 wt.% Sn. The influence of microalloying with Sn was observed to be more pronounced on the tensile strength as compared to the yield strength. Similar trend in the tensile strength has been observed in a few other Al alloys microalloyed with Sn [SERC1999, MOHA2008]. On the other hand, trace additions of Sc has been reported to have a more effect on yield strength than on the tensile strength of Al–Mg alloys [KAIS2008].

Table 4.5. Tensile properties of cast and homogenized Al–Cu–Mg alloys with different Sn contents

Sn wt.%	Young's Modulus (GPa)	Yield Strength (MPa)	Ultimate Tensile Strength (MPa)	Total Elongation (%)
0	62	81	120	1.1
0.02	68	90	162	2.2
0.04	73	95	176	1.5
0.06	64	99	187	1.0
0.08	64	98	170	1.8
0.1	63	95	161	2.8

Figure 4.13 shows the variation in percentage elongation of the alloys as a function of Sn content. The percentage elongation of the alloy decreased with increase in Sn content from 0.02 wt.% up to 0.06 wt.%. Further increase in Sn content increased the percentage elongation. The total elongation was minimum and maximum for the alloys with 0.06 wt.%

Sn and 0.1 wt.% Sn, respectively. The Young's modulus (*E*) of the alloy increased by 16 % due to the trace addition of 0.04 wt.% Sn. Further increase in Sn content decreased the *E* value.

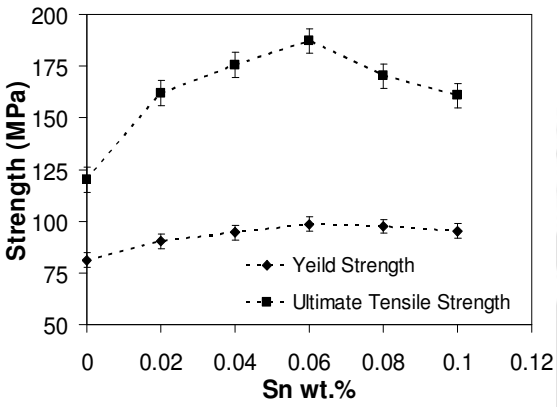

(a)

Fig.4.12. Variation of YS and UTS of homogenized Al–Cu–Mg alloys as a function of Sn wt.%

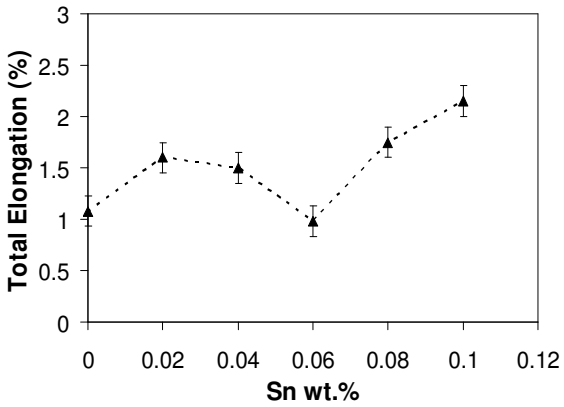

(b)

Fig.4.13. Variation of ductility of homogenized Al–Cu–Mg alloys as a function of Sn wt.%

Thus in both cast and solutionized conditions, the investigated Al–Cu–Mg alloy revealed maximum strength and hardness when microalloyed with 0.06 wt.% Sn. However, a loss of ductility could be observed in this composition. UTS of the alloy increased by 56 % whereas the ductility reduced by 9 % due to addition of 0.06 wt.% Sn. It may also be noted that the alloys with Sn exhibited higher strength in comparison to the alloy without Sn. Similar behavior has been reported for the Al–7%Si–0.35%Mg alloy, which acquired the best mechanical properties upon 0.05 wt.% Sn addition [MOHA2008]. But addition of 0.15 wt.% Sn is reported to lower the YS, UTS and hardness values, and raise the ductility and toughness of these cast alloys. Similar trend of YS and UTS observed in the presently investigated alloy have also been reported for powder metallurgy processed Al–4.4Cu–0.8Si–0.5Mg alloy with Sn concentration up to 0.1 wt.% [SERC1999]. The strength values attained a maximum with 0.05 wt.% Sn addition, but decreased with further addition of Sn. The percentage elongation of the Al–Cu–Si–Mg alloy was higher due to addition of 0.1 wt.% Sn. Following the above reported trends, 0.1 wt.% Sn addition resulted in an increase in ductility in the present Al–Cu–Mg alloy system. Such beneficial increase in

strengthening with increase in alloying element often gets limited to certain percentage of the alloying element and is apparently a general feature of Al alloys as pointed out by the literature. Strength of the Al–Mg alloy, for example, increased with increase in Sc content up to 0.4 wt.%, but decreased with further additions of Sc [KAIS2008].

The higher strength and lower ductility of the investigated Al–Cu–Mg alloy with 0.06 wt.% Sn content can be attributed to the amount, composition and morphology of Phase-*D*. The morphology of the Phase-*D* changed from platelet form to script form and the amount of this phase increased with increase in Sn content up to 0.06 wt.%. The Cu content in Phase-*D* increased with increase in Sn percentage with a concomitant decrease in Mn. It appears that the failure of the material may have initiated at regions containing a preponderance of Phase-*D*. Al–Cu–Mg–0.1 wt.% Sn alloy was observed to have the best combination of strength and ductility among all the investigated alloys.

The ductility of the cast and homogenized alloys presented above is considerably lower than the expected value. In order to understand the reason for this low ductility or low failure strain of these alloys, the fractured surfaces were examined under SEM. Figure 4.14 shows the typical SEM images of the fractured surfaces of the samples. Fractographs revealed predominantly brittle mode of fracture features with few regions exhibiting dimples. The microstructures of these samples discussed earlier also reveal micro-porosities at grain boundary regions. The micro-porosities can clearly be observed from the low magnification SEM images of the fractured surfaces shown in Figure 4.15. From the fractographs, one can presume that failure initiated from the regions of micro-porosities or from brittle second phase particle-matrix interface located at the grain boundary regions. The evidences of de-bonding between these brittle second phase particles with the matrix can clearly be observed from the high magnification fractographs (*cf.* Figure 4.14). Subsequently, growth and final failure occurred through the soft matrix regions by micro-void coalescence mechanism. The presence of dimple features close to the second phases supports this argument. One way to eliminate these defects is to plastically deform these alloys, which highlights the reason for using these alloys only in the wrought form.

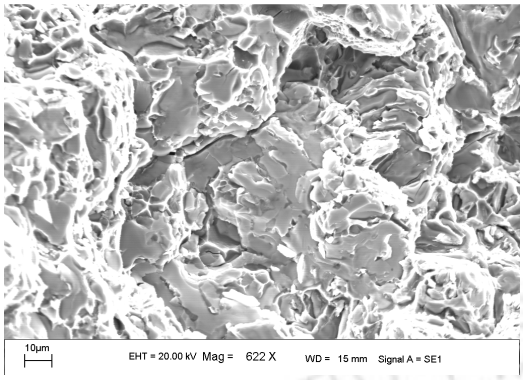

(a)

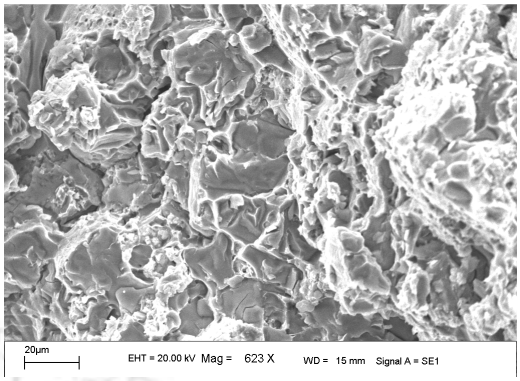

(b)

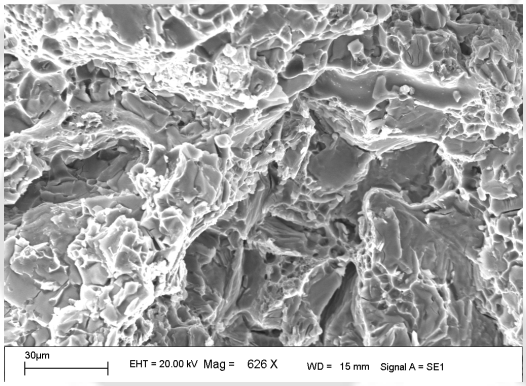

(c)

Fig.4.14. High magnification tensile fractographs of homogenized (a) Alloy-*A* (b) Alloy-*D* and (c) Alloy-*F*.

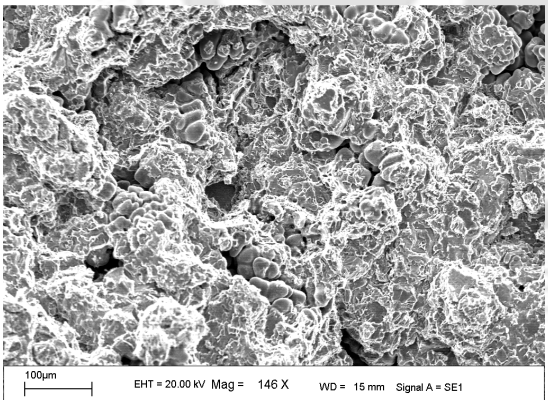

(a)

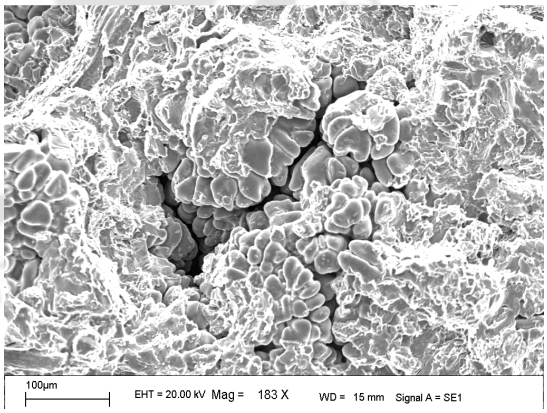

(b)

Fig.4.15. Low magnification tensile fractographs showing micro-porosities in homogenized (a) Alloy-*D* and (b) Alloy-*F*

4.3.2.2 Tensile properties of rolled alloys

Rolled and homogenized alloys

Warm rolled samples were homogenized (*cf.* Table 3.2; heat treatment-*5*) and then tensile properties were investigated. The tensile test results for the rolled and homogenized alloys are shown in Table 4.6. Figure 4.16(a) depicts the variation of YS and UTS with Sn content for the rolled Al–Cu–Mg alloys. YS and UTS of the alloy increased with increase in Sn content up to 0.06 wt.%. The strength gradually decreased with further addition of Sn. The alloy with 0.06 wt.% Sn exhibited the maximum YS of 165 MPa and UTS of 205 MPa. YS and UTS of the base alloy increased by 29 % and 13 %, respectively, upon addition of 0.06 wt.% Sn. Microalloying with Sn is observed to influence YS more than UTS of the alloy in the rolled condition. The Table 4.6 also lists the percentage increase in YS and UTS of these alloys w.r.t the cast and homogenized alloys (*cf.* Table 4.5), revealing the effect of rolling. This increase in strength observed in the rolled condition is attributed to the improvement in chemical homogeneity, elimination of segregation, coring and shrinkage porosities.

Table 4.6. Tensile properties of rolled and homogenized Al–Cu–Mg alloys with different Sn wt.%

Sn wt.%	Young's Modulus (GPa)	YS (MPa)	% increase in YS w.r.t the cast and homogenized alloys	UTS (MPa)	% increase in UTS w.r.t the cast and homogenized alloys	Total Elongation (%)
0	67.2	128	58	182	52	7.0
0.02	65.0	145	61	193	19	9.0
0.04	61.7	147	54	193	10	8.6
0.06	62.9	165	66	205	10	5.5
0.08	66.9	160	63	198	17	7.0
0.1	62.8	134	41	178	11	7.5

Figure 4.16(b) shows the variation in percentage elongation of the rolled alloy with Sn content. The trend is similar to the one observed in the case of the cast and homogenized alloys, *i.e.* the percentage elongation of the alloy decreased with increase in Sn content from 0.02 wt.% up to 0.06 wt.%. Further increase in Sn content increased the percentage

elongation. The total elongation was minimum and maximum for the alloys with 0.06 wt.% and 0.02 wt.% Sn, respectively. The elongation of all the alloys increased due to rolling, *viz.* from 1 % in the cast and homogenized condition to 5.5 % in the rolled and homogenized condition (in case of Alloy-*E*). This may be due to the cold wielding of micro-porosities during the rolling process.

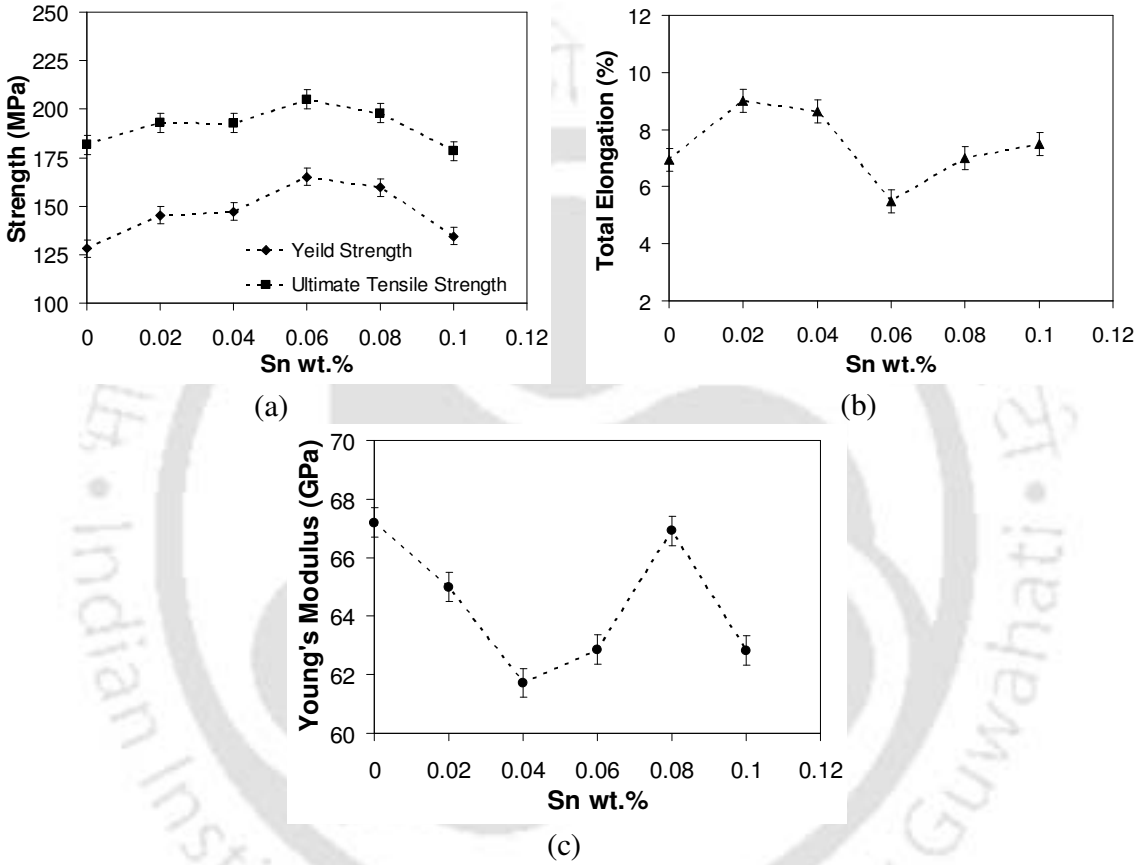

Fig.4.16. Variation of (a) strength (b) ductility and (c) Young's modulus of rolled and homogenized Al–Cu–Mg alloys with Sn content

Figure 4.16(c) shows the variations in Young's Modulus (*E*) with Sn content for the rolled and homogenized alloys. *E* of the rolled alloy decreased by 8 % due to the trace addition of 0.04 wt.% Sn. Further increase in Sn content increased the *E* value. Comparison of the *E* value with Table 4.5 indicates that *E* value was not affected by rolling. It is generally accepted that *E* value is dependent on the composition of the alloy rather than on the thermo-mechanical treatment.

Maximum strength among the rolled and homogenized Al–Cu–Mg alloys was observed while microalloying with 0.06 wt.% Sn. YS of the alloy increased by 29 % whereas the ductility reduced by 21 % upon addition of 0.06 wt.% Sn. It may also be noted that the rolled alloys microalloyed with Sn exhibited higher strength when compared to the base alloy.

Rolled and peak aged alloys

Rolled samples were peak aged (*cf.* Table 3.2; heat treatment-*6*) and their tensile properties were determined. The peak ageing time for the alloys was determined to be 24 h at 170 °C from their age-hardening behavior (to be discussed in section 4.3.3).

Tensile test results for the rolled and peak aged alloys are shown in Table 4.7. The Table 4.7 also lists the percentage increase in YS and UTS of these alloys w.r.t the rolled and homogenized alloys (*cf.* Table 4.6), revealing the effect of ageing. Figure 4.17(a) illustrates the variation of YS and UTS with Sn content in the alloys. YS and UTS of the alloys increased with increase in Sn content up to 0.06 wt.%. The strength gradually decreased with further additions of Sn. The alloy with 0.06 wt.% Sn was observed to have a maximum YS of 371 MPa and UTS of 416 MPa. YS and UTS of the alloy increased by 7 % and 16 % respectively, upon 0.06 wt.% Sn addition. The YS and UTS increased considerably by the precipitation hardening treatment. However, this was achieved at the expense of the ductility. The *E* value decreased due to precipitation hardening. It may also be noted that for design consideration, YS is the criteria (rather than UTS). Hence the increase in YS in the present alloy is of importance for applications.

Figure 4.17(b) shows the variation in percentage elongation of the rolled and peak aged alloys with Sn content. The percentage elongation of the alloy decreased with increase in Sn content from 0.02 wt.% up to 0.06 wt.%. Further increase in Sn content increased the percentage elongation. The total elongation was minimum and maximum for the alloys with 0.06 wt.% and 0.02 wt.% Sn, respectively.

Table 4.7. Tensile properties of rolled and peak-aged Al–Cu–Mg alloys with different Sn wt.%

Sn wt.%	Young's Modulus (GPa)	YS (MPa)	% increase in YS w.r.t the rolled and homogenized alloys	UTS (MPa)	% increase in UTS w.r.t the rolled and homogenized alloys	Total Elongation (%)
0	62.7	347	171	360	98	0.8
0.02	58.7	335	131	365	89	1.2
0.04	52.6	356	142	394	104	0.7
0.06	53.0	371	129	416	102	0.6
0.08	56.2	352	125	393	99	0.8
0.1	61.2	338	152	348	96	0.7

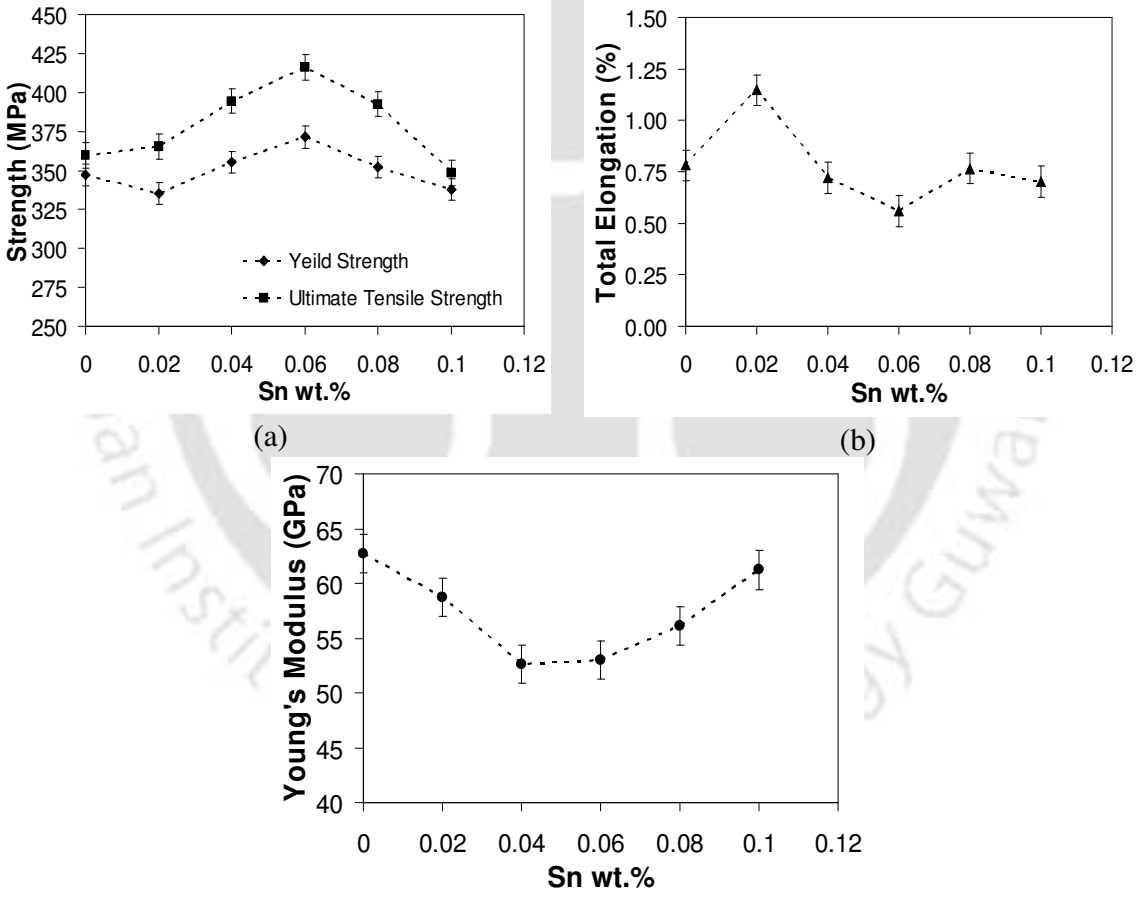

Fig.4.17. Variation of (a) strength (b) ductility and (c) Young's modulus of rolled and peak aged Al–Cu–Mg alloys with Sn content

Figure 4.17(c) shows the variations in Young's modulus of the rolled and peak aged alloys with Sn wt.%. *E* decreased by 16 % upon addition of 0.04 wt.% Sn. Further increase in Sn content increased the *E* value.

Maximum strength with a considerable loss in ductility was observed in rolled and peak aged alloys containing 0.06 wt.% Sn. UTS of the alloy increased by 16 %, whereas, the ductility reduced by 28 % upon addition of 0.06 wt.% Sn. The overall tensile properties were significantly affected by the age hardening treatment. With age hardening treatment, strength was considerably increased but there was a loss in ductility for all the alloys in rolled condition. The UTS of rolled Alloy-*A* increased by 98 %, while the total elongation decreased by 89 % when peak ageing heat treatment was given.

4.3.3 Age-hardening behavior

The cast alloys were solutionized at 525 ^{o}C for 10 h followed by water quenching. They were then age hardened at 170 ºC for 52 h (*cf.* Table 3.2; heat treatment-*4*). To understand the age hardening behavior of these alloys, samples were taken out at regular intervals of time and the Vickers hardness values were determined.

Figure 4.18 shows the variation in hardness of the alloys as a function of ageing time. Hardness increased with ageing time up to a maximum value for all the alloys. Further ageing resulted in a decrease in hardness which is the typical age hardening behavior of Al-Cu alloys. For a constant ageing time, the hardness increased with increase in Sn content up to 0.06 wt.%. Further addition of Sn resulted in a decrease in the hardness. This variation of hardness with Sn content at any ageing time resembles the data shown in Figure 4.11.

Peak hardness was achieved upon 24 h of ageing for all the alloys at 170 ºC. Peak ageing time of 24 h has been reported for 2219 Al alloy containing small amounts of Si [VESN2003] and in Al–5.9%Cu–0.22%Mg alloy [ZHON2006]. The peak hardness value of 142 VHN of Alloy-*A* is in close agreement with the reported values of 150 VHN [ZHON2006] observed in 2519Al alloy containing Ag and 154 VHN [XIAO2009] reported for Al–Cu–Mg–Mn–Zr-Ag alloy. It may be noted that the variation in hardness for Alloy-*A* is similar to that reported in the literature. VHN of 130 has been reported for 2219 alloy

when aged between 163-190 °C for 18-36 h [ASMHVOL4]. Ag has been reported to accelerate the peak ageing of these alloys at elevated temperatures and the rapid hardening observed was attributed to the formation of Mg-Ag co-clusters [REIC1998]. But Figure 4.18 reveals that addition of trace amounts of Sn has no significant influence on the peak ageing time of the Al-Cu-Mg alloys, even though the hardness of the alloy is influenced by the Sn content.

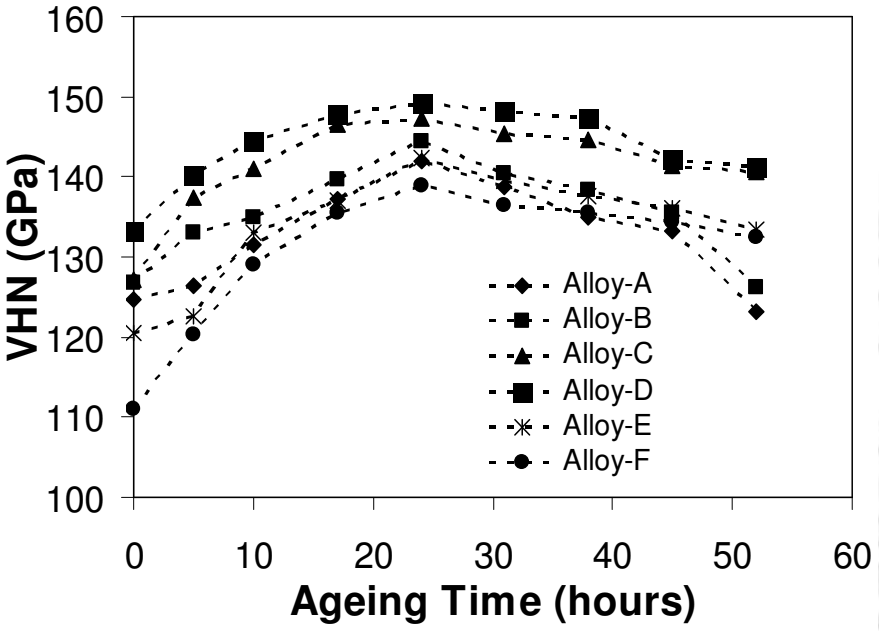

Fig.4.18. Isothermal age-hardening curves of Al–Cu–Mg alloys with varying Sn contents

Microalloying elements can alter the properties in aluminum alloys by changing the morphology, chemistry, structure, spatial distribution and size of the precipitates [SATO2003]. Trend in variation of strength and hardness with Sn concentration, identical to as observed in the present investigation, have been previously reported for Al–Cu–Mg alloys [SERC1999]. Precipitation in Al–Cu–Mg alloys with high Cu:Mg ratios generally occurs through the formation of θ', along with S or S' (Al_2CuMg) phase [SERC1999, TAYL1978]. Mg reacts with Sn to form Mg_2Sn in Al-Cu-Mg-Sn alloys [SERC1999, SULL1949]. This prevents the formation of Sn clusters and so no direct precipitation of θ' is possible. Hence Sn addition in Al-Cu-Mg alloys is not expected to contribute to the

ageing kinetics. On the other hand, trace addition of Mg to Al–Cu alloys exhibits a strong tendency to form Mg/Cu/vacancy complexes in the atomic scale, which are regarded as effective heterogeneous nucleation sites for GP zones [HIRO2000]. Hence, Mg results in rapid hardening at short ageing times and at comparatively low temperatures [SATO2003, REIC1999]. However, very few reports are available to establish the effect of trace additions of Sn, Cd or In on the nucleation and growth of θ' in Al-Cu-Mg alloys. Two possible mechanisms operating at two different temperature ranges have been proposed [SILC2002]; *viz*. (i) heterogeneous nucleation of small particles of the microalloying element occurring at 200 °C and above, and (ii) incorporation of atoms of the microalloying element into the θ' nuclei, principally at lower temperatures. In the former case, large (~ 5 nm diameter) spherical Sn particles precipitate in a short duration (~3 min at 200 °C), [RING1995, RING2000]. These particles of Sn act as effective nucleation sites. These particles being stable are not expected to enter into the θ' phase. Similar mechanism has been reported in alloys containing In [HTCH2000]. In the latter mechanism, Sn enters into the rim of θ', reduces the misfit at the edges of θ' and subsequently reduces the interfacial energy [RING1995, SILC1955]. The latter mechanism appears to be appropriate to the alloys in the present investigation in which the precipitation temperature was 170 °C. This is because, peak hardness is generally achieved with the coherent particles of GP-zones before the particles effectively lose coherency due to growth. This presumption is further supported by TEM studies [POLM1952] which revealed that the platelets formed at the peak hardness are of smaller diameter in the alloys containing Sn. Though trace additions of Cd, In or Sn slow down low temperature ageing, they improve age hardening at elevated temperatures in several Al-Cu alloys due to formation of fine and uniform dispersion of θ' phase at these temperatures [SATO2003, HARD1951, HARD1953]. Therefore, trace additions of Sn result in finer and uniformly dispersed θ' precipitates which enhance the particle-matrix coherency. As a consequence of this, the growth of the precipitates is suppressed, resulting in better thermal stability of the investigated Al–Cu–Mg alloys.

4.4 Precipitation strengthening and reaction kinetics

Differential scanning calorimeter (DSC) studies were undertaken to understand the kinetics of the precipitation reaction in the investigated alloys. The DSC studies were performed at constant heating rates as detailed in section 3.6. The kinetic parameters of the rate equation were determined from the experimental results. The rate equations relating rate of transformation, molar fraction of precipitates, temperature and activation energy were arrived for all the alloys. The activation energy (ΔE) for the reaction peaks and the effect of Sn addition on ΔE are discussed below. XRD studies were resorted to identify possible precipitation or crystallization occurring at the temperature ranges revealed from the DSC thermograms.

4.4.1 Differential Scanning Calorimeter (DSC) studies

Calorimetry has been employed since 1930's to study precipitation reaction(s) in Al-Cu alloys [HARD1954, HIRA1964, THOM1969, ZAHR1974, ZAHR1975]. These studies cite the observation of several peaks in the thermograms, which have been assigned to specific reactions. These reports show that in spite of a general agreement, the features observed vary depending upon the processing conditions of the alloys. In one such study, 2219 Al alloys were processed under different thermo-mechanical conditions such as T31, T42, T81, T87, T851 and O tempers [PAPA1981]. Interestingly, the DSC curves showed four features for the alloys processed under T31 and T42 tempers, *viz*. an endothermic (dissolution) reaction between 50 and 200 ºC, an exothermic (precipitation) reaction between 200 and 300 ºC, multiple endothermic (dissolution) reactions between 300 and 550 ºC, and a superimposed exothermic (precipitation) reaction between 400 and 475 ºC. DSC curves of samples aged at elevated temperatures, do not show many of these reactions. These studies have established that the positions and the number of features observed in the DSC curves of Al-Cu-Mg alloys depend strongly on the composition and processing conditions. The exothermic reaction occurring between 200 and 300 ºC and the melting endotherm around 500 ºC appear to be the common features observed in all conditions in

these alloys. It is now well established that the exothermic reaction occurring between 200 and 300 ºC is the signature of precipitation of θ' [PAPA1981].

In the current investigations, DSC curves of the alloys were obtained at heating rates (ϕ) of 10 ˚C/min, 15 ˚C/min, 20 ˚C/min and 25 ˚C/min. The DSC was set to record exothermic reactions as downward heat flow peaks (troughs) and *vice versa*. The area under the peak gives the value of enthalpy of the respective reaction. Figure 4.19 shows the DSC curves obtained for the investigated Al–Cu–Mg alloys during the heating cycle for a constant heating rate of 20 ˚C/min. The DSC curves of all the samples exhibited two features, *viz*. one in the temperature range of 200 ºC to 300 ºC and the other in the temperature range of 450 ºC to 550 ºC. The exothermic peak(s) in the low temperature range correspond to the precipitation reaction(s), whereas the endotherm(s) at the high temperature range correspond to the melting of the alloy phase(s). Figure 4.20 (a-f) show the truncated parts of the DSC curves of the alloys obtained at different heating rates in the temperature range of 200 ºC to 350 ºC where the precipitation reaction(s) was (were) observed. Figure 4.20 (a) and (d) show two exothermic (θ' precipitation reaction) peaks in the DSC curves obtained in the heating cycle of Alloy-*A* and Alloy-*D*, respectively. For Alloy-*A,* the first peak was observed in the temperature range from 245 ˚C to 258 ˚C and the second peak in the temperature range from 267 ˚C to 288 ˚C. The corresponding temperature ranges were 233 ˚C to 252 ˚C and 271 ˚C to 297 ˚C, respectively for Alloy-*D*. For all the other alloys, only one broad exothermic peak could be observed in the temperature range from 250 ˚C to 300 ˚C. The optical micrographs of solutionized and water quenched alloys have already been discussed in section 4.2.3. The micrographs revealed a two-phase structure. Such alloys subjected to a constant heating rate can undergo precipitation reaction at some intermediate temperature. Grain boundaries are regions of higher energy than the regions well inside the grains. Due to this reason, early nucleation of the precipitate phase occurs at the grain boundaries. The DSC curves of Alloy-*A* and Alloy-*D* revealed that the precipitation reaction occurs in two stages, which shows that precipitation at the grain boundaries precedes the precipitation inside the grains. The two well-resolved exothermic peaks in the DSC curves of Alloy-*A* indicate two-step precipitation mechanism. Upon microalloying with Sn, the nature of these precipitation

reactions varied indicating that Sn present in the grain boundaries and inside the grains influences the respective precipitation mechanisms. The on-set (T_o), peak (T_p) and end (T_e) temperatures of both the exothermic peaks were determined from the DSC curves and the corresponding data are shown in Table 4.8 and Table 4.9. Figure 4.21 (a) and (b) show the variation of peak temperatures (T_p) for Alloy-*A* and Alloy-*D* with heating rate (ϕ) for the first and second exothermic peaks, respectively. The peak temperature (T_P) of both exothermic peaks increased with increase in heating rate for all the alloys. This behavior is expected in any kinetically driven reaction, hence the reaction kinetics can be interpreted using kinetic relations discussed in section 3.6.

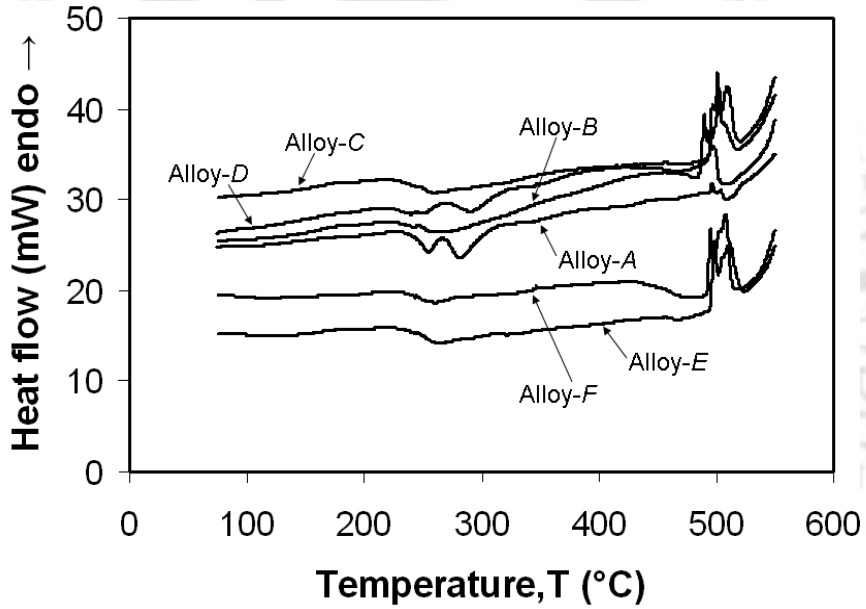

Fig.4.19. DSC curves of all the investigated alloys recorded at constant heating rate of 20 ˚C/min

kinetic parameters of the exothermic reactions were evaluated by the procedure given in section 3.6. Mole fractions of precipitate (Y) and precipitation rate (dY/dt) determined as a function of temperature were used to model the kinetics of the precipitation process. Rate of fraction transformed $(dY/dT)\phi$, where ϕ is the constant heating rate ($\phi = dT/dt$), can be determined from Y values obtained for different temperatures. Figure 4.22 shows the typical plots of Y *vs.* T and $[(dY/dT)\phi]$ *vs.* T for both the exothermic peaks observed in the DSC curves of Alloy-*A*. The variation of Y with temperature is sigmoidal in

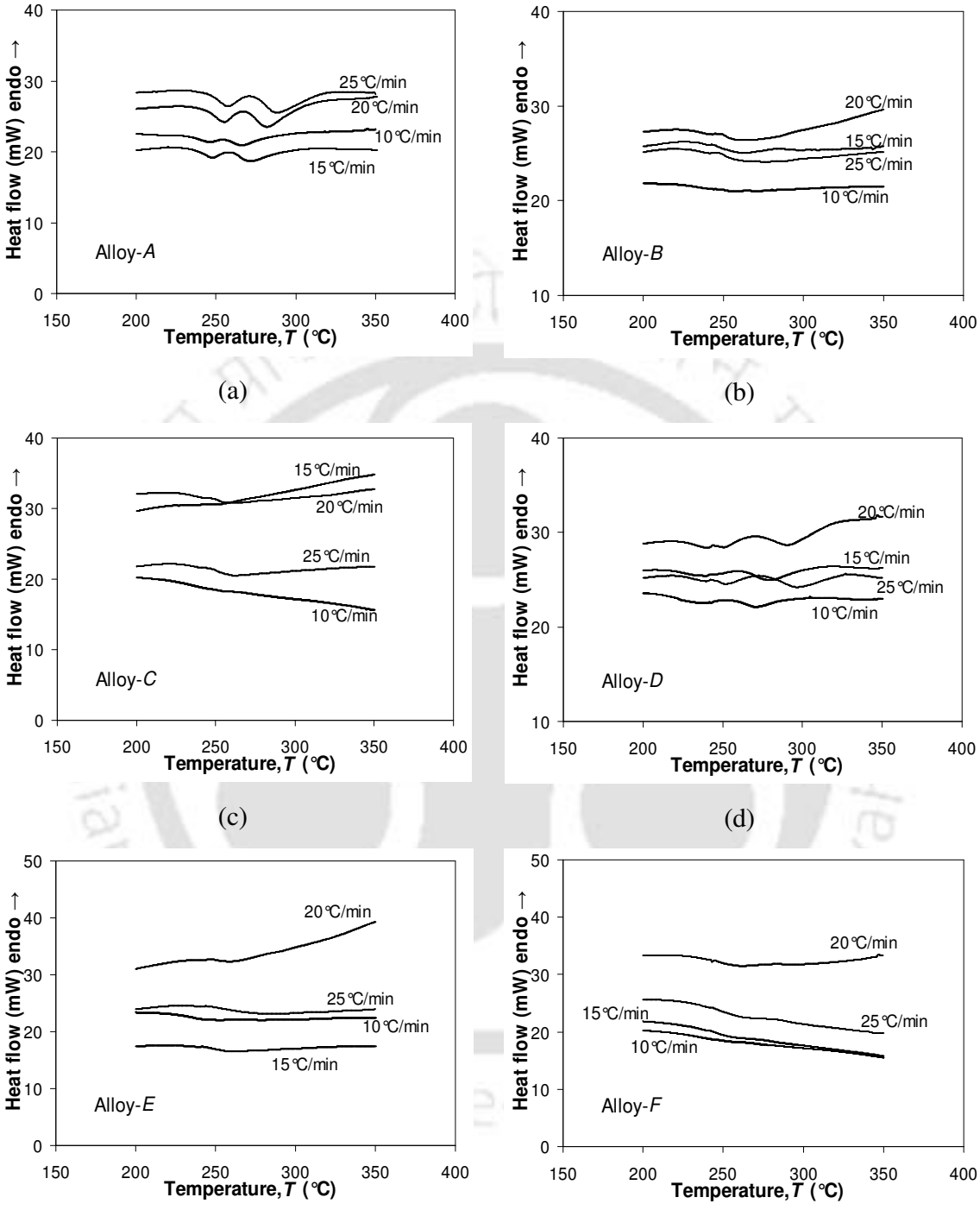

Fig.4.20. DSC curves highlighting the exothermic peak(s) observed at different heating rates for (a) Alloy-*A* (b) Alloy-*B* (c) Alloy-*C* (d) Alloy-*D* (e) Alloy-*E* and (f) Alloy-*F*

Table 4.8. Onset, end and peak temperatures corresponding to the first exothermic peak in the DSC curves of the alloys

Sample ID	Heating Rate ϕ (˚C/min)	Onset Temperature T_o (˚C)	End Temperature T_e (˚C)	Peak Temperature T_p (˚C)
Alloy-*A*	10	236	253	245
	15	237	259	247
	20	244	263	255
	25	246	268	258
Alloy-*B*	10	207	351	255
	15	211	360	261
	20	213	333	269
	25	222	366	274
Alloy-*C*	10	214	340	253
	15	225	303	252
	20	220	357	261
	25	218	350	261
Alloy-*D*	10	203	255	234
	15	219	258	239
	20	225	268	242
	25	215	274	252
Alloy-*E*	10	208	344	252
	15	246	351	261
	20	234	303	263
	25	247	391	287
Alloy-*F*	10	210	300	250
	15	225	306	254
	20	234	292	260
	25	243	289	264

Table 4.9. Onset, end and peak temperatures corresponding to the second exothermic peak in the DSC curves of the alloys

Sample	Heating Rate ϕ (˚C/min)	Onset Temperature T_o (˚C)	End Temperature T_e (˚C)	Peak Temperature T_p (˚C)
Alloy-*A*	10	256	289	268
	15	262	292	272
	20	270	304	282
	25	275	315	288
Alloy-*D*	10	259	304	271
	15	264	299	280
	20	275	317	292
	25	279	325	297

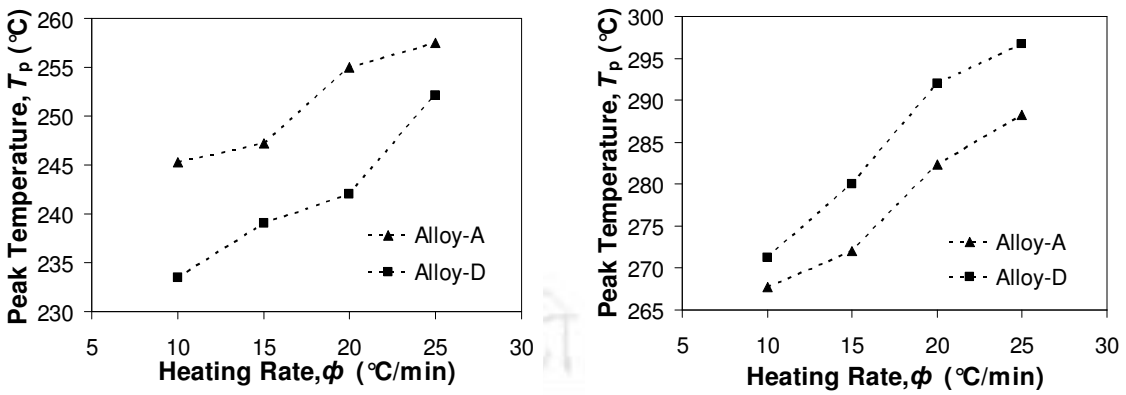

Fig.4.21. Shift in peak temperature of Alloy-*A* and Alloy-*D* with heating rate for the (a) first exothermic peak, and the (b) second exothermic peak.

shape, and these sigmoids shift to higher temperatures with increase in heating rate. The rate of transformation (dY/dt) increases up to the peak temperature (T_p) and then decreases considerably towards the peak end temperature (T_e). The resulting curve has an asymmetric 'bell' shape.

Activation energy (ΔE) for the reaction was estimated from the mean slope of plots of $\ln[(dY/dT)\phi]$ *vs.* $(1000/T)$ for given Y values. In the present study, the above plots were made for a wide range of Y values (0.1 to 0.9) so as to obtain a good estimate of ΔE. These plots are shown in Figure 4.23 to Figure 4.28 for the exothermic peaks observed in the DSC curves of the investigated alloys. The next step is to evaluate the function $f(Y)$ and the frequency factor k_0, the detailed methodology of which has already been explained in section 3.6.

The values of $f(Y)$ and k_0 obtained are substituted in the rate equation and the kinetic equation is obtained for each of the exothermic peaks. From this rate equation, $\frac{\partial Y}{\partial t}$ values are generated corresponding to different Y values, which gives the predicted variation of $\frac{\partial Y}{\partial t}$ with temperature T. The predicted curve fits well with the experimental plot of $\frac{\partial Y}{\partial t}$ *vs.* T for a wide range of Y values from 0.05 to 0.95, which establishes the reasonable accuracy of the kinetic equations modeled for the peaks. The frequency factor k_0, and the functions $f(Y)$ and $E(Y)$ were also determined for all the exothermic peaks in the DSC curves using

the above procedure. The procedures adopted for Alloy-*A* are detailed below to serve as a typical example.

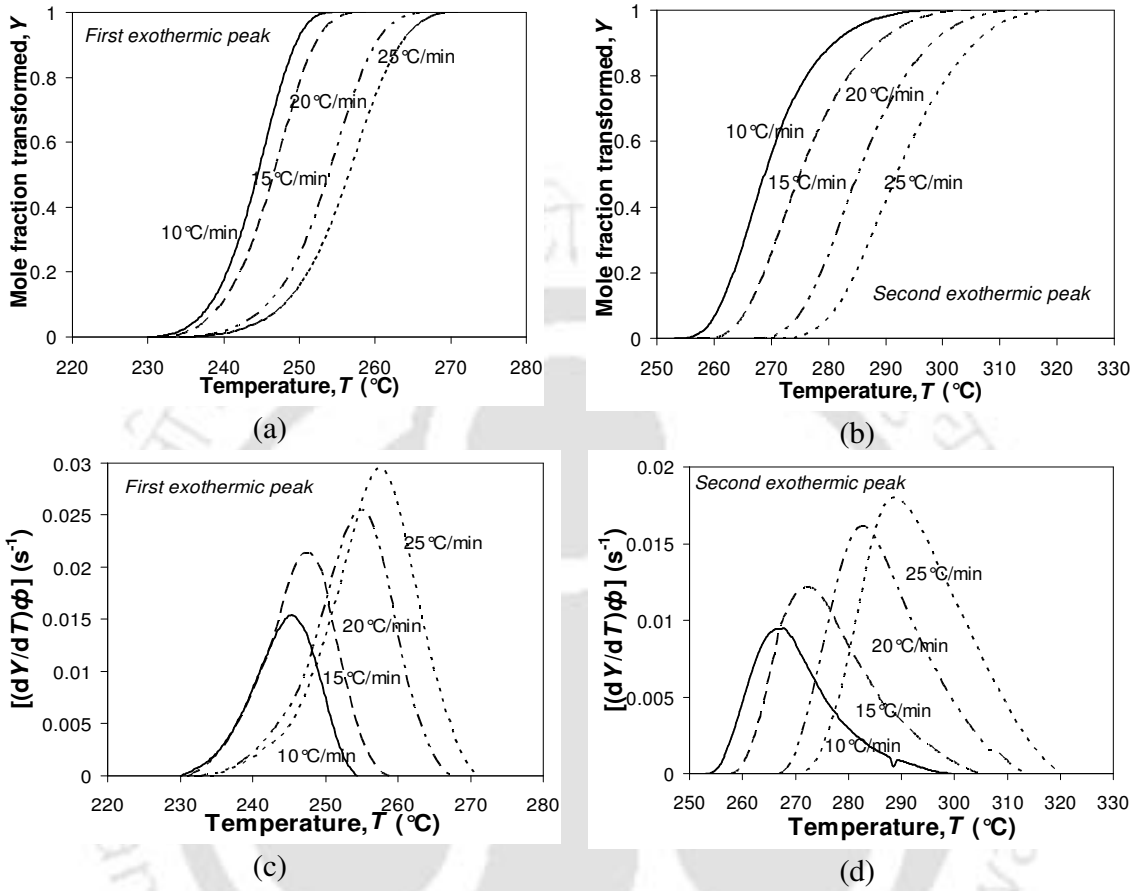

Fig.4.22. Plots of *Y vs. T* and [(d*Y*/d*T*)ϕ] *vs. T* for the two exothermic peaks of Alloy-*A*

Figure 4.23(a) shows the plots of ln[(d*Y*/d*T*)ϕ] *vs.* (1000/*T*) for the first exothermic peak of Alloy-*A*, from which the ΔE values were obtained for different mole fractions. The mean activation energy obtained for the reaction peak is 96.3 kJ/mole. The functional form of $E(Y)$ can be expressed as

$$E(Y) = (20.082Y^4 + 182.02Y^3 - 422.47Y^2 + 239.16Y + 66.092) \times 10^3 \quad (4.1)$$

Similarly, the term $\ln[f(Y)k_0]$ in Eq. (3.3) was obtained from the *y*-intercepts of ln[(d*Y*/d*T*)ϕ] *vs.* (1000/*T*) plots. This term can be parameterized using a fourth order polynomial function given by

$$\ln[f(Y)k_0] = -10.082Y^4 + 70.835Y^3 - 121.13Y^2 + 64.589Y + 9.8493 \quad (4.2)$$

Rearranging Eq. (4.2), one can obtain

$$\ln[f(Y)] + \ln(k_0) = -10.082Y^4 + 70.835Y^3 - 121.13Y^2 + 64.589Y + 9.8493 \quad (4.3)$$

Since $\ln(k_0)$ is a constant for a given peak, the above relation can be simplified to

$$\ln(k_0) = 9.8493 \quad (4.4)$$

$$\ln[f(Y)] = -10.082Y^4 + 70.835Y^3 - 121.13Y^2 + 64.589Y \quad (4.5)$$

These two equations yield

$$k_0 = 1.89\times10^4\ \mathrm{s}^{-1}$$

and $$f(Y) = e^{\left(-10.082Y^4+70.835Y^3-121.13Y^2+64.589Y\right)} \quad (4.6)$$

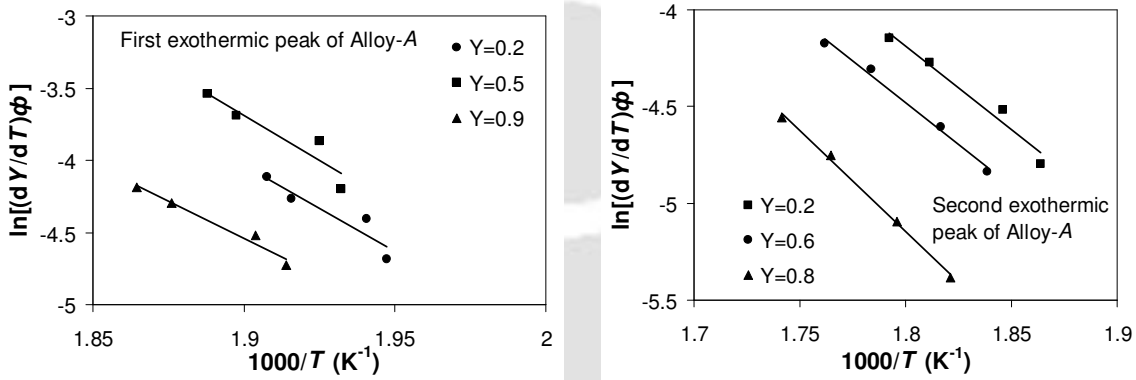

(a) (b)

Fig.4.23. Plots of $\ln[(\mathrm{d}Y/\mathrm{d}T)\phi]$ *vs.* $(1000/T)$ for given Y values corresponding to the (a) first exothermic peak, and (b) second exothermic peak of Alloy-*A*.

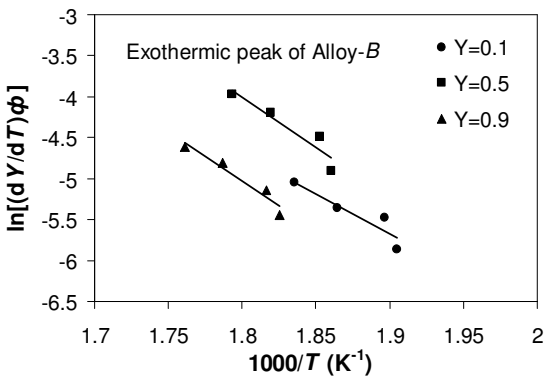

Fig.4.24. Plots of $\ln[(\mathrm{d}Y/\mathrm{d}T)\phi]$ *vs.* $(1000/T)$ for given Y values corresponding to the exothermic peak of Alloy-*B*.

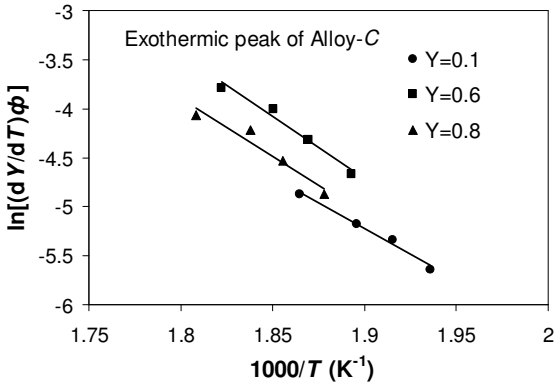

Fig.4.25. Plots of $\ln[(\mathrm{d}Y/\mathrm{d}T)\phi]$ *vs.* $(1000/T)$ for given Y values corresponding to the exothermic peak of Alloy-*C*.

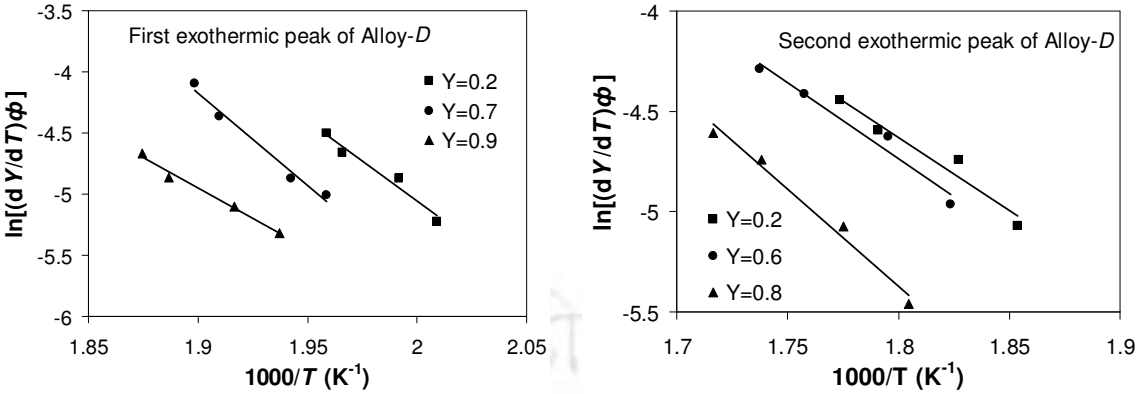

(a) (b)

Fig.4.26. Plots of ln[(d*Y*/d*T*)ϕ] *vs.* (1000/*T*) for given *Y* values corresponding to the (a) first exothermic peak, and (b) second exothermic peak of Alloy-*D*.

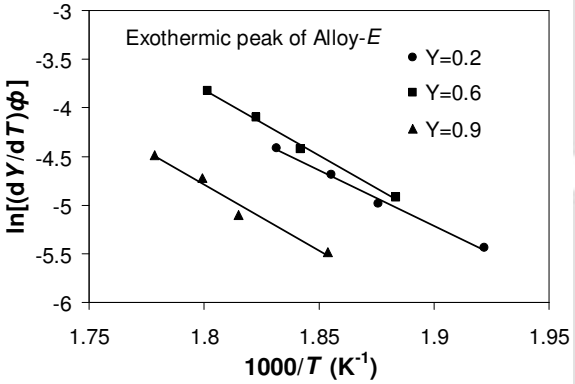

Fig.4.27. Plots of ln[(d*Y*/d*T*)ϕ] *vs.* (1000/*T*) for given *Y* values corresponding to the exothermic peak of Alloy-*E*.

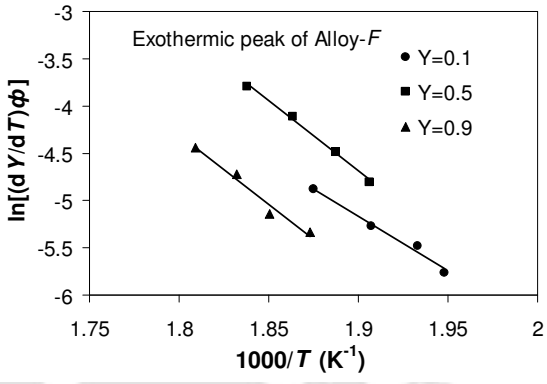

Fig.4.28. Plots of ln[(d*Y*/d*T*)ϕ] *vs.* (1000/*T*) for given *Y* values corresponding to the exothermic peak of Alloy-*F*.

Substituting for $f(Y)$, $E(Y)$ and k_0 in Eq. (2.7), the predicted values of rate of transformation $\left(\frac{\partial Y}{\partial t}\right)$ were estimated for different values of *Y*. The predicted plot of $\frac{\partial Y}{\partial t}$ *vs.* *T* agrees well with the experimental $\frac{\partial Y}{\partial t}$ *vs.* *T* curve as shown in Figure 4.29(a).

The same procedure was adopted for the second exothermic peak of Alloy-*A*. Plots of ln[(d*Y*/d*T*)ϕ] *vs.* (1000/*T*) were made for different values of *Y*, following Eq. (3.3). These plots are shown in Figure 4.23(b) for $Y = 0.2$, 0.6 and 0.8. ΔE was determined as 78.0 kJ/mole and k_0 was evaluated to be 2.83×10^3 s^{-1}. The corresponding expressions for $E(Y)$ and $f(Y)$ are

$$E(Y) = (115.52Y^4 + 97.768Y^3 - 233.57Y^2 + 100.36Y + 60.145) \times 10^3 \quad (4.7)$$

$$f(Y) = e^{\left(7.3019Y^4 + 54.637Y^3 - 76.701Y^2 + 30.179Y\right)} \quad (4.8)$$

The predicted and experimental curves of $\frac{\partial Y}{\partial t}$ *vs.* T shown in Figure 4.29(b) indicate a good agreement between the two.

The procedure described above was adopted for analyzing the exothermic peaks in the DSC curves of all the investigated alloys. Table 4.10 shows the values of k_0 and mean ΔE for the exothermic peak(s) corresponding to all the alloys. Table 4.11 shows $f(Y)$ and $E(Y)$ obtained for the different cases. Figure 4.29 to Figure 4.34 show the experimental as well as predicted plots of $\frac{\partial Y}{\partial t}$ *vs.* T for all the investigated alloys. Once again the good fit of the calculated reaction rates with the experimental values validates the procedure adopted and provides confidence to the parameters determined from the analysis.

Figure 4.35 shows the variation of ΔE with Sn wt.% for the first exothermic peak in the DSC curves of the investigated Al–Cu–Mg alloys. ΔE remains almost constant for alloys with Sn content up to 0.06 wt.% and increases with further addition of Sn. This shows that addition of Sn up to 0.06 wt.% has no significant influence on the precipitation reaction as depicted by the nearly constant ΔE value. However, further addition of Sn does not favour the precipitation process as depicted by the steep increase in ΔE. ΔE value for the second exothermic reaction was 78.0 kJ/mole for the base alloy (Alloy-*A*) where as it was found to be 69.0 kJ/mole for the alloy with 0.06 wt.% Sn (Alloy-*D*). The lower value of ΔE of the second exothermic peak obtained for the alloy with 0.06 wt.% Sn shows that Sn addition favours the second precipitation reaction. It has to be pointed out that it is difficult to distinguish if the two exotherms were overlapping especially when the reaction enthalpy is low. Hence the present reasoning is based on the DSC data obtained for the investigated alloys.

Table 4.10. Values of mean ΔE and k_0 obtained for the exothermic peaks observed in the DSC curves of the alloys.

Sample ID	Exothermic peak	Activation energy ΔE (kJ/mole)	Frequency factor k_0 (s^{-1})
Alloy-*A*	First	96.3	1.89×10^4
	Second	78.0	2.83×10^3
Alloy-*B*	First	97.5	2.56×10^4
Alloy-*C*	First	99.5	1.44×10^5
Alloy-*D*	First	99.1	2.48×10^3
	Second	69.0	8.55×10^4
Alloy-*E*	First	105.9	3.04×10^4
Alloy-*F*	First	116.7	3.97×10^5

Table 4.11. Functional forms of $f(Y)$ and $E(Y)$ obtained for the exothermic peaks observed in the DSC curves of the alloys.

Sample ID	Exothermic peak	Values of $f(Y)$ and $E(Y)$
Alloy-*A*	First	$f(Y)=e^{\left(-10.082Y^4+70.835Y^3-121.13Y^2+64.589Y\right)}$ $E(Y) = (20.082Y^4 + 182.02Y^3 - 422.47Y^2 + 239.16Y + 66.092) \times 10^3$
	Second	$f(Y)=e^{\left(7.3019Y^4+54.637Y^3-76.701Y^2+30.179Y\right)}$ $E(Y) = (115.52Y^4 + 97.768Y^3 - 233.57Y^2 + 100.36Y + 60.145) \times 10^3$
Alloy-*B*	First	$f(Y)=e^{\left(40.012Y^4-45.584Y^3-20.154Y^2+32.915Y\right)}$ $E(Y) = (249.85Y^4 - 338.69Y^3 + 15.787Y^2 + 108.39Y + 71.941) \times 10^3$
Alloy-*C*	First	$f(Y)=e^{\left(23.622Y^4-28.729Y^3-21.337Y^2+30.237Y\right)}$ $E(Y) = (166.35Y^4 - 246.48Y^3 + 3.2454Y^2 + 95.781Y + 77.654) \times 10^3$
Alloy-*D*	First	$f(Y)=e^{\left(23.142Y^4+20.456Y^3-51.196Y^2+22.247Y\right)}$ $E(Y) = (175.66Y^4 - 59.722Y^3 - 103.61Y^2 + 58.256Y + 54.155) \times 10^3$
	Second	$f(Y)=e^{\left(120.23Y^4-194.98Y^3+119.1Y^2-31.349Y\right)}$ $E(Y) = (643.05Y^4 - 1060.6Y^3 + 671.52Y^2 - 185.6Y + 78.247) \times 10^3$
Alloy-*E*	First	$f(Y)=e^{\left(-11.043Y^4+35.479Y^3-57.588Y^2+41.33Y\right)}$ $E(Y) = (12.016Y^4 + 40.745Y^3 - 160.13Y^2 + 147.09Y + 71.875) \times 10^3$
Alloy-*F*	First	$f(Y)=e^{\left(12.879Y^4-1.317Y^3-45.472Y^2+42.625Y\right)}$ $E(Y) = (120.76Y^4 - 128.32Y^3 - 100.99Y^2 + 150.53Y + 81.746) \times 10^3$

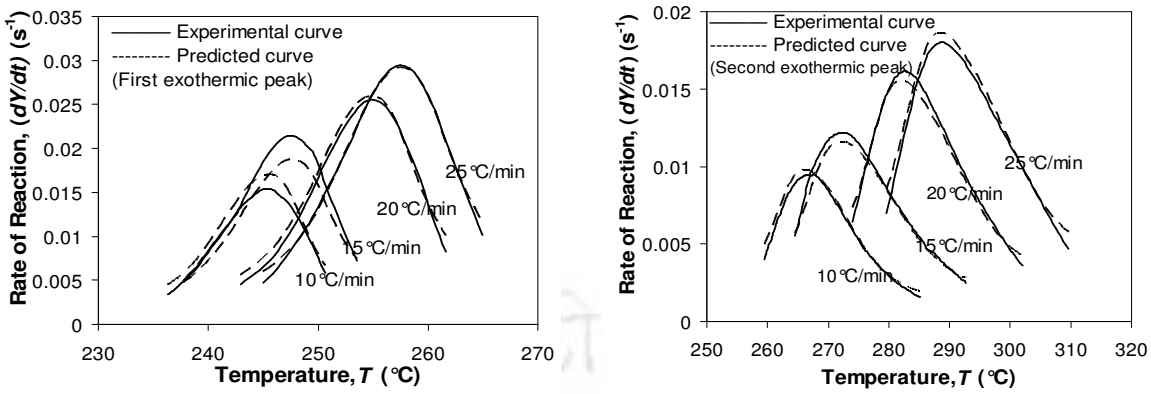

(a) (b)

Fig.4.29. Experimental and predicted variations of $\frac{\partial Y}{\partial t}$ with T at different ϕ for the (a) first exothermic, and (b) second exothermic peak of Alloy-*A*.

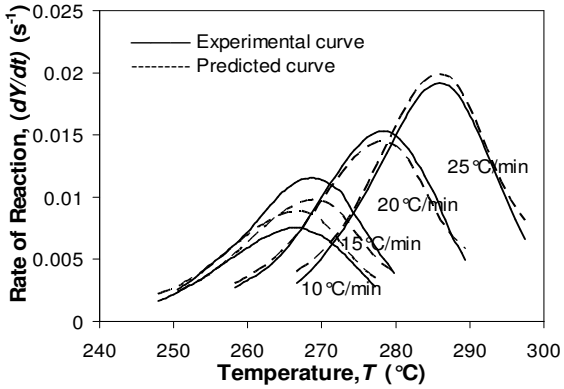

Fig.4.30. Experimental and predicted variations of $\frac{\partial Y}{\partial t}$ with T at different ϕ for the exothermic peak of Alloy-*B*.

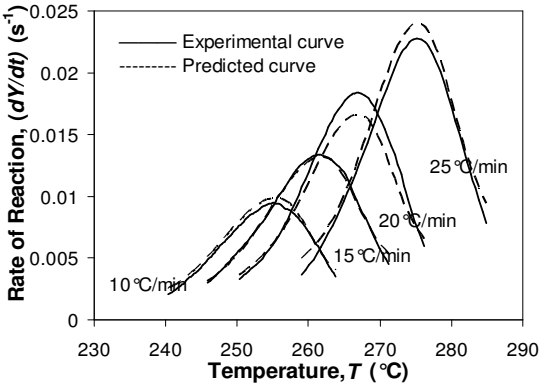

Fig.4.31. Experimental and predicted variations of $\frac{\partial Y}{\partial t}$ with T at different ϕ for the exothermic peak of Alloy-*C*

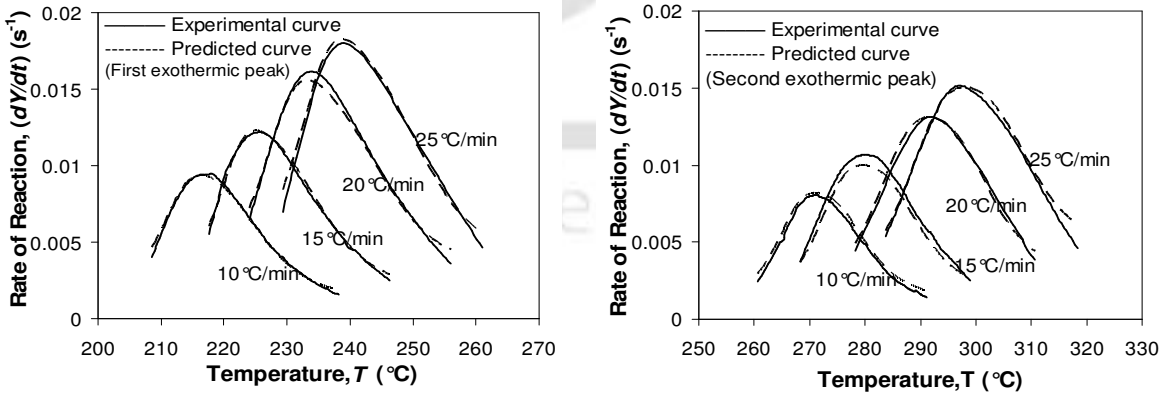

(a) (b)

Fig.4.32. Experimental and predicted variations of $\frac{\partial Y}{\partial t}$ with T at different ϕ for the (a) first exothermic, and (b) second exothermic peak of Alloy-*D*.

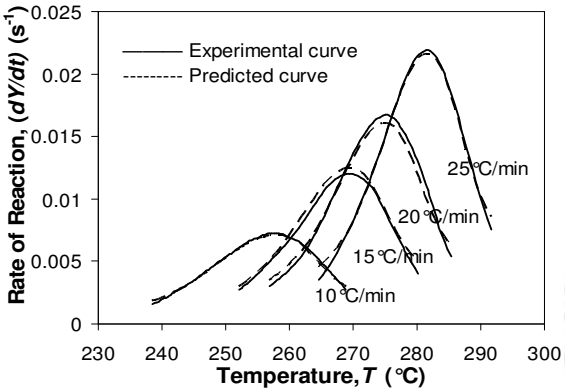

Fig.4.33. Experimental and predicted variations of $\frac{\partial Y}{\partial t}$ with T at different ϕ for the exothermic peak of Alloy-*E*

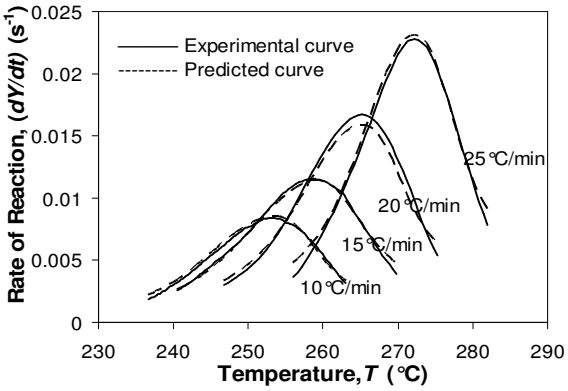

Fig.4.34. Experimental and predicted variations of $\frac{\partial Y}{\partial t}$ with T at different ϕ for the exothermic peak of Alloy-*F*

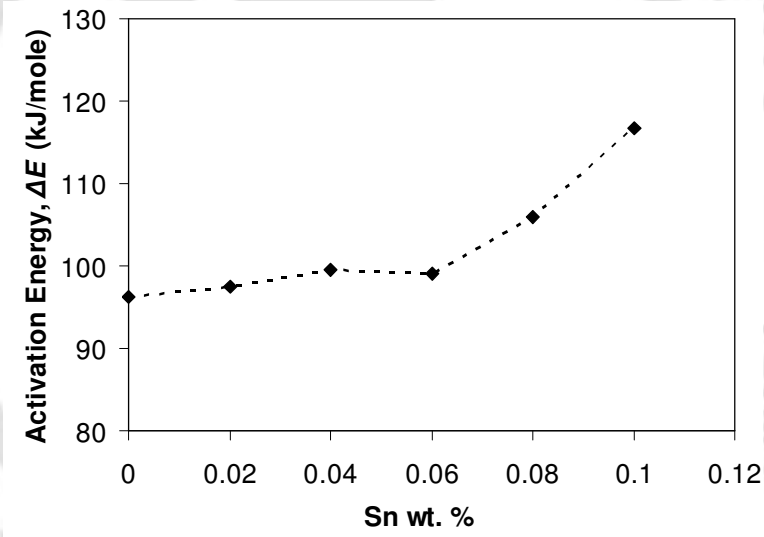

Fig.4.35. Variation of activation energy of the first exothermic peaks with Sn content of the Al–Cu–Mg alloys.

4.4.2 X-Ray diffraction (XRD) studies

The kinetics of the precipitation reaction(s) observed in the DSC curves of various alloy compositions could be understood by the above analysis. XRD studies were performed to identify the crystalline phase(s) formed during the precipitation reaction. Table 4.8 and 4.9 list the peak reaction temperatures observed using DSC technique. In order to identify the crystalline phases precipitating at these temperatures, three selected

alloys (Alloy-*A*, Alloy-*D* and Alloy-*F*) were first solutionized at 500 ˚C followed by water quenching. After the solutionizing heat treatment, the samples were aged at 350 ˚C for 10 h (just after the completion of the precipitation reactions) and water quenched. Figure 4.36 shows the XRD patterns of the three selected alloys in aged and water quenched condition.

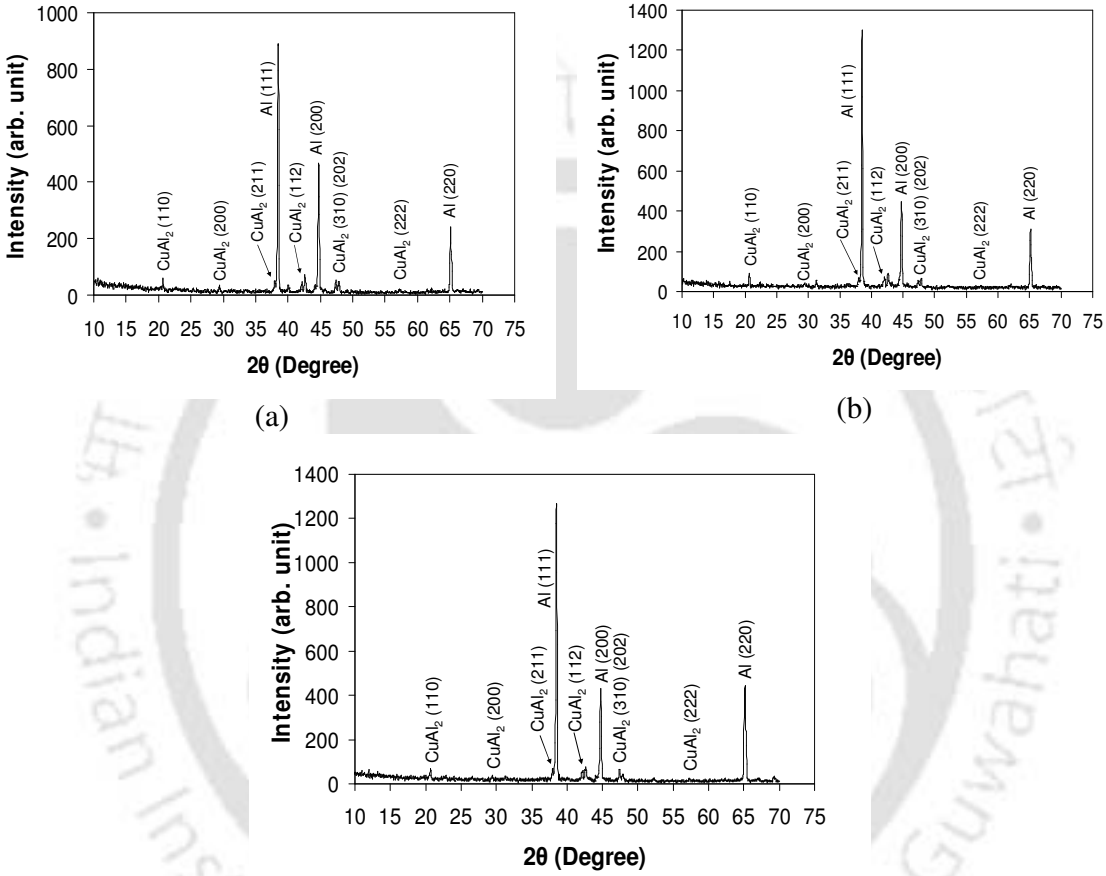

Fig.4.36. XRD patterns of aged and water quenched (a) Alloy-*A* (b) Alloy-*D*, and (c) Alloy-*F*

The ageing conditions were chosen such that the alloys attained the maximum hardness value (*cf.* section 4.3.1). Analysis of the XRD patterns reveals the presence of $CuAl_2$ along with the Al matrix as major phases in all the processed alloys. The Al matrix phase has been identified as a face centered cubic crystal with space group *Fm3m* and lattice parameter a = 4.049 Å. The $CuAl_2$ phase exhibited tetragonal crystal structure with *I4/mcm* space group and lattice parameters, a = 6.053 Å and c = 4.870 Å. These structural data are

in agreement with those reported in the literature [ELAG2007, MIAO2000, XIAO2009]. Trace amounts of Sn in Alloy-*D* and Alloy-*F* did not show any noticeable influence on the unit cell volume of the two constituent phases. Furnace cooled samples (XRD patterns not shown here) also revealed the presence of these two major constituent phases after the heat treatment.

4.5 High temperature deformation behavior

The results of the hot compression tests carried out on the Al-Cu-Mg alloys are presented and discussed in the following sub-sections. The development and the analysis of the constitutive equations relating flow stress (σ), deformation temperature (T), strain rate ($\dot{\varepsilon}$), Zener-Hollomon parameter (Z) and activation energy for deformation (Q) are discussed.

4.5.1 Flow stress behavior

The flow curves (σ *vs.* ε plots) obtained for the investigated alloys at various strain rates ($\dot{\varepsilon}$) and deformation temperatures (T) are shown in Figure 4.37 to Figure 4.42. The curves indicate strain-hardening behavior during plastic deformation. At the onset of plastic deformation, flow stress (σ) increases rapidly. The σ increases at a decreasing rate with increase in ε up to a maximum stress (σ_p). Beyond the peak strain (ε_p), *i.e.* the ε to reach the maximum stress, the σ either decreases with increase in ε or attains saturation. The former behavior is observed when the softening rate is higher than the work hardening rate, while the latter phenomenon occurs when the softening rate is equal to the work hardening rate [CAVA2002, MEDI1996, QING2009, YANG2006]. Flow softening after attaining the peak stress was observed in all the alloys at low $\dot{\varepsilon}$ of 0.001 s^{-1}. Undulations were observed at low $\dot{\varepsilon}$ in the flow curves beyond the ε_p in all alloys microalloyed with Sn. These undulations persist up to 450 ºC in the alloys containing Sn, the only exception being the alloy with 0.06 wt.% Sn in which the undulations were not observed beyond 350 ºC.

The peak flow stress (σ_p) for all the alloys determined at various deformation conditions are presented in Table 4.12. σ_p was highest for the alloy deformed at T = 300°C and $\dot{\varepsilon}$ = 1.0 s^{-1}. σ_p decreased with increase in T and decrease in $\dot{\varepsilon}$. At a given T, σ_p increased with increase in $\dot{\varepsilon}$. At any given $\dot{\varepsilon}$, σ_p decreased with increase in deformation T. These observations are in general agreement with earlier reports on metallic alloys [CHEN2008, EVAN1990, QING2009, YANG2006, ZHAN2007].

4.5.2 Constitutive modeling

Zener-Hollomon parameter approach

As discussed in section 2.5.1, the constitutive equations relating $\dot{\varepsilon}$ to σ and T are:

$$\dot{\varepsilon} = A_1 \sigma^{n_1} \exp\left(-\frac{Q}{RT}\right) \tag{2.16}$$

$$\dot{\varepsilon} = A_2 \exp(\beta\sigma) \exp\left(-\frac{Q}{RT}\right) \tag{2.17}$$

$$\dot{\varepsilon} = A_3 [\sinh(\alpha\sigma)]^n \exp\left(-\frac{Q}{RT}\right) \tag{2.18}$$

As pointed out earlier, though σ is generally taken as the peak flow stress (σ_p) [MCQU2002, MEDI1996], in a few instances the steady state flow stress (σ_s) has also been used. The term α is the stress multiplier. n_1, β, n, A_1, A_2 and, A_3 are material constants. The hyperbolic sine law (Eq. 2.18) has been found to be the most suitable form for explaining the high temperature deformation behavior of metallic alloys [CHEN2008, LIAN2008, MCQU2002, MEDI1996, SHAO2008, ZHAN2007]. In the present study, peak stress σ_p was used in the place of σ in the above expressions.

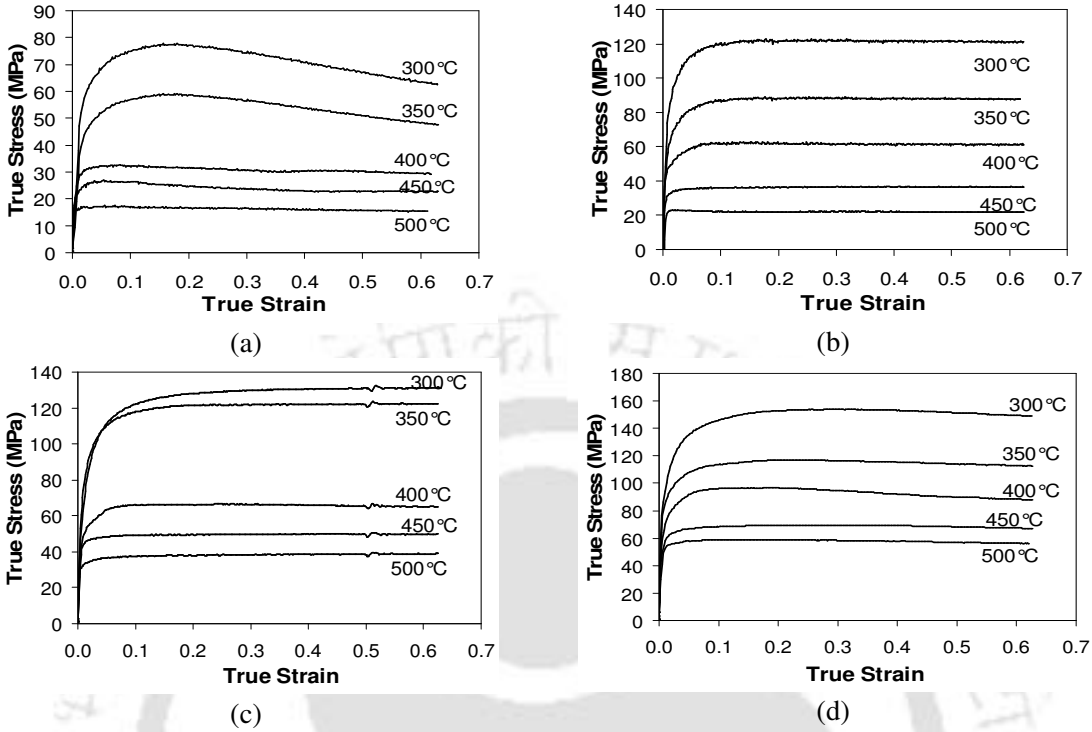

Fig.4.37. Flow curves of Alloy-*A* at $\dot{\varepsilon}$ of (a) 0.001 s^{-1} (b) 0.01 s^{-1} (c) 0.1 s^{-1}, and (d) 1.0 s^{-1}

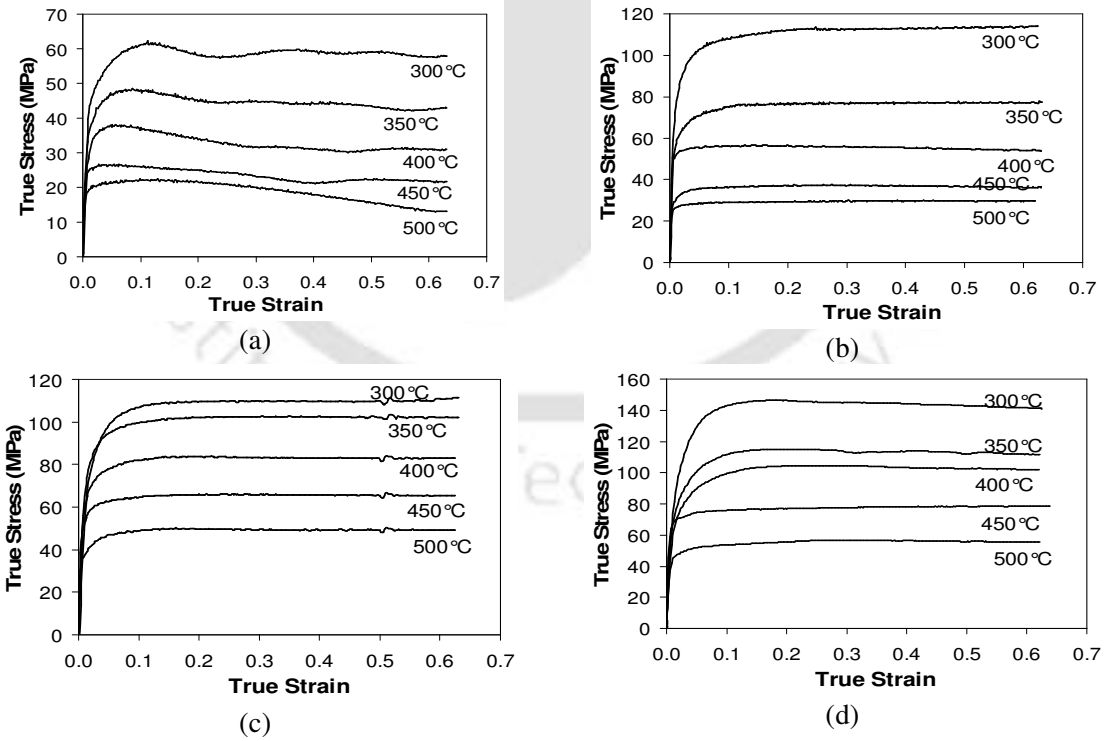

Fig.4.38. Flow curves of Alloy-*B* at $\dot{\varepsilon}$ of (a) 0.001 s^{-1} (b) 0.01 s^{-1} (c) 0.1 s^{-1}, and (d) 1.0 s^{-1}

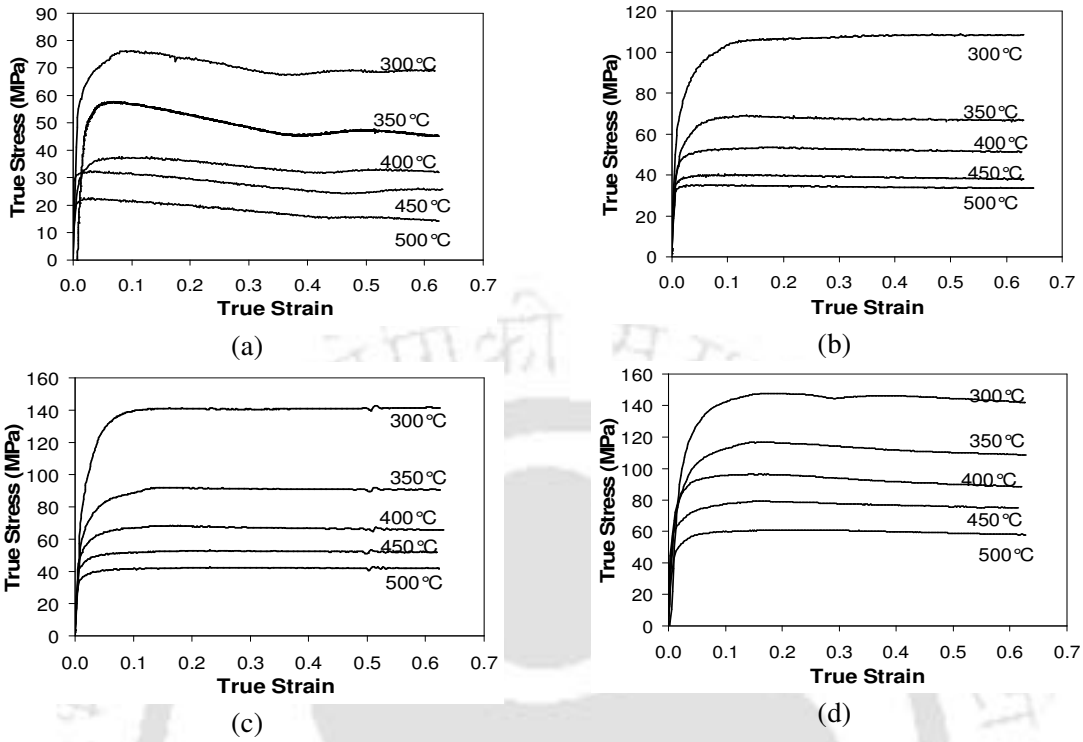

Fig.4.39. Flow curves of Alloy-*C* at $\dot{\varepsilon}$ of (a) 0.001 s^{-1} (b) 0.01 s^{-1} (c) 0.1 s^{-1}, and (d) 1.0 s^{-1}

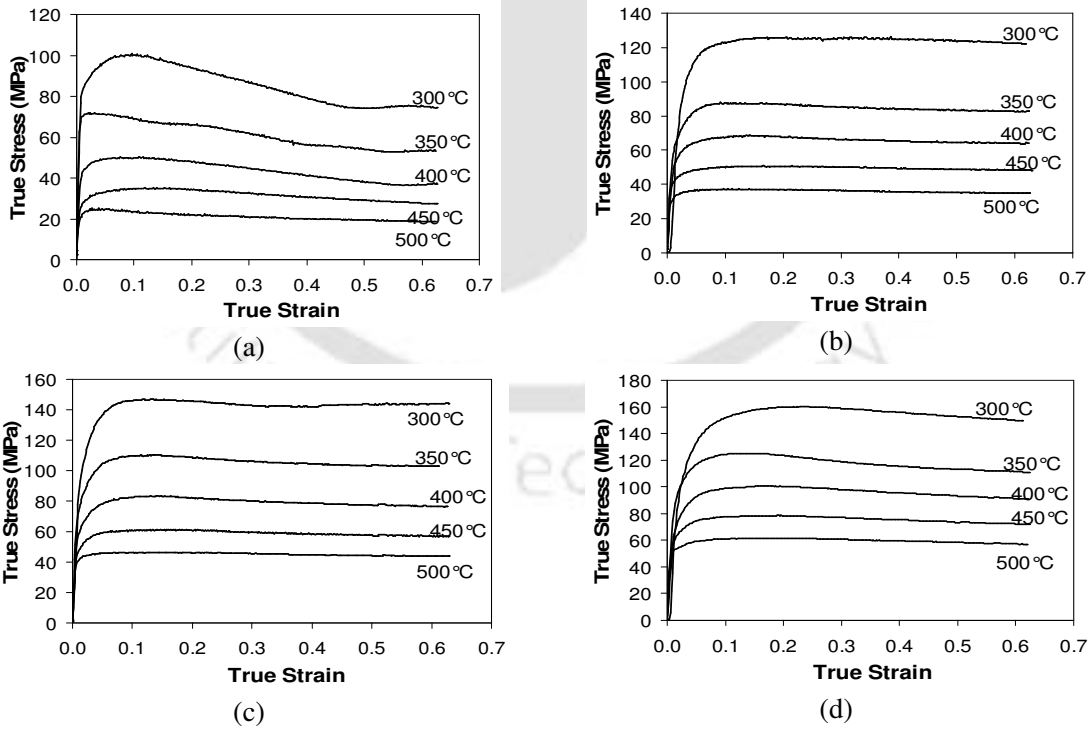

Fig.4.40. Flow curves of Alloy-*D* at $\dot{\varepsilon}$ of (a) 0.001 s^{-1} (b) 0.01 s^{-1} (c) 0.1 s^{-1}, and (d) 1.0 s^{-1}

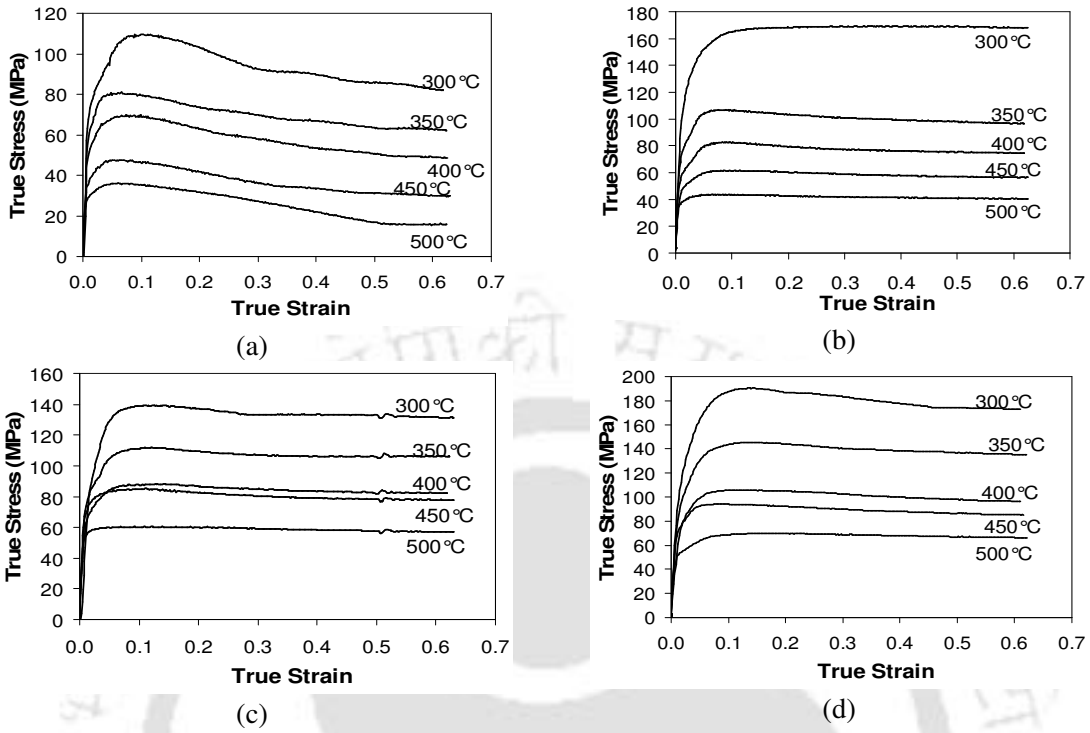

Fig.4.41. Flow curves of Alloy-*E* at $\dot{\varepsilon}$ of (a) 0.001 s^{-1} (b) 0.01 s^{-1} (c) 0.1 s^{-1}, and (d) 1.0 s^{-1}

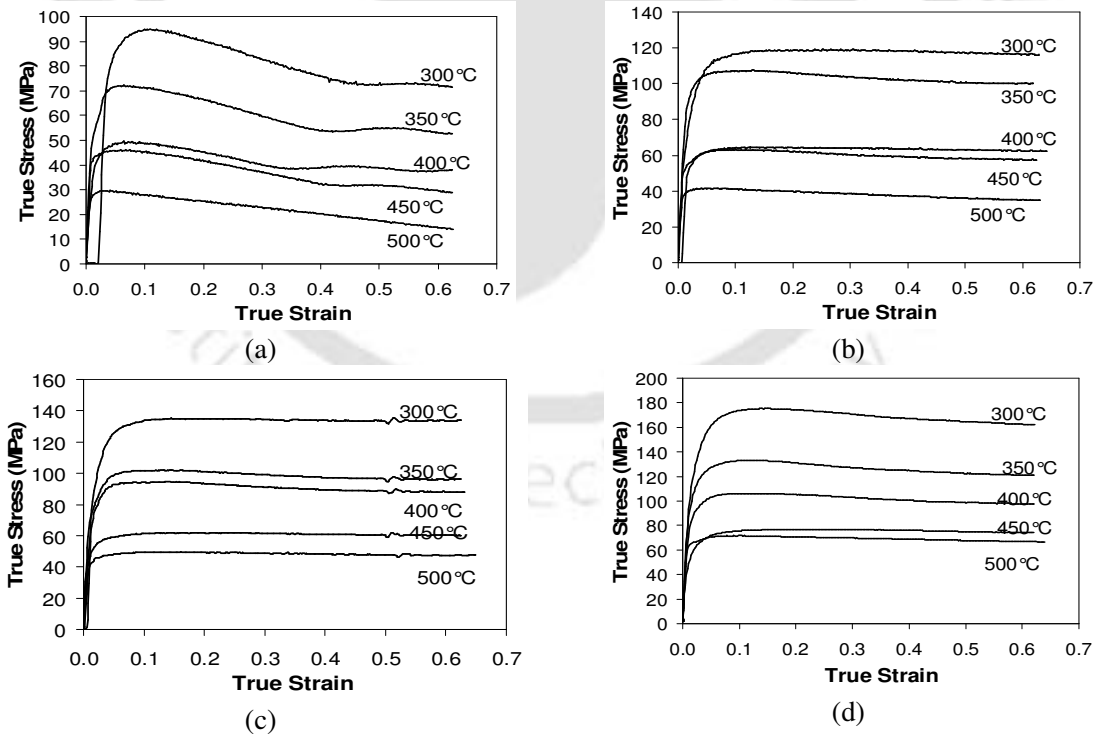

Fig.4.42. Flow curves of Alloy-*F* at $\dot{\varepsilon}$ of (a) 0.001 s^{-1} (b) 0.01 s^{-1} (c) 0.1 s^{-1}, and (d) 1.0 s^{-1}

Table 4.12. Peak stress values of the Al–Cu–Mg alloys at different deformation conditions

$\dot{\varepsilon}$ (s^{-1})	Temperature (°C)	Peak flow stress, σ_p (MPa)					
		Alloy-*A*	Alloy-*B*	Alloy-*C*	Alloy-*D*	Alloy-*E*	Alloy-*F*
0.001	300	77.83	62.23	76.35	100.26	109.62	94.98
	350	58.86	48.63	57.67	71.92	81.27	72.22
	400	32.28	38.04	37.65	50.13	69.88	49.70
	450	26.95	26.71	32.45	35.29	47.64	46.03
	500	17.61	22.6	22.53	25.20	36.12	29.62
0.01	300	122.9	113.43	108.65	126.06	169.53	119.29
	350	88.40	77.89	69.24	87.53	107.31	107.41
	400	62.79	56.69	53.51	68.59	82.84	64.68
	450	37.02	37.54	40.29	50.77	61.65	62.78
	500	22.29	30.10	35.10	37.12	43.78	41.49
0.1	300	131.47	110.04	141.88	146.75	139.29	135.11
	350	122.94	102.73	92.03	110.23	111.86	102.20
	400	66.63	83.93	68.39	83.46	88.17	94.77
	450	49.93	66.13	53.10	61.51	85.25	62.00
	500	38.99	50.16	42.66	46.50	60.61	49.62
1.0	300	153.82	146.61	147.79	160.21	190.41	175.22
	350	116.93	115.12	116.65	124.97	145.22	133.15
	400	96.85	104.65	96.38	100.65	105.83	106.02
	450	69.51	78.75	79.38	78.51	94.23	76.80
	500	58.89	56.53	60.89	61.56	69.90	71.58

Determination of the value of stress multiplier α is very important for this analysis. No single solution exists for α and its value for Al alloys found in the literature varies from 0.01 to 0.08. However, α = 0.052 has been widely used by researchers [MCQU2002, SPIG2003, BARD2003]. The value of α can also be defined as $\alpha \approx \beta / n_1$ [LIAN2008, CHEN2008], where β and n_1 are taken as the average values of the slopes of the $\ln(\dot{\varepsilon})$ *vs.* σ plots and $\ln(\dot{\varepsilon})$ *vs.* $\ln(\sigma)$ plots, respectively, in the range of T studied. Figure 4.43 shows the corresponding plots for Alloy-*A* and Alloy-*D*. The values of β and n_1 were evaluated for all the investigated alloys by this method. The values of α determined were 0.016, 0.014,

0.016, 0.013, 0.012 and 0.013 for Alloy-*A*, Alloy-*B*, Alloy-*C*, Alloy-*D*, Alloy-*E* and Alloy-*F*, respectively. α merely facilitates mathematical fitting procedure. Appropriate value of α ensures linear and parallel fits for the $\ln(\dot{\varepsilon})$ *vs.* $\ln[\sinh(\alpha\sigma)]$ data [BARD2003, BJØR2001, CAVA2002, CERR2007, GHOL2009, MEDI1996, MCQU2002, QING2009, SPIG2003]. The plots of $\ln(\dot{\varepsilon})$ *vs.* $\ln[\sinh(\alpha\sigma)]$ for all the alloys studied are shown in Figure 4.44 to Figure 4.49. $\alpha = 0.01$ yielded the best goodness of fit (R^2) value for the data. Hence in the present analysis, the optimal value of $\alpha = 0.01$ was used for all the investigated alloys.

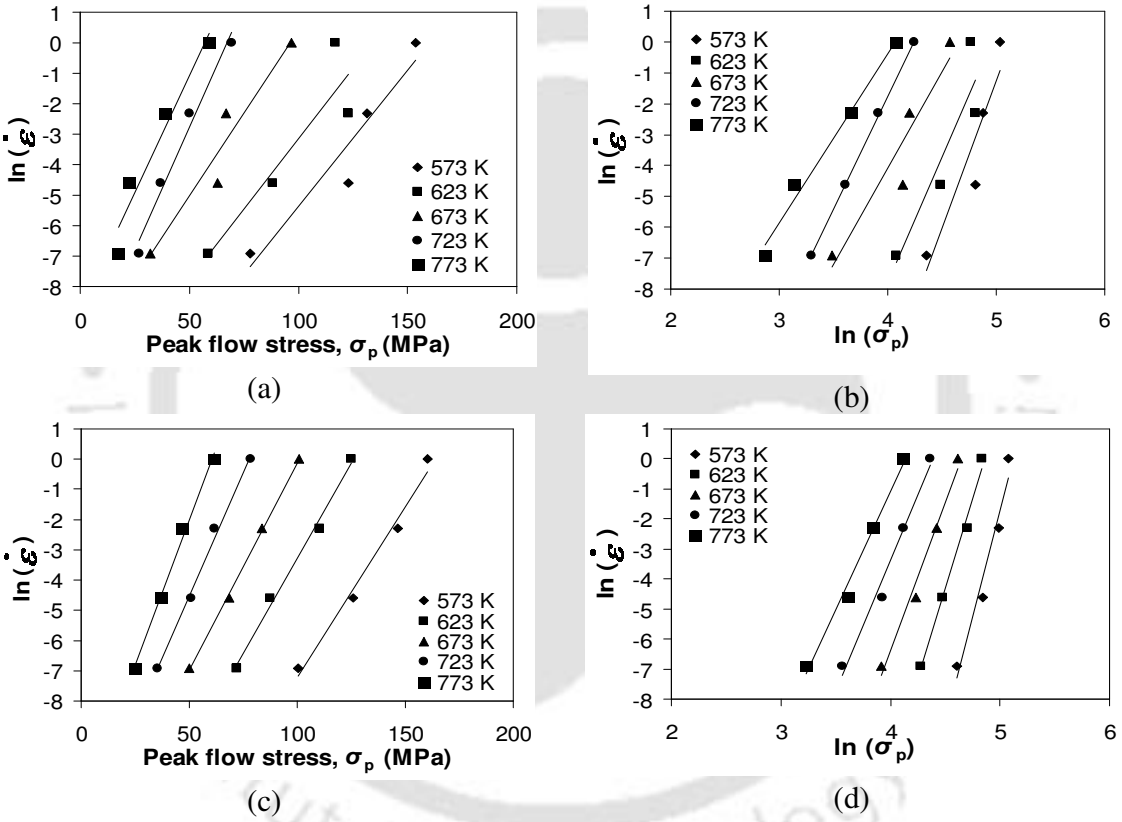

Fig.4.43. Plots of (a) $\ln \dot{\varepsilon}$ *vs.* σ_p for Alloy-*A* (b) $\ln \dot{\varepsilon}$ *vs.* $\ln \sigma_p$ for Alloy-*A* (c) $\ln \dot{\varepsilon}$ *vs.* σ_p for Alloy-*D*, and (d) $\ln \dot{\varepsilon}$ *vs.* $\ln \sigma_p$ for Alloy-*D*

The activation energy (Q) for high temperature deformation can be obtained from a plot of $\ln(\dot{\varepsilon})$ *vs.* $1/T$ at constant $[\sinh(\alpha\sigma)]$ value [GEOR1988]. The expression for Q therefore becomes:

$$Q = -R \left[\frac{\partial \ln \dot{\varepsilon}}{\partial \left(\frac{1}{T} \right)} \right]_{\sinh(\alpha\sigma)} \tag{4.9}$$

Eqn. 4.9 can also be expressed by the following relationship, which is considered as the general equation for evaluating the activation energy term when the hyperbolic-sine constitutive modeling is being used [BARD2003, BJØR2001, CAVA2002, CERR2007, CHEN2008, GHOL2009, LIAN2008, SPIG2003]:

$$Q = R \left[\frac{\partial \ln \dot{\varepsilon}}{\partial \ln[\sinh(\alpha\sigma)]} \right]_T \left[\frac{\partial \ln[\sinh(\alpha\sigma)]}{\partial \left(\frac{1}{T} \right)} \right]_{\dot{\varepsilon}} \tag{2.22}$$

i.e. Q = *R n S*

where n is the mean slope of $\ln(\dot{\varepsilon})$ *vs.* $\ln[\sinh(\alpha\sigma)]$ plots at different T and S the mean slope of the $\ln[\sinh(\alpha\sigma)]$ *vs.* $1/T$ plots at various $\dot{\varepsilon}$. These plots for all the investigated Al–Cu–Mg alloys are shown in Figure 4.44 to Figure 4.49. Table 4.13 presents the values of n, S and Q obtained for all the alloys studied. Figure 4.50 plots the variation of Q with Sn wt.% in the investigated alloy system. Q value of 183.4 kJ/mole, obtained for Alloy-*A*, is in general agreement with the values reported for other Al alloys [BARD2003, CAVA2002, EVAN1990, MCQU2002]. Q increased to 223.3 kJ/mol with the addition of 0.06 wt.% Sn but decreased when the Sn content was increased beyond 0.08 wt.%.

The Zener-Hollomon parameter (Z) can be expressed as

$$Z = \dot{\varepsilon} \exp\left(\frac{Q}{RT} \right) = A_3 [\sinh(\alpha\sigma)]^n \tag{2.21}$$

Taking logarithm of Eq. (2.21), one gets

$$\ln(Z) = \ln(A_3) + n \ln[\sinh(\alpha\sigma)] \tag{4.10}$$

from which A_3 and n can be obtained as mentioned in section 2.5.1. Figure 4.51 shows the $\ln(Z)$ *vs.* $\ln[\sinh(\alpha\sigma)]$ plots, in which the solid lines represent linear fit to the data. The values of $\ln(Z)$ at various $\dot{\varepsilon}$ and deformation T are presented in Table 4.14 to Table 4.19 for

all the alloys studied. It is evident that Z increases with increase in $\dot{\varepsilon}$ and decrease in T. Dynamic recrystallization is generally favoured at low $\dot{\varepsilon}$ and high T, *i.e*, at low Z values [QING2009].

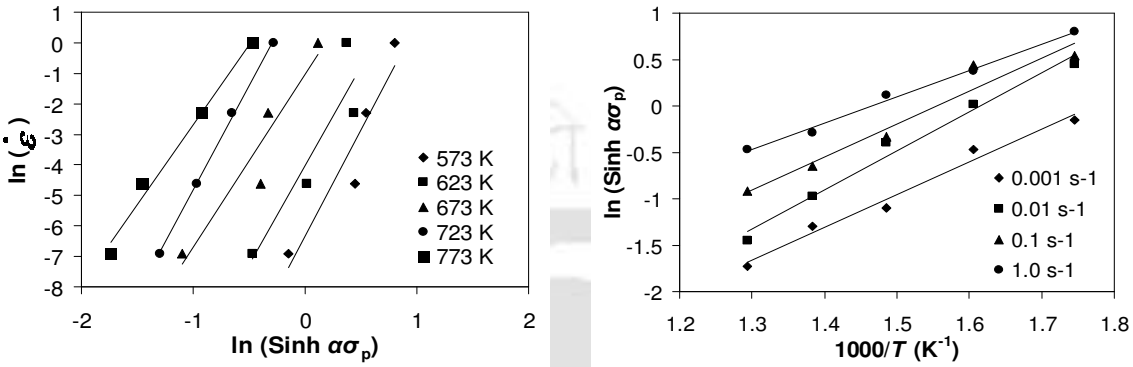

(a) (b)

Fig.4.44. Plots of (a) ln (sinh $\alpha\sigma_p$) *vs.* ln $\dot{\varepsilon}$ and (b) ln (sinh $\alpha\sigma_p$) *vs.* 1000/T for Alloy-*A*

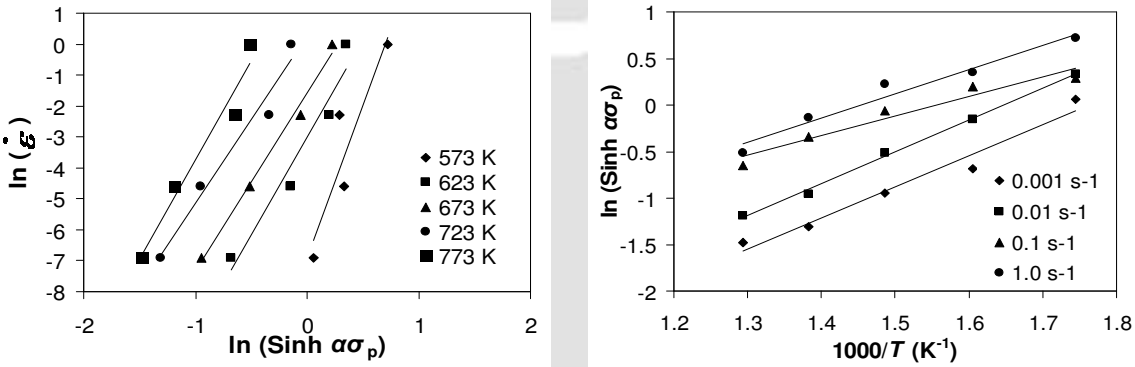

(a) (b)

Fig.4.45. Plots of (a) ln (sinh $\alpha\sigma_p$) *vs.* ln $\dot{\varepsilon}$ and (b) ln (sinh $\alpha\sigma_p$) *vs.* 1000/T for Alloy-*B*

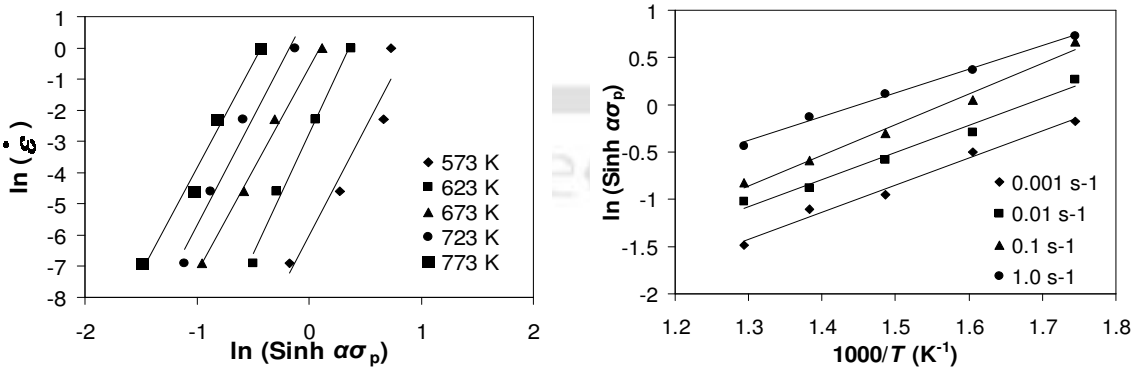

(a) (b)

Fig.4.46. Plots of (a) ln (sinh $\alpha\sigma_p$) *vs.* ln $\dot{\varepsilon}$ and (b) ln (sinh $\alpha\sigma_p$) *vs.* 1000/T for Alloy-*C*

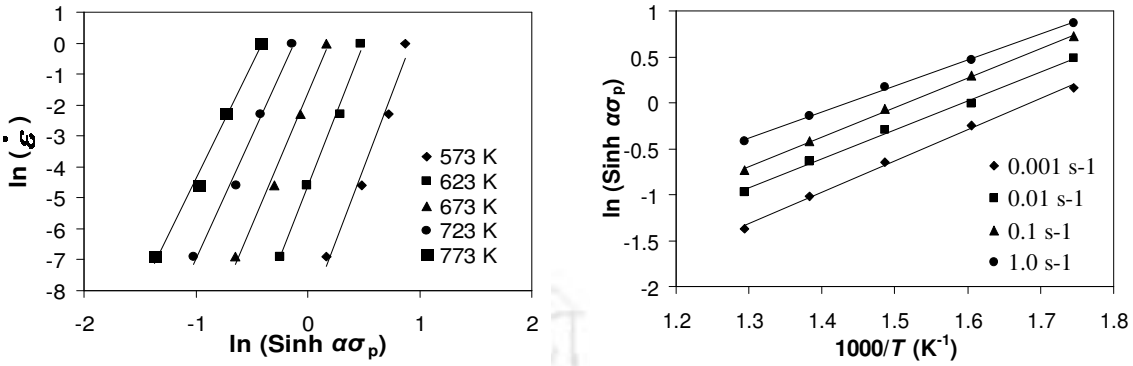

(a) (b)

Fig.4.47. Plots of (a) ln (sinh $\alpha\sigma_p$) *vs.* ln $\dot{\varepsilon}$ and (b) ln (sinh $\alpha\sigma_p$) *vs.* 1000/T for Alloy-*D*

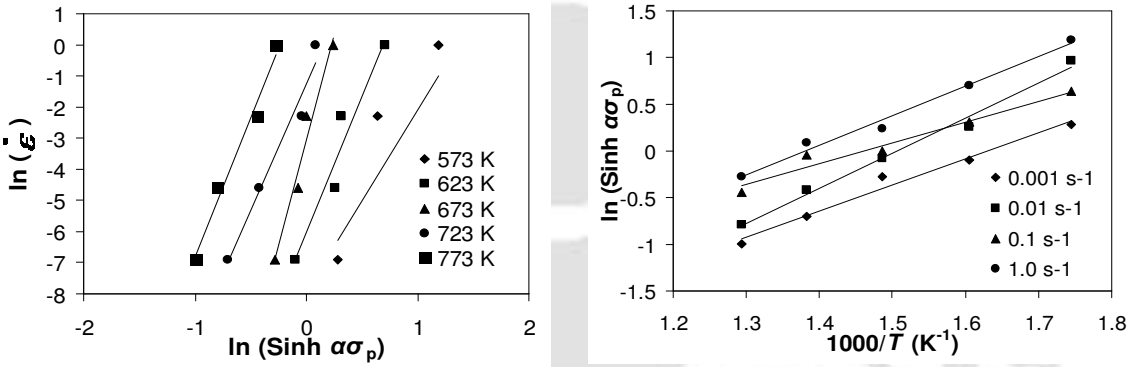

(a) (b)

Fig.4.48. Plots of (a) ln (sinh $\alpha\sigma_p$) *vs.* ln $\dot{\varepsilon}$ and (b) ln (sinh $\alpha\sigma_p$) *vs.* 1000/T for Alloy-*E*

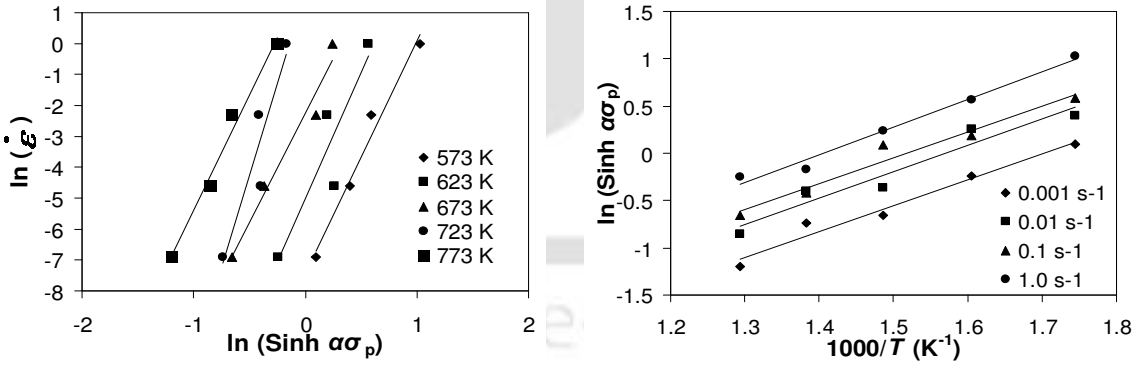

(a) (b)

Fig.4.49. Plots of (a) ln (sinh $\alpha\sigma_p$) *vs.* ln $\dot{\varepsilon}$ and (b) ln (sinh $\alpha\sigma_p$) *vs.* 1000/T for Alloy-*F*

Table 4.13. Values of the constants α, n, S, A_3 and Q corresponding to the Al–Cu–Mg alloys

Sample ID	α (MPa^{-1})	n	S	A_3 (s^{-1})	Q (kJ/mole)
Alloy-*A*	0.01	6.24	3.53	$7.83x10^{13}$	183.4
Alloy-*B*	0.01	6.77	2.86	$1.28x10^{12}$	161.2
Alloy-*C*	0.01	6.97	2.87	$4.16x10^{12}$	166.3
Alloy-*D*	0.01	8.55	3.14	$5.37x10^{16}$	223.3
Alloy-*E*	0.01	9.09	2.98	$1.25x10^{16}$	225.5
Alloy-*F*	0.01	8.4	2.8	$1.96x10^{14}$	195.5

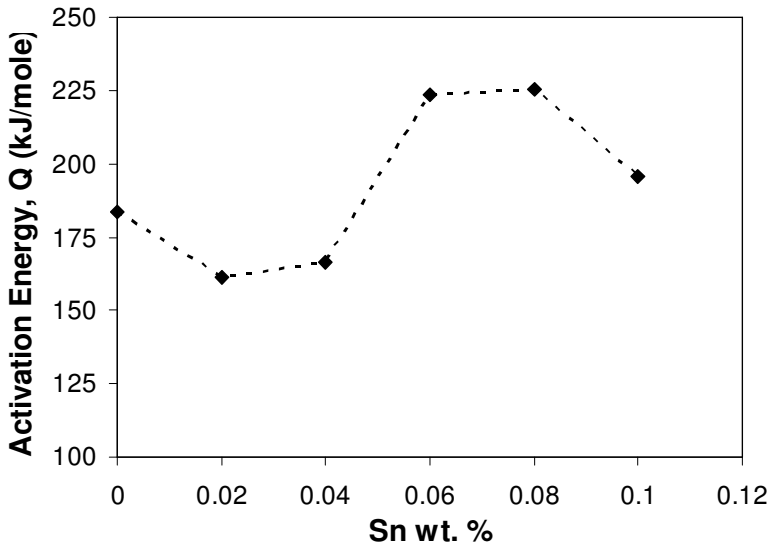

Fig.4.50. Variation of activation energy of deformation with Sn content in Al–Cu–Mg alloys

Table 4.14. Values of ln (Z) for Alloy-*A* at various deformation conditions

$\dot{\varepsilon}$ (s^{-1})	T (K)				
	573	623	673	723	773
0.001	31.59	28.5	25.87	23.6	21.63
0.01	33.89	30.8	28.17	25.9	23.93
0.1	36.19	33.1	30.47	28.2	26.23
1.0	38.49	35.4	32.77	30.51	28.53

Table 4.15. Values of ln (*Z*) for Alloy-*B* at various deformation conditions

$\dot{\varepsilon}$ (s^{-1})	*T* (K)				
	573	623	673	723	773
0.001	26.93	24.21	21.90	19.91	18.17
0.01	29.23	26.51	24.20	22.21	20.47
0.1	31.53	28.82	26.50	24.51	22.78
1.0	33.83	31.12	28.81	26.81	25.08

Table 4.16. Values of ln (*Z*) for Alloy-*C* at various deformation conditions

$\dot{\varepsilon}$ (s^{-1})	*T* (K)				
	573	623	673	723	773
0.001	28.01	25.20	22.82	20.76	18.97
0.01	30.31	27.51	25.12	23.06	21.28
0.1	32.61	29.81	27.42	25.37	23.58
1.0	34.91	32.11	29.73	27.67	25.88

Table 4.17. Values of ln (*Z*) for Alloy-*D* at various deformation conditions

$\dot{\varepsilon}$ (s^{-1})	*T* (K)				
	573	623	673	723	773
0.001	39.97	36.20	33.00	30.24	27.84
0.01	42.27	38.51	35.30	32.54	30.14
0.1	44.57	40.81	37.61	34.85	32.44
1.0	46.87	43.11	39.91	37.15	34.75

Table 4.18. Values of ln (*Z*) for Alloy-*E* at various deformation conditions

$\dot{\varepsilon}$ (s^{-1})	*T* (K)				
	573	623	673	723	773
0.001	40.43	36.63	33.40	30.61	28.18
0.01	42.74	38.94	35.70	32.91	30.49
0.1	45.04	41.24	38.00	35.22	32.79
1.0	47.34	43.54	40.31	37.52	35.09

Table 4.19. Values of ln (*Z*) for Alloy-*F* at various deformation conditions

$\dot{\varepsilon}$ (s^{-1})	*T* (K)				
	573	623	673	723	773
0.001	34.14	30.84	28.04	25.62	23.52
0.01	36.44	33.15	30.34	27.92	25.82
0.1	38.74	35.45	32.64	30.23	28.12
1.0	41.04	37.75	34.95	32.53	30.42

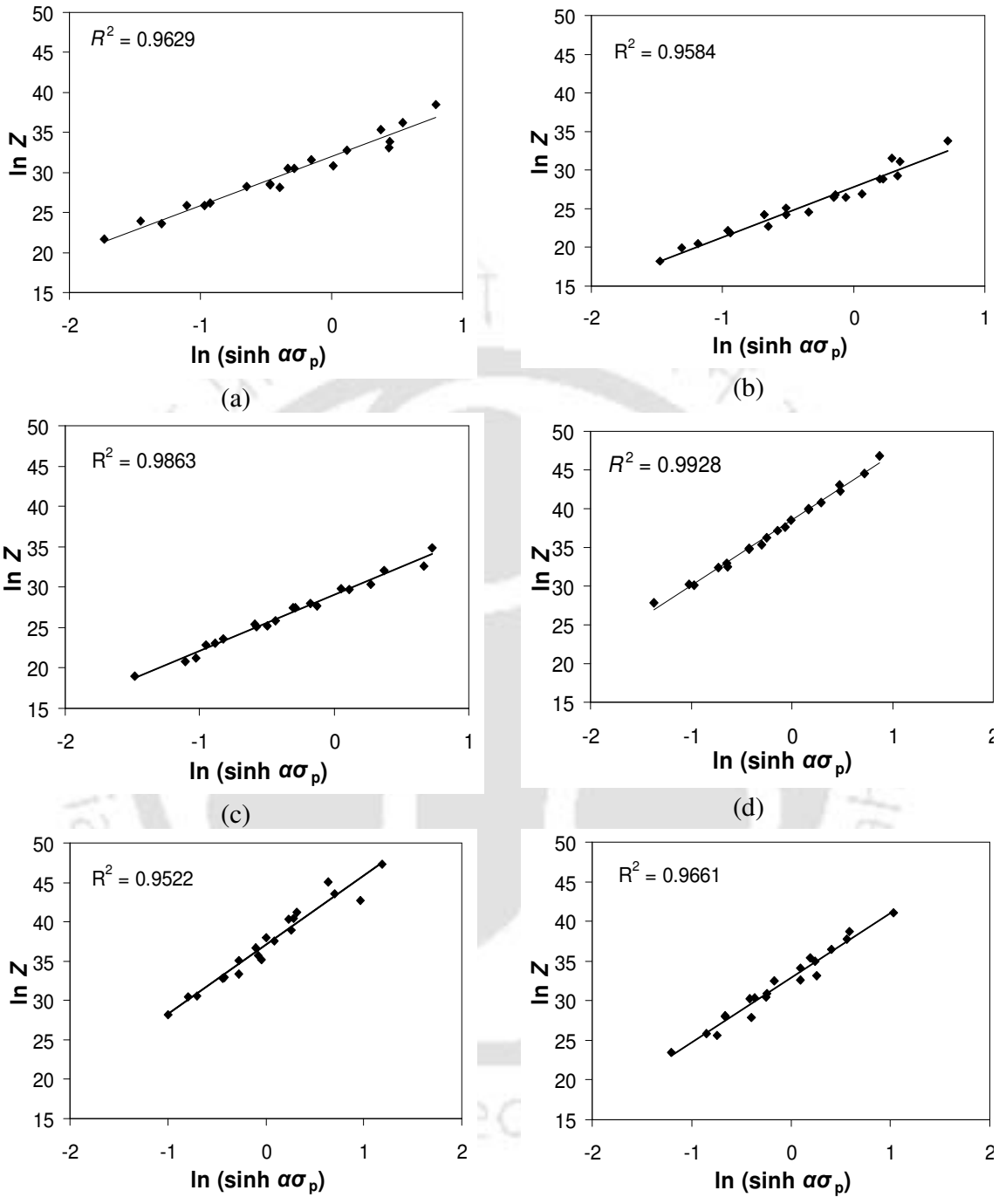

Fig.4.51. Plots of ln (sinh $\alpha\sigma_p$) *vs.* ln *Z* for (a) Alloy-*A* (b) Alloy-*B* (c) Alloy-*C* (d) Alloy-*D* (e) Alloy-*E*, and (f) Alloy-*F*

Prediction of peak flow stress

The general expression for the peak flow stress (σ_p) during any deforming condition can be derived from Eq. (2.18), and the same can be expressed as

$$\sigma_p = \frac{1}{\alpha}\sinh^{-1}\left[\frac{\dot{\varepsilon}\exp\left(\frac{Q}{RT}\right)}{A_3}\right]^{\frac{1}{n}} \tag{4.11}$$

The peak stress during deformation at any T and $\dot{\varepsilon}$ can be determined since the constants α, n, S, A_3 and Q of Eq. (4.11) are known. These constants corresponding to the six investigated alloys are shown in Table 4.13.

To establish confidence in the values obtained for the constants in the constitutive equation, the σ values corresponding to the T and $\dot{\varepsilon}$ at which experiments were carried out were determined using Eq. (4.11). A comparison of the peak stress determined by Eq. (4.11) and the experimentally obtained values is given in Tables 4.20 to 4.25. The plots of the predicted *vs*. experimental peak stress values of the alloys are shown in Figure 4.52. For perfect prediction, all the points should lie on the solid line inclined at 45° to the x-axis. Sets of dashed lines representing the boundaries of ± 13 % deviations are also shown in the figures. The figures show that most of the points lie very close to the line of prefect prediction for all the alloys.

It is seen that the percentage error in prediction of peak stress for Alloy-*A* is less than ±13 % for 16 out of 20 data values. Although the maximum absolute error in the prediction is –22.6 MPa, the percentage error is only 14.69 for this case. The absolute error is high since the actual stress value is also high. However, the % error is only 14.69. Similarly for low values of actual stress (*viz*. 23.15 MPa), though the absolute error is only 4 MPa, the % error shows a high value of 17.27. Errors of these levels are expected when the values which are to be predicted vary over a wide range (*eg*. in the present case σ_p varies from 18 to 154 MPa). The percentage error in the prediction of peak stress for Alloy-*D* is less than ±13 % for all of 20 data values. Maximum absolute error in the prediction is

–10.15 MPa, where the percentage error is 5.96. The RMS errors for the prediction of σ_p for Alloy-*A,* Alloy-*B,* Alloy-*C,* Alloy-*D,* Alloy-*E,* and Alloy-*F* are 8.53, 9.33, 4.84, 3.24, 10.03 and 7.52, respectively. It was observed that 16, 15, 20, 20, 18 and 17 numbers out of 20 data points fall within ±13 % deviation line for Alloy-*A,* Alloy-*B,* Alloy-*C,* Alloy-*D,* Alloy-*E,* and Alloy-*F,* respectively. This establishes the confidence in the values of parameters obtained for prediction of peak flow stress during hot deformation by constitutive modeling.

Table 4.20. Comparison of experimental and predicted values of peak flow stress, σ_p for Alloy-*A*.

Strain rate (s^{-1})	Temperature (°C)	Experimental peak flow stress (MPa)	Predicted peak flow stress (MPa)	Error (MPa)	% error
0.001	300	77.83	83.61	-5.78	-7.43
0.001	350	59.15	54.40	4.75	8.03
0.001	400	32.62	36.66	-4.04	-12.37
0.001	450	26.95	25.78	1.17	4.33
0.001	500	17.61	18.89	-1.28	-7.28
0.01	300	122.9	111.15	11.75	9.56
0.01	350	89.11	75.29	13.82	15.51
0.01	400	62.97	51.85	11.12	17.66
0.01	450	37.02	36.86	0.16	0.43
0.01	500	23.15	27.15	-4.00	-17.27
0.1	300	131.29	142.53	-11.24	-8.56
0.1	350	122.45	120.50	1.95	1.59
0.1	400	66.76	72.00	-5.24	-7.84
0.1	450	50.03	52.12	-2.09	-4.18
0.1	500	38.76	38.76	0.00	-0.01
1.0	300	153.84	176.44	-22.60	-14.69
1.0	350	116.93	131.46	-14.53	-12.43
1.0	400	96.85	97.26	-0.41	-0.43
1.0	450	69.48	72.35	-2.87	-4.14
1.0	500	58.92	54.70	4.22	7.16

Table 4.21. Comparison of experimental and predicted values of peak flow stress, σ_p for Alloy-*B*.

Strain rate (s^{-1})	Temperature (°C)	Experimental peak flow stress (MPa)	Predicted peak flow stress (MPa)	Error (MPa)	% error
0.001	300	92.5	78.55	13.95	15.08
0.001	350	48.63	55.32	-6.69	-13.76
0.001	400	38.04	40.26	-2.22	-5.85
0.001	450	26.71	30.35	-3.64	-13.64
0.001	500	22.60	23.64	-1.04	-4.59
0.01	300	113.43	102.91	10.52	9.27
0.01	350	77.89	74.63	3.26	4.19
0.01	400	56.69	55.25	1.44	2.53
0.01	450	37.54	42.05	-4.51	-12.02
0.01	500	30.10	32.92	-2.82	-9.37
0.1	300	110.04	130.83	-20.79	-18.90
0.1	350	102.73	120.50	-17.77	-17.30
0.1	400	83.93	74.54	9.39	11.19
0.1	450	66.13	57.60	8.53	12.90
0.1	500	50.16	45.50	4.66	9.28
1.0	300	146.61	161.30	-14.69	-10.02
1.0	350	115.12	125.61	-10.49	-9.11
1.0	400	104.65	98.15	6.50	6.21
1.0	450	78.75	77.48	1.27	1.62
1.0	500	56.53	62.09	-5.56	-9.84

Table 4.22. Comparison of experimental and predicted values of peak flow stress, σ_p for Alloy-*C*.

Strain rate (s^{-1})	Temperature (°C)	Experimental peak flow stress (MPa)	Predicted peak flow stress (MPa)	Error (MPa)	% error
0.001	300	76.35	77.89	-1.54	-2.02
0.001	350	57.67	54.76	2.91	5.04
0.001	400	37.65	39.81	-2.16	-5.73
0.001	450	32.45	29.98	2.47	7.61
0.001	500	22.53	23.33	-0.80	-3.54
0.01	300	108.65	101.39	7.26	6.68
0.01	350	69.24	73.32	-4.08	-5.89
0.01	400	53.51	54.17	-0.66	-1.24
0.01	450	40.29	41.17	-0.88	-2.18
0.01	500	35.10	32.19	2.91	8.28
0.1	300	141.88	128.30	13.58	9.57
0.1	350	122.03	120.50	1.53	1.25
0.1	400	68.39	72.57	-4.18	-6.12
0.1	450	53.10	55.95	-2.85	-5.36
0.1	500	42.66	44.13	-1.47	-3.44
1.0	300	147.79	157.69	-9.90	-6.70
1.0	350	116.65	122.22	-5.57	-4.77
1.0	400	96.38	95.09	1.29	1.34
1.0	450	79.38	74.80	4.58	5.78
1.0	500	60.89	59.78	1.11	1.82

Table 4.23. Comparison of experimental and predicted values of peak flow stress, σ_p for Alloy-*D*.

Strain rate (s^{-1})	Temperature (°C)	Experimental peak flow stress (MPa)	Predicted peak flow stress (MPa)	Error (MPa)	% error
0.001	300	100.26	100.56	-0.30	-0.30
0.001	350	71.92	70.31	1.61	2.24
0.001	400	50.13	50.28	-0.15	-0.30
0.001	450	35.29	37.10	-1.81	-5.14
0.001	500	25.2	28.28	-3.08	-12.23
0.01	300	126.06	122.21	3.85	3.06
0.01	350	87.53	88.00	-0.47	-0.54
0.01	400	68.59	64.14	4.45	6.49
0.01	450	50.77	47.85	2.92	5.76
0.01	500	37.12	36.69	0.43	1.16
0.1	300	146.75	145.64	1.11	0.75
0.1	350	110.23	108.25	1.98	1.80
0.1	400	83.46	80.76	2.70	3.23
0.1	450	61.51	61.17	0.34	0.56
0.1	500	46.5	47.33	-0.83	-1.78
1.0	300	160.21	170.36	-10.15	-6.33
1.0	350	124.97	130.61	-5.64	-4.51
1.0	400	100.65	100.05	0.60	0.59
1.0	450	78.51	77.24	1.27	1.61
1.0	500	61.56	60.53	1.03	1.68

Table 4.24. Comparison of experimental and predicted values of peak flow stress, σ_p for Alloy-*E*.

Strain rate (s^{-1})	Temperature (°C)	Experimental peak flow stress (MPa)	Predicted peak flow stress (MPa)	Error (MPa)	% error
0.001	300	109.62	116.58	-6.96	-6.35
0.001	350	81.27	84.83	-3.56	-4.38
0.001	400	69.88	62.65	7.23	10.35
0.001	450	47.64	47.39	0.25	0.52
0.001	500	36.12	36.83	-0.71	-1.97
0.01	300	169.53	138.19	31.34	18.49
0.01	350	107.31	103.41	3.90	3.63
0.01	400	82.84	77.95	4.89	5.91
0.01	450	61.65	59.74	1.91	3.09
0.01	500	43.78	46.79	-3.01	-6.89
0.1	300	139.29	161.07	-21.78	-15.63
0.1	350	111.86	120.50	-8.64	-7.72
0.1	400	88.17	95.63	-7.46	-8.46
0.1	450	85.25	74.52	10.73	12.58
0.1	500	60.61	59.01	1.60	2.63
1.0	300	190.41	184.82	5.59	2.93
1.0	350	145.22	146.07	-0.85	-0.59
1.0	400	105.83	115.43	-9.60	-9.08
1.0	450	94.23	91.72	2.51	2.67
1.0	500	69.9	73.66	-3.76	-5.38

Table 4.25. Comparison of experimental and predicted values of peak flow stress, σ_p for Alloy-*F*.

Strain rate (s^{-1})	Temperature (°C)	Experimental peak flow stress (MPa)	Predicted peak flow stress (MPa)	Error (MPa)	% error
0.001	300	94.98	98.84	-3.86	-4.07
0.001	350	72.22	71.84	0.38	0.52
0.001	400	49.70	53.41	-3.71	-7.47
0.001	450	46.03	40.84	5.19	11.27
0.001	500	29.62	32.13	-2.51	-8.46
0.01	300	119.29	120.72	-1.43	-1.20
0.01	350	107.41	90.14	17.27	16.08
0.01	400	64.68	68.23	-3.55	-5.49
0.01	450	62.78	52.75	10.03	15.97
0.01	500	41.49	41.77	-0.28	-0.67
0.1	300	135.11	144.49	-9.38	-6.94
0.1	350	102.2	120.50	-18.30	-17.91
0.1	400	94.77	85.92	8.85	9.34
0.1	450	62.00	67.43	-5.43	-8.76
0.1	500	49.62	53.90	-4.28	-8.63
1.0	300	175.22	169.61	5.61	3.20
1.0	350	133.15	134.06	-0.91	-0.68
1.0	400	106.02	106.28	-0.26	-0.24
1.0	450	76.80	84.97	-8.17	-10.64
1.0	500	71.58	68.83	2.75	3.84

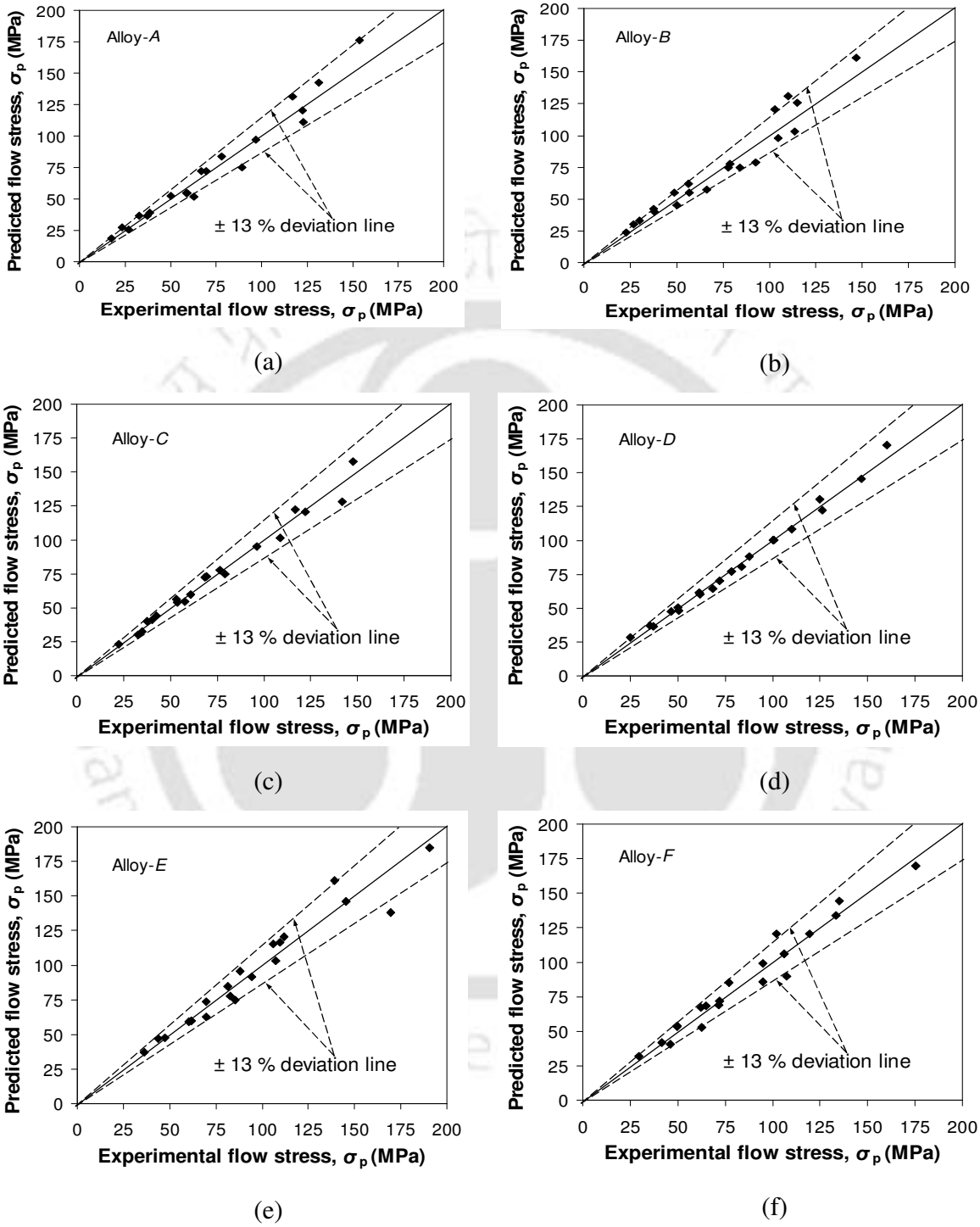

Fig.4.52. Variation of predicted σ_p with experimental σ_p for (a) Alloy-*A* (b) Alloy-*B* (c) Alloy-*C* (d) Alloy-*D* (e) Alloy-*E*, and (f) Alloy-*F*

4.6 Prediction of flow stress by Multiple Linear Regression (MLR) analysis

The above analyses successfully predicted σ_p at different deforming conditions of $\dot{\varepsilon}$ and T. Flow stress (σ) in terms of all the three independent parameters, *i.e.* strain (ε), strain rate ($\dot{\varepsilon}$) and deformation temperature (T), can be predicted using regression analysis and artificial neural network modeling. Multiple linear regression (MLR) analysis was carried out with the basic relation expressed as:

$$\sigma = A\ \varepsilon^m \dot{\varepsilon}^n T^l \tag{2.39}$$

where σ is the flow stress, ε is the true strain, $\dot{\varepsilon}$ is the true strain rate and T is the deformation Temperature. A, m, n and l are constants, that have to be derived for each of the alloys. Taking natural logarithm on both sides, Eq. (2.39) can be expressed as:

$$\ln\sigma = \ln A + m\ln\varepsilon + n\ln\dot{\varepsilon} + l\ln T \tag{4.12}$$

The coefficients A, m, n, and l were obtained by MLR analysis using the 'REGRESS' function available in the statistical tool box of MATLAB™ (version 7.0) software. The detailed procedure involved in the analysis has been described in section 2.5.4. The function B = REGRESS(Y, X) returns the regression coefficients of a linear model $Y = XB$. X is a matrix of size $i \times p$, with rows corresponding to number of observations and columns to predictor variables. Y is a vector of size $i \times 1$, which denotes response observations. In the present analysis, 90 sets of independent variables were used to evaluate the regression coefficients. Therefore, Y (90×1) matrix denotes the flow stresses, X (90×4) matrix denotes the input variables (ε, $\dot{\varepsilon}$,T) and B (4×1) matrix denotes the regression coefficients. The coefficients of Eq. (2.39) determined by MLR analysis for all the alloys and they are given in Table 4.26.

From Eq. (2.39), the values of σ at different deformation conditions were determined. Table 4.27 to Table 4.32 give the experimental and predicted σ values for all the alloys. Figure 4.53 shows the plots of experimental values of σ and σ values predicted by MLR analysis for the investigated alloys. For perfect prediction, all the points should lie on the solid line shown in the figure, which is inclined at 45° to the x-axis. Dashed lines

representing the boundaries of ±10 % deviations are also shown in the figures. It was observed that 14, 7, 23, 19, 11 and 17 numbers out of 30 data points fall within ±10 % deviation line for Alloy-*A,* Alloy-*B,* Alloy-*C,* Alloy-*D,* Alloy-*E,* and Alloy-*F,* respectively. The RMS errors for the prediction of σ for Alloy-*A,* Alloy-*B,* Alloy-*C,* Alloy-*D,* Alloy-*E,* and Alloy-*F* are 14.99, 13.51, 7.39, 8.31, 19.73 and 12.06, respectively. From the above, it can be concluded that the MLR analysis provides reasonable predictions for σ for various combinations of $\dot{\varepsilon}$ and *T*. Though this simple procedure yields reasonably good prediction of σ, these data are not suitable for the generation of processing maps for hot deformation. Hence, ANN modeling was attempted for obtaining better prediction of σ.

Table 4.26. Values of the coefficients of the regression analysis equation used for predicting σ values of the alloys

Sample ID	ln *A*	*m*	*n*	*l*
Alloy-*A*	20.10	– 0.04	0.14	– 2.61
Alloy-*B*	16.99	– 0.04	0.15	– 2.68
Alloy-*C*	17.69	– 0.05	0.14	– 2.21
Alloy-*D*	18.13	– 0.08	0.12	– 2.28
Alloy-*E*	17.68	– 0.12	0.11	– 2.19
Alloy-*F*	17.27	– 0.09	0.12	– 2.13

Table 4.27. Comparison of experimental and MLR predicted values of flow stress, σ of Alloy-*A*.

Experimental flow stress (MPa)	Predicted flow stress (MPa)	Error (MPa)	% error
87.4	70.1	17.3	19.8
22.2	27.6	-5.4	-24.4
122.4	145.3	-22.9	-18.7
66.1	68.6	-2.5	-3.8
49.3	50.4	-1.1	-2.3
121.6	102.0	19.7	16.2
62.6	48.1	14.5	23.1
36.2	35.4	0.8	2.3
121.5	94.5	27.0	22.2
37.9	37.3	0.6	1.6
88.7	67.1	21.6	24.4
22.0	26.5	-4.4	-20.0
129.9	139.1	-9.2	-7.1
66.3	65.6	0.7	1.0
49.7	48.3	1.4	2.8
121.6	99.2	22.4	18.4
61.2	46.8	14.3	23.4
36.4	34.4	2.0	5.5
121.9	92.0	29.9	24.5
38.5	36.3	2.2	5.8
88.2	65.8	22.5	25.5
22.1	25.9	-3.8	-17.4
131.1	136.3	-5.2	-4.0
65.4	64.3	1.1	1.7
49.1	47.3	1.8	3.7
121.3	97.6	23.6	19.5
61.3	46.1	15.2	24.8
36.5	33.9	2.6	7.2
122.4	90.5	31.9	26.1
38.7	35.7	3.0	7.8

Table 4.28. Comparison of experimental and MLR predicted values of flow stress, σ of Alloy-*B*.

Experimental flow stress (MPa)	Predicted flow stress (MPa)	Error (MPa)	% error
75.0	65.1	10.0	13.3
29.0	31.0	-2.0	-6.8
106.9	127.7	-20.8	-19.5
82.1	70.2	11.9	14.5
64.5	54.9	9.6	14.9
112.2	87.5	24.7	22.1
56.4	48.1	8.3	14.8
37.1	37.6	-0.6	-1.5
102.2	90.4	11.8	11.5
49.6	43.0	6.6	13.3
76.6	62.6	14.0	18.3
29.7	29.8	-0.1	-0.3
109.7	122.8	-13.1	-11.9
83.3	67.5	15.8	18.9
65.9	52.8	13.1	19.9
112.5	85.4	27.1	24.1
55.2	46.9	8.3	15.0
36.9	36.7	0.2	0.5
102.6	88.2	14.4	14.0
49.1	42.0	7.1	14.4
77.1	61.5	15.6	20.3
29.7	29.3	0.4	1.4
109.8	120.6	-10.8	-9.8
82.3	66.3	16.0	19.5
65.1	51.9	13.2	20.3
113.4	84.2	29.2	25.8
54.0	46.3	7.7	14.3
36.4	36.2	0.2	0.4
101.9	87.0	14.9	14.7
49.2	41.4	7.8	15.8

Table 4.29. Comparison of experimental and MLR predicted values of flow stress, σ of Alloy-*C*.

Experimental flow stress (MPa)	Predicted flow stress (MPa)	Error (MPa)	% error
67.9	69.1	-1.2	-1.7
34.8	31.4	3.4	9.7
139.5	133.4	6.1	4.4
66.9	70.7	-3.8	-5.6
51.8	54.5	-2.7	-5.3
106.1	93.7	12.4	11.7
53.1	49.6	3.5	6.5
39.8	38.3	1.6	3.9
91.7	91.6	0.1	0.1
42.2	41.7	0.5	1.2
67.5	65.3	2.2	3.2
34.4	29.7	4.7	13.6
140.8	126.1	14.7	10.4
67.1	66.8	0.3	0.5
52.6	51.5	1.1	2.1
108.4	90.4	17.9	16.6
52.0	47.9	4.1	7.9
38.8	36.9	1.8	4.7
90.9	88.4	2.5	2.7
42.1	40.2	1.9	4.5
66.9	63.6	3.3	4.9
33.7	28.9	4.7	14.0
141.1	122.9	18.2	12.9
66.1	65.1	1.0	1.5
51.4	50.2	1.2	2.3
108.4	88.6	19.8	18.3
51.3	46.9	4.4	8.6
37.8	36.2	1.6	4.2
90.6	86.6	3.9	4.4
42.3	39.4	2.9	6.9

Table 4.30. Comparison of experimental and MLR predicted values of flow stress, σ of Alloy-*D*.

Experimental flow stress (MPa)	Predicted flow stress (MPa)	Error (MPa)	% error
37.1	36.7	0.4	1.0
146.1	153.4	-7.3	-5.0
82.4	79.6	2.8	3.4
60.8	60.9	0.0	-0.1
125.5	111.7	13.8	11.0
67.6	57.9	9.7	14.3
50.6	44.3	6.3	12.5
45.8	45.4	0.4	1.0
36.3	33.8	2.5	6.9
142.7	141.1	1.6	1.1
80.0	73.2	6.8	8.5
59.9	56.0	3.9	6.5
124.9	105.9	19.0	15.2
65.3	54.9	10.4	15.9
49.4	42.0	7.4	14.9
44.9	43.0	1.9	4.2
35.4	32.5	3.0	8.3
143.5	135.7	7.8	5.5
77.5	70.4	7.1	9.1
57.8	53.8	4.0	6.9
122.4	102.7	19.8	16.2
64.2	53.3	10.9	17.0
48.3	40.7	7.6	15.8
43.7	41.7	2.0	4.5
87.5	82.8	4.6	5.3
108.6	102.4	6.3	5.8
85.3	76.2	9.1	10.7
104.4	97.1	7.3	7.0
83.4	73.2	10.1	12.1
102.9	94.1	8.8	8.5

Table 4.31. Comparison of experimental and MLR predicted values of flow stress, σ of Alloy-*E*.

Experimental flow stress (MPa)	Predicted flow stress (MPa)	Error (MPa)	% error
105.8	99.9	5.9	5.6
43.3	45.7	-2.4	-5.5
138.8	180.4	-41.6	-30.0
87.5	96.0	-8.5	-9.7
84.9	74.2	10.7	12.6
168.4	129.3	39.2	23.3
79.1	68.8	10.3	13.0
60.2	53.2	7.1	11.8
109.3	118.8	-9.5	-8.7
60.1	54.4	5.7	9.6
100.9	88.0	12.9	12.8
41.7	40.3	1.4	3.4
133.3	158.9	-25.6	-19.2
85.0	84.6	0.4	0.5
80.4	65.4	15.0	18.7
168.7	119.3	49.4	29.3
76.1	63.5	12.5	16.5
57.8	49.1	8.7	15.1
106.2	109.7	-3.4	-3.2
58.3	50.2	8.1	14.0
97.9	83.0	15.0	15.3
40.6	38.0	2.7	6.5
133.1	149.8	-16.7	-12.6
81.9	79.8	2.1	2.6
78.4	61.6	16.7	21.4
168.1	113.9	54.2	32.3
74.4	60.6	13.8	18.6
56.6	46.8	9.8	17.2
106.1	104.6	1.5	1.4
57.1	47.9	9.2	16.1

Table 4.32. Comparison of experimental and MLR predicted values of flow stress, σ of Alloy-*F*.

Experimental flow stress (MPa)	Predicted flow stress (MPa)	Error (MPa)	% error
107.1	85.9	21.2	19.8
41.0	40.2	0.9	2.1
133.7	158.1	-24.3	-18.2
94.4	85.7	8.7	9.2
61.3	66.7	-5.4	-8.7
118.6	111.7	6.9	5.8
64.1	60.5	3.6	5.6
61.8	47.1	14.7	23.8
101.1	106.6	-5.5	-5.5
49.2	49.9	-0.7	-1.4
103.7	77.4	26.3	25.3
38.5	36.2	2.3	6.0
134.4	142.5	-8.1	-6.0
91.0	77.2	13.8	15.2
61.4	60.1	1.3	2.1
118.1	104.6	13.5	11.4
63.6	56.7	6.9	10.9
59.0	44.1	14.9	25.2
97.2	99.9	-2.7	-2.8
48.2	46.7	1.5	3.0
100.6	73.8	26.8	26.7
36.0	34.5	1.5	4.1
132.5	135.8	-3.3	-2.5
88.4	73.6	14.8	16.8
59.4	57.3	2.2	3.7
116.3	100.7	15.6	13.4
62.4	54.6	7.8	12.5
57.5	42.5	15.0	26.1
95.7	96.1	-0.4	-0.4
47.6	45.0	2.6	5.5

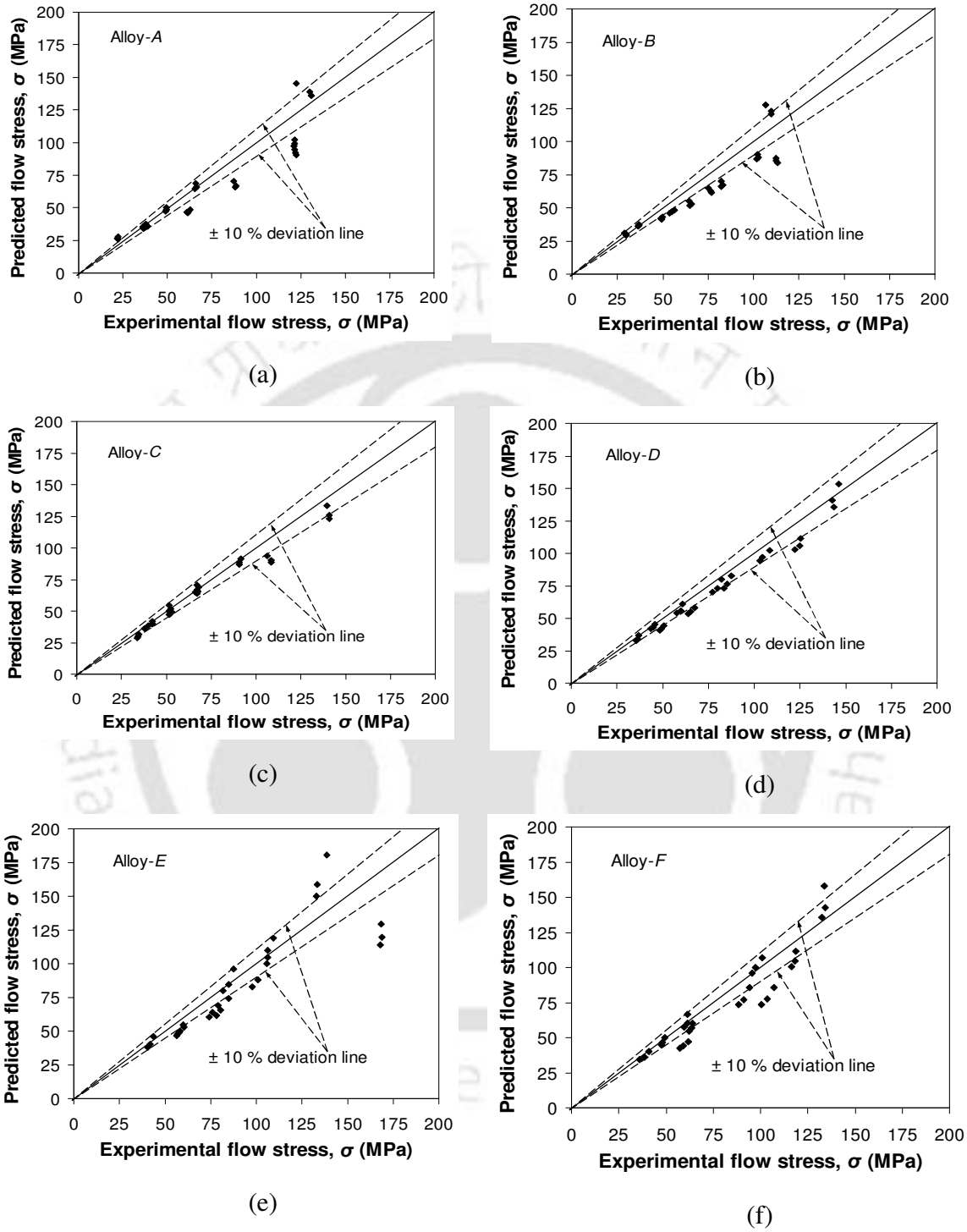

Fig.4.53. Variation of MLR predicted flow stress with experimental flow stress for (a) Alloy-*A* (b) Alloy-*B* (c) Alloy-*C* (d) Alloy-*D* (e) Alloy-*E*, and (f) Alloy-*F*

4.7 Prediction of flow stress by Artificial Neural Network modeling

In order to obtain better prediction of σ during hot deformation of the investigated alloys, artificial neural network (ANN) modeling was carried out. This was based on the concept that

$$\sigma = \sigma (\varepsilon, \dot{\varepsilon}, T) \tag{2.19}$$

The deformation flow stress σ can be predicted by ANN, which is a data driven model, if sufficient number of data sets is available. A typical ANN architecture consists of three layers, *viz.* an input layer consisting of three neurons representing the external parameters of $\varepsilon, \dot{\varepsilon}$ and T, a hidden layer containing n numbers of neurons and an output layer with one neuron representing σ. Appropriate values for the weight and bias of the network architecture for each alloy was arrived at by training the network using several data sets.

During the modeling, ε, T and $\ln(\dot{\varepsilon})$ values were transformed to lie within the range of 0.1 and 0.9. When the neural network is trained by minimizing the sum-squared error, the order of the error is independent of the magnitude of the target value. Therefore, it is likely that percentage error may be more in the case of target values of lower magnitude. In order that the percentage error in prediction is more or less uniform for low and high values of σ, normalized values of $\ln(\sigma)$ were taken as the output layer of the network. The output was then operated by exponential function to get the values of σ. Justification for this can be given as follows [ROBI2003]: Let us consider that for a particular flow stress value of σ^*, the predicted value is given by $\ln(\sigma^*+e)$ where e is the error in prediction. The corresponding predicted σ value is then obtained by taking the exponential of the $\ln(\sigma^*+e)$ term. Therefore, the percentage error in prediction is expressed as [ROBI2003]:

$$\frac{\exp(\ln\sigma^*+e)-\sigma^*}{\sigma^*} = \exp(e)-1 \tag{4.13}$$

Since this percentage error is a function solely of e and is independent of σ^*, the error is expected to be fairly uniform irrespective of the target value.

Modeling of σ for various combinations of $\varepsilon, \dot{\varepsilon}$ and T was carried out by ANN. For each alloy, a total number of 120 input-output data sets (for combination of 4 true strain

rates, 5 deformation temperatures and 6 true strain values considered) were obtained from the compression tests. It was decided to use 48 data sets for the network training, 36 data sets for the testing and 18 data sets from the remaining, for validation purpose. The validation data sets were not used earlier for the testing or training purposes. Both training and testing of the network was carried our independently. A number of numerical trials were carried out with single hidden layer neural network. The *tansig, logsig* and *purelin* transfer functions were tried with while simultaneously varying the number of neurons in the hidden layer, in order to arrive at the best network architecture and processing function for each of the investigated alloys. The RMS functional error used as a measure of performance, can be expressed as

$$RMS_{err}^{f} = \sqrt{\frac{\sum(\sigma - \sigma^*)^2}{n\sigma^2}} \qquad (4.14)$$

where σ is the experimental value and σ^* is the predicted value of the flow stress. Both training and testing errors were calculated separately. Effective error for training and testing data is given by:

$$\text{Effective error} = \text{max. of } [RMS_{err}^{f} \text{ of training data, } RMS_{err}^{f} \text{ of testing data}] \qquad (4.15)$$

The sum squared training error goal for σ was fixed at 0.00001. After a number of trials with various initial weights and biases, the best neural network architecture was frozen for which (i) functional RMS error was minimum, (ii) minimum number of data sets has a deviation error of 10 %, (iii) maximum deviation during testing and training is within 20 %, and (iv) minimum variation in RMS functional error during training and testing. Table 4.33 shows the details of the ANN architecture for all the investigated alloys.

Once the network was frozen, it was required to establish the confidence in the network architecture for the prediction of σ. Therefore, the trained network was used for prediction of σ using the 18 validation data sets. Table 4.34 gives the values of maximum absolute error, maximum percentage error and RMS error calculated for all the alloys during training, testing and validation stages separately. Table 4.35 to Table 4.40 give the detailed experimental and predicted σ values along with the associated errors for validation data sets of all the alloys studied.

Figures 4.54, 4.55 and 4.56 show the plots of experimental *vs*. predicted values of σ for all the alloys during training, testing and validation, respectively. Dashed lines representing the boundaries of ±10 % deviations are also shown in the figures. Figures reveal that most of the points lie very close to the line of prefect prediction. During validation, it was observed that 18, 17, 17, 16, 17 and 15 out of 18 data points fall within ±10 % deviation line for Alloy-*A,* Alloy-*B,* Alloy-*C,* Alloy-*D,* Alloy-*E,* and Alloy-*F,* respectively. Though the percentage errors in prediction were comparatively high for the few data with deviations above ±10 %, their absolute errors were low, especially in the cases of low σ.

The observation that 0, 1, 1, 2, 1 and 3 out of 18 data points fall outside ±10 % deviation line for Alloy-*A,* Alloy-*B,* Alloy-*C,* Alloy-*D,* Alloy-*E,* and Alloy-*F,* respectively shows very good prediction of σ by ANN modeling. This observation together with the low RMS errors registered, highlight the superior prediction capability of this technique.

Table 4.33. Best fit network architectures for the investigated alloys.

Sample ID	Hidden neurons	1st transfer function	2nd transfer function
Alloy-*A*	9	*tansig*	*purelin*
Alloy-*B*	8	*logsig*	*purelin*
Alloy-*C*	3	*logsig*	*purelin*
Alloy-*D*	5	*tansig*	*purelin*
Alloy-*E*	9	*tansig*	*purelin*
Alloy-*F*	8	*logsig*	*purelin*

Table 4.34. Maximum absolute error, maximum percentage error and RMS error obtained for the alloys during training, testing and validation

Alloy ID	Training			Testing			Validation		
	Max. Error (MPa)	Max. % Error	RMS Error (MPa)	Max. Error (MPa)	Max. % Error	RMS Error (MPa)	Max. Error (MPa)	Max. % Error	RMS Error (MPa)
Alloy-*A*	1.63	2.00	0.45	-6.00	-9.61	2.78	4.69	7.61	2.37
Alloy-*B*	2.24	4.13	0.95	-14.91	14.90	6.11	-8.96	12.86	3.41
Alloy-*C*	2.81	-5.84	1.22	9.58	11.82	4.26	13.54	10.25	6.70
Alloy-*D*	-3.69	3.65	1.27	8.89	-4.59	2.50	13.98	11.19	5.40
Alloy-*E*	2.69	-6.26	0.83	-9.01	-19.59	4.68	-5.39	-13.75	2.11
Alloy-*F*	-4.45	-4.67	1.27	-11.48	-15.18	4.98	17.05	23.17	8.32

Table 4.35. Comparison of experimental and predicted values of flow stress, σ for the validation test of Alloy-*A*

Experimental flow stress (MPa)	Predicted flow stress (MPa)	Error (MPa)	Percentage error (%)
61.27	57.17	4.10	6.70
120.07	120.93	-0.86	-0.71
49.31	46.84	2.47	5.01
36.22	36.88	-0.66	-1.83
121.47	119.59	1.88	1.55
66.03	68.33	-2.30	-3.48
61.61	56.92	4.69	7.61
121.71	123.47	-1.76	-1.44
49.66	50.39	-0.73	-1.46
36.43	36.91	-0.48	-1.32
121.87	122.88	-1.01	-0.83
65.86	67.81	-1.95	-2.97
61.25	57.96	3.29	5.37
121.71	124.76	-3.05	-2.51
49.13	49.21	-0.08	-0.16
36.52	35.86	0.66	1.80
122.42	118.38	4.04	3.30
65.09	64.44	0.65	1.00

Table 4.36. Comparison of experimental and predicted values of flow stress, σ for the validation test of Alloy-*B*

Experimental flow stress (MPa)	Predicted flow stress (MPa)	Error (MPa)	Percentage error (%)
56.09	56.01	0.08	0.14
64.5	59.71	4.79	7.43
111.82	120.78	-8.96	-8.02
24.96	26.69	-1.73	-6.94
102.19	105.86	-3.67	-3.59
83.61	89.37	-5.76	-6.89
76.57	78.90	-2.33	-3.05
55.84	55.54	0.30	0.53
65.91	67.90	-1.99	-3.02
36.91	36.95	-0.04	-0.12
102.58	101.04	1.54	1.50
49.07	42.76	6.31	12.86
77.1	77.80	-0.70	-0.91
54.82	55.33	-0.51	-0.93
65.08	64.73	0.35	0.54
21.82	20.55	1.27	5.80
101.9	100.48	1.42	1.39
83.02	82.44	0.58	0.70

Table 4.37. Comparison of experimental and predicted values of flow stress, σ for the validation test of Alloy-*C*

Experimental flow stress (MPa)	Predicted flow stress (MPa)	Error (MPa)	Percentage error (%)
52.74	48.91	3.83	7.26
139.47	131.74	7.73	5.55
51.76	54.79	-3.03	-5.85
39.84	39.45	0.39	0.99
141.14	131.10	10.04	7.12
67.98	69.76	-1.78	-2.63
52.62	47.67	4.95	9.40
140.76	130.41	10.35	7.35
52.59	53.29	-0.70	-1.33
38.76	38.69	0.07	0.19
140.95	129.68	11.27	7.99
66.69	67.90	-1.21	-1.81
51.8	46.49	5.31	10.26
141.06	128.91	12.15	8.61
51.35	51.85	-0.50	-0.97
37.76	37.90	-0.14	-0.38
141.65	128.11	13.54	9.56
65.83	66.06	-0.23	-0.35

Table 4.38. Comparison of experimental and predicted values of flow stress, σ for the validation test of Alloy-*D*

Experimental flow stress (MPa)	Predicted flow stress (MPa)	Error (MPa)	Percentage error (%)
67.49	68.53	-1.04	-1.55
46.43	45.40	1.03	2.23
124.38	122.10	2.28	1.83
34.28	32.10	2.18	6.35
125.49	116.18	9.31	7.42
82.11	80.81	1.30	1.59
66.37	64.59	1.78	2.69
45.48	44.25	1.23	2.70
118.87	122.21	-3.34	-2.81
30.87	28.46	2.41	7.80
124.89	110.91	13.98	11.20
78.67	79.58	-0.91	-1.15
64.66	63.67	0.99	1.53
44.17	42.76	1.41	3.19
112.92	118.69	-5.77	-5.11
27.66	26.81	0.85	3.06
122.44	109.42	13.02	10.64
76.62	75.70	0.92	1.20

Table 4.39. Comparison of experimental and predicted values of flow stress, σ for the validation test of Alloy-*E*

Experimental flow stress (MPa)	Predicted flow stress (MPa)	Error (MPa)	Percentage error (%)
105.82	106.40	-0.58	-0.55
84.9	84.99	-0.09	-0.10
143.72	142.78	0.94	0.65
60.24	60.14	0.10	0.17
109.31	109.29	0.02	0.02
86.67	87.07	-0.40	-0.46
100.85	101.61	-0.76	-0.76
77.27	82.66	-5.39	-6.97
80.36	80.60	-0.24	-0.29
33.38	37.97	-4.59	-13.75
106.24	107.12	-0.88	-0.83
83.5	85.61	-2.11	-2.53
97.93	97.63	0.30	0.30
78.35	77.99	0.36	0.46
136.71	137.18	-0.47	-0.34
56.59	56.38	0.21	0.38
106.13	104.95	1.18	1.11
82.18	86.73	-4.55	-5.54

Table 4.40. Comparison of experimental and predicted values of flow stress, σ for the validation test of Alloy-*F*

Experimental flow stress (MPa)	Predicted flow stress (MPa)	Error (MPa)	Percentage error (%)
107.07	102.16	4.91	4.58
118.61	130.34	-11.73	-9.89
49.23	50.34	-1.11	-2.26
118.61	128.46	-9.85	-8.31
103.7	103.60	0.10	0.09
118.1	129.07	-10.97	-9.29
48.19	48.99	-0.80	-1.66
117.25	128.43	-11.18	-9.53
100.58	102.25	-1.67	-1.66
116.26	125.30	-9.04	-7.78
88.03	79.39	8.64	9.81
47.59	48.94	-1.35	-2.83
45.45	34.92	10.53	23.17
135.5	136.57	-1.07	-0.79
93.5	76.45	17.05	18.23
30.5	29.59	0.91	2.98
89.52	76.29	13.23	14.77
24.5	25.15	-0.65	-2.66

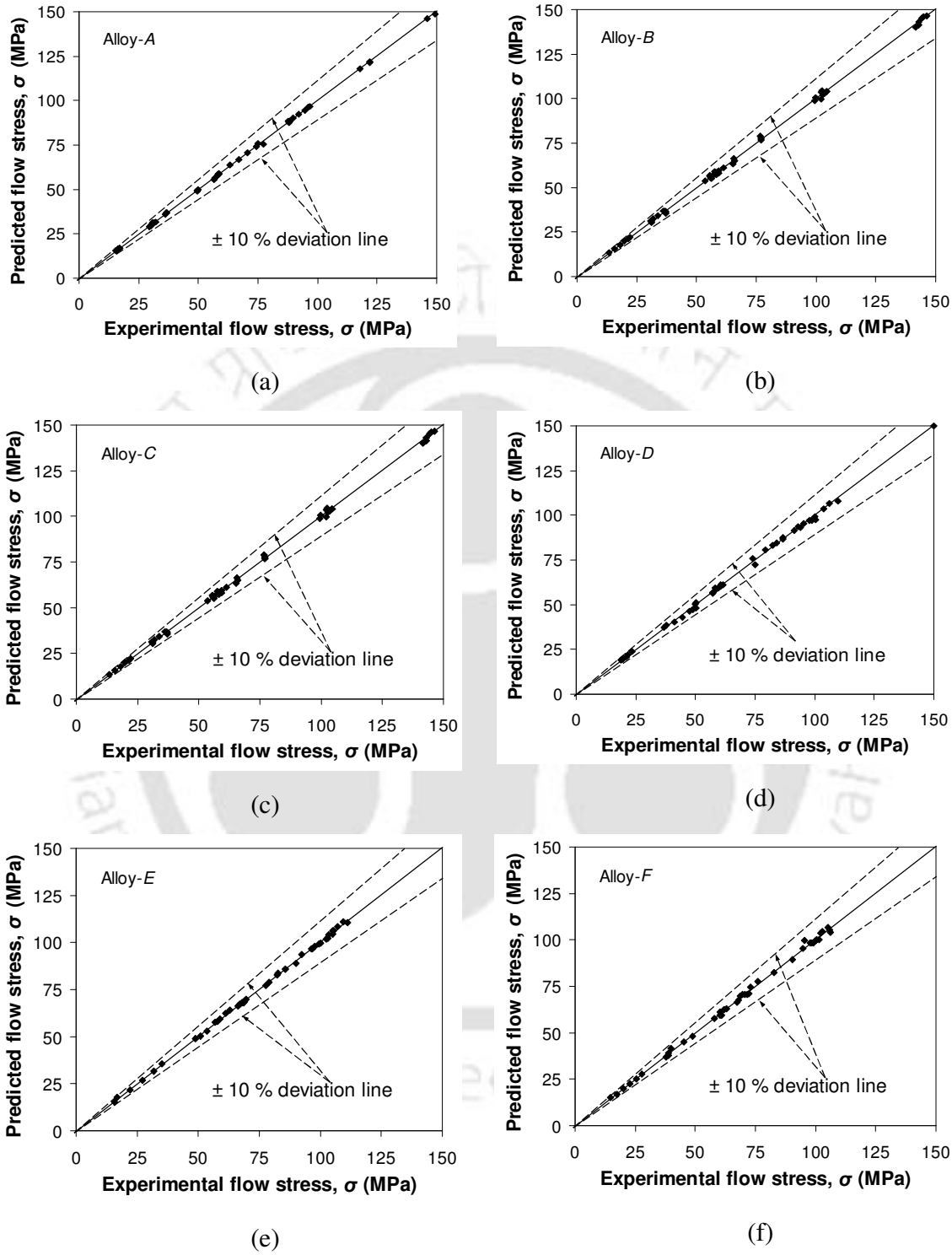

Fig.4.54. Variation of predicted flow stress with experimental flow stress for the training data set of (a) Alloy-*A* (b) Alloy-*B* (c) Alloy-*C* (d) Alloy-*D* (e) Alloy-*E*, and (f) Alloy-*F*

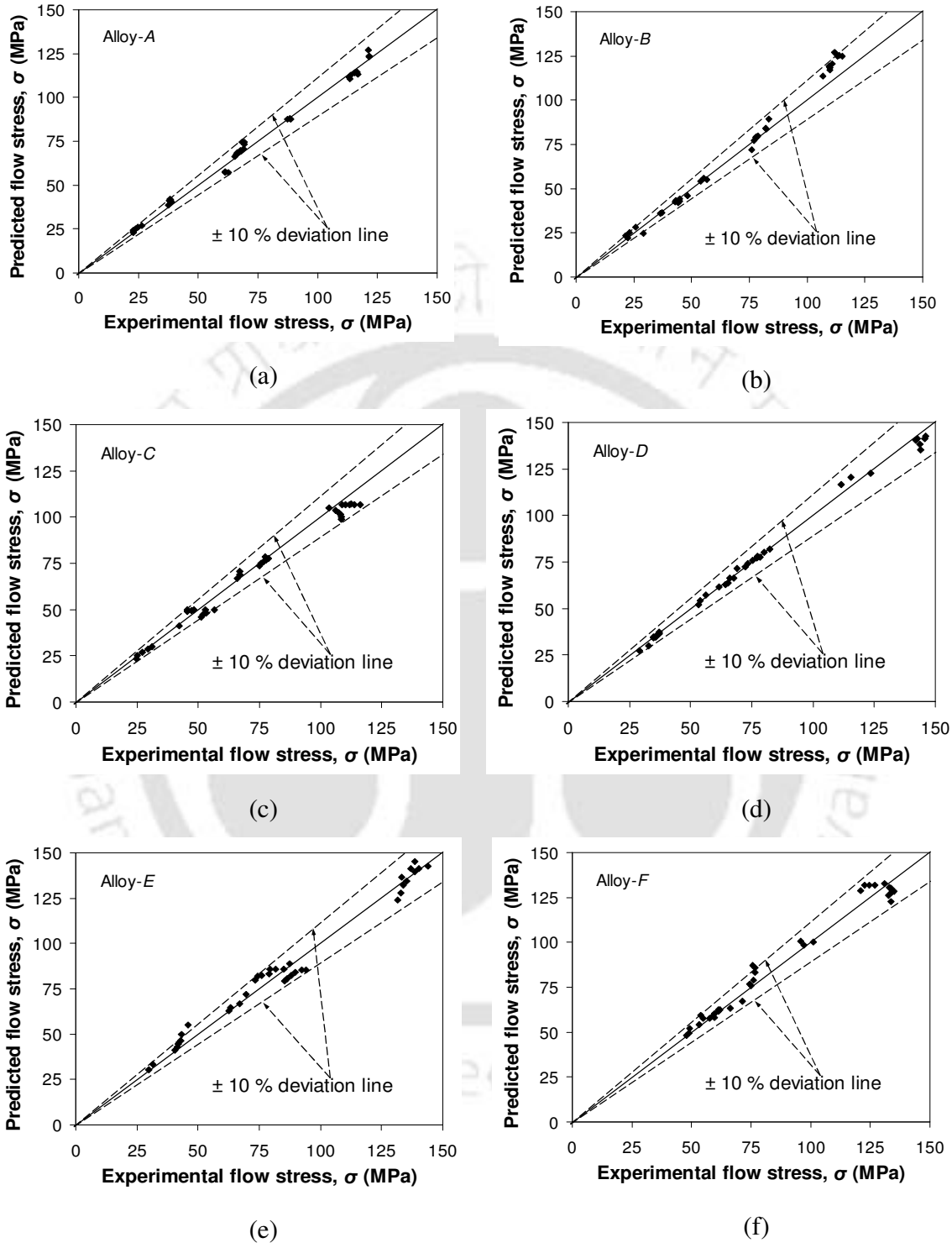

Fig.4.55. Variation of predicted flow stress with experimental flow stress for the testing data set of (a) Alloy-*A* (b) Alloy-*B* (c) Alloy-*C* (d) Alloy-*D* (e) Alloy-*E*, and (f) Alloy-*F*

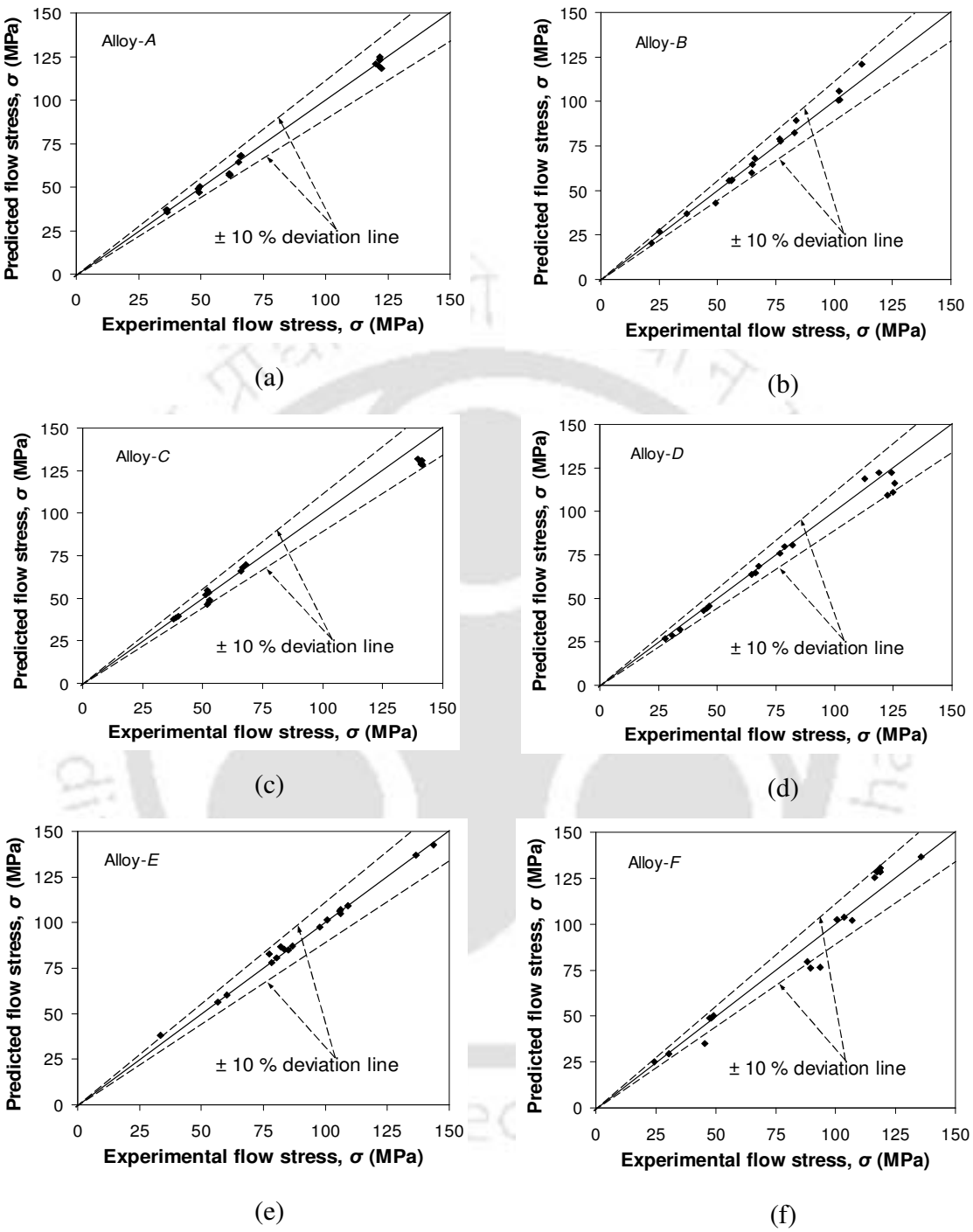

Fig.4.56. Variation of predicted flow stress with experimental flow stress for the validation data set of (a) Alloy-*A* (b) Alloy-*B* (c) Alloy-*C* (d) Alloy-*D* (e) Alloy-*E*, and (f) Alloy-*F*

4.8 Generation of processing maps for hot workability

The ANN modeling carried out provided very good prediction of flow stress, σ ($\varepsilon, \dot{\varepsilon}, T$) in the process domain of investigation. The σ thus predicted can be used to generate processing maps, which would delineate the process domains for safe working of the alloys. Since this would be of considerable importance for industrial processing of these alloys, processing maps were generated using these data.

Workability is an important parameter in mechanical working of materials which is dependent on externally controllable variables like strain (ε), strain rate ($\dot{\varepsilon}$), deformation temperature (T) and the inherent flow characteristics of the material. In power dissipation map, efficiency of power dissipation is contour plotted as a function of T and $\dot{\varepsilon}$ at a particular ε value. Instability map separates out the regions of stable and unstable flow. A processing map is an explicit representation of the response of the material to the imposed process parameters. Processing map is obtained by the superimposition of instability map on the power dissipation efficiency map. The detailed procedure of generating the processing maps by DMM has already been discussed in section 2.5.3. The following sections deal with the processing maps generated for Al–Cu–Mg alloys taken up for study in this thesis work.

Processing maps

The first step towards the generation of hot deformation processing map is to obtain the power dissipation map. The basis for obtaining the power dissipation map is the Dynamic Materials Model (DMM) [PRAS1984, PRAS1997]. According to this model, the workpiece is considered as a dissipater part of the processing system. Considering the plot σ *vs.* $\dot{\varepsilon}$ (Figure 2.8) at constant T and ε, the total power absorbed by the workpiece during plastic flow can be considered as the sum of the dissipater content, G (representing the temperature rise), and the dissipater co-content J (representing the dissipation through metallurgical processes). The dissipater element can be considered to be nonlinear, dynamic, and/or irreversible. The factor that partitions power between G and J is the strain-

rate sensitivity (m) of flow stress. The efficiency of power dissipation for a nonlinear dissipater may be expressed as a dimensionless parameter η (*c.f.* Section 2.5.3), which is the relative rate of entropy production during hot deformation characterizing the dissipative microstructure under different T and $\dot{\varepsilon}$ conditions. In other words, η as a function of T and $\dot{\varepsilon}$ represents the power dissipation characteristic of the workpiece material.

Fig. 4.57 (a) and (d) show the contour plots for the efficiency of power dissipation and m at various T and $\dot{\varepsilon}$ for Alloy-*A* after deforming it to a ε of 0.2. The following observations are evident from these figures: (i) At T < ~370 ºC and for $\dot{\varepsilon} \geq 0.1$ s^{-1}, η < 20 %. In this regime, the values of m are very low. (ii) At T above 450 ºC, η > 20 % for the entire range of $\dot{\varepsilon}$. The $m \leq 0.3$ in this region. (iii) For $\dot{\varepsilon}$ in the range of 0.001-0.01 s^{-1} and T < 420 ºC, η > 30 %. The m > 0.10 in this regime. (iv) η > 45 % at T < 425 ºC and $\dot{\varepsilon}$ < 0.003 s^{-1}. The η contours in this domain are generally widely spaced. In this regime, m > 0.20. (v) The region covering temperatures between 400 and 500 ºC and $\dot{\varepsilon}$ > 0.03 s^{-1} represents the regime of dynamic recrystallization (DRX). (vi) For $\dot{\varepsilon}$ < 0.03 s^{-1} and T between 400 and 480 ºC, values of η and m show an increasing trend with decreasing $\dot{\varepsilon}$. This could probably correspond to the wedge cracking regime. DRX generally occurs at regimes where efficiency of power dissipation is between 50-55 % for low stacking fault energy (SFE) materials like Al. From the above observations, it is also evident that the efficiency of power dissipation is higher for the regime having higher m values.

Figure 4.57 (b) and (c) show the iso-efficiency plots obtained for Alloy-*A* when deformed to ε of 0.4 and 0.6, respectively. As is evident from the figures, the features described above are essentially unchanged though the values of power dissipation efficiency increased with increase in ε from 0.2 to 0.6. The contour plots of m obtained for ε of 0.4 and 0.6 show the same trend in η variation as observed in the case of samples strained at 0.2. Since the trend remains the same (although the values of m estimated were different), these plots are not included here for discussion.

Iso-efficiency plots obtained for Alloy-*A* to Alloy-*F*, after deformation to a ε of 0.2 are shown in Figure 4.58 (a) to (f), respectively. For the alloy with 0.02 wt.% Sn, the efficiency of power dissipation is found to vary in the range of 15 to 40 % in the entire

process domain studied. The η contours are more widely spaced for Alloys *B*, *C* and *D*, as compared to that of the base alloy (Alloy-*A*). Upon increasing the Sn content to 0.04 wt.% [Figure 4.58(c)], the iso-efficiency contours in the regime of T < ~420 ºC and $\dot{\varepsilon}$ > 0.01 s^{-1}, are found to be more widely spaced for which η is in the range of 10-25 %. However, the contour plots are found to be closely spaced in the range where T > 420 ºC and $\dot{\varepsilon}$ < 0.01 s^{-1}. The maximum value of the efficiency of power dissipation reaches 65 % in this regime.

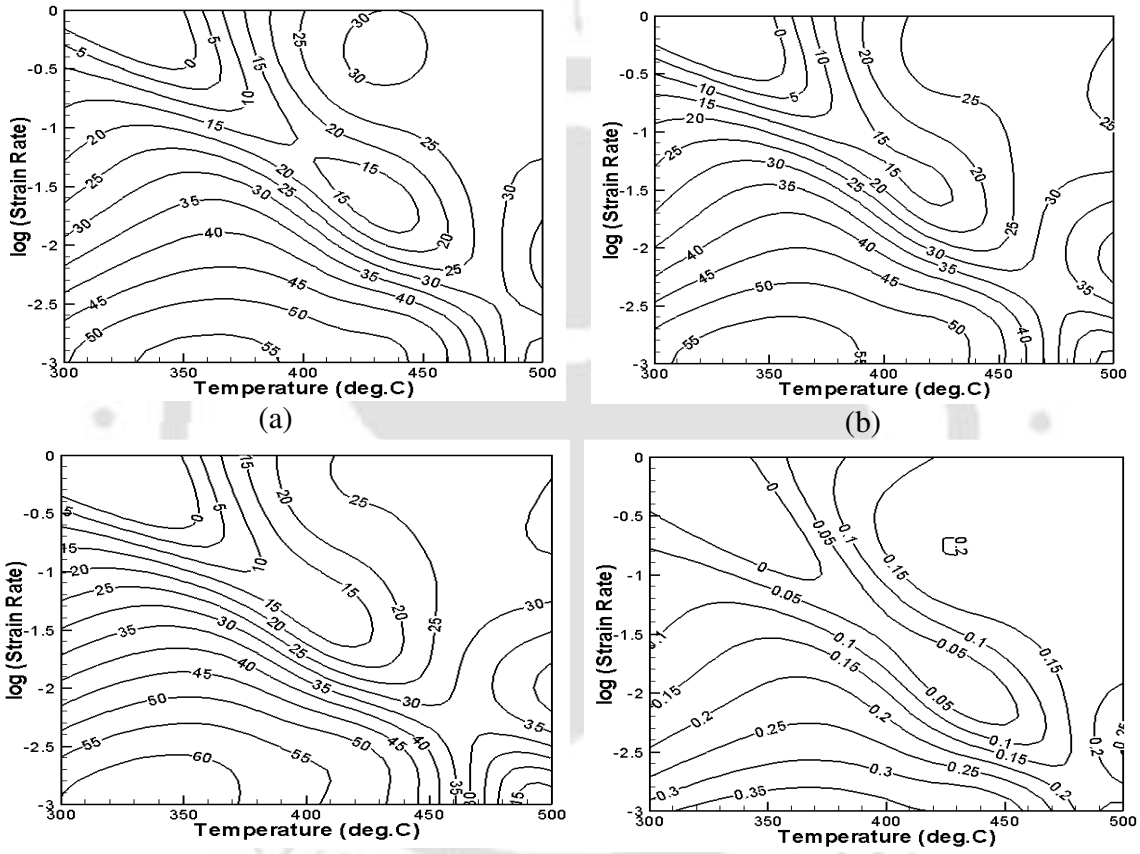

Fig.4.57. Contour plots of η at ε of (a) 0.2 (b) 0.4 (c) 0.6 and (d) contour plot of m at ε of 0.2 for Alloy-*A*

Figure 4.58(d) indicates that the contour plots are more widely spaced for Alloy-*D*. However in the $\dot{\varepsilon}$ range 0.158 to 0.025 s^{-1}, the power dissipation efficiency contours are closely spaced compared to other regions of the plot. The efficiency of power dissipation increases continuously with increase in T and/or decrease in $\dot{\varepsilon}$. The maximum efficiency of

power dissipation obtained is 35 % in the case of Alloy-*D*. This high value is observed at $T > 480$ ºC and for $0.0032\ s^{-1} < \dot{\varepsilon} < 0.01\ s^{-1}$.

Figures 4.58 (e) and (f) indicate that the power dissipation efficiency contour lines are very closely spaced for Alloys-*E* and *F* (which have Sn contents above 0.06 wt.%). A region with widely spaced contour lines is observed near the top left corner of the figure. Inspection of the plots obtained at ε of 0.4 and 0.6 indicates similar features, though the values of the power dissipation efficiency increased with increase in ε. The maximum value of power dissipation efficiency of 70 % nearly spanning the entire range of temperatures studied is obtained for Alloy-*F* at $\dot{\varepsilon} < 0.0015\ s^{-1}$. It is also observed that the contour lines obtained for this alloy is closely spaced for $\dot{\varepsilon} < 0.03\ s^{-1}$, whereas, these contour line spacings widen up in the range $0.03 < \dot{\varepsilon} < 0.3\ s^{-1}$.

A convenient way of locating the optimum processing conditions is to locate regimes where the iso-efficiency contours are widely spaced. Several dynamic metallurgical processes contribute to power dissipation during the hot deformation of materials. These metallurgical processes have characteristic ranges of efficiencies of power dissipation. Depending upon the microstructure, some of these processes may occur simultaneously and/or interactively. When more than one major power dissipation processes having different characteristics occur simultaneously, the energy of dissipation of one of the processes can become equal to that of another. In such a case, the value of *J* will reach its maximum (J_{max}). The most favourable conditions for processing of materials are generally those which provide the highest *J* dissipated in the most efficient fashion. These *J* values generally lie within the safe regions, though there are exceptions such as when flow instability results in internal defects during deformation *etc*. The regime indicating metallurgical instability during plastic flow can be obtained by the instability condition given by the expression (*c.f.* Eq. 2.35)

$$\xi\left(\dot{\varepsilon}\right) = \frac{\partial \ln\left(\frac{m}{m+1}\right)}{\partial \ln \dot{\varepsilon}} + m \leq 0 \qquad (2.35)$$

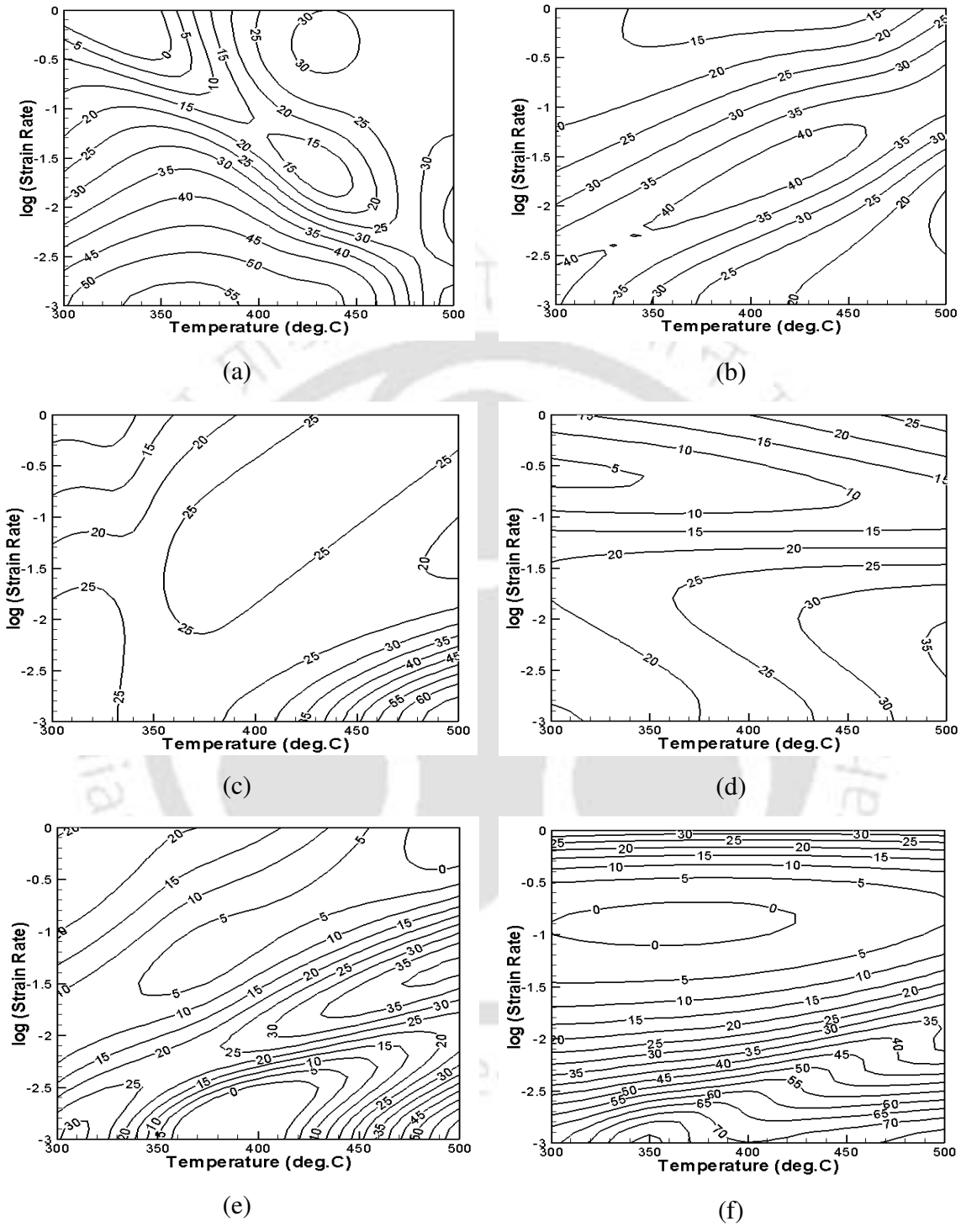

Fig.4.58. Contour plots of η at ε of 0.2 for (a) Alloy-*A* (b) Alloy-*B* (c) Alloy-*C* (d) Alloy-*D* (e) Alloy-*E*, and (f) Alloy-*F*

Figure 4.59 (a), (b) and (c) shows instability maps for Alloy-*A* at ε values of 0.2, 0.4, and 0.6, respectively. The regions in the $\dot{\varepsilon}$ -*T* plane, where the values of parameter ζ are negative are indicative of unstable metal flow. The flow instabilities arise due to irreversible changes in the microstructure during plastic flow of the material (*c.f.* section 2.5.3). The figures indicate the regions where the contour lines of efficiency of power dissipation are closely spaced as the regime of plastic instability (shaded regions in the figures). The two regions where the material can be considered as safe for hot working are the (i) region existing at high *T* (> ~420 ºC) for $\dot{\varepsilon}$ > 0.03 s^{-1}, and (ii) low $\dot{\varepsilon}$ region (< 0.0019 s^{-1}) existing at all temperatures studied. Though the nature of these two stable regions remains almost similar, stability is obtained in the case of the latter even for a slight increase in $\dot{\varepsilon}$. It can also be noted from Figures 4.59 (a), (b) and (c), that the Alloy-*A* has four regions of instability at a ε = 0.6. With increase in ε, the instability region at the highest temperature (500 ºC at a ε = 0.2) increases in size and spreads to lower temperatures (say, up to 460 ºC at a ε = 0.6).

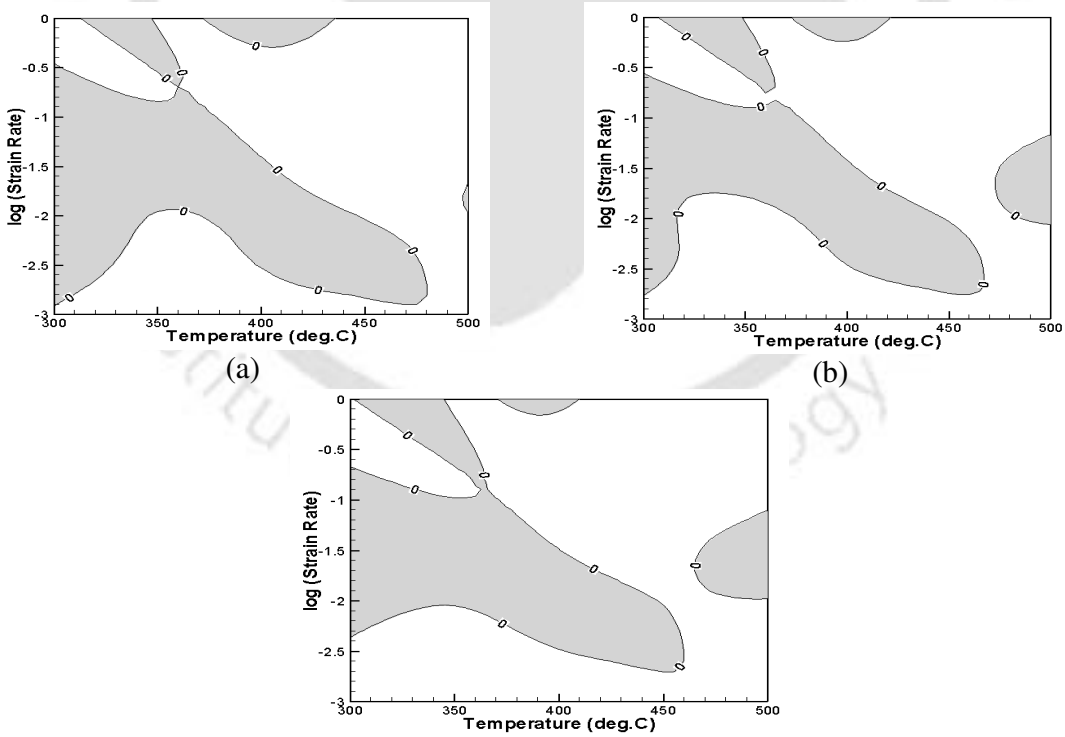

Fig.4.59. Instability (shaded) regions for Alloy-*A* at ε of (a) 0.2 (b) 0.4 and (c) 0.6

The instability maps after deforming to a ε of 0.6 for all the alloys under investigation are shown in Figure 4.60 (a) to (f). With the addition of Sn, the regimes of instability are found to be different compared to that of Alloy-*A*. With Sn addition, the instability regions are found to lie almost parallel to the iso-efficiency lines. This statement can be understood if one makes a comparison with Figure 4.58. The maximum in the efficiency of power dissipation is obtained where *m* has its maximum value. The process parameters at which the efficiency of power dissipation is maximum for the different alloys are listed in Table 4.41 along with the corresponding *m* values.

Table 4.41. Process parameters for maximum power dissipation efficiency values of the alloys

Sample ID	Maximum power dissipation efficiency (%)	Strain-rate ranges (s^{-1})	Temperature ranges (°C)	Maximum strain rate sensitivity factor (*m*)
Alloy-*A*	60	0.001-0.003	300-400	0.45
Alloy-*B*	60	0.001-0.003	450-500	0.45
Alloy-*C*	65	0.001-0.003	430-500	0.50
Alloy-*D*	40	0.001-0.01	440-500	0.25
Alloy-*E*	70	0.001-0.003	450-500	0.35
Alloy-*F*	70	0.001-0.003	300-500	0.50

Figure 4.61(a) shows the processing map for Alloy-*A* for a ε of 0.6, obtained by superimposing Figure 4.57(c) and Figure 4.59(c). The shaded areas in the figure indicate unstable regions. The figure indicates lower values of efficiency of power dissipation for unstable regions as compared to the adjacent stable regions. The stable regions of Alloy-*A* after a ε of 0.6 are observed at: (i) high *T* (> 400 ºC) and for $0.02 < \dot{\varepsilon} < 1$ s^{-1} and (ii) very low $\dot{\varepsilon}$ (< 0.003 s^{-1}) at all temperatures studied. From the processing map, it can be concluded that Alloy-*A* can be safely deformed under the above mentioned conditions. As mentioned at the beginning of this chapter, power dissipation map can provide insight on various dissipative microstructures during the hot working process. In the domain of DRX, the maximum efficiency of power dissipation is generally about 50-55 % for high stacking fault energy materials like Al [PRAS1997].

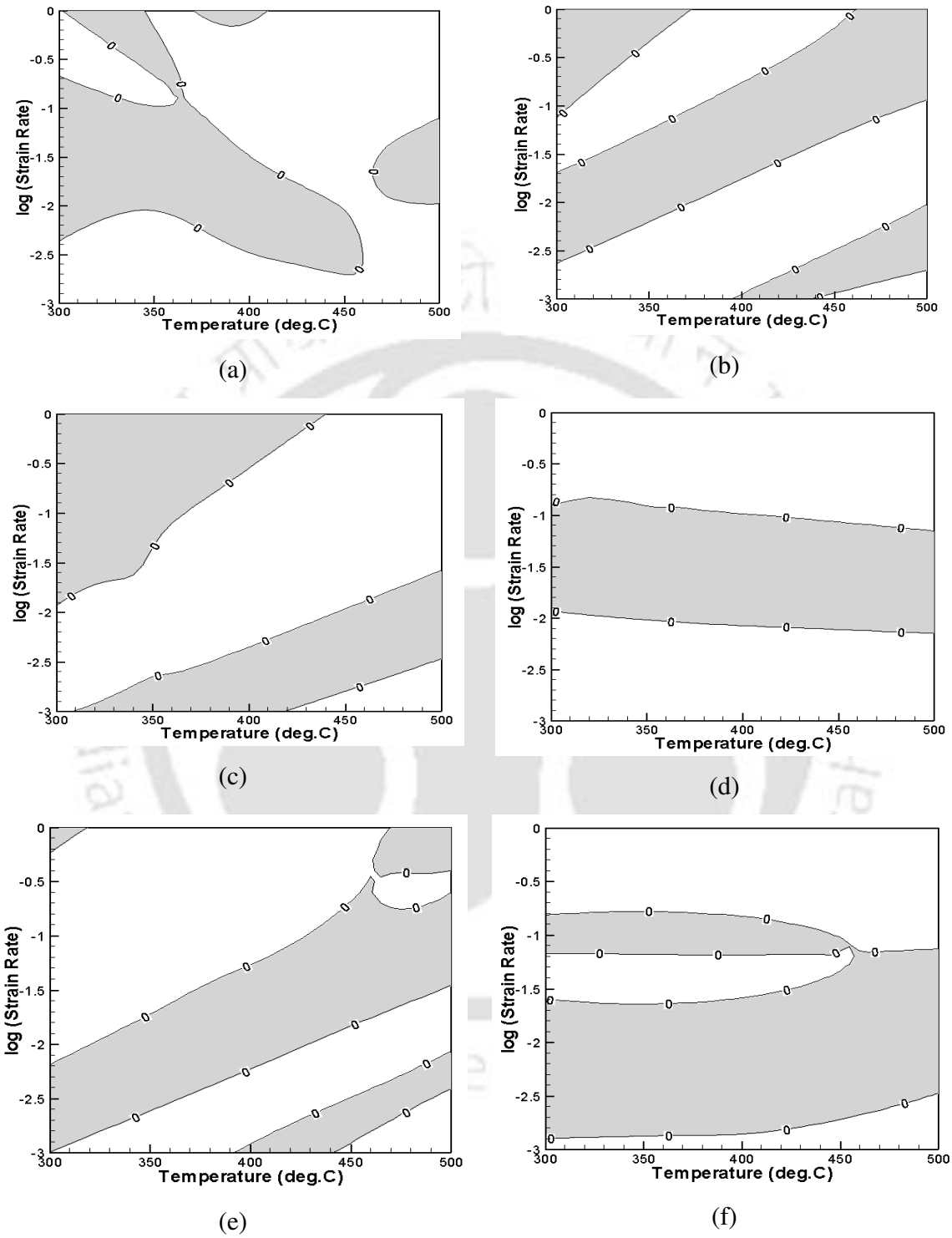

Fig.4.60. Instability regions at ε of 0.6 for (a) Alloy-*A* (b) Alloy-*B* (c) Alloy-*C* (d) Alloy-*D* (e) Alloy-*E* and (f) Alloy-*F*

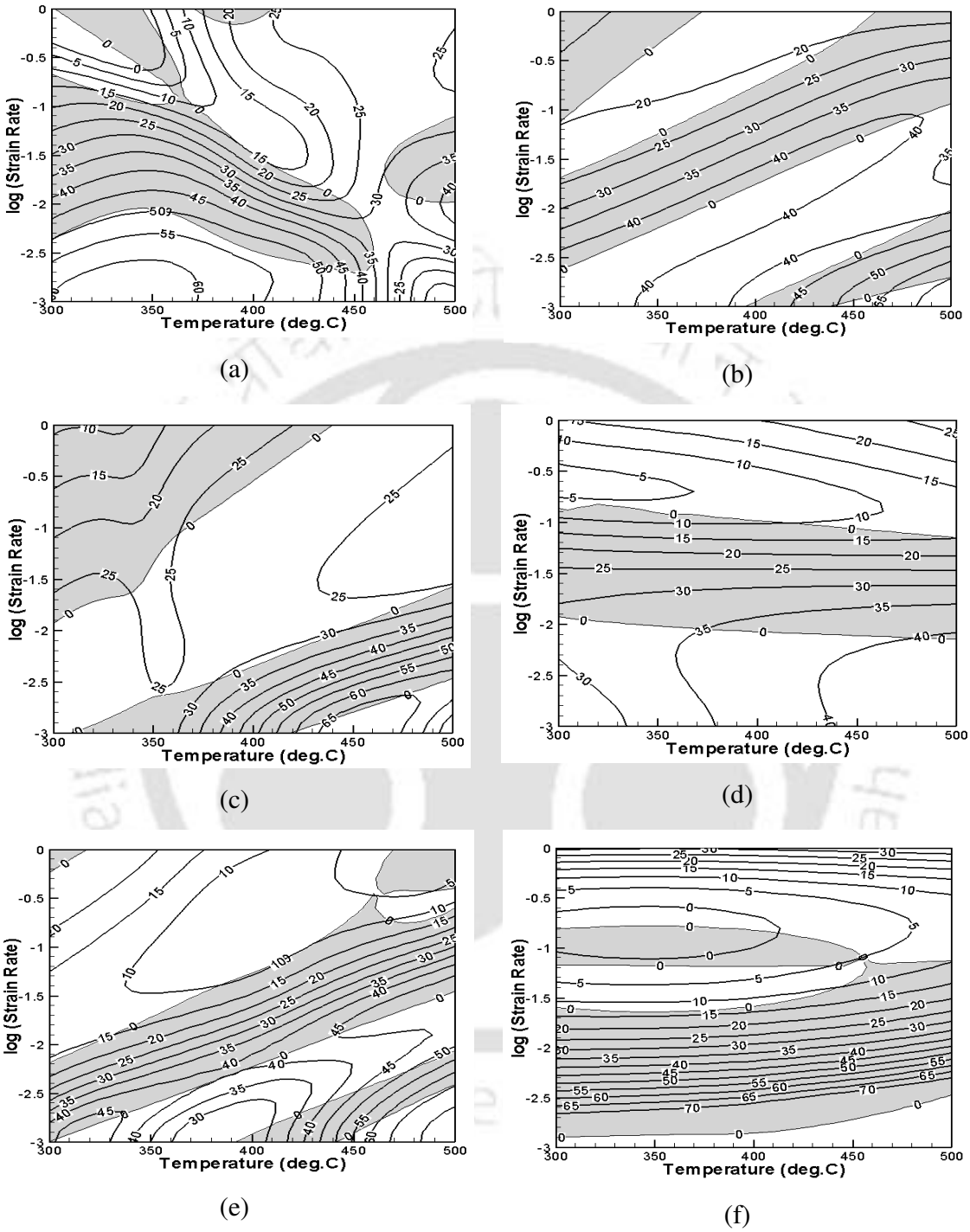

Fig.4.61. Processing maps at ε of 0.6 for (a) Alloy-*A* (b) Alloy-*B* (c) Alloy-*C* (d) Alloy-*D* (e) Alloy-*E* and (f) Alloy-*F*

To study the dissipative microstructures formed during hot deformation, the microstructures of specimens deformed to a ε of 0.6 under various $\dot{\varepsilon}$ and T were observed using optical microscope. Optical micrographs of Alloy-*A* in the undeformed condition reveal second phases at the grain boundary regions (Figure 4.62 *cf.* section 4.2.2). Figure 4.63 reveals features of flow localization/shear band formation at 300 ºC and $\dot{\varepsilon}$ of 0.01 s^{-1}. Since this region falls in the region of major instability [the large shaded region in Figure 4.61(a)], this shaded region can be considered as an instability region due to shear band formation. The microstructure of the sample deformed at T = 300 ºC and $\dot{\varepsilon}$ of 0.001 s^{-1}, shown in Figure 4.64(a), reveals small recrystallized grains at the grain boundaries, which indicates partial recrystallization or the initiation of the recrystallization process. The grain boundaries are irregular in shape. Nucleation of fine crystals in the matrix during hot deformation, especially at the grain boundary regions is the typical feature of DRX. DRX is a beneficial process [GAND1982] in hot deformation since it not only gives a stable flow and good workability to the material by simultaneously softening it, but also reconstitutes the microstructure [STYL1994]. The material can be deformed safely at very low $\dot{\varepsilon}$ ($\dot{\varepsilon}$ < 0.003 s^{-1}) and T in the range 300-470 ºC. Though the processing map for Alloy-*A* [Figure 4.61(a)] indicates the regime of high T and very low $\dot{\varepsilon}$ as safe, the iso-efficiency contour plots indicate steep gradient in the efficiency values. Though, the microstructure of the alloy deformed at 500 ºC at a $\dot{\varepsilon}$ of 0.001 s^{-1} reveals DRX [Figure 4.64(b)], wedge cracks are also observed along the grain boundaries (Figure 4.65). This clearly shows initiation of defects in this regime under the above process conditions. Hence, deformation of Alloy-*A* at 0.001 < $\dot{\varepsilon}$ < 0.003 and T range of 470-500 ºC is to be avoided. The above studies indicate that the safe regimes for hot working of Alloy-*A* are (i) very low $\dot{\varepsilon}$ (< 0.003 s^{-1}) at T < 450 ºC and, (ii) high T (> 400 ºC) and 0.02 < $\dot{\varepsilon}$ < 1 s^{-1}. Microscopic investigation of the sample processed in the latter domain did not reveal any microstructural instability, which prompted the above conclusion. DRX in Al alloys has been shown to occur at lower $\dot{\varepsilon}$ and is sensitive to the impurity content [PRAS1997].

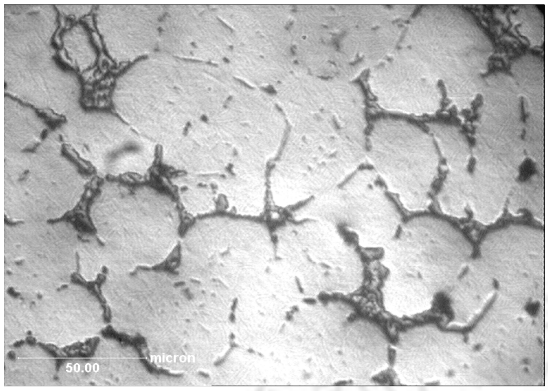

Fig.4.62. Optical micrograph of Alloy-*A* in undeformed condition

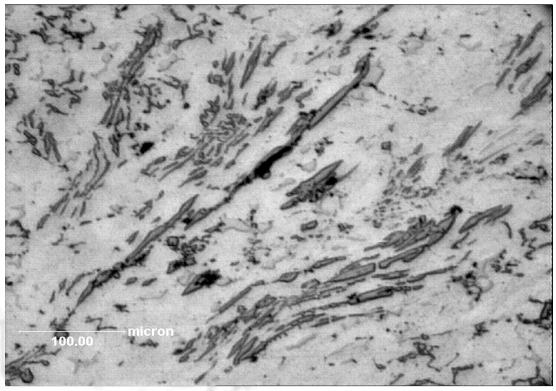

Fig.4.63. Optical micrograph showing shear band formation in Alloy-*A* deformed at $\dot{\varepsilon}$ = 0.01 s^{-1}, T = 300°C

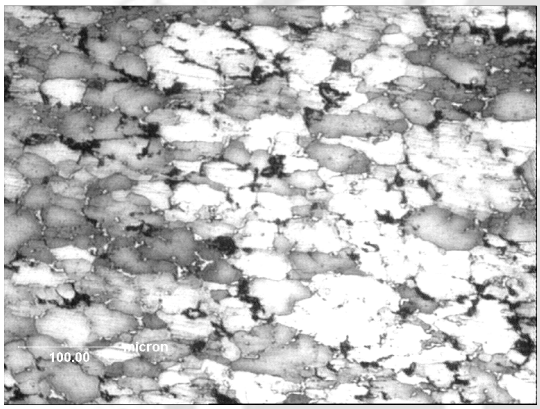

(a)

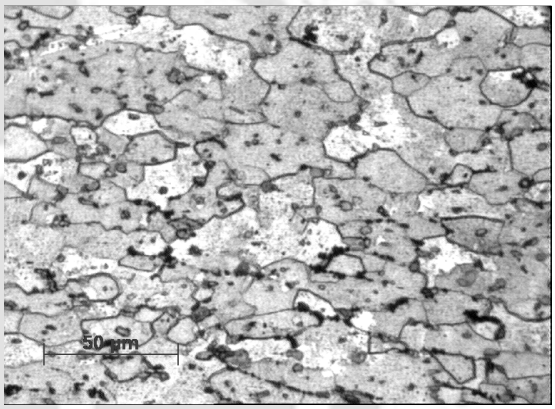

(b)

Fig.4.64. Optical micrographs showing DRX in Alloy-*A* deformed at (a) $\dot{\varepsilon}$ = 0.001 s^{-1}, T = 300°C and (b) $\dot{\varepsilon}$ = 0.001 s^{-1}, T = 500°C

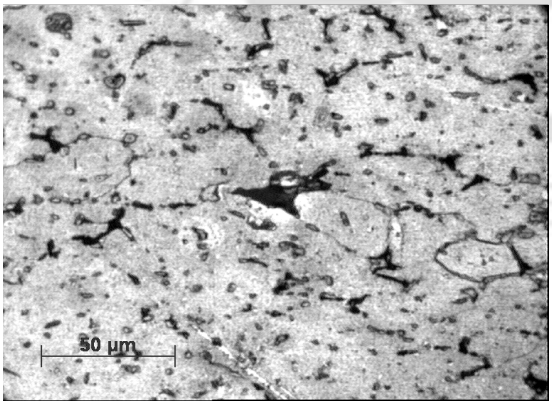

(a)

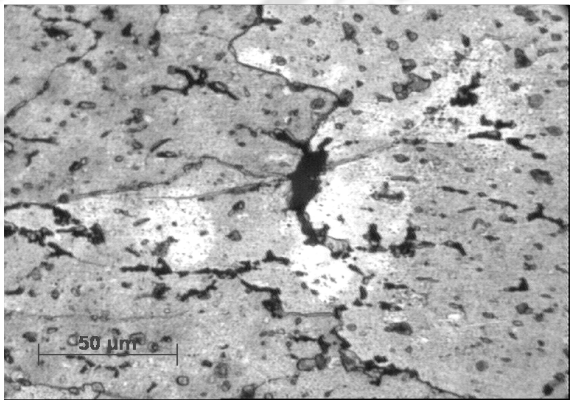

(b)

Fig.4.65. Optical micrographs showing wedge cracking in Alloy-*A* deformed at $\dot{\varepsilon}$ = 0.001 s^{-1}, T = 500°C

The processing maps obtained for Alloys-*B* to *F* are shown in Figures 4.61 (b) to (f), respectively. In all the figures, flow instability regimes are represented by shaded regions. Figure 4.61(b) indicates the three regimes of flow instability lying diagonally in the figure for Alloy-*B*. The major flow instability for Alloy-*B* is due to matrix cracking as revealed by the optical micrograph (Figure 4.66) of the sample deformed at a $\dot{\varepsilon}$ of 0.1 s^{-1} and *T* = 450 ºC. The inter-crystalline cracking along grain boundaries due to the formation of low melting phases or segregation of alloying elements at grain boundaries can occur when deformed at high $\dot{\varepsilon}$ and high *T* [PRAS1997]. Figure 4.61(c) indicates the two regimes of flow instability for Alloy-*C*: *viz.*, one at high $\dot{\varepsilon}$ and low *T* and the other towards low $\dot{\varepsilon}$ and high *T*. Optical micrograph of the sample strained at a $\dot{\varepsilon}$ of 0.1 s^{-1} and 350 ºC [Figure 4.67(a)] reveals shear band formation indicating the flow instability at low *T* and high $\dot{\varepsilon}$ due to this phenomenon. Figure 4.67(b) confirms flow instability at the other regime (which is at $\dot{\varepsilon}$ of 0.01 s^{-1} and 500 ºC) due to matrix cracking. Optical microscopic investigation of the undeformed Alloy-*D* indicated the presence of second phases (Figure 4.68). Figure 4.61(d) shows only one regime of flow instability for the alloy containing 0.06 wt.% Sn (Alloy-*D*). The flow instability regime corresponds to $\dot{\varepsilon}$ in the range of 0.1 to 0.01 s^{-1} and *T* in the range of 300-500 ºC. Microscopic studies of the samples deformed at 350 ºC and $\dot{\varepsilon}$ of 0.1 s^{-1} (Figure 4.69) as well as at 500 ºC and $\dot{\varepsilon}$ of 0.01 s^{-1} (Figure 4.70), reveal adiabatic shear band formation as the major metallurgical phenomenon causing flow instability in this regime. The metallurgical phenomenon occurring at $\dot{\varepsilon} < 0.01$ s^{-1} in the entire range of temperatures studied has been identified as DRX (Figure 4.71). Though this region is marked as a stable region in the instability map (at 500 ºC and $\dot{\varepsilon}$ of 1.0 s^{-1}), microscopic investigation revealed features of matrix cracking at high $\dot{\varepsilon}$ and *T* (Figure 4.72). The crack path was found to be along the grain boundaries. The volume fraction of the second phase with script morphology at the grain boundary was maximum in Alloy-*D* (*cf.* section 4.2.3). From these observations, one can conclude that the safe processing zone for Alloy-*D* is at low $\dot{\varepsilon}$ (< 0.01 s^{-1}) for the entire range of temperatures studied.

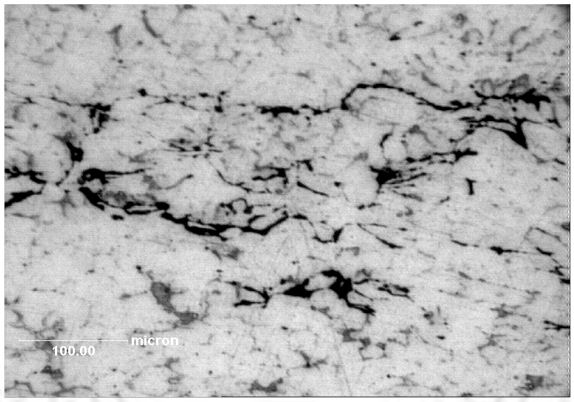

Fig.4.66. Optical micrograph showing matrix cracking in Alloy-*B* deformed at $\dot{\varepsilon}$ = 0.1 s^{-1}, *T* = 450°C

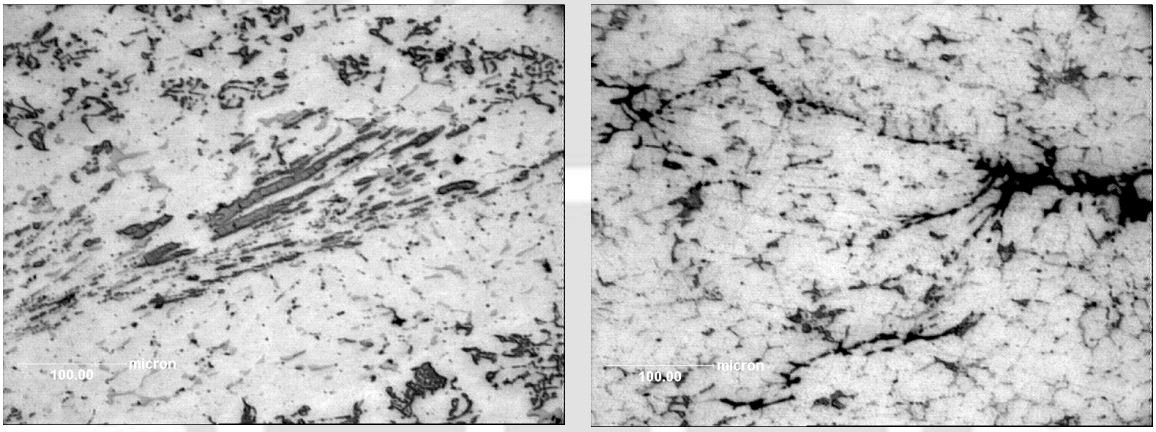

(a) (b)

Fig.4.67. Optical micrographs in Alloy-*C* showing (a) shear band formation when deformed at $\dot{\varepsilon}$ = 0.1 s^{-1}, *T* = 350°C (b) matrix cracking when deformed at $\dot{\varepsilon}$ = 0.01 s^{-1}, *T* = 500°C

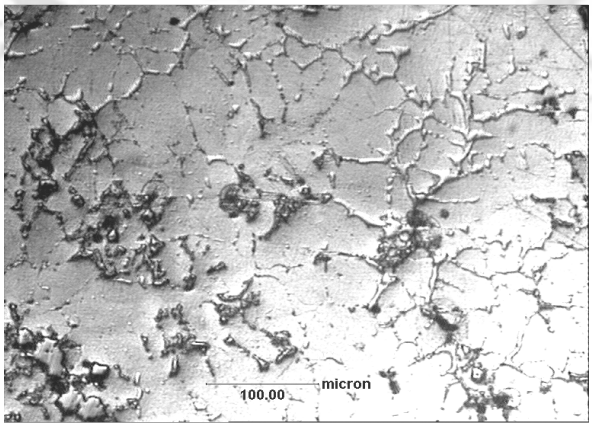

Fig.4.68. Optical micrograph of Alloy-*D* in undeformed condition

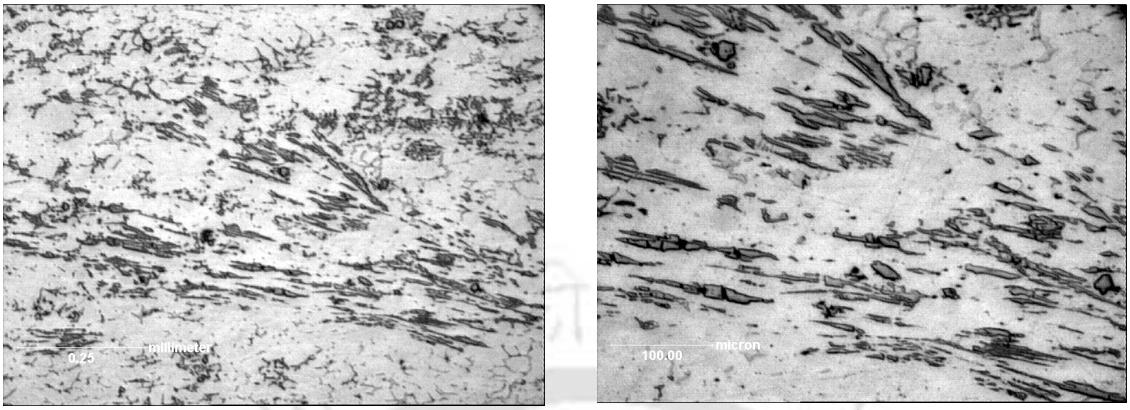

(a) (b)

Fig.4.69. (a) low magnification and (b) high magnification optical micrographs showing shear band formation in Alloy-*D* deformed at $\dot{\varepsilon}$ = 0.1 s^{-1}, *T* = 350°C

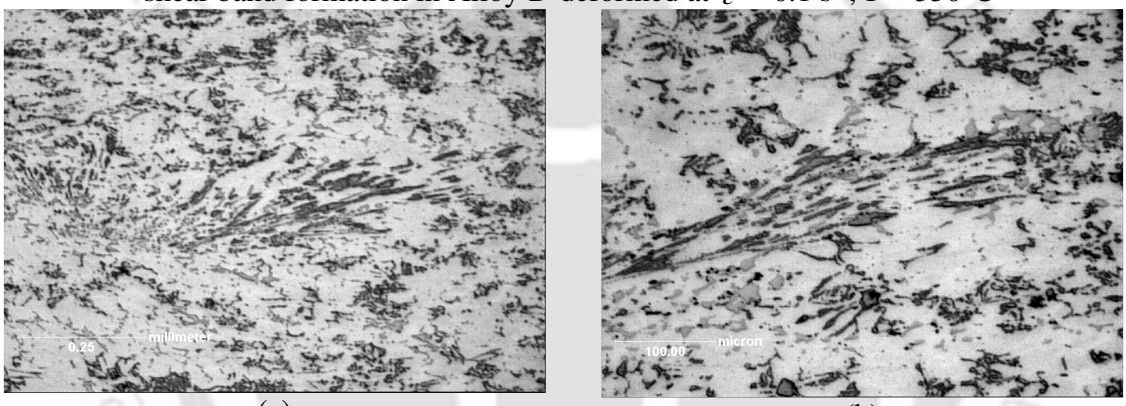

(a) (b)

Fig.4.70. (a) low magnification and (b) high magnification optical micrographs showing shear band formation in Alloy-*D* deformed at $\dot{\varepsilon}$ = 0.01 s^{-1}, *T* = 500°C

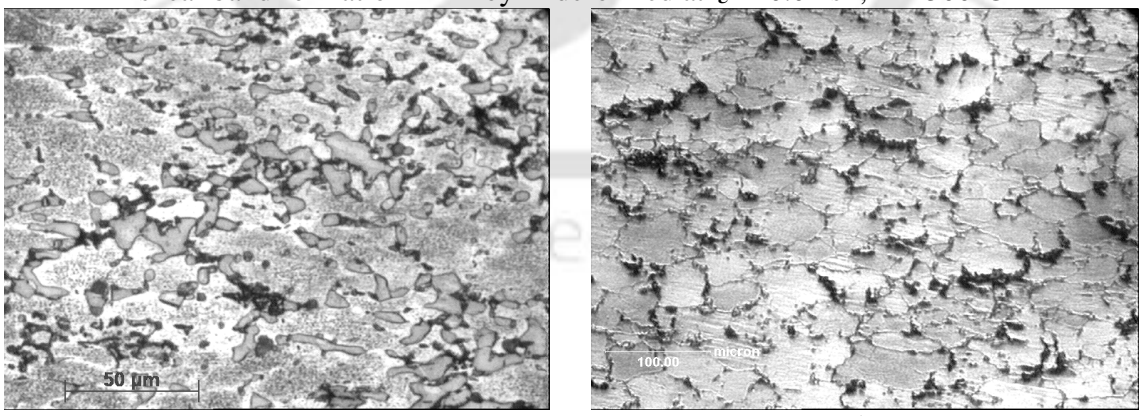

(a) (b)

Fig.4.71. Optical micrographs showing DRX in Alloy-*D* deformed at (a) $\dot{\varepsilon}$ = 0.001 s^{-1}, *T* = 300°C and (b) $\dot{\varepsilon}$ = 0.001 s^{-1}, *T* = 500°C

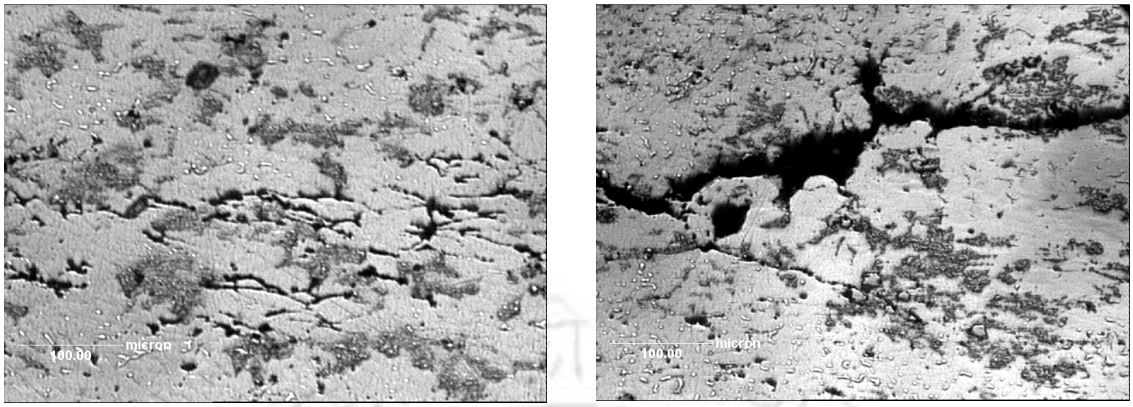

(a) (b)

Fig.4.72. (a) low magnification and (b) high magnification optical micrographs showing matrix cracking in Alloy-*D* deformed at $\dot{\varepsilon}$ = 1.0 s^{-1}, *T* = 500°C

Processing map for Alloy-*E* is shown in Figure 4.61(e). The map shows two regions of instability (shaded regions) lying parallel to the iso-efficiency contours. The major instability region with η lying between 10 to 40 % has closely spaced contour lines. Optical micrographs of the samples deformed at 400 ºC and at $\dot{\varepsilon}$ = 0.01 s^{-1} reveal shear bands indicating the major source of instability in this region (Figure 4.73).

Processing map for Alloy-*F* is shown in Figure 4.61(f). Figure 4.74 shows the microstructure of the undeformed sample. The instability zones as observed in the processing map of Alloy-*F* are predominantly due to inter-crystalline cracking as shown by the optical micrographs (Figure 4.75 and 4.76). The metallurgical phenomenon occurring at $\dot{\varepsilon}$ < 0.003 s^{-1} in the entire range of temperatures studied was however identified as DRX (Figure 4.77), which is similar to the cases of Alloy-*A* and Alloy-*D*.

A comparison of the processing maps developed shows the following common features:

1. The instability regions are found to lie parallel to the iso-efficiency contour lines.
2. With the addition of Sn up to 0.06 wt.%, the proportion of stable/unstable region increases. With further increase in Sn content, the stable regions decrease in size drastically.
3. Shear band formation and inter-crystalline cracking are the two major sources of flow instability in these alloys.

4. Most stable regions are characterized by DRX.
5. High efficiency of power dissipation values need not always correspond to most stable regions in these alloys. This might be due to the fact that more than one process is responsible for the flow instability in these alloys.

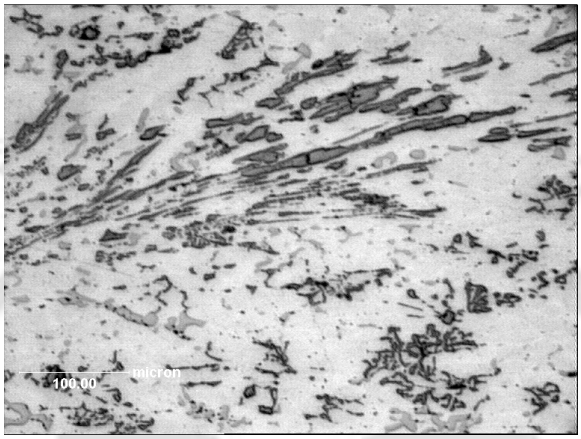

Fig.4.73. Optical micrograph showing shear band formation in Alloy-*E* deformed at $\dot{\varepsilon} = 0.01\ s^{-1}$, $T = 400°C$

Fig.4.74. Optical micrograph of Alloy-*F* in undeformed condition

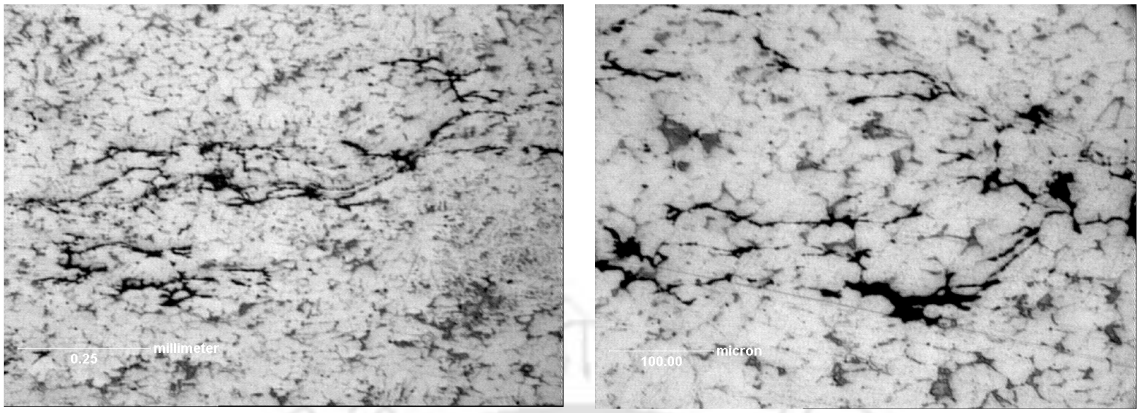

(a) (b)

Fig.4.75. (a) low magnification and (b) high magnification optical micrographs showing matrix cracking in Alloy-*F* deformed at $\dot{\varepsilon}$ = 0.01 s^{-1}, *T* = 300°C

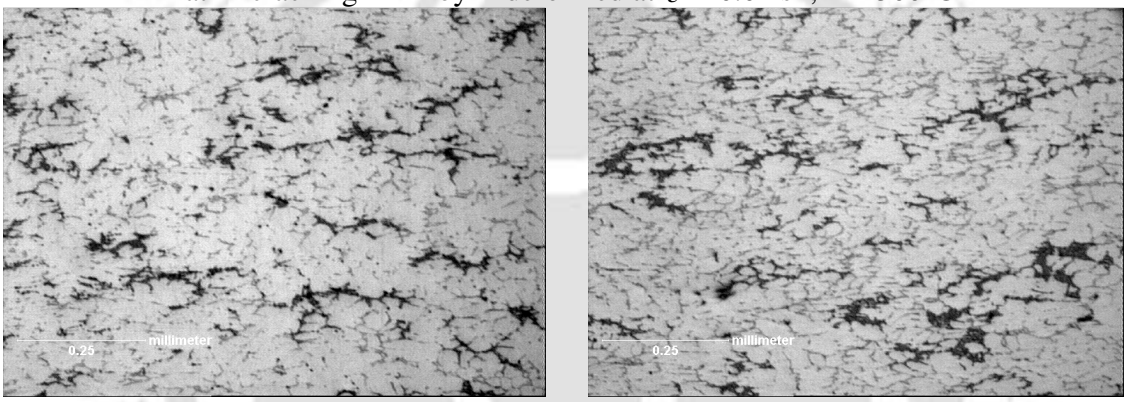

(a) (b)

Fig.4.76. Optical micrographs showing mild matrix cracking initiations in Alloy-*F* deformed at (a) $\dot{\varepsilon}$ = 0.01 s^{-1}, *T* = 500°C (a) $\dot{\varepsilon}$ = 0.1 s^{-1}, *T* = 400°C

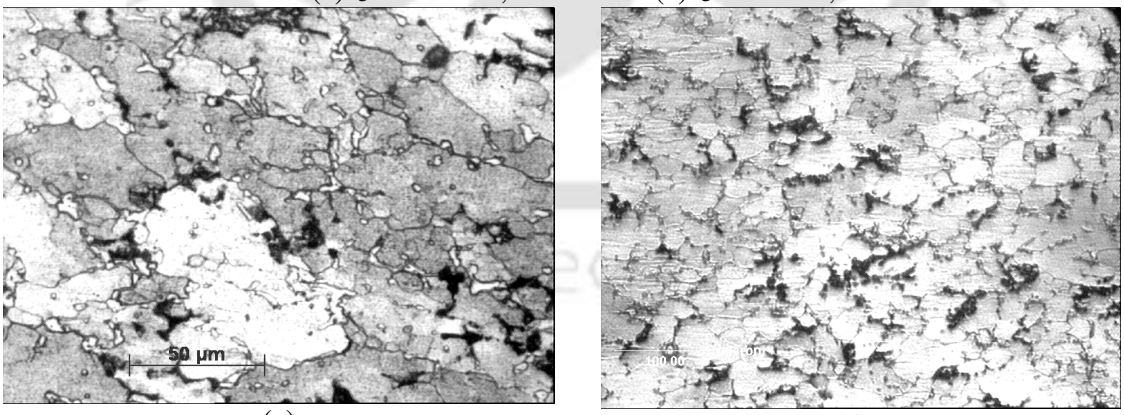

(a) (b)

Fig.4.77. Optical micrographs showing DRX in Alloy-*F* deformed at (a) $\dot{\varepsilon}$ = 0.001 s^{-1}, *T* = 300°C and (b) $\dot{\varepsilon}$ = 0.001 s^{-1}, *T* = 500°C

Chapter 5

Conclusion and Scope of Future Work

5.1 Conclusions

The experimental and modeling studies performed on the Al-Cu-Mg alloys with and without trace amounts of Sn were presented in the earlier chapters. These investigations revealed the importance of heat-treatment of the cast alloys by a systematic study of their microstructure and properties. Hot deformation studies backed by modeling work were used to understand the workability of these alloys and the metallurgical changes in these alloys during deformation. These investigations yielded many new findings, which are highlighted below:

- Al-Cu-Mg alloys with nominal composition of Al–5.9wt.%Cu–0.5wt.%Mg containing $0 \leq Sn \leq 0.1$ wt.% have been prepared by casting route.
- Two types of second phases were observed at the grain boundary regions of the as-cast alloy matrix. One was $CuAl_2$ and the other was Al–Cu–Si–Fe–Mn phase having script morphology. The cast alloys revealed only $CuAl_2$ phase with platelet morphology after solutionizing and water quenching.
- Observation of the as-cast alloy microstructure showed that microalloying with Sn did not have any influence on the grain refinement of the Al alloy.
- The grain size of the heat-treated alloy increased with increase in Sn content up to 0.06 wt.% .
- Hardness, YS and UTS of all the alloys increased with increase in Sn wt.% up to 0.06. Further addition of Sn resulted in a decrease in these properties.

- The rolled and homogenized alloys exhibited higher strength and ductility than the cast and homogenized alloys. Hence, rolling is suggested for obtaining these alloys with better mechanical properties.
- Peak hardness in all the alloys was attained when aged at 170 °C for 24 h. Addition of trace amounts of Sn had no influence on the peak ageing time.
- Precipitation hardening of rolled alloys yielded the highest strength for these alloys. The reduction in ductility observed in the peak aged alloys can be improved by optimizing the ageing conditions.
- DSC studies showed two exothermic peaks in the temperature region of 200 ºC to 300 ºC in the case of the base alloy (Alloy-*A*) and the alloy with 0.06 wt.% Sn (Alloy-*D*). For all the other alloys, only one exothermic peak could be observed in this temperature range. Activation energy analysis indicated that Sn addition up to 0.06 wt.% had no adverse effect on the precipitation process.
- XRD patterns of the heat treated alloys showed evidence of $CuAl_2$ precipitation in the Al matrix.
- Flow softening after attaining the peak stress was observed in all the alloys at low strain rate of 0.001 s^{-1}.
- Undulations were observed in the flow curves in all alloys microalloyed with Sn at low strain rates and lower temperatures.
- The solved constitutive equations for high temperature deformation yielded good prediction of peak flow stress for all the alloys within the range of temperatures and strain rates investigated. The peak flow stress during deformation were predicted using the above lay within an RMS error of 8.53, 9.33, 4.84, 3.24, 10.03 and 7.52 for alloys *A*-*F*, respectively.
- The activation energy for hot deformation for alloys with Sn wt.% > 0.04 was higher than that of the base alloy. The high activation energy of the alloys with Sn wt.% > 0.04 shows that these alloys are relatively difficult to deform, in spite of the fact that these alloys exhibit better mechanical properties.
- Flow stresses at various strains, strain rates and temperatures during hot deformation were predicted for all these alloys using MLR analysis and ANN modeling for the first

time. While the former gave reasonably good predictions, the latter's excellent predictions revealed its superiority over the former in the current predictions.

- Processing maps were generated for all the investigated alloys. To the best of the investigator's knowledge, this is the first attempt made to develop such maps for microalloyed Al alloys.
- The power dissipation efficiency maps of these alloys revealed that the maximum efficiency was between 60 % and 70 % for all the alloys except for the alloy with 0.06 wt.% Sn, which showed a low value of 40 %.
- The instability maps generated for the alloys showed (i) only one instability regime in the alloy with 0.06 wt.% Sn and (ii) very narrow processing regimes for the alloy with 0.1 wt.% Sn.
- Instability during deformation is mainly driven by shear band formation and/or inter-crystalline cracking. The safe processing zones are regions characterized by DRX.

The investigations carried out show the influence of microalloying Al–5.9wt.%Cu–0.5wt.%Mg alloy with Sn on its microstructure, mechanical properties and hot deformation behavior. It is evident that heat-treatment and/or mechanical working of the as-cast alloy is necessary in order to obtain alloys with improved microstructure and mechanical properties. Microalloying the base alloy with 0.06 wt.% Sn resulted in an alloy exhibiting the best combination of mechanical properties among all the alloys investigated. Strengthening occurs in these alloys by the precipitation of the $CuAl_2$ phase.

Microstructural investigation of the hot worked samples in conjunction with modeling studies provided a deep insight on the metallurgical changes occurring during hot deformation in these alloys. The safe processing zone for these alloys has a strong dependence on Sn content. The safe processing zone narrowed for alloys with Sn wt.% higher than 0.06. Excellent prediction of flow stress as a function of temperature, strain and strain rate by the ANN modeling showed the superiority of this technique for flow stress prediction of these alloys.

5.2 Scope for future work

The present investigations were focused on understanding the influence of trace additions of Sn to a commercially available Al-Cu-Mg alloy which is considered to be a high strength light weight alloy. The considerable improvement achieved in the microstructure and mechanical properties shows the advantage of microalloying of Al alloys with Sn. These investigations have not only yielded many interesting results but have also pointed towards several possible directions of further research. Some of these are enumerated below:

1. For high temperature deformation behavior of the investigated alloy system, flow stress can be modeled in terms of strain, strain rate, deformation temperature and percentage of Sn additions *i.e.* $\sigma = f(\varepsilon, \dot{\varepsilon}, T, composition)$. The superiority of the ANN modeling over MLR method shows that the former is the appropriate technique for such investigation.
2. The present high temperature deformation studies are limited to high temperature compression tests. It would be interesting to extend this work to high strain rates (~ 10 to 100 s^{-1}) and over a wider temperature range.
3. Further investigation of these alloys under high resolution TEM would throw more light on the nature of the various phases present in these alloys under various heat treatment conditions.
4. Determination of other properties such as fracture toughness, fatigue behavior, corrosion resistance and elevated temperature creep properties would help in assessing the potential of these alloys for light weight structural applications.
5. Effect of microalloying Al alloys with elements other than Sn is worthy of investigation, due to the immense potential to tailor the mechanical properties of these materials.

References

[AASMANUL] User manual, *Analytical methods*, Flame atomic absorption spectrometry (AAS) (Make: VARIAN, The Netherlands, Model: SPECTRA DUO).

[ABOU2005] Abou El-khair M.T, *Materials Letters* **59** (2005) 894.

[ALUMMATT] www.aluminium.matter.org.uk

[ASMHVOL2] ASM handbook, *Properties and Selection: Nonferrous Alloys and Special-Purpose Materials(a)*, ASM international **2** (1990).

[ASMHVOL4] ASM handbook, *Heat treatments*, ASM international **4** (1991).

[ASMHVOL9] ASM handbook, *Metallography and microstructures*, ASM international **9** (1985).

[ASTM1997] Annual handbook on ASTM standards, *Metals test methods and analytical procedures*, vol. 03.01 section **3** (1997).

[AUGI1978] J. A. Augis and J. E. Bennett, *Journal of thermal analysis* 13 (1978) 283.

[AVRA1939] M. Avrami, *Journal of Chemical Physics* **7** (1939) 1103.

[AVRA1940] M. Avrami, *Journal of Chemical Physics* **8** (1940) 212.

[AVRA1941] M. Avrami, *Journal of Chemical Physics* **9** (1941) 177.

[BARD2003] F. Bardi, M. Cabibbo, E. evangelista, S. Spigarelli and M. Vukcevic, *Material Science and Engineering A* **339** (2003) 43.

[BASS2008] Paola Bassani, E. Gariboldi and D. Ripamonti, *Journal of Thermal Analysis and Calorimetry* **91** (2008) 29.

[BEFF1995] O. Beffort, C. Solenthaler, P.J. Uggowitzer and M.O. Speidel, *Material Science and Engineering A* **191** (1995) 121.

[BERL2000] L.B. Ber, *Material Science and Engineering A* **280** (2000) 91.

[BHAD2007] H. K. D. H. Bhadeshia, *Solid Solutions: The Hume-Rothery Rules*, (2007).

[BJØR2001] Bjørn Rønning and Nils Ryum, *Metallurgical and Materials Transations A* **32** (2001) 769.

[BOCH2007] L.L. Rokhlin, N.R. Bochvar, N.P. Leonova and E.V. Lysova, *Russian Metallurgy (Metally)* **2007** (2007) 331.

[CAVA2002] P. Cavaliere, *Journal of Light Metals* **2** (2002) 247.

[CERR2002] E. Cerri, S. Spigarelli, E. Evangelista and P. Cavaliere, *Material Science and Engineering A* **324** (2002) 157.

[CERR2007] E. Cerri, P. Leo and P.P. De Marco, *Journal of Materials Processing Technology* **189** (2007) 97.

[CHAK1998] D.J. Chakrabarti, B.K. Cheong and D.E. Laughlin, *Automotive Alloys II*, TMS, Warrendale, PA (1998).

[CHAT1973] D.K. Chatterjee and K.M. Entwistle, *Journal of the Institute of Metals* **101** (1973) 53.

[CHEN2008] Z.Y. Chen, S.Q. Xu and X.H. Dong, *Acta Metallurgica Sinica (English Letters)* **21(6)** (2008) 451.

[CHOJ2001] J.R. Cho, W.B. Bae, W.J. Hwang and P. Hartley, *Journal of Materials Processing Technology* **118** (2001) 356.

[DAVI2005] David A. Freedman, *Statistical Models: Theory and Practice*, Cambridge University Press. (2005).

[DENN1982] R. Dennis Cook, *Sociological Methodology* **13** (1982) 313.

[DONO1983] A. Varschavsky and E. donoso, *Thermochimica Acta* **69** (1983) 341.

[DONO1985] E. donoso, *Material Science and Engineering A* **74** (1985) 39.

[DORN1961] P. Ward Flynn, J. Mote and J.E. Dorn, *Trans. Met. Soc. AIME* **221** (1961) 1148.

[ELAG2007] V.I. Elagin, *Metal Science and Heat Treatment* **49** (2007) 427.

[EMAD2002] D. Emadi, L.V. Whiting, V.Y. Gertsman and M. Sahoo, *AFS Transactions* 06-**118** (2002) 1.

[ESABNAUS] www.esabna.com

[EVAN1990] E. Evangelista, A. Forcellesa, F. Gabrielli and P. Mengucci, *Journal of Materials Processing Technology* **24** (1990) 323.

[FROS1982] H.J. Frost and M.F. Ashby, *Deformation Mechanism Maps*, New York and Oxford, Pergamon Press. (1982).

[GABA2007] A. Gabar, M. A. Gaffar, M.S. Mostafa and E. F. Abo Zeid, *Journal of Alloys and Compounds* **429** (2007) 167.

[GAND1982] C.Gandhi, *Metallurgical Transactions A* **13** (1982) 1233.

[GANG2009] Meng Gang, Li Bolong, Li Hongmei, Huang Hui and Nie Zuoren,

Material Science and Engineering A **517** (2009) 132.

[GARG1993] A. Garg, Y. C. Chang and J. M. Howe, *Acta Materialia* **41(1)** (1993) 235.

[GEOR1988] George E. Dieter, *Mechanical Metallurgy*, SI Metric edition (1988).

[GHOL2009] A. Gholamzadeh and A. Karimi Taheri, *Mechanics Research Communications* **36** (2009) 252.

[GHOS1980] A.K. Ghosh, *Acta Metallurgica* **28** (1980) 1443.

[GUPT1988] A.K. Gupta, A.K. Jena and M.C. Chaturvedi, *Scripta Metallurgica* **22** (1988) 369.

[GUPT1999] A.K. Gupta and D.J. Lloyd, *Metallurgical and Materials Transations A* **30** (1999) 879.

[HALL1951] E.O. Hall, *Proceedings of the Physical Society*, London **643** (1951) 747.

[HANS1982] N. Hansen and B. Ralph, *Acta Metallurgica* **30** (1982) 411.

[HARD1951] H.K. Hardy, *Journal of the Institute of Metals* **80** (1951-52) 483.

[HARD1953] H.K. Hardy, *Journal of the Institute of Metals* **82** (1953-54) 236.

[HARD1954] H. K. Hardy and T. J. Heal, *Progress in Metal Physics*, Paragon Press, Oxford. **5** (1954).

[HEIN2000] A. Heinz, A. Haszler, C. Keidel, S. Moldenhauer, R. Benedictus and W.S. Miller, *Material Science and Engineering A* **80** (2000) 102.

[HIRA1964] K. Hirano and H. Iwasaki, *Trans. Jpn Inst. of Met*. **5** (1964) 162.

[HIRO2000] S. Hirosawa, T. Sato, A. Kamio and H.M. Flower, *Acta Materialia* **48**

(2000) 1797.

[HONG1999] YI Hong-kun and ZHENG Zi-qiao, *Journal of Central South University of Technology: Natural science* **30(3)** (1999) 292.

[HORN2001] Erhard Hornbogen, *Journal of Light Metal* **1** (2001) 127.

[HTCH2000] C.R. Htchinson, X. Fan, S.J. Pennycock and G.J. Shiflet, *Materials Science Forum* **331-337** (2000) 965.

[HUME1942] J. H. Frye and W. Hume-Rothery, *Proceedings of the Royal society*, London **181** (1942) 1.

[HUTC2000] C.R. Hutchinson and S.P. Ringer, *Metallurgical and Materials Transations A* **31** (2000) 2721.

[JENA1989] A.K. Jena, A.K. Gupta and M.C. Chaturvedi, *Acta Metallurgica* **37** (1989) 885.

[JOHN1939] W.A. Johnson and K.F. Mehl, *Trans. TMS AIME* **135** (1939) 416.

[JONA1969] J.J.Jonas, C.M.Sellars and W.J.McG.Tegart, *Metall. Rev*. **14(1)** (1969) 1.

[JONE2003] M.J. Jones and F.J. Humphreys, *Acta Materialia* **51** (2003) 2149.

[KAIB2001] R. Kaibyshev, I. Kazakulov, D. Gromov, F. Musin, D.R. Lesuer and T.G. Nieh, *Scripta Materialia* **44** (2001) 2411.

[KAIB2002] R. Kaibyshev, O. Sitdikov, I. Mazurina and D.R. Lesuer, *Material Science and Engineering A* **334** (2002) 104.

[KAIS2008] M.S. Kaiser, S. Datta, A. Roychowdhury and M.K. Banerjee, *Journal of Materials Engineering and Performance* **17(6)** (2008) 902.

[KEYMETAL] www.keytometals.com

[KISS1957] H. E. Kissinger, *Analytical Chemistry* **29** (1957) 1702.

[KUMA1987] A.K.S. Kalyan Kumar, MS Thesis, Indian Institute of Science, Bangalore, India. (1987).

[KUTU1996] V.V. Kutumba Rao and T. Rajagopalachary, *Bulletin of Material Science* **19** (1996) 677.

[LIAN2008] Liang Wen-jie, Pan Qing-lin, He Yun-bin, Li Yun-chun and Zhang Xiao-gang, *Journal of Central South University and Technology* **15** (2008) 289.

[LIVA1982] R.J. Livak, *Metallurgical Transactions A* **13** (1982) 1318.

[LUOA1993] A. Luo, D.J. Lloyd, A. Gupta and W.V. Youdelis, *Acta Metallurgica et Materialia* **41** (1993) 769.

[LUTO1969] M.J. Luton and C.M. Sellars, *Acta Metallurgica* **17** (1969) 1033.

[MCQU1990] H.J. McQueen, E. Evangelista and N.D. Ryan, *Proc. Recrystallization, Ed. T. Chandra, TMS-AIME*, Warrendale, Pa. (1990).

[MCQU2002] H.J. McQueen and N.D. Ryan, *Material Science and Engineering A* **322** (2002) 43.

[MCQU2005] H.J. McQueen and M.E. Kassner, *Material Science and Engineering A* **410** (2005) 58.

[MEDI1996] S.F. Medina and C.A. Hernandez, *Acta Materialia* **44(1)** (1996) 137.

[METHVOL2] Metals handbook: *Properties and selections: Non-ferrous alloys and pure metals*, 9th edition, H. Baker, Managing Editor, American Society for Metals. **2** (1979).

[MIAO2000] W.F. Miao and D.E. Laughlin, *Metallurgical and Materials Transactions A* **31** (2000) 361.

[MOHA2008] A.M.A. Mohamed, F.H. Samuel, A.M. Samuel, H.W. Doty and S. Valtierra, *Metallurgical and Materials Transactions A* **39** (2008) 490.

[MOND1976] L.F. Mondolfo, *Aluminum Alloys, Structure and Properties*. London: Butterworths. (1976).

[MUKH1999] A.K. Mukhopadhyay, *Scripta Materialia* **41(6)** (1999) 667.

[MURA1991] R.V. Muraleedharan, *Journal of thermal analysis* **37** (1991) 2729.

[MURA2001] M. Murayama, K. Hono, *Scripta Materialia* **44(4)** (2001) 701.

[NAGA2007] P. Naga Raju, K. Srinivasa Rao, G.M. Reddy, M. Kamaraj and K. Prasad Rao, *Material Science and Engineering A* **464** (2007) 192.

[NARA2000] S.V.S. Narayana Murty, B. Nageshwara Rao and B.P. Kashyap, *International Materials Reviews* **45** (2000) 15.

[NIEJ2001] J.F. Nie and B.C. Muddle, *Material Science and Engineering A* **319-321** (2001) 448.

[OCEN2001] Vladivoj Ocenasek and Margarita Slamova, *Materials Characterization* **47** (2001) 157.

[OMAR1996] A. Al Omar, J.M. Cabrera and J.M. Prado, *Scripta Materialia* **34** (1996) 1303.

[OROW1948] E. Orowan, *Symp. Int. Stress, J. Met*. (1948) 451.

[PAPA1981] John M. Papazian, *Metallurgical Transations A* **12** (1981) 269.

[PAPA1982] John M. Papazian, *Metallurgical Transations A* **13** (1982) 761.

[PATR2002] Patricia Donnadieu, Guy F. Dirras and Joel Douin, *Materials Science Forum* **396-402** (2002) 1019.

[PETC1953] N.J. Petch, *Journal of the Iron and Steel Institute. London* **173** (1953) 25.

[POLM1952] I.J. Polmear and H.K. Hardy, *Journal of the Institute of Metals* **81** (1952-53) 427.

[PRAS1984] Y.V.R.K. Prasad, H.L. Gegel, S.M. Doraivelu, J.C. Malas, J.T. Morgan, K.A. Lark and D.R. Barker, *Metallurgical Transactions A* **15** (1984) 1883.

[PRAS1990] Y.V.R.K.Prasad, *Indian Journal of Technology* **28** (1990) 435.

[PRAS1991] Y.V.R.K Prasad and N. Ravichandran, *Bulletin of Material Science* **14** (1991) 1241.

[PRAS1997] Y.V.R.K. Prasad and S. Sasidhara, *Hot Working Guide: A Compendium of Processing Maps*, ASM International, Materials Park, OH. (1997).

[PRAS2000] Y.V.R.K. Prasad, T. Seshacharyalu, S.C. Medeiors and W.G. Frazier, *Material Science and Technology* **16** (2000) 511.

[QING2009] Xiao Yan Liu, Qing Lin Pan, Yun Bin He, Wen Bin Li, Wen Jie Liang, and Zhi Min, *Material Science and Engineering A* **500** (2009) 150.

[RAJA1997] T.V. Rajan, C.P. Sharma and Ashok Sharma, *Heat treatment - Principles and techniques*, 7th printing - revised edition. (1997).

[RAJR1981] Rishi Raj, *Metallurgical Transactions* **12A** (1981) 1089.

[RAMA2006] S. Ramanathan, R. Karthikeyan, V. Deepak Kumar and G. Ganesan, *J. Material Science and Technology* **22(5)** (2006) 611.

[RAOK1990] K.P. Rao, Y.V.R.K. Prasad and K. Sivaram, *Materials Letters*. **10(1)** (1990) 66.

[RAVI1991] N. Ravichandran and Y.V.R.K Prasad, *Metallurgical Transactions A* **22** (1991) 2339.

[REIC1998] L. Reich, M. Murayama and K. Hono, *Acta Materialia* **46** (1998) 6053.

[REIC1999] L. Reich, S.P. Ringer and K. Hono, *Philosophical Magazine Letters A* **79** (1999) 639.

[RING1995] S.P. Ringer, K. Hono and T. Sakurai, *Metallurgical and Materials Transactions A* **26** (1995) 2207.

[RING2000] S.P. Ringer and K. Raviprasad, *Materials Forum* **24** (2000) 59.

[ROBE1984] W. Roberts, *Deformation Processing and Structure*, Ed. G. Krauss, ASM, Metals Park, OH. (1984).

[ROBI2003] P.S. Robi and U.S. Dixit, *Journal of Materials Processing Technology* **142** (2003) 289.

[ROKH2007] L.L. Rokhlin, T.V. Dobatkina, N.R. Bochvar, E.V. Lysova and I.E. Tarytina, *Russian Metallurgy (Metally)* **2007** (2007) 335.

[RYEN2006] Øyvind Ryen, Oscar Nijs, Emma SjÖlander, BjØrn holmedal, Hans-Erik EkstrÖm, and Erik Nes, *Metallurgical Transactions A* **37** (2006) 1999.

[SAKA1984] T.Sakai and J.J. Jonas, *Acta Metallurgica* **32** (1984) 189.

[SAKU1992] T. Sakurai and T. Eto, Aluminum alloys: Their physical and mechanical

properties, *Proc. 3rd Int. Conf. Aluminum* (eds. L. Arnberg, O. Lohne, E. Nes and N. Ryum) **1** (1992) 208.

[SARK1990] S. B. Sarkar and H.S. Ray, *Journal of thermal analysis* **36** (1990) 231.

[SATI1993] Satish V. Kailas, Y.V.R.K. Prasad and S.K. Biswas, *Metallurgical Transactions A* **24** (1993) 2513.

[SATO2003] Tatsuo Sato, Shoichi Hirosawa and Kiyoshige Hirose, *Metallurgical and Materials Transactions A* **34** (2003) 2745.

[SCHA2001] G.B. Schaffer, S.H. Huo, J. Drennan and G.J. Auchterlonie, *Acta Materialia* **49** (2001) 2671.

[SCHM1981] C.G. Schmidt and A.K. Miller, *Res. Mech.* **3** (1981) 108.

[SELL1966] C.M. Sellars and W.J. McG. Tegart, *Mem. Sci. Rev. Metall.* **63** (1966) 731.

[SERC1999] T.B. Sercombe and G.B. Schaffer, *Material Science and Engineering A* **268** (1999) 32.

[SHAO2008] Y. Wang, W.Z. Shao, L. Zhen, L. Yang and X.M. Zhang, *Material Science and Engineering A* **497** (2008) 479.

[SILC1955] J.M. Silcock, T.J. Heal and H.K. Hardy, *Journal of the Institute of Metals* **84** (1955) 23.

[SILC2002] J.M. Silcock and H.M. Flower, *Scripta Materialia* **46** (2002) 389.

[SMIT1998] George W. Smith, *Thermochimica Acta*. **317** (1998) 7.

[SMIT1999] Tracy J. Smith, Hans J. Maier, Huseyin Sehitoglu, Eric Fleury and John Allison, *Metallurgical and Materials Transations A* **30** (1999) 133.

[SPIG2003] S. Spigarelli, M. Cabibbo, E. Evangelista and J. Bidulska, *Journal of Materials Science* **38** (2003) 81.

[STAR2004] M.J. Starink, N. Gao, and J.L. Yan, *Material Science and Engineering A* **387-389** (2004) 222.

[STYL1994] C.M. Styles, I. Sinclair, P.J. Gregson and S.M. Flitcroft, *Material Science and Technology* **10** (1994) 475.

[SUBSTECH] www.substech.com

[SUKU2008] K. Sukumaran, K.K. Ravikumar, S.G.K. Pillai, T.P.D. Rajan, M. Ravi, R.M. Pillai, B.C. Pai, *Material Science and Engineering A* **490** (2008) 235.

[SULL1949] A.H. Sully, H.K. Hardy and T.J. Heal, *Journal of the Institute of Metals* **76** (1949) 269.

[SUZU1980] H. Suzuki, M. Kanno and G. Itoh, *Journal of Japan Institute of Light metals* **30** (1980) 609.

[TAKU1998] H. Takuda, H. Fujimoto and N. Hatta, *Journal of Materials Processing Technology* **80-81** (1998) 513.

[TALE1998] Eric M. Taleff, Gregory A, Henshall, T.G. Nieh, Donald R. Lesuer and Jeffrey Wadsworth, *Metallurgical and Materials Transactions A* **29** (1998) 1081.

[TAMI1992] M. Tamizifar and G.W. Lorimer, Aluminum alloys: Their physical and mechanical properties, *Proc. 3rd Int. Conf. Aluminum* (eds. L. Arnberg, O. Lohne, E. Nes and N. Ryum) **1** (1992) 220.

[TAYL1978] J.A. Taylor, B.A. Parker and I.J. Polmear, *Metal Science Journal* **12**

(1978) 478.

[TEGA1968] W.J. McG. Tegart, "Ductility" Chap. 5, *American Society of Metals*, Metals Park, Ohio. (1968).

[THOM1969] D. S. Thompson, *Thermal Analysis*, Academic Press, New York. **2** (1969) 1147.

[USPATENT] U.S. Patent 3,263,484.

[VENU1993] S.Venugopal, S.L.Mannan and Y.V.R.K.Prasad, *Material Science and Engineering A* **60** (1993) 63.

[VESN2003] Vesna Maksimovic, Slavica Zec, Velimir Radmilovic and Milan T. Jovanovic, *Journal of the Serbian Chemical Society* **68(11)** (2003) 893.

[VIET1966] J.T. Vietz and I.J. Polmear, *Journal of Institute of Metals* **94(12)** (1966) 410.

[VONC2007] Maja Voncina, Primoz Mrvar, Franc Zupanic and Jozef Medved, *Materials and Geoenvironment* **54** (2007) 457.

[WANG2005] S.C. Wang and M.J. Starink, *International Materials reviews* **50** (2005) 193.

[WANG2007] Guiqing Wang, Qingzhou Sun, Li Shan, Zhongkui Zhao and Liu Yan, *Journal of Materials Engineering and Performance* **16(6)** (2007) 752.

[WANG2008] J. Wang, D. Yi, X. Su and F. Yin, *Materials Characterization* **59** (2008) 965.

[WENS2009] S.P. Wen, Z.B. Xing, H. Huang, B.L. Li, W. Wang and Z.R. Nie, *Material Science and Engineering A* **516** (2009) 42.

[WILL1997] William D. Callister Jr., *Material science and engineering: An introduction*, 4th edition, John Wiley & Sons, Inc. (1997).

[WILM1906] Wilm A, DRP 244554 (German patent) (1906).

[WUND1990] B. Wunderlich, *Thermal Analysis*, Academic Press, New York. (1990).

[XIAO2009] Xiao Yan Liu, Qing Lin Pan, Cong Ge Lu, Yun Bin He, Wen Bin Li and Wen Jie Liang, *Material Science and Engineering A* **525** (2009) 128.

[YANG2006] Yang Hui, Li Zhen-hong and Zhang Zhi-liang, *Journal of Zhejiang University Science A* **7(8)** (2006) 1453.

[YANG2008] Yang Sheng, YI Danqing, Zhang Hong and YAO Sujuan, *Journal of Wuhan University of Technology-Mater. Sci*. Ed. **23(5)** (2008) 694.

[YUAN2000] G.C. Yuan, Z.J. Li, Y.X. Lou and X.M. Zhang, *Material Science and Engineering A* **280** (2000) 108.

[YULI2004] K. Yu, W. Li, S. Li and J. Zhao, *Material Science and Engineering A* **368** (2004) 88.

[ZAHR1974] A. M. Zahra and M. Lafitte, *Scripta Metallurgica* **8** (1974) 165.

[ZAHR1975] A. M. Zahra and C. Y. Zahra, *Scripta Metallurgica* **9** (1975) 879.

[ZAKH2003] V.V. Zakharov, *Metal Science and Heat Treatment* **45** (2003) 246.

[ZENE1944] C. Zener and J.H. Holloman, *Journal of Applied Physics* **15** (1944) 22.

[ZHAN2000] B.L. Zhang, M.S. Maclean and T.N. Baker, *Material Science and Technology* **16** (2000) 897.

[ZHAN2007] Hui Zhang, Luoxing Li, Deng Yuan and Dashu Peng, *Material*

Characterization **58** (2007) 168.

[ZHAO1994] D. Zhao, P.K. Chaudhury, M. Thirukkonda and J.J. Valencia, *Intermetallic Matrix Composites III*, (eds. J.J.Graves, R.R.Bowman and J.J.Lewandowski), Pittsburgh, Materials Research Society. **350** (1994) 273.

[ZHEN1996] ZHENG Zi-qiao, YIN Den-feng and TAN Chen-yu, *Journal of Central South University of Technology: Natural science* **27(6)** (1996) 695.

[ZHEN1998] ZHENG Zi-qiao, HUANG Bi-ping and YIN Den-feng, *Journal of Central South University of Technology: Natural science* **29(1)** (1998) 42.

[ZHON2006] LI Hui-zhong, ZHANG Xin-ming, CHEN Ming-an and ZHOU Zhuo-ping, *Journal of Central South University of Technology* **13** (2006) 130.

[ZIEG1965] H. Ziegler, *Progress in Solid Mechanics*, (ed. I.N. Sneddon and R. Hill), John Wiley & Sons. 4, New York. (1965).

[ZURA1997] J.M. Zurada, *Introduction to Artificial Neural systems*, Jaico Publishing House, Delhi. (1997).

List of Publications

International Journals:

1. Sanjib Banerjee, P. S. Robi, A. Srinivasan and Praveen Kumar Lakavath, High Temperature Deformation Behavior of Al–Cu–Mg Alloys Microalloyed with Sn, *Materials Science and Engineering A*. **527** (2010) 2498-2503.

2. Sanjib Banerjee, P. S. Robi, A. Srinivasan and Praveen Kumar Lakavath, Effect of Trace Additions of Sn on Microstructure and Mechanical Properties of Al–Cu–Mg Alloys, *Materials and Design*. **31** (2010) 4007-4015.

3. Sanjib Banerjee, P. S. Robi and A. Srinivasan, Calorimetric Study of Precipitation Kinetics of Al–Cu–Mg and Al–Cu–Mg–0.06 wt.% Sn Alloys, *Metals and Materials International*. (Accepted, DOI: 10.1007/s12540-010-0802-4).

4. Sanjib Banerjee, P. S. Robi and A. Srinivasan, Constitutive Modeling for High Temperature Flow Behavior of Al–6.2%Cu–0.6%Mg Alloys with Trace Additions of Sn, *Metallurgical and Materials Transactions A*. (Communicated).

International Conference Proceedings:

1. Sanjib Banerjee, P. S. Robi, A. Srinivasan and Praveen Kumar Lakavath, Study on Micro Structural and Mechanical Properties of Al–Cu–Mg Alloys Microalloyed with Sn in Cast, Annealed and Rolled Conditions, *Proceedings of the International Conference: 63rd Annual Technical Meeting of "The Indian Institute of Metals" (NMD-ATM 2009), November 14-17, 2009, Page 226-227, Kolkata, West Bengal.*